

ANALYSIS OF CONJUGATE HEAT TRANSFER AND PRESSURE DROP IN MICROCHANNELS FOR DIFFERENT ASPECTS RATIOS

by:

MARC ROBERT GREENLAND

Submitted in partial fulfilment of the requirement for the degree

MASTERS IN ENGINEERING

in the:

Department of Mechanical and Aeronautical Engineering

Faculty of Engineering, Built Environment and Information Technology

University of Pretoria



UNIVERSITEIT VAN PRETORIA
UNIVERSITY OF PRETORIA
YUNIBESITHI YA PRETORIA

04 March 2016

ABSTRACT

Title: Analysis of Conjugate Heat Transfer and Pressure Drop in Microchannels for Different Aspect Ratios

Author: Marc Robert Greenland (Student number: 25086457)

Supervisors: Dr J. Dirker and Prof J.P. Meyer (co-supervisor)

Department: Mechanical and Aeronautical Engineering

University: University of Pretoria

Degree: Master of Engineering (Mechanical Engineering)

In this study the heat transfer and hydrodynamic parameters were experimentally investigated for a single microchannel housed in a stainless steel solid base material for different aspect ratios in the laminar regime with water as the working fluid. The stainless steel base material had a low thermal conductivity (15.1 W / mK) which magnified the conjugative effects in order to better understand the heat transfer. Rectangular microchannels with a height and width of $0.64 \text{ mm} \times 0.41 \text{ mm}$ for Test Section 1, $0.5 \text{ mm} \times 0.5 \text{ mm}$ for Test Section 2 and $0.43 \text{ mm} \times 0.58 \text{ mm}$ for Test Section 3 were considered. The overall width of the solid substrate was 1.5 mm and the length was 50 mm for all of the test sections. The aspect ratio of the channel and the solid substrate was kept equal. A constant heat flux of 10 W / cm^2 was applied to the bottom outer wall of the test section. A sudden contraction inlet and a sudden expansion outlet manifold contained pressure ports, to measure the pressure drop across the test sections, and thermocouples measured the mean inlet and outlet fluid temperatures. Thermocouples were used to measure the outer top and side wall temperatures at four equally spaced positions along the axial direction. The amount of axial heat conduction was below 0.6% for all of the test sections and therefore warranted the use of a two-dimensional conduction model to determine the heat transfer parameters at the fluid to solid interface based on the outer measured wall temperatures. The local Nusselt number decreased, along the axial direction but increased towards the exit for all of the test sections. The average Nusselt number increased with the flow rate and the critical Reynolds number for fully turbulent flow Test Section 1 was 1950, for Test Section 2 was 2250 and for Test Section 3 was 1650. The average Nusselt number was directly related to the perimeter of the microchannels' two side walls and the bottom wall (not the top wall), and thus decreased as the aspect ratio of the channel increased. The experimentally determined Nusselt numbers were larger for all three test sections when compared to common acceptable correlations. The friction factor decreased with the flow rate and was smaller in magnitude when compared to conventional theories. The diabatic friction factor magnitudes were smaller than the adiabatic friction factors. The friction factor decreased as the aspect ratio decreased, where the aspect ratio was calculated by taking the

maximum of the microchannels width or height, divided by the minimum of the two. The possibility of a relationship could exist between the Colburn j-factor and the friction factor when considering the results for Test Section 1 and Test Section 2 but the results for Test Section 3 were significantly different.

Keywords: microchannel, heat transfer, pressure drop, single phase, laminar, stainless steel, water

PUBLICATIONS

Greenland, MR, Dirker, J, and Meyer, JP, (2012). Conjugate Three-Dimensional Numerical Analysis of Heat Transfer in a Minichannel with Changing Geometrical Constraints and Thermal Conductivity. 8th South African Conference on Computational and Applied Mechanics SACAM, 3-5 September 2012

Article submitted for review to an international journal in parallel to the examination of the main dissertation: Greenland, MR, Dirker, J, Meyer, JP. Analysis of Heat Transfer in Microchannels for Different Aspects Ratios with Negligible Axial Conduction.

ACKNOWLEDGMENTS

I would like to thank the following people/institutions for their support during my studies:

- My parents for all their support and encouragement throughout the years.
- My beautiful wife for being my pillar of strength, encourager and listening ear. Thank you for understanding when I had to spend many hours working and for all the proof reading. You are the best.
- To Dr. Dirker for all his guidance, patience and encouragement. It was a pleasure completing my studies under him.
- To Prof. Meyer for his knowledge and financial support throughout my studies.
- To my close friends and family for all your prayers, advice and support.
- To all the funding institutions which made this study possible.

TABLE OF CONTENTS

Abstract.....	i
Publications	iii
Acknowledgments.....	iii
List of Figures	vii
List of Tables	x
Nomenclature	xi
1. Chapter 1 – Introduction	1
1.1. Background.....	1
1.2. Problem Statement	2
1.3. Objective.....	3
1.4. Dissertation Layout	4
2. Chapter 2 – Literature Study	5
2.1. Introduction	5
2.2. Heat Transfer in Microchannels - Review.....	5
2.3. Pressure Drop and Friction Factor for Microchannels - Review.....	6
2.4. Conjugate Heat Transfer.....	6
2.5. The Effect of the Thermal Conductivity of the Solid Substrate on the Heat Transfer Rate.....	6
2.6. The Effect of Varying Geometric Parameters	7
2.7. Critical Reynolds Number	9
2.8. The Entrance Length of Thermal Developing Flow.....	9
2.9. The Effect of the Channel Surface Roughness	10
2.10. Viscous Dissipation within Microchannels	10
2.11. Summary of the Literature Study.....	11
3. Chapter 3 – Test Section and Test Facility Design	12
3.1. Introduction	12
3.2. Geometric and Physical Parameters for the Microchannel	12
3.3. Numerical Analysis of the Microchannel Test Section	14
3.4. Analytical Calculation of the Microchannel Test Sections.....	20
3.5. Microchannel Test Section Design and Construction	22
3.6. Insulation of the Test Section.....	32
3.7. Microchannel Test Facility Design.....	32
3.8. Instrumentation Calibration	36



3.9.	Summary of the Test Section and Test Facility Design	38
4.	Chapter 4 – Test Procedure and Measured Results	39
4.1.	Introduction	39
4.2.	Experimental Procedure.....	39
4.3.	Experimental Results	40
4.4.	Pressure Drop Measurements	53
4.5.	Summary of the Test Procedure and Measured Results	54
5.	Chapter 5 – Data Reduction/Analysis	56
5.1.	Introduction	56
5.2.	Heat Transfer Coefficient	56
5.3.	Reynolds number and Prandtl Number	68
5.4.	Friction Factor	69
5.5.	Colburn J-Factor	70
5.6.	Energy Balance	70
5.7.	Uncertainty Analysis	71
5.8.	Summary of the Data Reduction/Analysis	72
6.	Chapter 6 – Data Reduction Results.....	73
6.1.	Introduction	73
6.2.	Energy Balance	73
6.3.	Friction Factor	74
6.4.	Heat Transfer.....	79
6.5.	Colburn J-Factor	90
6.6.	Summary of the Data Reduction Results	93
7.	Chapter 7 – Conclusion and Recommendations	95
7.1.	Conclusion	95
7.2.	Recommendations for Future Work	99
	References	100
Appendix A - Calculation of Dimensional Parameters For the Microchannel Test Section	A1
A1.	Introduction	A1
A2.	MatLab® Code.....	A1
A3.	Conclusion	A2
Appendix B - Numerical Analysis Used to Aid the Microchannel Test Section Design	B1
B 1.	Introduction	B1
B 2.	Numerical Model and Boundary Conditions	B1

B 3.	Verification and Validation of the Numerical Model	B4
B 4.	Conclusion	B6
Appendix C - Analytical Analysis Used to Aid the Microchannel Test Section Design		C1
C 1.	Introduction	C1
C 2.	Heat transfer calculations.....	C1
C 3.	Hydrodynamic Calculations.....	C3
C 4.	Conclusion	C5
Appendix D - Microchannel Test Setups and Arrangements		D1
D1.	Introduction	D1
D2.	Literature Study	D1
D3.	Conclusion	D5
Appendix E - Overview of Prior Test Section Designs Considered in this Investigation		E1
E1.	Introduction	E1
E 2.	Test Section Design Revision 1	E1
E 3.	Test Section Design Revision 2	E2
E4.	Conclusion	E3
Appendix F - Microchannel Fabrication Techniques		F1
F1.	Introduction	F1
F2.	Literature Study	F1
F3.	Conclusion	F2
Appendix G - Test Section Insulation Calculations		G1
G1.	Introduction	G1
G2.	Insulation Material Selection and Calculations	G1
G3.	Conclusion	G4
Appendix H - Uncertainty Analysis		H1
H 1.	Introduction	H1
H 3.	Uncertainty Theory.....	H1
H4.	Instrumentation Uncertainty	H2
H5.	Uncertainty of Common Parameters	H4
H 5.	Uncertainty of Numerical Model – Heat Transfer Coefficient.....	H9
H 7.	Conclusion and Uncertainty Results	H13

LIST OF FIGURES

Figure 1.1 Test section schematic layout	4
Figure 3.1 Microchannel geometric parameters	12
Figure 3.2 Peak temperature at different copper solid section heights (H_s) for different Re numbers.....	15
Figure 3.3 Peak temperature at different brass solid section heights (H_s) for different Re numbers.....	16
Figure 3.4 Peak temperature at different stainless steel solid section heights (H_s) for different Re numbers	17
Figure 3.5 Temperature profiles in x-y plane: $A_c = 0.25 \text{ mm}^2$, $Re = 2300$; (a) $H_s = 1 \text{ mm}$, $z = 10 \text{ mm}$; (b) $H_s = 1 \text{ mm}$, $z = 40 \text{ mm}$, (c) $H_s = 1.5 \text{ mm}$, $z = 10 \text{ mm}$, (d) $H_s = 1.5 \text{ mm}$, $z = 40 \text{ mm}$, (e) $H_s = 2 \text{ mm}$, $z = 10 \text{ mm}$, (f) $H_s = 2 \text{ mm}$, $z = 40 \text{ mm}$	18
Figure 3.6 Expected peak temperatures versus the Reynolds number, (a) $W_s = 1.5 \text{ mm}$ & $A_c = 0.25 \text{ mm}^2$, (b) $W_s = 1.5 \text{ mm}$ & $A_c = 0.5 \text{ mm}^2$, (c) $W_s = 1.5 \text{ mm}$ & $A_c = 0.75 \text{ mm}^2$, (d) $W_s = 1.5 \text{ mm}$ & $A_c = 1 \text{ mm}^2$	19
Figure 3.7 Mean Nusselt number versus Reynolds number for varying $H_s = 1 \text{ mm}$, $H_s = 1.5 \text{ mm}$ and $H_s = 2 \text{ mm}$	21
Figure 3.8 Fluid outlet temperature (a) and average channel surface temperature (b) versus Reynolds number for varying $H_s = 1 \text{ mm}$, $H_s = 1.5 \text{ mm}$ and $H_s = 2 \text{ mm}$	21
Figure 3.9 Differential pressure drop versus Reynolds number for varying $H_s = 1 \text{ mm}$, $H_s = 1.5 \text{ mm}$ and $H_s = 2 \text{ mm}$	22
Figure 3.10 Test section assembly: Inlet and outlet tubes; pressure taps; thermocouples; stainless steel microchannel; and heater test section housing	24
Figure 3.11 Top view of the microchannel test section assembly	25
Figure 3.12 Section view through line A-A showing the components of the microchannel test section assembly.....	25
Figure 3.13 Section view through line B-B showing the pressure port.....	25
Figure 3.14 Section view through line C-C showing the microchannel base and the microchannel lid.....	26
Figure 3.15 The microchannel assembly isometric view.....	27
Figure 3.16 Drawing of the thermocouple placement onto the stainless steel test section... ..	27
Figure 3.17 The microchannel assembly isometric view.....	28
Figure 3.18 Heater assembly: Heater element at the bottom and layered heater block	28
Figure 3.19 Stainless steel microchannel (a) machined using a sawing process, (b) machined using a drawing process	29
Figure 3.20 Clamping jig with drawing tool in milling machine	29
Figure 3.21 Complete assembled test section showing the inlet and outlet manifolds; the main test section body; heater power wire; and the thermocouples.....	30

Figure 3.22 Test Section 1 cross-section: (a) actual measured channel dimensions, (b) photograph of inlet side of the channel and (c) photograph of the outlet side of the channel	31
Figure 3.23 Test Section 2: (a) actual measured channel dimensions, (b) photograph of inlet side of the channel and (c) photograph of the outlet side of the channel.....	31
Figure 3.24 Test Section 3: (a) actual measured channel dimensions, (b) photograph of inlet side of the channel and (c) photograph of the outlet side of the channel.....	31
Figure 3.25 Schematic of the experimental test setup	33
Figure 3.26 Labelling/naming convention of the temperature measurements	37
Figure 4.1 Left side wall temperatures versus the thermocouple axial location for different flow rates: Test Section 1	41
Figure 4.2 Right side wall temperatures versus the thermocouple axial location for different flow rates: Test Section 1	42
Figure 4.3 Left side wall temperatures versus the thermocouple axial location for different flow rates: Test Section 2	42
Figure 4.4 Right side wall temperatures versus the thermocouple axial location for different flow rates: Test Section 2	43
Figure 4.5 Left side wall temperatures versus the thermocouple axial location for different flow rates: Test Section 3	44
Figure 4.6 Right side wall temperatures versus the thermocouple axial location for different flow rates: Test Section 3	44
Figure 4.7 Side temperatures difference versus the thermocouple axial location for different flow rates: Test Section 1	46
Figure 4.8 Side temperatures difference versus the thermocouple axial location for different flow rates: Test Section 2	46
Figure 4.9 Side temperatures difference versus the thermocouple axial location for different flow rates: Test Section 3	47
Figure 4.10 Average side wall temperature difference versus the microchannel offset distance within solid substrate.....	47
Figure 4.11 Top wall temperatures versus the thermocouple axial location for different flow rates: Test Section 1	48
Figure 4.12 Top wall temperatures versus the thermocouple axial location for different flow rates: Test Section 2.....	48
Figure 4.13 Top wall temperatures versus the thermocouple axial location for different flow rates: Test Section 3.....	49
Figure 4.14 Average wall temperature versus the volumetric flow rate for the different axial measuring locations: Test Section 1	50
Figure 4.15 Average wall temperature versus the volumetric flow rate for the different axial measuring locations: Test Section 2	51
Figure 4.16 Average wall temperature versus the volumetric flow rate for the different axial measuring locations: Test Section 3	51
Figure 4.17 Average wall temperature gradient versus the axial measuring locations for different flow rates.....	52

Figure 4.18 Difference between the inlet and outlet fluid temperatures versus the volumetric flow rate for the three different test sections	53
Figure 4.19 Diabatic and Adiabatic pressure drop over the test section versus the volumetric flow rate for the three different test sections: Test Section 1; Test Section 2; and Test Section 3	54
Figure 5.1 Labelling/naming convention of the temperature measurements	57
Figure 5.2 Percentage of axial conduction versus Reynolds number, based on the average fluid temperature	58
Figure 5.3 Symmetric numerical model showing the boundary conditions and the temperature measuring locations	59
Figure 5.4 Numerical model mesh: (a) Test Section 1, (b) Test Section 2, and (c) Test Section 3.....	60
Figure 5.5 0.50 mm offset analysis, (a) numerical model mesh, (b) temperature contour plot where $T_{\infty} = 50\text{ }^{\circ}\text{C}$ and $h = 25\text{ }000\text{ W/m}^2\text{K}$	62
Figure 5.6 0.0625 mm offset analysis, (a) numerical model mesh, (b) temperature contour plot where $T_{\infty} = 50\text{ }^{\circ}\text{C}$ and $h = 25\text{ }000\text{ W/m}^2\text{K}$	62
Figure 5.7 0.125 mm offset analysis, (a) numerical model mesh, (b) temperature contour plot where $T_{\infty} = 50\text{ }^{\circ}\text{C}$ and $h = 25\text{ }000\text{ W/m}^2\text{K}$	62
Figure 5.8 Symmetric analysis, (a) numerical model mesh, (b) temperature contour plot where $T_{\infty} = 50\text{ }^{\circ}\text{C}$ and $h = 25\text{ }000\text{ W/m}^2\text{K}$	64
Figure 5.9 Structure of the three-dimensional h-matrix.....	65
Figure 5.10 Flow diagram of the procedure to populate the h-matrix used in determining the heat transfer coefficient.....	66
Figure 5.11 Structure of the two-dimensional h-matrix after the interpolation based on the free stream temperature	67
Figure 6.1 Energy balance for Test Section 1, Test Section 2 and Test Section 3 across the Reynolds number measuring range	73
Figure 6.2 Hydrodynamic entrance length at specific Reynolds numbers for Test Section 1, Test Section 2 and Test Section 3	75
Figure 6.3 Diabatic and adiabatic friction factors versus the Reynolds number for the experimental data and Shah & London correlation, Test Section 1	77
Figure 6.4 Diabatic and adiabatic friction factors versus the Reynolds number for the experimental data and Shah & London correlation, Test Section 2	78
Figure 6.5 Diabatic and adiabatic friction factors versus the Reynolds number for the experimental data and Shah & London correlation, Test Section 3	78
Figure 6.6 Diabatic friction factors versus the Reynolds number for the experimental data for Test Section 1, Test Section 2 and Test Section 3	79
Figure 6.7 Local Nusselt numbers along the length of the microchannel test section for Reynolds number testing range – Test Section 1	80
Figure 6.8 Local Nusselt numbers along the length of the microchannel test section for Reynolds number testing range – Test Section 2	81
Figure 6.9 Local Nusselt numbers along the length of the microchannel test section for Reynolds number testing range – Test Section 3	82

Figure 6.10 Thermal entrance length over the Reynolds number testing range for Test Section 1, Test Section 2 and Test Section 3	84
Figure 6.11 Average experimental and theoretical Nusselt numbers over the Reynolds number (logarithmic axis) testing range for Test Section 1, Test Section 2 and Test Section 3.....	86
Figure 6.12 Average experimental Nusselt numbers over the Reynolds number testing range for Test Section 1, Test Section 2 and Test Section 3.....	88
Figure 6.13 Peak temperatures for a different channel aspect ratios and Reynolds numbers, analysis as performed in Section 3.3	89
Figure 6.14 Colburn j-factor versus the Reynolds number for the experimental data for Test Section 1, Test Section 2 and Test Section 3	91
Figure 6.15 Colburn j-factor and the friction factor versus the Reynolds number for the experimental data for Test Section 1, Test Section 2 and Test Section 3	92
Figure 6.16 Ratio of the Colburn j-factor to the friction factor across the Reynolds number for the experimental data for Test Section 1, Test Section 2 and Test Section 3	93

LIST OF TABLES

Table 3.1 Geometric and test section parameters range and specified values	14
Table 3.2 Dimensions of the three proposed microchannels to be fabricated	20
Table 3.3 Microchannel test section comparison between design and actual dimensions and the % deviation including the measuring uncertainty of 0.01 mm	32
Table 3.4 Measured parameter uncertainty summary	36
Table 3.5 Calibration coefficient and uncertainty for each thermocouple after calibration	38
Table 5.1 Numerically obtained wall temperatures for unsymmetrical channel layout and symmetric numerical model results	63
Table 5.2 Measured parameter uncertainty summary	71
Table 5.3 Uncertainties of the equations used for a specified range.....	71
Table 6.1 Summary of Reynolds numbers where the Nusselt number increased at the third and fourth measuring positions	83
Table 6.2 Test section dimensions and perimeter	90
Table 7.1 Summary of all the analysed/reduced results	98



NOMENCLATURE

A_c	Channel cross-sectional area	m^2
A_{flux}	Heater area	m^2
A_{ins}	Cross sectional area of the insulation	
A_s	Channel solid interface area	m^2
b	Constant	--
C	Calibration coefficient	--
$C_{,1,2,3,4}$	Correlation coefficient	---
c	Constant	--
Cp_f	Specific heat of the working fluid	kJ/kgK
Cp_s	Specific heat of the solid substrate	kJ/kgK
D_h	Hydraulic diameter	mm
D	Diameter	mm
f	Friction factor	--
f_{app}	Apparent friction factor	--
f_{dev}	Developing friction factor	--
G_z	Graetz number	--
H_c	Height of the channel	Mm
h	Convective heat transfer coefficient	W/m^2K
h_{ave}	Mean convective heat transfer coefficient	W/m^2K
$h_{i,inter}$	Interpolated convective heat transfer coefficient	W/m^2K
h_{inc}	Convective heat transfer coefficient increment	W/m^2K
h_{max}	Convective heat transfer coefficient, maximum	W/m^2K
h_{matrix}	Convective heat transfer coefficient, matrix	W/m^2K
H_s	Height of the solid substrate	Mm
h_{sur}	Convective heat transfer coefficient of the surrounding	W/m^2K
$,i$	Incremental step	--
I	Electrical current	Ampere
j	Colburn J-factor	--
$,j$	Incremental step	--
K	Constant	--
$,k$	Incremental step	--
K_n	Non-dimensionless number	-
K_{SC}	Sudden contraction pressure coefficient	--
K_{SE}	Sudden expansion pressure coefficient	--
k_f	Thermal conductivity of the working fluid	W/mK
k_{ins}	Thermal conductivity of the insulation	W/mK
$K(\infty)$	Hagenbach's factor	--
k_{plast}	Thermal conductivity of the test section housing	W/mK
k_s	Thermal conductivity of the solid substrate	W/mK
k_1, k_2	Constants	--
L	Length in axial direction of test section	mm
L_h	Hydrodynamic entrance length	mm
L_s	Test section channel length	mm
L_t	Thermal entrance length	mm
L^+	Dimensionless length	--
n	Number for averaging	--
m	Calibration gradient	$^{\circ}C/mm$
M	Axial conduction number	--
\dot{m}	Mass flow rate	kg/s
Nu	Nusselt number	--



$Nu_{,local}$	Local Nusselt number	--
Nu_m	Mean Nusselt number	--
Nu_∞	Developed Nusselt number	--
P	Perimeter	m
ΔP	Pressure drop	Pa
$\Delta P_{measured}$	Measure pressure drop	Pa
ΔP_{losses}	Pressure drop losses	Pa
Po	Poiseuille number	--
Pr	Prandtl number	--
q	Heat flux	W/m ²
q_f	Heat transfer in the working fluid	W/m ²
$Q_{conduction}$	Heat transfer due to conduction	W
$Q_{conduction,in}$	Heat transfer due to conduction, in	W
Q_{in}	Heat transfer rate in	W
Q_{loss}	Heat transfer rate lost to environment	W
Q_{out}	Heat transfer rate out	W
Q_{tot}	Total heat transfer	W
q_s	Heat transfer in the solid substrate	W/m ²
R	Uncertainty result	--
r_1, r_2, r_3	Radius of test section insulation layers	mm
Ra	Relative roughness	--
Re	Reynolds number	--
$Re_{,critical}$	Critical Reynolds number	--
R_{cond}	Thermal resistance for conduction	K/W
R_{conv}	Thermal resistance for convection	K/W
R_t	Thermal resistance	K/W
R_{tot}	Total thermal resistance	K/W
$R_{t,out}$	Thermal resistance based of the outlet fluid temperature	K/W
T	Temperature	°C
T_{ave}	Average temperature	°C
$T_{\infty,inc}$	Free stream temperature increment	°C
$T_{\infty,max}$	Free stream temperature maximum	°C
T_∞	Free stream temperature	°C
T_{bulk}	Bulk fluid temperature	°C
$T_{cal,therm}$	Calibrated thermocouple temperature	°C
T_{DAQ}	Temperature measured by DAQ	°C
T_{dif}	Difference between the outlet and inlet mean fluid temperature	°C
T_f	Mean temperature of the working fluid	°C
ΔT_f	change in mean temperature of working fluid	°C
T_{in}	Mean inlet fluid temperature	°C
T_{max}	Maximum temperature within the solid substrate	°C
$T_{\infty,interp}$	Interpolated free stream temperature	°C
T_{out}	Mean outlet fluid temperature	°C
T_{pt100}	PT 100 temperature	°C
T_s	Mean surface temperature	°C
ΔT_s	Change in surface temperature	°C
T_{side1}	Side wall temperature 1	°C
T_{side2}	Side wall temperature 2	°C
$T_{side,i,interp}$	Side wall interpolated temperature	°C
$T_{side,ave,i,measured}$	Measured average side wall temperatures	°C
$T_{side,ave}$	Average side wall temperature	°C
T_{sur}	Ambient temperature	°C
T_{top}	Top wall temperature	°C
$T_{top,i,interp}$	Top wall interpolated temperature	°C



$T_{top,i,measured}$	Measured top wall temperatures	°C
$T_{wetted\ sur}$	Wetted surface temperature	°C
u	Mean velocity in x co-ordinate	m/s
v	Mean velocity in y co-ordinate	m/s
V	Fluid velocity	m/s
ΔV	Electrical potential difference	volts
w	Mean velocity in z co-ordinate	mm
W_c	Width of the channel	mm
W_s	Width of the solid substrate	mm
x	x co-ordinate	--
x^*	dimensionless length	--
y	y co-ordinate	--
z	z co-ordinate	--
Greek Symbols		
α_c	Aspect ratio of the channel	--
α_s	Aspect ratio of the solid substrate	--
ϕ	Volume fraction	--
ρ_f	Density of the working fluid	kg/m ³
ρ_s	Density of the solid substrate	kg/m ³
μ_{eff}	Effective viscosity of the working fluid	kg/ms
μ_f	Viscosity of the working fluid	kg/ms
$\mu_{roughness}$	Roughness viscosity of the working fluid	kg/ms

CHAPTER 1

INTRODUCTION

1.1. BACKGROUND

The transfer of energy has been around since the beginning of time and plays a vital part in all physical systems. It exists in different domains, namely: thermal, mechanical, electrical, magnetic, sound, light, chemical, elastic, nuclear and gravitational. The study of thermal energy transfer was sparked by the discovery and fascination of fire, where objects could be heated by adding energy, thus allowing the cooking of food; boiling of water; and keeping warm. Observations of the change of temperatures slowly evolved into a now developed field of study: heat transfer.

The extraction of heat from man-made systems is prevalent in everyday life, for example: the internal combustion engine. Heat and mechanical energy is generated from the combustion of fuel and air within the engine, the heat is commonly extracted from the engine via a coolant fluid. Another example where heat extraction is prevalent is in air conditioner systems; thermal energy is extracted from the air in a room via an evaporator. Electronic components generate heat which is commonly extracted via a heat sink and fan system. In such systems two main heat transfer mechanisms are present: conduction: transfer of heat as a result of a temperature difference within a solid medium and convection: transfer of heat between a solid surface and an adjacent liquid or gas that is in motion.

There has been an exponential growth in computing, electronics and compact integrated circuitry (IC) technologies over the last several decades. Technology has allowed electronic components to decrease in size and increase in computing capacity. As a result the heat generated, per footprint size, by these devices has become greater and the need for high density thermal management is required. Conventional methods of cooling IC components is with the use of aluminium or copper fins such as air-cooled heat sinks, but due to the decreasing footprint size of the IC components the heat sinks cannot extract the heat effectively. This poses a limitation on using conventional thermal management techniques for small footprint, high density applications as the required heat transfer rates cannot be achieved, Solovitz, Stevanovic and Beapre (2006)

With the current advancements within the miniaturisation industry, the field of heat transfer has evolved to incorporate mini/micro-scale research. Tuckerman and Pease (1981) were the first pioneers to research microchannels as a means to extract heat from IC components. Microchannel/minichannels cooling is achieved by using small channels, with hydraulic diameters smaller than 3 mm, Kandlikar and William (2003),

which are embedded into a solid conductive material through which a working fluid is pumped to extract heat. The research indicated that the use of microchannels is an effective method for high density heat exchange. This marked the beginning of microchannel heat exchanger research which is now an independent field of study in heat transfer.

Extensive experimental microchannel heat transfer research has been conducted but the results obtained vary significantly depending on the geometry, test setup arrangement and testing conditions, Morini (2004). Large variances has led to an inconsistency when comparing the microchannel results to conventional macro-scale correlations and theory. Many different opinions exist between researches owing to the variance of their findings, Herwig and Hausner (2003), ranging from: inability to perform accurate measurements; not including additional heat transfer mechanisms (such as axial conduction, conjugate effects and viscous dissipation); geometric inaccuracies (such as wall roughness and dimensional inaccuracies); incorrect data reduction methods; effect of molecular interaction of the working fluid; entrance effects; and secondary flow within the channel. With such large variance in the experimental results, numerical and analytical models have been utilised to explore the causes of the deviations.

A combination of experimental and numerical or experimental and analytical research is commonly utilised for the reason that all the heat and dynamic effects cannot accurately be measured with the use of only experimental results.

For conjugate heat transfer, (combination of heat transfer in solids and fluids) conduction and convection are the heat transfer mechanisms in the solid and fluid domain respectively. Convection is most commonly the limiting mechanism as the heat transfer coefficient can be 95 times lower than the conduction heat transfer coefficient. But, in certain geometric cases the conduction within the solid domain can be the ruling limiting factor for heat transfer. This can occur when the solid substrate of the micro heat exchanger has a low thermal conductivity and the volume of the material is significantly less than that of the fluid substrate. Conventional/macro-scale heat transfer theory and correlations for square/rectangular channels are predominantly convection based, but if conduction is the limiting factor such theories and correlations will not predict the heat transfer rate correctly.

1.2. PROBLEM STATEMENT

The continual physical size decrease of electronic components has caused a surge within micro heat exchanging research for the reason that the requirement for high density small foot print cooling is becoming a necessity in the electronic industry. Knowledge of heat transfer in the micro regime is not fully understood due to the vast variation of experimental results obtained, Morini (2004). By not having consistent heat and dynamic correlations it is hampering the ability to accurately predict these

parameters and ultimately is slowing the growth of micro-scale heat exchanging analysis techniques which can be used.

Implementation of microchannel cooling for high density small footprint applications has a direct effect on the physical size of the micro heat exchangers. As the physical size of the micro heat exchanger decreases, the base material which the microchannels are housed in also decreases. With the decreasing of the base material and the increase of the heat density, the conduction in the solid substrate is becoming an important design parameter in the optimisation of microchannel heat exchangers, Morini (2006). Conventional methods of designing heat exchangers based on the convective parameters of the working fluid yields poor results when the conduction in the solid domain becomes the limiting factor. Therefore, the understanding of the heat conduction within the solid base of microchannel heat exchangers is required.

For solid base materials which have a lower thermal conductivity, such as stainless steel and silicone, when compared to copper or aluminium, the effect of the conduction plays an important role when predicting the heat transfer parameter of a microchannel heat exchanger. The effect of the heat transferring through the solid domain influences the convection to the working fluid. The understanding of microchannel heat transfer, in low conductive solid base material heat exchangers, is conjugative in nature.

With the design of tube-type heat exchangers, the tube diameter (one variable) is used to determine the hydraulic diameter but for a rectangular channel the height and width is used (two variables). There are infinitely many combinations of height and width (aspect ratio) when considering a microchannel heat exchanger layout. The effects of the aspect ratio influences the heat transfer rate and pressure drop across the heat exchanger, especially when the conduction within the solid base material is the limiting parameter. Therefore, an aspect ratio should exist which optimises the heat transfer within certain geometric parameters.

1.3. OBJECTIVE

The objective of this study is to experimentally determine the heat transfer and dynamic characteristics of a single microchannel housed in a low thermal conductive solid base material for different aspect ratios in the laminar flow regime. The heat transfer within the solid base material will be the primary focus. A low thermal conductive base was selected to magnify the conjugate heat transfer effect to better understand this phenomenon.

The objectives are defined below:

- The design of the microchannel test sections and the selection of the best suitable solid substrate material are to be performed. The cross sectional area of the fluid domain ($W_c \times H_c$) and the overall width (W_s) of the microchannel will remain constant, (see Figure 1.1). Therefore the aspect ratio and the height of

the test section will vary. The test section is to be heated with a constant heat flux from the bottom wall and water will be used as the working fluid.

- The fabrication technique for the test sections are to be investigated and the best suitable method used.
- Test facility is to be designed, constructed and commissioned to accommodate the test parameters as determined by test section design.
- Experimental tests are to be conducted on the three test sections in the laminar regime where thermal and hydrodynamic parameters are to be measured.
- The measured data are to be presented and discussed.
- The measured data are to be reduced, using analytical calculations and numerical models, to obtain thermal and hydrodynamic parameters of the microchannel test sections.
- The results obtained are to be compared to other relevant literature.

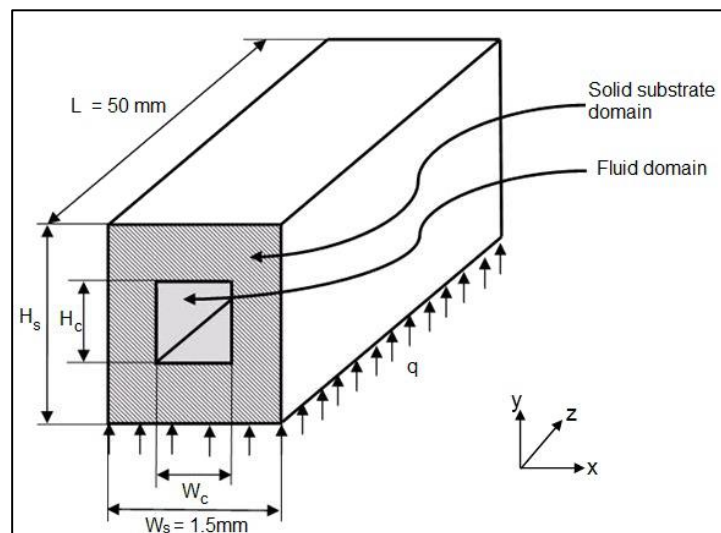


Figure 1.1 Test section schematic layout

1.4. DISSERTATION LAYOUT

The dissertation continues in Chapter 2 by reviewing the existing literature directly related to the problem statement and objective as laid out in Section 1.3. In Chapter 3 the test section as well as the test facility design is discussed in detail. The experimental procedure and the unprocessed results are presented in Chapter 4. In Chapter 5 the data reduction/analysis methodology is discussed followed by the presentation of the processed results in Chapter 6. The last chapter consists of a conclusion of the work completed and recommendations for future research.

CHAPTER 2

LITERATURE STUDY

2.1. INTRODUCTION

The literature relevant to rectangular micro and mini channel heat transfer is discussed in this chapter. Effects of the internal forced convection and conjugate heat transfer will be investigated. The concept of microchannels was introduced by Tuckerman and Piece in 1981, thereafter many correlations have been derived for the Nusselt number, friction factor and thermal resistances. Many of the microchannel related findings do not agree with conventional theory or with other published work Hetsroni et al. (2005). Experimental and numerical research in the laminar regime of rectangular channels will be the focus of this chapter.

The classification of channel sizes varies from author to author. Kandlikar and William (2003) suggested that the hydraulic diameter for a microchannel is smaller than 200 μm , for a minichannel the hydraulic diameter is from 200 μm to 3 mm and any channel above 3 mm is classified as a conventional macro-scale channel. It can be noticed that the term micro and mini channels is used interchangeably within literature, Dixit and Ghosh (2015).

2.2. HEAT TRANSFER IN MICROCHANNELS - REVIEW

A review of published microchannel research was performed by Papautsky, Ameer and Frazier (2001); Obot (2002); Lee, Garimella and Liu (2005); Morini (2006); and Dixit and Ghosh (2015) with the goal to obtain a better understanding of the research conducted to date. The authors found that there were large discrepancies in the published heat transfer coefficients; critical Reynolds numbers; and friction factors. Papautsky, Ameer and Frazier (2001) and Morini (2004) concluded that it is evident that further systematic studies with accurate experimental results are required to add to the research knowledge field. Obot (2002) also concluded that the large deviations between the microchannel results, compared to the macro scale theory, is chronologically decreasing as a result of improved fabrication and more accurate measuring techniques.

Herwig and Hausner (2003) published an opinion on why there is a discrepancy between different microchannel heat transfer and dynamic results. They stated that ignoring certain effects resulted in irregularities of results such as: axial heat conduction; conjugate heat transfer effects; temperature dependant properties;

pressure dependant properties; and surface roughness. Therefore concluding that there is no difference between micro and macro channel heat transfer and pressure drops.

2.3. PRESSURE DROP AND FRICTION FACTOR FOR MICROCHANNELS - REVIEW

The friction factor is obtained from the pressure drop over the channel, the channels hydraulic diameter and the mass flow rate. Morini (2004) found that for laminar flow, five authors published that the friction factor was lower, fourteen authors published that it was higher, and twenty authors published that it was approximately the same for conventional theories for macro scale channels. From the comparison Morini (2004) concluded that the relative surface roughness of the microchannel walls had a large effect on the friction factor and pressure drop. The effect of the surface roughness will be discussed in more detail later on in this chapter. It was observed that the friction factor was also largely case specific and that there was no convergence to a single correlation, Dixit and Ghosh (2015).

2.4. CONJUGATE HEAT TRANSFER

When heat transfer is governed by convection and conduction it is termed, 'conjugate'. The effect of conjugate heat transfer becomes important when the heat conduction in the material wall reaches the same order of magnitude as the internal convection, Morini (2006). Conjugate heat transfer effects are predominant at low Reynolds numbers and low thermal conductivity of the microchannel solid substrate. Conjugate effects are generally investigated mainly via numerical, and/or experimental/numerical methods as the exact thermal properties cannot be measured due to size constraints. In recent times the use of computational fluid dynamics (CFD) has become more widely accepted as the technology of the software and analysis techniques have improved, Shah (2006)

2.5. THE EFFECT OF THE THERMAL CONDUCTIVITY OF THE SOLID SUBSTRATE ON THE HEAT TRANSFER RATE

For conjugate heat transfer the thermal conductivity of the solid substrate directly impacts the thermal behaviour of microchannel heat exchanger. Qu and Mudawar (2002) conducted a numerical analysis on a fixed microchannel geometry with the channel width, height and wall thickness of 57 μm , 180 μm and 21 μm respectively. They concluded that the wall temperature gradients are linear in the axial direction; small amounts of heat transfer occurred in the corners of the microchannel; if one wall was heated the thickness of the opposite wall had a small effect on the heat transfer rate; by increasing the thermal conductivity of the solid substrate it reduced the temperature of the heated base but had a small effect on the exit fluid temperature.

Weisberg and Bau (1992) found that the constant heat flux case tended to an isothermal case as the conductivity of the fluid was set equal to the microchannel solid thermal conductivity.

A numerical study was performed by Lelea (2007) on micro tubes to determine the effect of axial conduction on partially heated micro tubes. Three different solid substrate materials were analysed: stainless steel ($k_s = 15.9 \text{ W / mK}$), silicone ($k_s = 189 \text{ W / mK}$) and copper ($k_s = 389 \text{ W / mK}$). Two tube cross-sections were analysed with outer diameters of 0.1 mm and 0.5 mm and an inner diameter of 0.1 mm for both at a Reynolds number range of 0 – 200. It was found that the axial conduction was a function of the Reynolds number and the thermal conductivity of the solid substrate. A negligible amount of axial conduction was present for the stainless steel test section where as for the copper test section the axial conduction was significant.

Maranzana, Perry and Maillet (2004) studied the effect of axial conduction in mini and microchannels. They derived a new non-dimensional number, M , which quantified the relative quantity of the axial conduction. The effect of axial conduction can be ignored if M is smaller than 10^{-2} .

2.6. THE EFFECT OF VARYING GEOMETRIC PARAMETERS

The effect of varying geometric parameters of the solid substrate has an effect on the heat transfer of the microchannel. Majority of the research conducted to study the effects of varying geometric parameters are numerical based where the model is validated using experimental results or conventional heat transfer theory. Geometric parameters are commonly optimised by maximising the thermal conductance or minimising the thermal resistance of the test section.

Kawano et al. (1998) performed a numerical study to determine the effect of the wall thickness and the thermal conductivity of the microchannel solid substrate. The model was validated with conventional theory. The channel dimensions were 200 μm square and the wall thicknesses ranged from 100 μm to 1000 μm . There was a significant change in the Nusselt number for the different thickness of walls for the lower thermal conductive materials and a smaller change for the cases where the thermal conductivity was high. The direct effect of the thermal conductivity was also seen for channels of the same dimensions, the Nusselt number was higher when the thermal conductivity was high. Therefore the effect of conduction needs to be taken into account, a Nusselt number correlation was suggested.

Bello-Ochende and Meyer (2009) performed a scale analysis to optimise the channels dimensions using the intersection of asymptotic method. The optimal channel dimensions were obtained in terms of the Poiseuille number and the Bejan number to maximise the thermal conductance of the microchannel heat sink. They conducted a numerical study on two different microchannel configurations, firstly, a fully enclosed microchannel and secondly, a microchannel with an adiabatic lid. Optimal aspect ratios

of the microchannels were obtained for a fixed pressure drop and solid volume. The heat transfer parameters varied significantly for each test case.

Kou, Lee and Chen (2008) performed numerical optimisation to reduce the thermal resistance, $R_t = \frac{T_{max} - T_{min}}{q}$ for fully developed flow of a silicon based microchannel with an adiabatic lid, where T_{max} is the maximum temperature, T_{in} is the average inlet fluid temperature and q is the heat flux. All fluid properties remained constant and optimal channel dimensions were obtained for different power inputs and pressure drops over the channel. It was concluded that a change in the height had a smaller effect on the thermal resistance when compared to a change in width of the microchannel.

Lee, Garimella and Liu (2005) performed laminar flow experimental and numerical research on five different copper rectangular microchannels. The microchannel widths ranged from 194 μm to 534 μm and the height of the channel was 5 times the width. A three-dimensional conjugate numerical model and a simplified thin wall model were compared to the experimental results which compared well only when the inlet and boundary conditions were carefully matched. It was also found that the mismatch between the inlet and boundary conditions precluded the comparison between conventional correlations.

Peng and Peterson (1996) performed experimental tests on stainless steel microchannels with varying dimensions. It was concluded that the heat resistance of the solid substrate for small channels was more important than for larger channels.

Gamrat, Favre-Marinet and Asendrych (2005) used a conjugate numerical model to determine the effects of different geometric entrances on the heat transfer for a microchannel array. The entrance effects were related to the Reynolds number and the spacing of the microchannels. The numerical model compared well to other published research. Experimental results were also obtained and a significant decrease in the Nusselt number was found when compared to the numerical results. The numerical model proved useful in interpreting the experimental results where complex measuring of heat fluxes and temperature fields were not possible.

Koo and Kleinstreuer (2003) experimentally observed the flow behaviours in microchannels/tubes and how it affected the friction factor. They concluded that the entrance effects should be taken into account in microfluid systems as it was a function of the channels aspect ratio, channel length and Reynolds number. The effect became greater for higher aspect ratio short channels at higher Reynolds numbers.

Baby and Sobhan (2014) compared the effects of what irregular (actual) and regular (ideal) cross sections had on the pressure drop over a meso-channel. Three different channels sizes were used in the investigation, namely, 500 μm x 300 μm , 500 μm x 500 μm and 1000 μm x 700 μm . The channels were micro-machined into aluminium and photographs of the actual channel profiles were taken. Hydrodynamic and heat transfer parameters were experimentally obtained. Precise separate numerical models of the regular and irregular channels were solved and the results obtained

varied significantly. The experimental results compared well to the numerical model of the irregular channels. It was concluded that for small channels, such as microchannels, modelling of the irregular channel dimensions must be incorporated in order to obtain accurate numerical predictions. Comparing experimental observations to theoretical or numerical results of ideal channel geometries could lead to incorrect hydrodynamic and heat transfer results.

2.7. CRITICAL REYNOLDS NUMBER

At a specific Reynolds number the flow transitions from laminar to turbulent. This point is termed the critical Reynolds number. Thermal and hydrodynamic characteristics change significantly between the laminar and the turbulent regimes and therefore it is an important parameter when considering the heat transfer and pressure drop for a heat exchanger. For conventional channels and tubes the critical Reynolds number is approximately 2300, Cengel (2006).

Wang and Peng (1994), Peng and Peterson (1995) and Peng and Peterson (1996) published experimental heat transfer results for tests performed on stainless steel microchannels with varying channel dimensions. The critical Reynolds numbers ranged from 1000 to 1500. The results obtained were largely dependent on the liquid temperature, velocity and microchannel size. The same experimental setup was used by Peng and Peterson (1996) and they found that the critical Reynolds numbers varied between 300 and 1000 based on the fluid temperature and type of working fluid used.

Hao, He and Zhu (2005) observed that a sudden contraction inlet condition induced the onset of early transition. The critical Reynolds number is a function of the channel shape, entrance shape, aspect ratio and surface roughness.

2.8. THE ENTRANCE LENGTH OF THERMAL DEVELOPING FLOW

The effect of the thermal entrance length in microchannels is an important factor when determining the heat transfer parameters as the thermal behaviour for developing and fully developed flow is significantly different.

A microchannel heat sink was modelled by Li, Peterson and Cheng (2004) using the classical Navier-Stokes and energy equations with no adjustments for surface roughness, double layer and hydrophilic properties. The rectangular microchannels had a width of 57 μm and a depth of 180 μm and were heated by a uniform heat flux on the bottom wall. The thermal entrance length was determined and a correlation for the mean Nusselt number was derived and tested and found to be comparable to other published works.

Wang, Hao and Cheng (2008) conducted experiments on a trapezoidal cross sectional shaped microchannel with a hydraulic diameter of 155 μm . Wall temperatures and local

Nusselt numbers were obtained from a numerical model, which were in good agreement to the experimental results. The thermal entrance length was given by: $L_t = 0.15 \cdot Re \cdot Pr \cdot D_h$ and the fully developed Nusselt number tended to 4, where Re is the Reynolds number, Pr is the Prandtl number and D_h is the hydraulic diameter.

2.9. THE EFFECT OF THE CHANNEL SURFACE ROUGHNESS

Natrajan and Christensen (2000) studied the effect of the surface roughness on the heat transfer coefficient for copper microchannels. It was found that for the smooth microchannel the Nusselt number compared well to conventional theory. For the rough channels there was an enhancement in the Nusselt number in the thermal developing regime and no difference when the flow was thermally developed.

The effects of wall surface roughness can influence the pressure drop over a microchannel. Shen et al. (2006) found that the surface roughness had a greater effect for laminar than for turbulent flow. The effect of the surface roughness was incorporated into the friction factor by determining an effective viscosity, μ_{eff} , which was equal to the fluid viscosity μ_f plus the roughness viscosity $\mu_{roughness}$. Weilin, Mala and Dongqing (2000) measured the pressure drop over trapezoidal adiabatic microchannels with a hydraulic diameter of 51 μm to 169 μm . The Reynolds number increased linearly from 0 to 500 thereafter the flow moved into the transition regime. The pressure gradient was found to be larger than the predicted laminar conventional theory and this contributed to the surface roughness of the channel walls. A roughness viscosity model was also used to incorporate the experimental results. Gamrat et al. (2008) performed experimental and numerical research for rough walled microchannels. It was concluded that the Poiseuille number increased with relative roughness and it was independent to the Reynolds number in the laminar regime. For a simplified approach the roughness effect was interpreted by using an effective roughness height.

Mala and Li (1999) suggested that the effect of surface roughness increased as the hydraulic diameter decreased. Natrajan and Christensen (2000) obtained the pressure drop over copper microchannels (with a hydraulic diameter of 600 μm and aspect ratio of 1:2) for one smooth and two increasingly rough channels ($R_a = 0.0125$ and $R_a = 0.0251$). It was found that the increasing roughness increased the pressure drop over the test section. The critical Reynolds number for the smooth channel was 1800, for the $R_a = 0.0125$ channel the critical Reynolds number was 1500 and for the $R_a = 0.0251$ channel the critical Reynolds number was 1300. Therefore, concluding that as the roughness increased the critical Reynolds number decreased.

2.10. VISCOUS DISSIPATION WITHIN MICROCHANNELS

For viscous fluids, the fluid will take on energy from the motion of the fluid (kinetic energy) and convert it into internal energy. This energy conversion causes the fluid to

heat up, this process is termed 'viscous dissipation'. Viscous dissipation was conventionally only taken into account for low viscosity fluid flow, but the rise in fluid temperature due to the viscous forces needs to be accounted for in microchannels Morini (2006). Judy, Maynes and Webb (2002) performed adiabatic experiments on square and circular microchannels and microtubes at a Reynolds number ranging from 8 to 2300 and the hydraulic diameter ranging from 15 μm to 150 μm . They found a maximum fluid temperature increase from the inlet to the outlet of the channel to be 6 °C due to viscous heating. Morini (2006) investigated the effects by deriving an analytical equation to account for viscous dissipation and compared it to other literature. An expression was developed for when viscous dissipation can be neglected for adiabatic and heated microchannels.

2.11. SUMMARY OF THE LITERATURE STUDY

Relevant micro and mini channel literature was reviewed in this chapter. The factors that influenced the internal forced convection and conjugative heat transfer were discussed and compiled in such a way that the large quantity of literature was summarised. Discrepancies existed between literature when comparing the Nusselt number and friction factor, authors have alluded to mechanisms for these discrepancies, but the fact of the matter is that the field of microchannel research has not yet converged to a single 'theory' or outcome.

The conduction within the solid substrate had an influence on the overall heat transfer parameters when the solid substrates' thermal conductivity was low and when the channels hydraulic diameter was small. Surface roughness of the channel wall influenced the pressure drop in laminar flow and the trend indicated that the critical Reynolds number decreased with an increase in the surface roughness. The entrance effect of the microchannel also had an influence on the laminar to transition Reynolds number.

CHAPTER 3

TEST SECTION AND TEST FACILITY DESIGN

3.1. INTRODUCTION

In this chapter the design and fabrication of the microchannel test sections and the design and assembly of the testing facility will be discussed. The microchannel test section was designed with the use of a three-dimensional numerical model and thereafter an analytical analysis was performed to confirm the results. The test section assembly (consisting of the housing, heater and inlet and outlet manifolds) was designed in CAD and was fabricated in-house. The test facility was built from the ground up to accommodate microchannel testing. Design of the test sections and test facility was vital to the outcomes of the research conducted.

3.2. GEOMETRIC AND PHYSICAL PARAMETERS FOR THE MICROCHANNEL

The driving and driven parameters for the microchannel test section were determined prior to the detailed analyses. They were selected based on the purpose of the study and the required outcomes. The defining geometric parameters are shown in Figure 3.1. The channel was symmetrical about the horizontal and vertical axes. A constant heat flux was applied to the bottom wall in line with other research efforts.

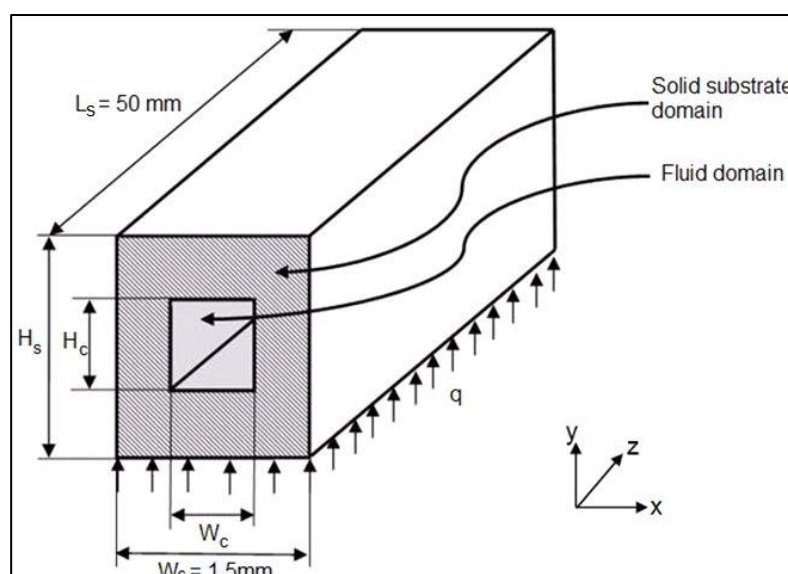


Figure 3.1 Microchannel geometric parameters

There are five geometric parameters that need to be selected in order to fully define the microchannel, assuming the channel is in the middle of the solid substrate, as depicted in Figure 3.1. These are: the total length of the channel; (L_s), the width (W_c) and height (H_c) of the channel; and the width (W_s) and height (H_s) of the solid substrate. For this study the length (L_s) of the channel was chosen to be constant at, 50 mm, this value will be validated in Section 3.4. The width of the solid substrate (W_s) was also chosen to be constant, at 1.5 mm, in order to keep the heat flux magnitude constant while the other geometric parameters changed.

Three additional dimensional parameters were defined, namely the cross sectional area, $A_c = H_c \cdot W_c$, the fluid channel aspect ratio $\alpha_c = W_c \div H_c$ and the solid substrate aspect ratio $\alpha_s = W_s \div H_s$ with reference to Figure 3.1. The aspect ratio of the fluid channel (α_c) and the solid substrate (α_s) were kept equal to each other in order to obtain a maximum wall thickness around the channel. The channel was centred within the solid substrate. Therefore, the dimension parameters, H_c and W_c were dependent on the height of the channel. The solid section height (H_s) and the cross sectional area (A_c), were selected as the varying parameters.

The width and length of the microchannel was fixed but the dimension range of the height (H_s) and the area of the fluid channel (A_c) must be defined. The magnitude of the dimensional parameters were determined with manufacturing constraints in mind. A minimal channel height (H_c) of 0.4 mm and channel wall of 0.2 mm were achievable with the manufacturing machinery available. With this in mind the dimensional range for the height (H_s) was 1 mm to 2 mm. Four different areas for the fluid channel were selected. An iterative process was required to solve for the test sections dimensions. The calculations and dimensional results are presented Appendix A, with a summary of the dimensional parameters given in Table 3.1.

Three common microchannel materials namely: copper, brass and stainless steel, were considered during the analyses because they have significantly different thermal conductivities (k_s). The working fluid was selected as water due to its availability and to allow for comparison with information from literature. The heat flux (q) was selected as 10 W/cm^2 , which was the maximum heat input which ensured that the working fluid remained in the liquid phase. The Reynolds number (Re) range was selected from 70 - 2300, as the scope of the study is for laminar flow¹. Table 3.1 summarised the geometric and test section parameters.

Because it is not possible to fabricate and test an infinite number of cases, the dimensional parameters obtained were used in analytical and numerical calculations to determine which microchannel test sections should be manufactured. Only three test sections could be built and tested and it was important to select three cases carefully.

¹ A Reynolds number of 2300 is commonly where transition occurs from laminar to turbulent, Cengel (2006).

Table 3.1 Geometric and test section parameters range and specified values

W_s [mm]	H_s [mm]	A_c [mm ²]	L_s [mm]	Re [--]	q [W/cm ²]
1.5	1 -2	0.25, 0.5, 0.75, 1.00	50	70 - 2300	10
Material	ρ_s [kg/m ³]	k_s [W/mK]	Cp_s [J/kgK]	ρ_s is the density of the solid and Cp_s is the specific heat of the solid	
Copper	8933	401	385		
Brass	8530	110	380		
Stainless Steel	8055	15.1	480		

3.3. NUMERICAL ANALYSIS OF THE MICROCHANNEL TEST SECTION

To design a microchannel test section, input values for some of the parameters are required. These include: the temperature magnitudes and temperature fields within the microchannel solid substrate; the change in the working fluid temperature from the inlet to the outlet; the amount of heat input to the system; the thermal conductivity of the solid substrate; and the dimensional parameters. A computational fluid dynamic (CFD) package (Fluent[®] and Gambit[®]) was used to determine the heat transfer characteristics of the microchannel test sections. Primarily the focus of the numerical analysis was to ensure that there would be a measurable difference in the wall temperatures. Analytical calculations were performed to determine the change in fluid temperature and pressure drop over the microchannel test section, this is performed in Section 3.4.

The numerical model was developed, validated and verified to ensure that the results obtained were credible and were similar to other published research. Results of all the numerical analyses were analysed to determine which three possible test sections should be fabricated and experimentally tested. Only the results of the numerical analyses are presented in this subsection, more details can be found in Appendix B.

CFD simulations were setup and performed in batches through a MatLab[®] base compiled program. The results were stored in text based files. Thereafter a post processing process was performed through MatLab[®] to obtain the results in a presentable manner.

3.3.1. NUMERICAL SIMULATION RESULTS

The first batch of simulations was performed with copper as the microchannel solid material. The results for $A_c = 0.5\text{mm}^2$ are shown in Figure 3.2. From the figure it is seen that the peak temperatures do not change significantly (less than 1°C) as the wall thickness (H_s) is changed. This causes some concern as these temperature changes cannot be captured or experimentally measured (with confidence) for the different cases of H_s . It was decided to change the material to one that had a lower thermal conductivity to increase the temperature gradient in the material therefore increasing the thermal resistance. This would increase the temperature change for the different cases of H_s .

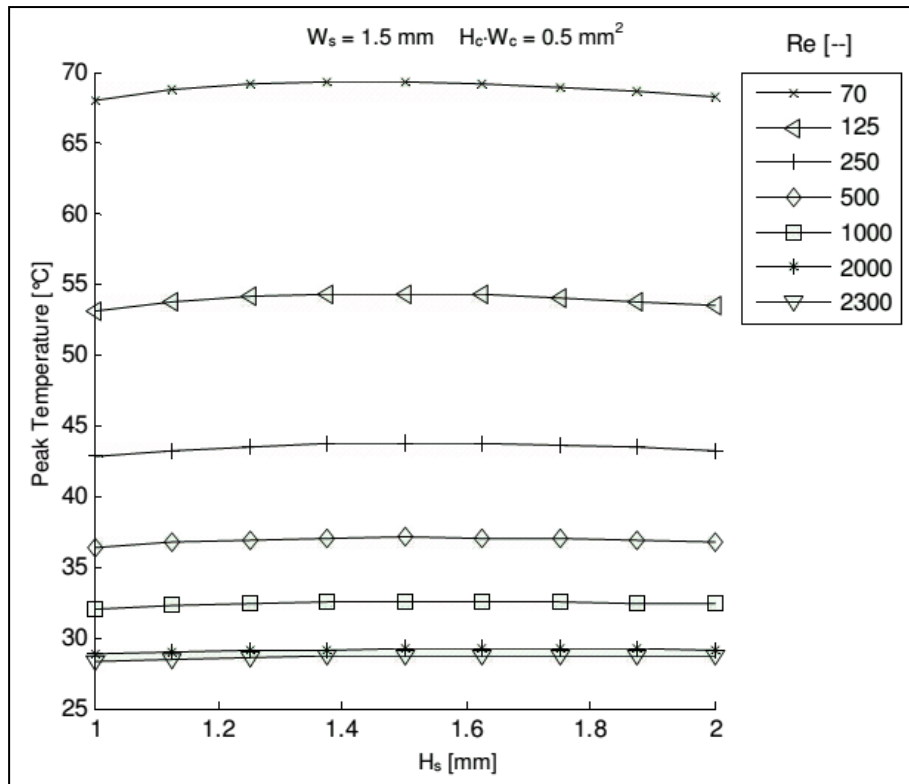


Figure 3.2 Peak temperature at different copper solid section heights (H_s) for different Re numbers

The next batch of simulations was run with brass as the microchannel solid material, which had a thermal conductivity approximately 3.6 times lower than that of copper. From Figure 3.3 it can be seen that the variation in the peak temperature is still small (below 1°C). From these results it can be concluded that the dominating heat transfer is conduction rather than convection, and therefore the importance of design and optimisation must be based around the fluid (convection) aspect of the microchannel for materials with high thermal conductivity and wall thicknesses above 0.2mm.

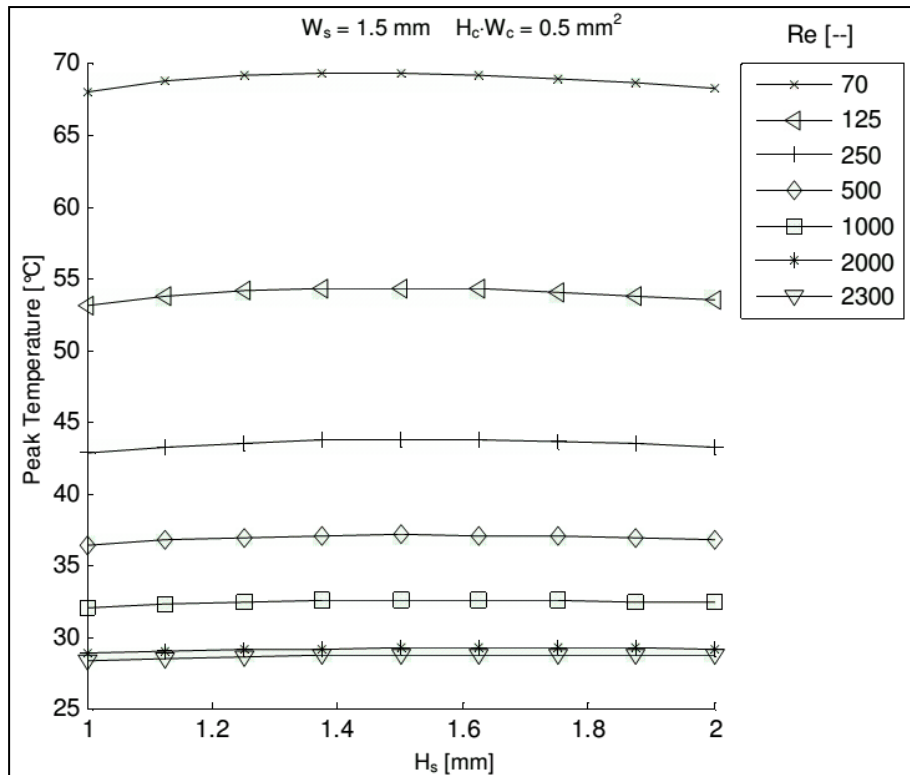


Figure 3.3 Peak temperature at different brass solid section heights (H_s) for different Re numbers

Stainless steel was then chosen due to its extremely low thermal conductivity, approximately 26.5 times less than that of copper. The results shown in Figure 3.4 show that there is a larger change in the peak temperatures (approximately 4°C). Therefore, stainless steel will suffice for the solid substrate solely because there are greater temperature changes for the range of channel height (H_s). Stainless steel also does not corrode, and therefore makes it suitable for water to be used as the cooling fluid.

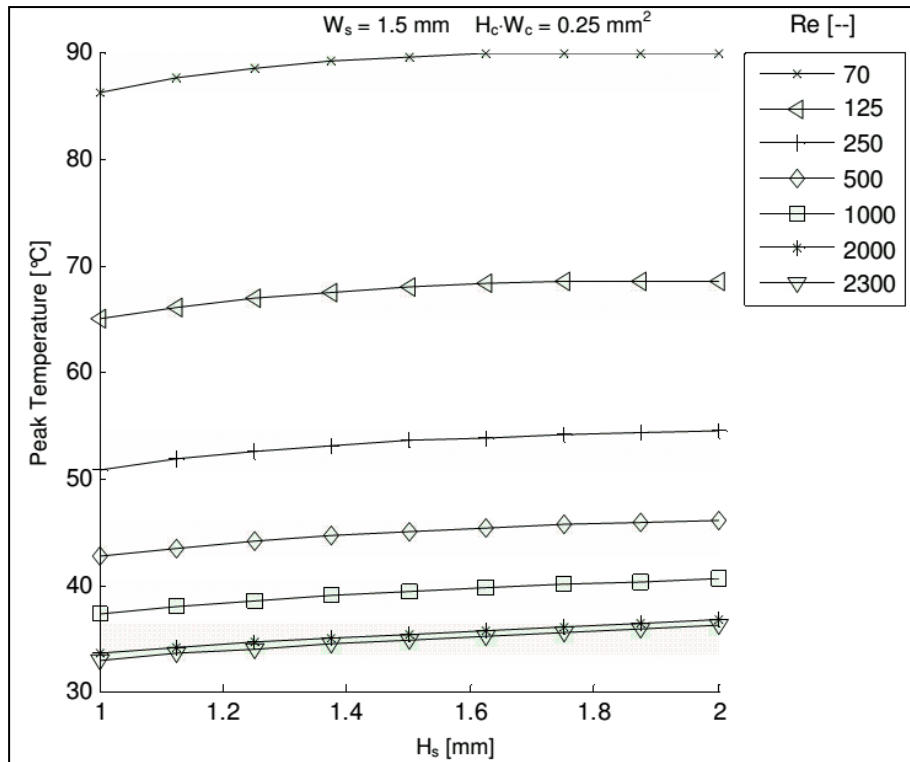


Figure 3.4 Peak temperature at different stainless steel solid section heights (H_s) for different Re numbers

Figure 3.5 shows the temperature cross section profiles for a Reynolds number of 2300 for two planes at $z = 10 \text{ mm}$ and $z = 40 \text{ mm}$, along the axial axis of channel, and the height (H_s) of 1 mm, 1.5 mm and 2 mm for stainless steel. The temperature profile pictures show that the largest temperature gradient is between the bottom wall and the channel, and the gradients decrease towards the top wall. It was observed that the temperature is more evenly distributed as the height of the channel (H_s) increases.

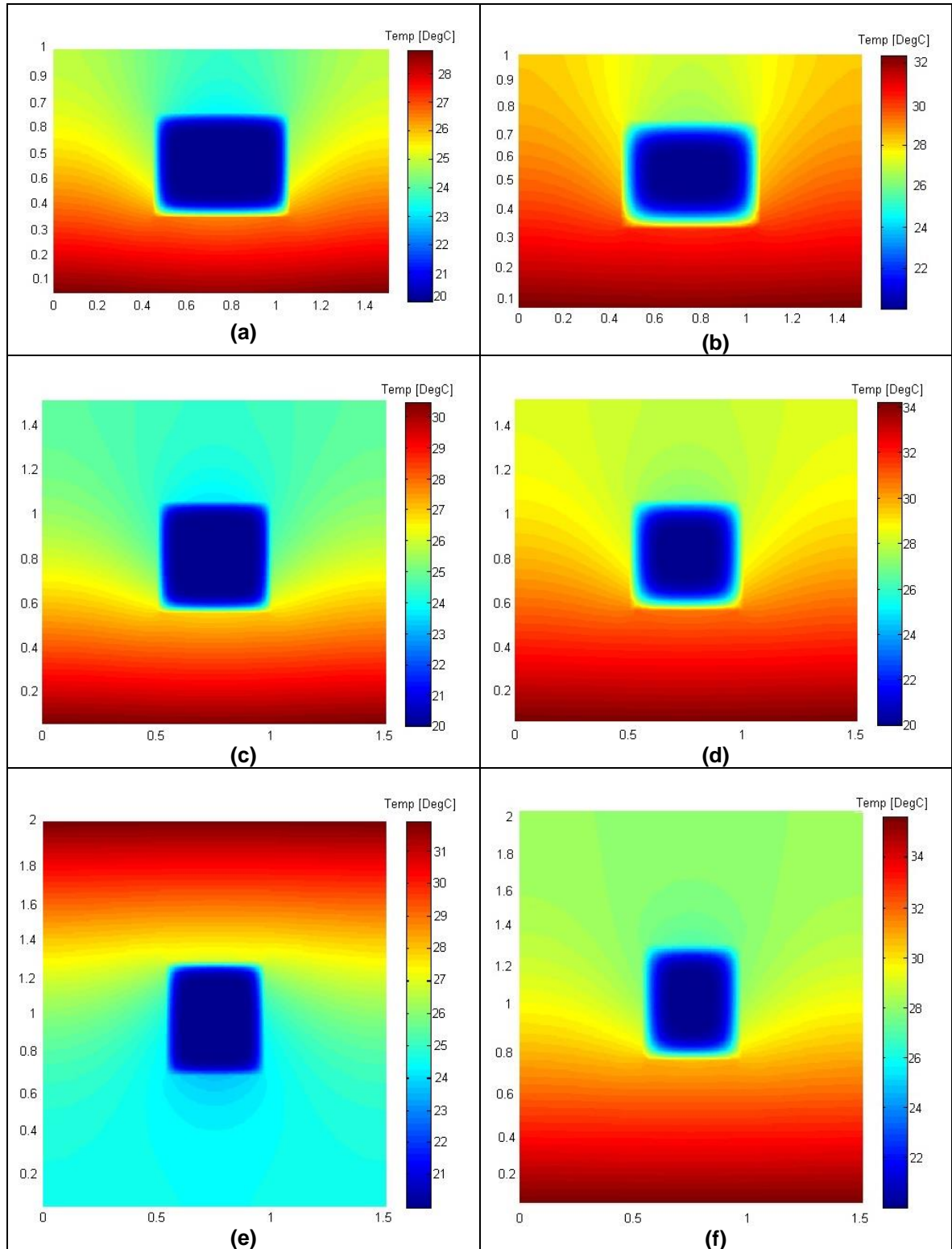


Figure 3.5 Temperature profiles in x-y plane: $A_c = 0.25$ mm², $Re = 2300$; (a) $H_s = 1$ mm, $z = 10$ mm; (b) $H_s = 1$ mm, $z = 40$ mm, (c) $H_s = 1.5$ mm, $z = 10$ mm, (d) $H_s = 1.5$ mm, $z = 40$ mm, (e) $H_s = 2$ mm, $z = 10$ mm, (f) $H_s = 2$ mm, $z = 40$ mm

3.3.2. SELECTION OF THE THREE MICROCHANNEL TEST SECTIONS FOR FABRICATION AND TESTING

The scope of the study allowed for a maximum of three test sections to be manufactured. Geometric parameter selection was primarily focused on obtaining the largest temperature difference in order to facilitate more accurate experimental measurements. Figure 3.6 shows the expected peak temperature results for the different cross sectional areas analysed numerically. As expected, the peak temperature reduces as the Reynolds number increases for all four graphs. The temperature change for a specific Reynolds number between different channel heights (H_s) increases as the cross sectional area (A_c) of the channel decreases. The cross sectional area (A_c) equal to 0.25 mm^2 has the largest temperature change for different channel heights (H_s) and therefore was selected. Maximum, minimum and middle channel heights (H_s) were selected as it covered the full range.

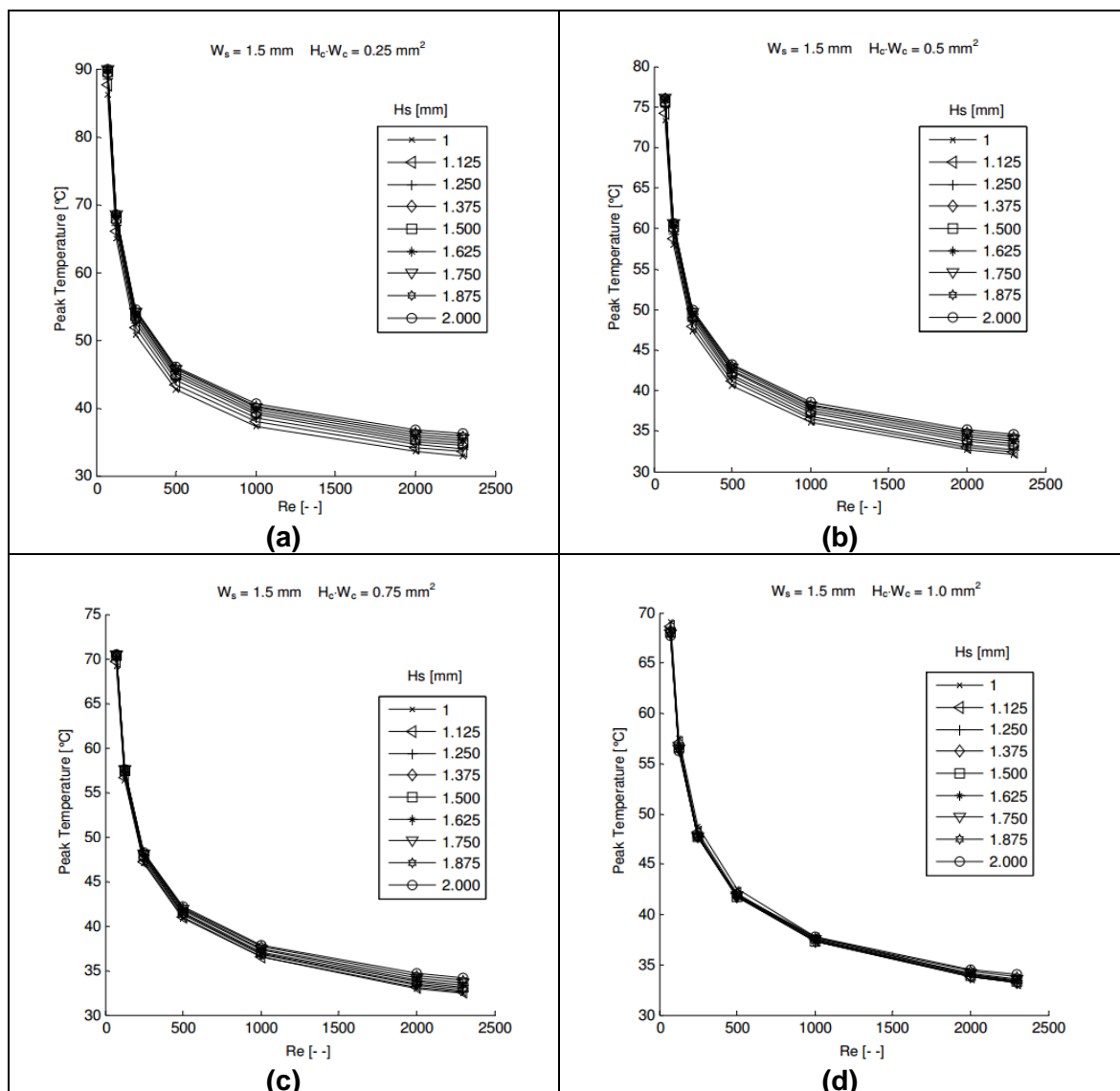
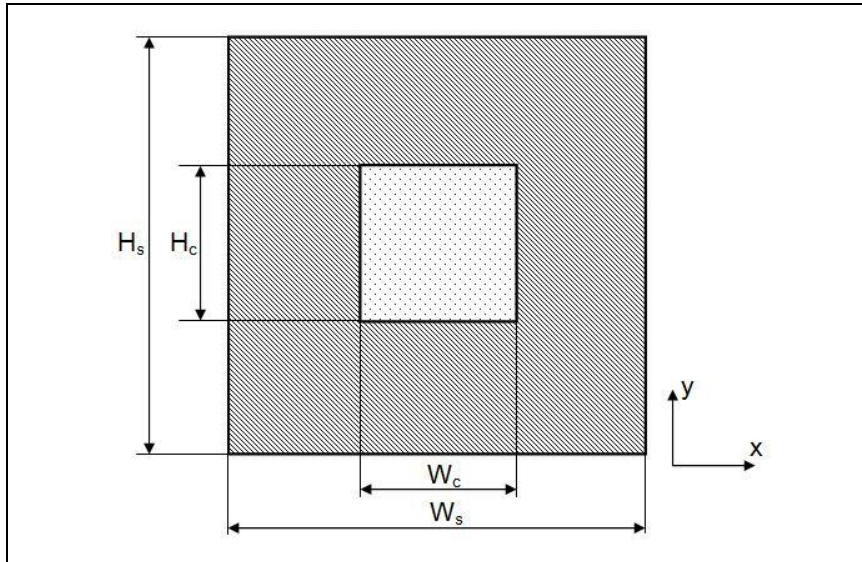


Figure 3.6 Expected peak temperatures versus the Reynolds number, (a) $W_s = 1.5 \text{ mm}$ & $A_c = 0.25 \text{ mm}^2$, (b) $W_s = 1.5 \text{ mm}$ & $A_c = 0.5 \text{ mm}^2$, (c) $W_s = 1.5 \text{ mm}$ & $A_c = 0.75 \text{ mm}^2$, (d) $W_s = A_c = 1 \text{ mm}^2$

Table 3.2 shows the proposed microchannel cross section dimensions for the three test sections.

Table 3.2 Dimensions of the three proposed microchannels to be fabricated



	Test section 1	Test section 2	Test section 3
H_c [mm]	0.41	0.50	0.58
W_c [mm]	0.61	0.50	0.43
H_s [mm]	1.00	1.50	2.00
W_s [mm]	1.5	1.50	1.50

3.4. ANALYTICAL CALCULATION OF THE MICROCHANNEL TEST SECTIONS

An analytical study was performed on the selected microchannels geometry using conventional theory and correlations to verify the findings obtained from the numerical analyses and to determine the predicted fluid temperature difference over the test sections. The Nusselt number was determined based on the Hausen correlation. Lastly the hydrodynamic pressure drop was calculated using the friction factor based on the Hagenbach's correction. Results obtained in this section will aid in the selection of the instrumentation required for the test rig. The detailed calculations are presented in Appendix C.

3.4.1. HEAT TRANSFER RESULTS

In Figure 3.7 it can be seen that the mean Nusselt number predictably increases with an increase in Reynolds number. The numerical value of the Nusselt number is similar for all three dimensional cases because the channels' cross-sectional area and mass flow

rate is constant. Figure 3.8a shows that the maximum outlet temperature is about 74 °C which will ensure that boiling of the fluid does not occur, thus resulting only in single phase flow. Figure 3.8b shows the average surface temperature on the microchannel wall is expected to reach a maximum temperature of approximately 60 °C at lowest Reynolds number.

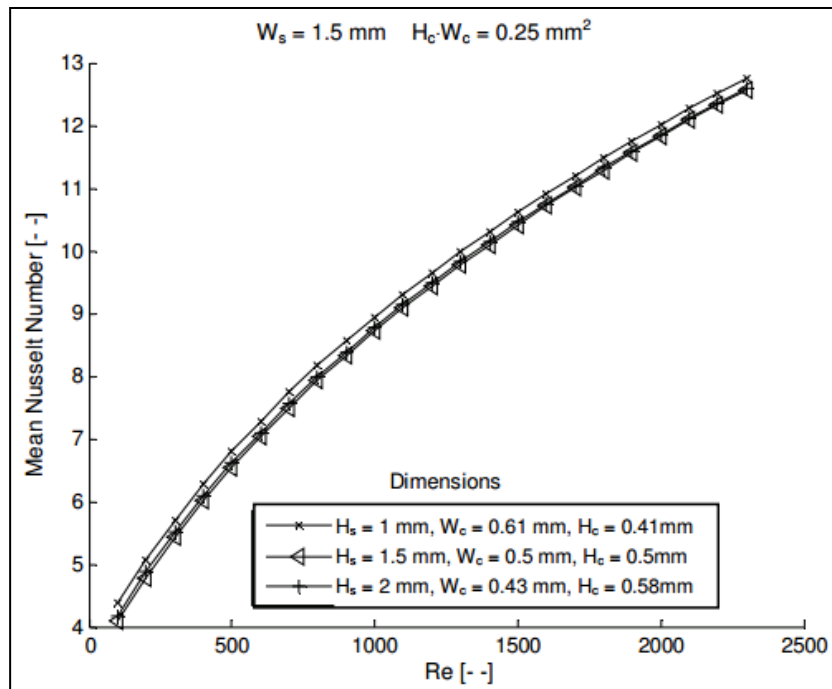


Figure 3.7 Mean Nusselt number versus Reynolds number for varying $H_s = 1 \text{ mm}$, $H_s = 1.5 \text{ mm}$ and $H_s = 2 \text{ mm}$.

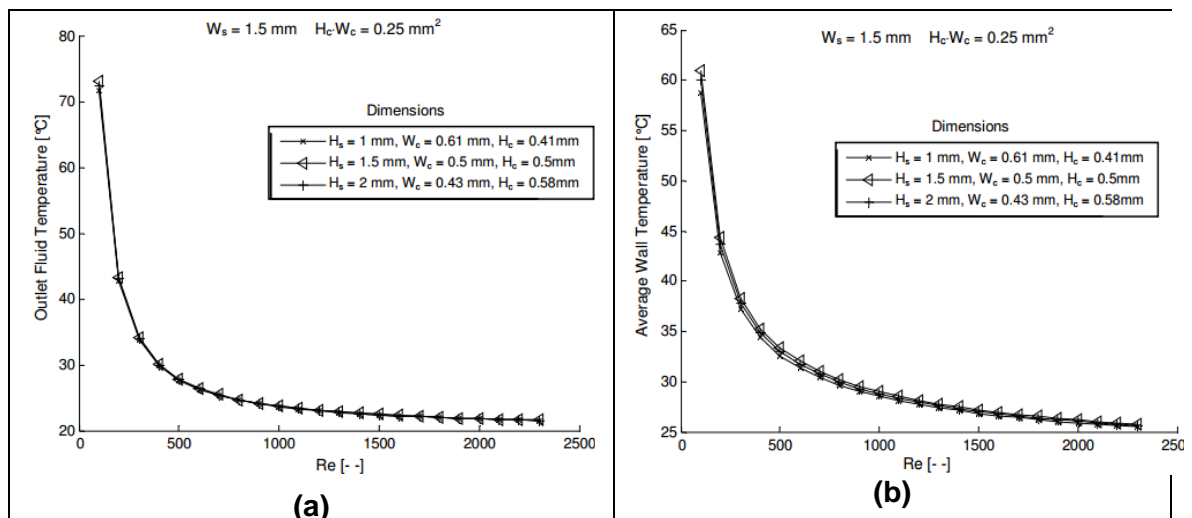


Figure 3.8 Fluid outlet temperature (a) and average channel surface temperature (b) versus Reynolds number for varying $H_s = 1 \text{ mm}$, $H_s = 1.5 \text{ mm}$ and $H_s = 2 \text{ mm}$.

3.4.2. HYDRODYNAMIC PRESSURE DROP CALCULATIONS

The pressure drop was calculated from the friction factor for flow in ducts Kandlikar et al. (2004) and the Hagenbach's correction incremental defect factor for the flow in the

developing regime, see Appendix C for the detailed calculations. The magnitude of the pressure drop over the test section aided in the selection of the pressure transducers as discussed in Section 3.7. The effect of the entrance and exit of the microchannel test section was ignored in this analysis. The pressure drop over the microchannels is shown in Figure 3.9. It was found that the pressure drop over the microchannel ranged from 0 kPa to approximately 44 kPa. The pressure drop over the different test sections is similar and increased as the Reynolds number increased. It can be seen that there is a jump in the differential pressure at about $Re = 2000$ because the flow in the channel changes from only developing to fully developed. This discrepancy is due to the different analytical approximation equations used for developing and fully developed flow.

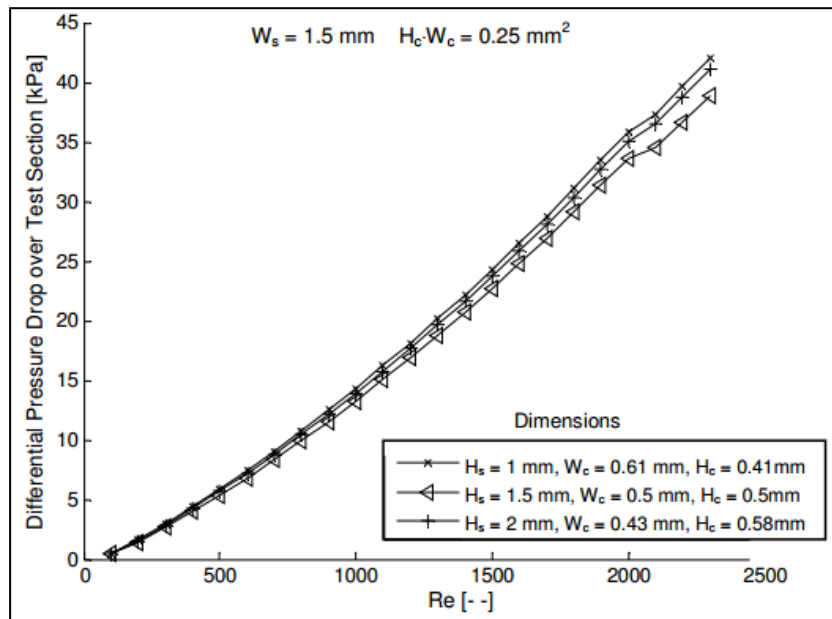


Figure 3.9 Differential pressure drop versus Reynolds number for varying $H_s = 1\text{mm}$, $H_s = 1.5\text{mm}$ and $H_s = 2\text{mm}$.

3.5. MICROCHANNEL TEST SECTION DESIGN AND CONSTRUCTION

The function of the test section is to measure the outer wall temperatures along the microchannel, the inlet fluid temperature, the outlet fluid temperature and the pressure drop over the microchannel. The test section was heated from the bottom wall while cold water was pumped through the microchannel. From the measured parameters the heat transfer and hydrodynamic behaviour of the test section can be understood and analysed. Temperatures were measured with the use of thermocouples which were positioned around the test section and the pressure drop was measured via pressure ports housed within the inlet and outlet manifolds using a pressure transducer.

The physical microchannel test section design and fabrication is discussed in this subsection. The design of the microchannel test section was based on the test sections used in other studies (Appendix D). Three different cross-section stainless steel test

sections were fabricated and assembled into three different clear cast acrylic (Perspex[®]) microchannel assemblies. The complete assembly incorporated a re-usable heater for all three test sections and location grooves or holes for the placement of thermocouples. Inlet and outlet manifolds were bolted onto the test section housing.

Three different revisions of the test section assembly designs were built and tested. Revision one and two had shortfalls which required re-design. Problems experienced with these test section assemblies were as follows: inability to position the thermocouples accurately; water leaks and; uneven heat flux distribution. Modifications were made to each revised test section to improve on the design. Only upon the third test section design were all the identified problems eliminated. The final test section design is discussed in detail here and a summary of the prior test section assemblies are reported on in Appendix E.

3.5.1. FINAL TEST SECTION DESIGN (3RD REVISION)

The microchannel test assembly is shown in Figure 3.10 where the main components are labelled. The test section assembly consisted of the microchannel assembly which housed the stainless steel microchannel, the heater block assembly and the inlet and outlet manifolds. Cold water at a constant temperature was supplied to the test section via the inlet pipe port to the inlet manifold and it flows through the microchannel assembly and then through the outlet manifold, with a sudden contraction at the inlet and a sudden expansion at the outlet. The microchannel was heated via the heater housed in the heater block assembly. The test section was connected to the test facility via inlet, outlet and pressure port pipes using flexible tubing.

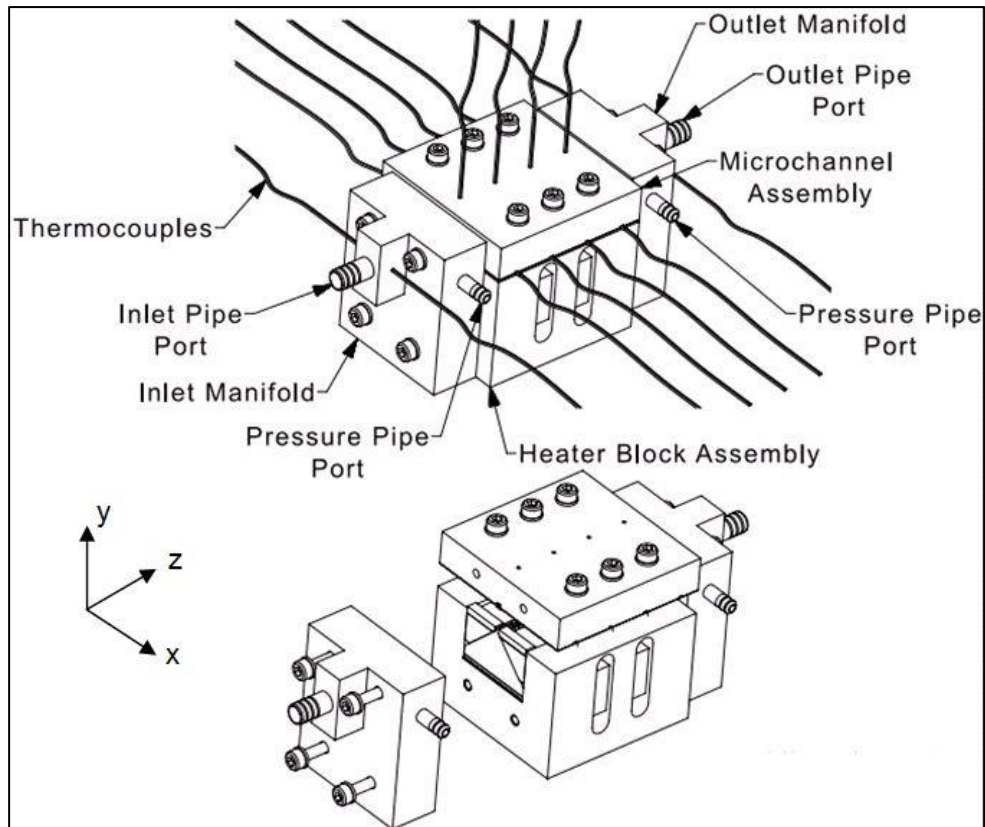


Figure 3.10 Test section assembly: Inlet and outlet tubes; pressure taps; thermocouples; stainless steel microchannel; and heater test section housing

Inlet and Outlet Manifolds

Figure 3.11 shows a top view of the microchannel test section assembly and Figure 3.12 shows a section view through line A-A. The assembly comprised of the Nylon inlet manifold which housed the copper inlet pipe, copper inlet flow mixer, inlet fluid thermocouples and a pressure port. Inlet pipe and mixer were soldered together and the glued to the Nylon manifold. Two thermocouples were positioned on the outer wall of the inlet pipe to measure the bulk inlet fluid temperatures. The upstream flow mixer ensured that any thermal developed flow was disturbed in order to obtain an accurate bulk fluid temperature. The inlet manifold was attached to the microchannel assembly, using M3 x 20 mm stainless steel screws, and was sealed using a rubber O-ring. Water flowed through the microchannel housed in the microchannel assembly and through the outlet manifold. The functionality of the outlet manifold is similar to the inlet manifold with an exception that the flow mixer was positioned upstream of the outlet fluid thermocouples and downstream of the pressure port. A sectional view through line B-B (reference to Figure 3.11) is shown in Figure 3.13 and shows the pressure port which comprises of a 1 mm hole drilled into the copper inlet and outlet pipe.

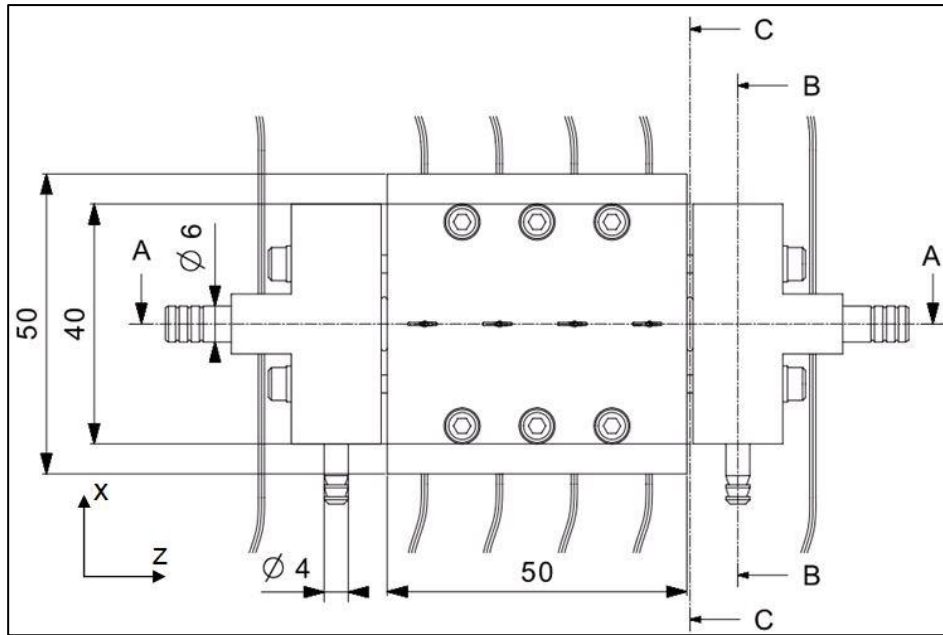


Figure 3.11 Top view of the microchannel test section assembly

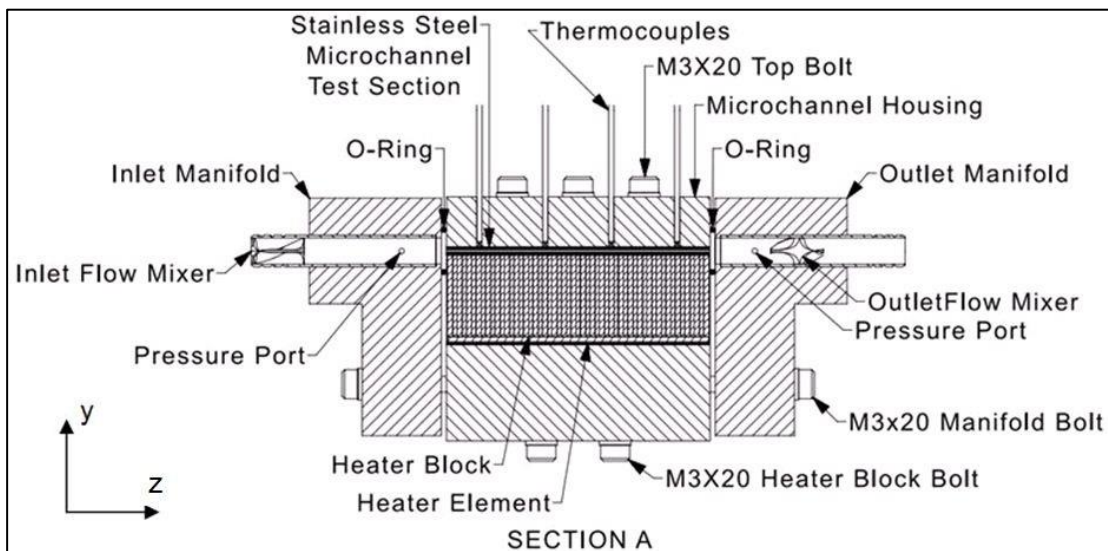


Figure 3.12 Section view through line A-A showing the components of the microchannel test section assembly

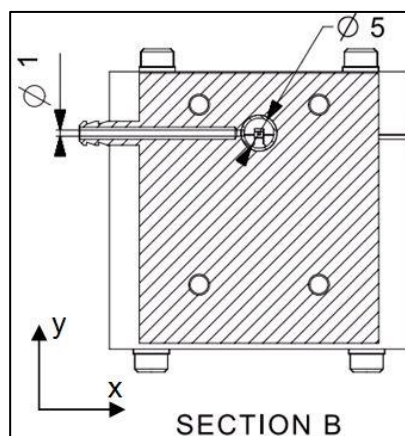


Figure 3.13 Section view through line B-B showing the pressure port

Microchannel Assembly

The microchannel assembly is shown in Figure 3.14 and Figure 3.15 and consists of the stainless steel microchannel, the stainless steel microchannel lid and the clear cast acrylic (Perspex®) microchannel housing. Three separate microchannel assemblies were manufactured, one for each test section: Test Section 1; Test Section 2; and Test Section 3.

The stainless steel microchannel test section consisted of two parts: the section where the channel was machined into, and the lid, as shown in Figure 3.14 Detail D. These two parts were glued together with a silver embedded epoxy which had the same thermal conductivity as stainless steel; therefore the thermal resistance between the microchannel and the lid did not have to be accounted for. Once the glue was applied the top half of the assembly was clamped and the inside of the channel was clean using a solvent (before the epoxy cured).

The microchannel housing contained grooves and holes through which the thermocouples could be positioned to measure the side and top wall temperatures of the microchannel and the microchannel lid. The locations of the thermocouples are shown in Figure 3.16. Four locations along the axial direction were selected to measure the change in the outer wall temperatures and are labelled as Location 1 at the inlet side through to Location 4 at the outlet side. Two side and one top wall temperatures were measured for each axial location. Thermocouples were thermally connected to the test section using a thermal conductive paste. The microchannel assembly was attached via screws to the heater block assembly which was re-used for all three test sections.

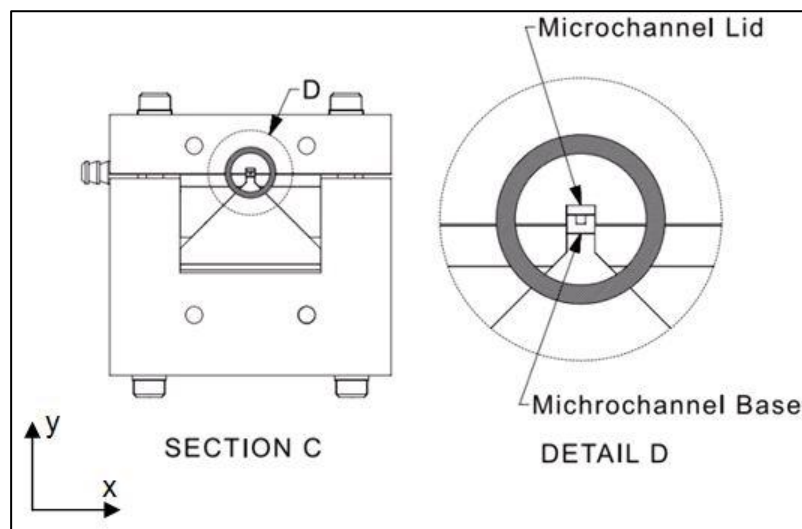


Figure 3.14 Section view through line C-C showing the microchannel base and the microchannel lid

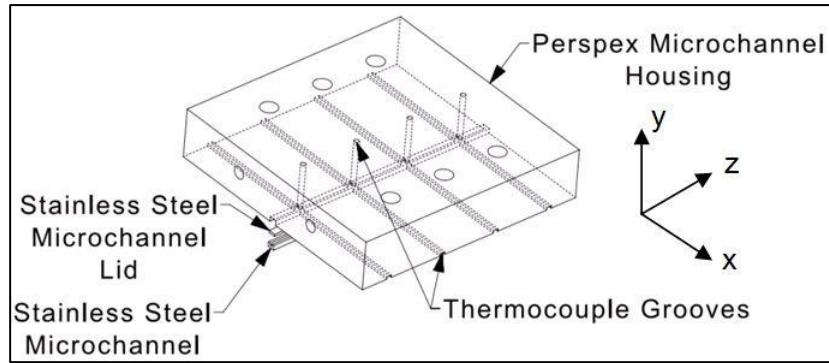


Figure 3.15 The microchannel assembly isometric view

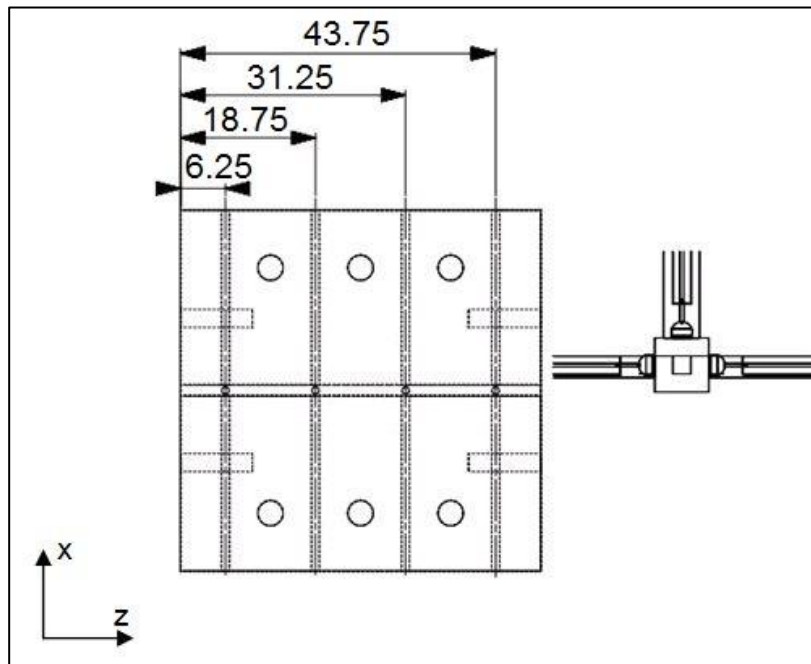


Figure 3.16 Drawing of the thermocouple placement onto the stainless steel test section

Heater Block Assembly

The heater block assembly consisted of the triangular heater block, the heater element and the Nylon assembly housing. A section view through line C-C (reference to Figure 3.11) is shown in Figure 3.17, and shows the heater block assembly arrangement. The heater element was fabricated from # 40 gauge constantan wire as it has a high resistance and the resistance properties of the wire remains fairly constant for a change in temperature. Heater wire was sandwiched between two layers of self-adhesive conductive pads. The heater block was fabricated from alternative layers of copper and fibreglass sheets, each 1 mm thick, see Figure 3.18. The thermal conductivity of the copper is 8000 times higher than that of the fibreglass sheet, therefore insulating the copper layers. The heater was constructed in this way to ensure that a near constant heat flux was supplied to the bottom of the microchannel as a very small amount of axial heat conduction was possible between the copper sheets. Qu and Mudawar (2002) used a similar heater construction to obtain a constant heat flux. The heater block was clamped to the heater element and Nylon assembly housing. A thermal

conductive paste was placed between the stainless steel microchannel and the heater block to reduce the thermal resistance.

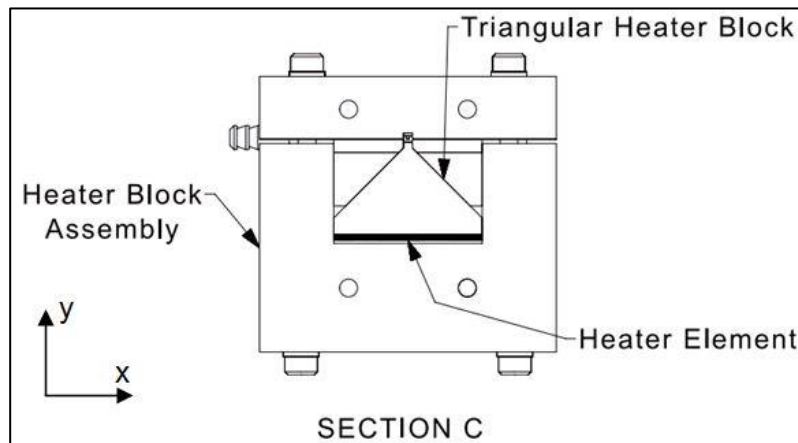


Figure 3.17 The microchannel assembly isometric view

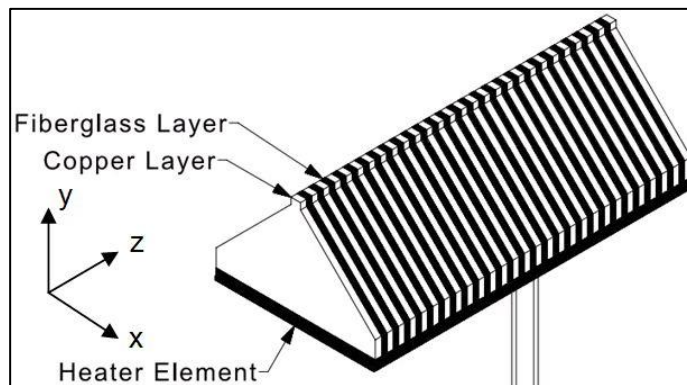


Figure 3.18 Heater assembly: Heater element at the bottom and layered heater block

3.5.2. FABRICATION AND ASSEMBLY OF TEST SECTION

The stainless steel microchannel fabrication and assembly is discussed in this section with special attention given to the fabrication of the stainless steel microchannel. A literature study (Appendix F) was performed on common methods used in fabricating microchannels. The assembly process was relatively simple and therefore will not be discussed in detail. All plastic and copper parts were fabricated using manual or CNC (Computer Numerical Controlled) machines.

High residual stresses exist in stainless steel and it is prone to excessive work hardening. Thus, the material was annealed before machining, to soften and to stress relieve it, by placing it in a furnace at 1010 °C to 1120 °C for a soaking time of 90 minutes and then followed by water or air quenching, as per the material data sheet. After annealing, the material was cut into 2 mm x 2 mm x 60 mm billets with two sides machined 90 ° to each other. The billet was clamped in a custom jig and machined to the channels outer dimension sizes (H_s and W_s).

Different manufacturing techniques were experimented with, to obtain the best shape and surface finish for the microchannel. Machine ability of stainless steel is low and requires fast hard cutting to eliminate the possibility of work hardening and glazing. Conventional end milling was first tried but due to the small size of the channel it was found unsuitable. Manufacturing of the channel was outsourced to a company that uses laser ablation, the quality and dimensional accuracy was very poor. Thereafter a sawing process was attempted using a 0.3 mm thick slitting saw, the bottom of the channel wall was not flat and the channel corners were not square, as seen in Figure 3.19(a). A drawing process was finally used where a custom tool (one for each test section) was ground from high speed steel; the machining arrangement is shown in Figure 3.20. The cutting tool remained stationary and the work piece moved in the direction as shown in Figure 3.20(a), the depth of cut per a single pass was 0.05 mm. A cross sectional photograph of a channel is shown Figure 3.19(b), where it can be seen that the corners of the channel are square, the side walls are parallel and the walls are flat.

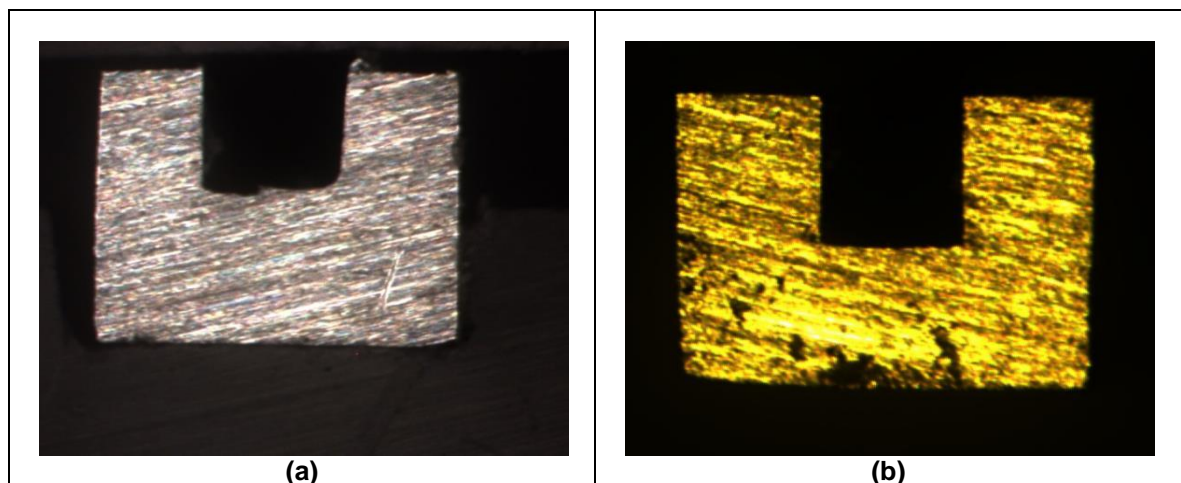


Figure 3.19 Stainless steel microchannel (a) machined using a sawing process, (b) machined using a drawing process

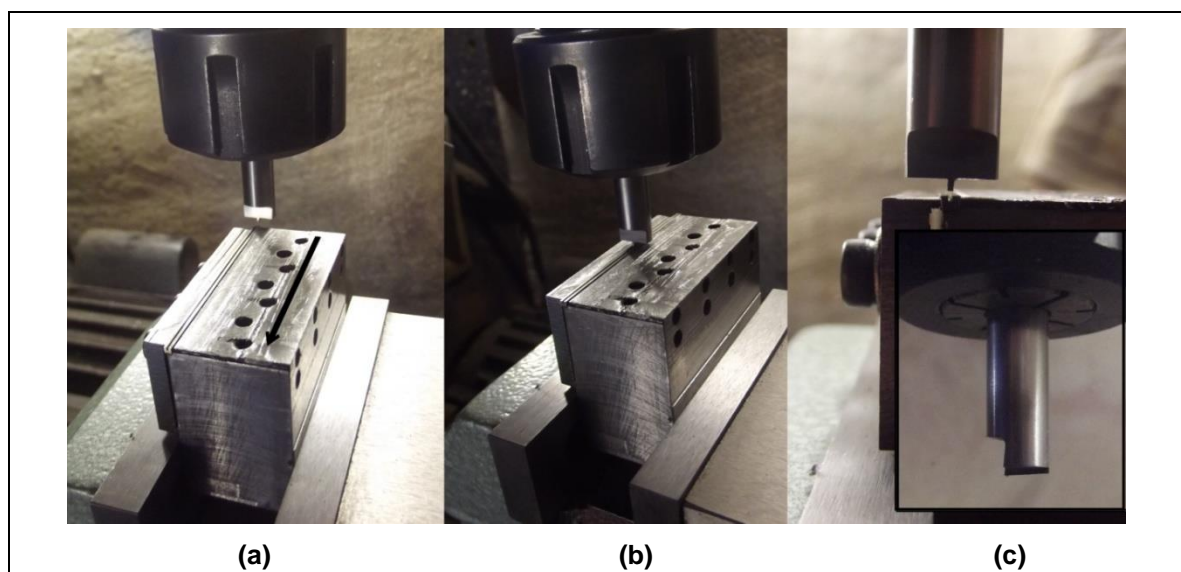


Figure 3.20 Clamping jig with drawing tool in milling machine

The test section was assembled and placed onto the testing rig. The complete assembled test section is shown in Figure 3.21. Thermocouples were pushed into the holes or grooves and secured at their intended positions with a small wooden wedge. The inlet and outlet fluid measuring thermocouples were permanently glued to the copper pipe. Pressure taps were connected to the pressure transducers; the heater power wires were connected to the power supply; and the inlet and outlet tubing were connected to the water circulation loop of the test rig.

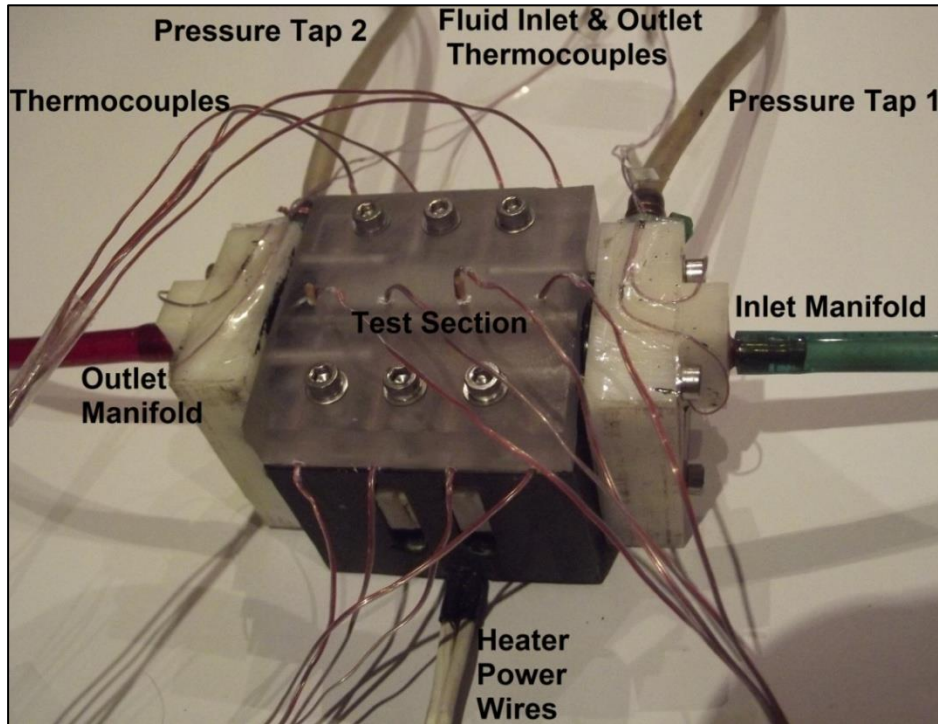


Figure 3.21 Complete assembled test section showing the inlet and outlet manifolds; the main test section body; heater power wire; and the thermocouples

3.5.3. FABRICATED MICROCHANNELS

The inlet and outlet cross-sections of all three test sections were photographed with a digital microscope after fabrication. Photographs were used to determine the microchannel's exact dimensions by using a reference length, the outer channel width (W_s), was measured using a micrometer. The other dimensions were obtained using an image processing software program, ImageJ®.

Figure 3.22 to Figure 3.24 shows the channel dimensions and the photographs taken of the inlet and outlet cross-section.

The centring of the microchannel within the stainless steel substrate was not ideal for all channels with the channel being offset to the left or the right from the centre. Dimensions between the inlet and the outlet were near exact and therefore it was assumed that the channels were uniform throughout the length of the test section. For Test Section 1 ($\alpha_c = 1.476$) there was an offset to the right of 0.12 mm, for Test Section 2 ($\alpha_c = 1.080$) an offset of 0.26 mm and for Test Section 3 ($\alpha_c = 0.645$) an offset of

0.06 mm. The length of all microchannel test sections was 50.00 mm as the ends were polished to within size and tolerance. From the photographs it is seen that the microchannels were machined square with sharp channel corners.

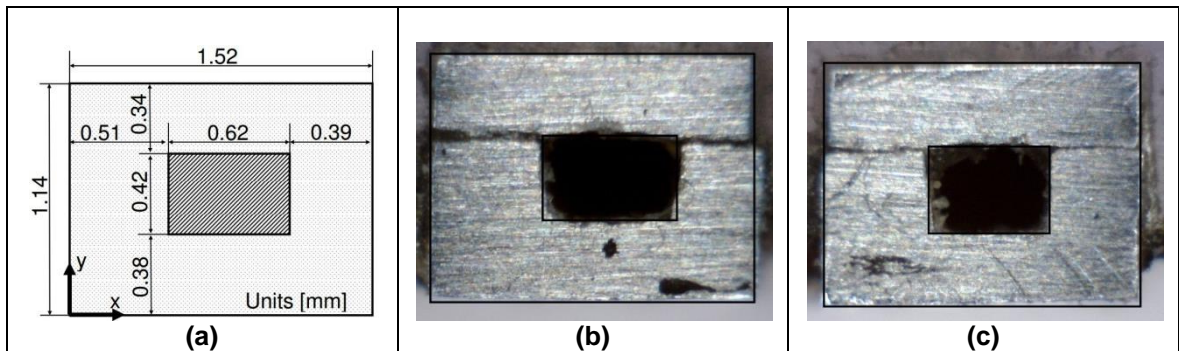


Figure 3.22 Test Section 1 cross-section: (a) actual measured channel dimensions, (b) photograph of inlet side of the channel and (c) photograph of the outlet side of the channel

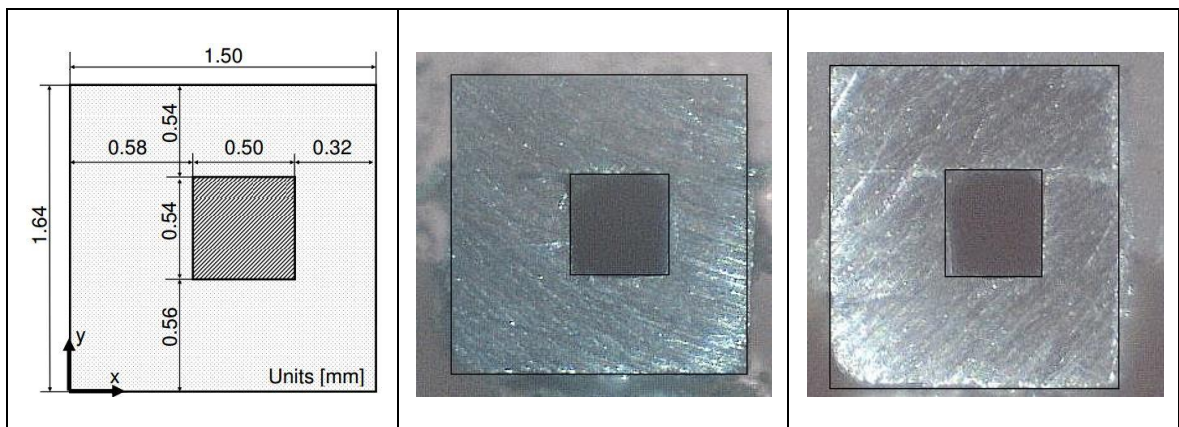


Figure 3.23 Test Section 2: (a) actual measured channel dimensions, (b) photograph of inlet side of the channel and (c) photograph of the outlet side of the channel

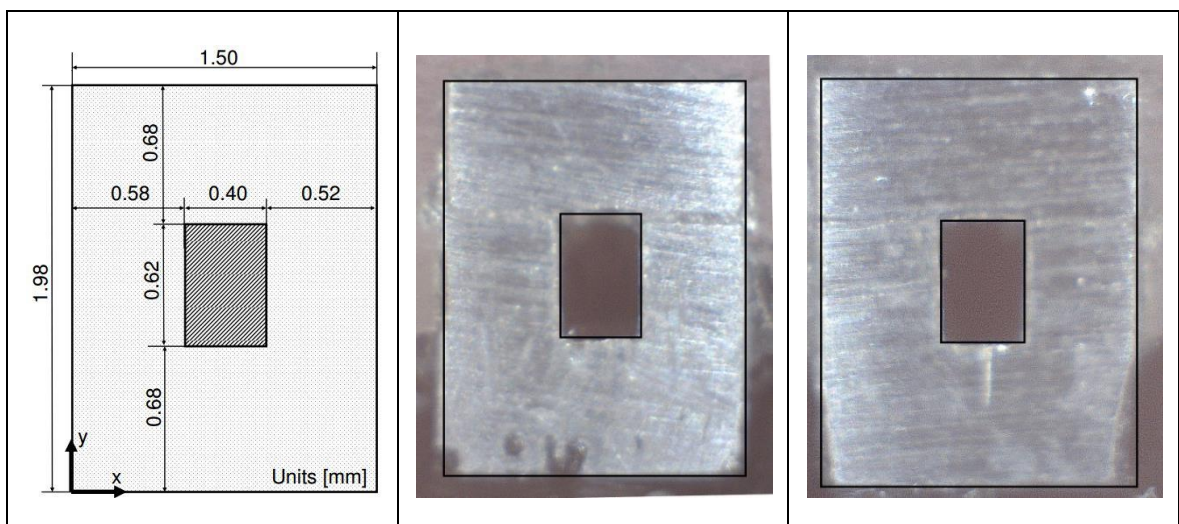


Figure 3.24 Test Section 3: (a) actual measured channel dimensions, (b) photograph of inlet side of the channel and (c) photograph of the outlet side of the channel

A direct comparison between the microchannels actual to design dimensions are shown in Table 3.3. A percentage deviation of the actual to the design dimensions was

calculated for each dimension, the measuring uncertainty of 0.01 mm was also included in the calculation. For Test Section 1 a 14.1 % deviation existed for the overall height of the channel test section, for Test Section 2 and 8.9 % deviation existed for the height of the microchannel and for Test Section 3 a 10.9 % existed for the height of the microchannel. All the percentage deviations of all the dimensional parameters were below 15 %. The measured dimensions were used in the data reduction as presented in the next chapter.

Table 3.3 Microchannel test section comparison between design and actual dimensions and the % deviation including the measuring uncertainty of 0.01 mm

Microchannel		H_c [mm]	W_c [mm]	H_s [mm]	W_s [mm]
Test Section 1	Design channel	0.41	0.62	1	1.5
	Actual channel	0.42	0.6	1.14	1.52
	% deviation	5.5	3.7	14.1	1.9
Test Section 2	Design channel	0.5	0.5	1.5	1.5
	Design channel	0.54	0.5	1.54	1.5
	% deviation	8.9	4.0	3.0	1.3
Test Section 3	Design channel	0.58	0.43	2	1.5
	Actual channel	0.52	0.4	1.98	1.5
	% deviation	10.9	8.4	1.4	1.3

3.6. INSULATION OF THE TEST SECTION

The test section had to be insulated externally because the plastic housings that encased the microchannel test sections were not sufficient. Isoboard[®] was used as the external insulation, as it has a low thermal conductivity ($k_{ins} = 0.03$ W/mK) and it is readily available from a local supplier. Detailed calculations are shown in Appendix G. Certain assumptions were made: firstly, a cylindrical geometry was used; secondly a surface temperature was assumed to be the average between the minimum and maximum temperatures in the microchannel test section (obtained from the CFD results) and thirdly, the test section was at steady state.

From the calculations, the thickness of the Isoboard[®] insulation required was 170mm in diameter to reduce the heat loss to about 1 % of the total heat input to the test section.

3.7. MICROCHANNEL TEST FACILITY DESIGN

A test facility was designed, built and commissioned which could meet the requirements for microchannel experimental testing. The test facility required microchannel specific test instrumentation which could accommodate the low flow rates and heat input to the

system. The selection of equipment, assembly and commissioning of the test facility played a major role to ensure that the outcomes of the study could be met.

A schematic drawing of the test facility is shown in Figure 3.25. A closed water loop system was used where the water was stored in a 22 litre tank. Water then flowed through a 15 μm filter and to the inlet of the pump, it was pumped using a magnetic coupled gear pump which ensured a constant pulsation free flow rate. The water then flowed through a gate valve which could be used to throttle the flow, if required, and to isolate the test section. Thereafter the water flowed through the microchannel test section and then through a Coriolis flow meter used to measure the mass flow rate of the fluid. The water re-entered the storage tank.

The water in the storage tank was kept at a constant temperature by pumping it through a tube-in-tube heat exchanger which was cooled using constant temperature water from a large submerged sump. Power to the test section was supplied by a DC power supply which could be voltage or current controlled. The temperatures, differential pressure, power supply voltage and current, and the flow rate were measured using a data acquisition system.

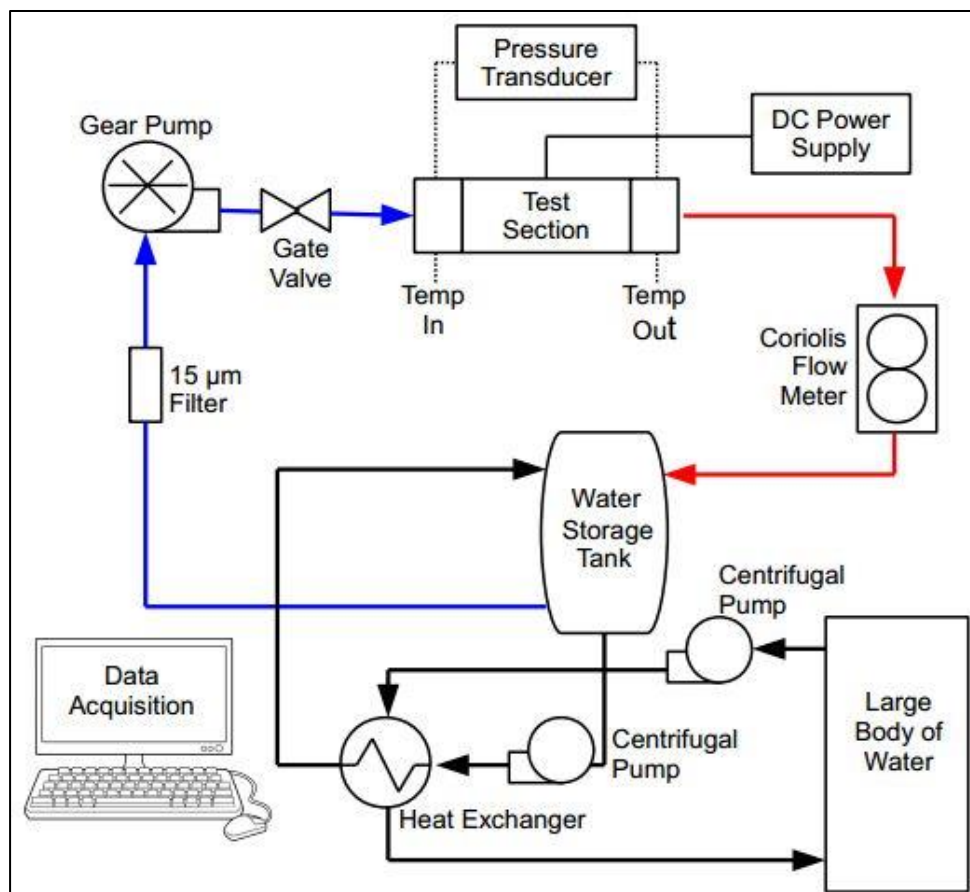


Figure 3.25 Schematic of the experimental test setup

The specification of the components, as shown in Figure 3.25, were vital to obtaining the desired facility requirements. From the test section design (Section 3.2 to

Section 3.4) the following parameters needed to be achieved by the experimental test setup:

- Flow rate: 0 – 70 ml/min
- Differential pressure measurements: 0 – 50 kPa
- Temperature measurements: 20 °C – 75 °C
- Test section power input: 7.5 W

The best possible components, within a budget, were selected to best suit the design requirements. A brief explanation and the parameters are given for the gear pump; flow meters; pressure transducers; thermocouples; heater element; power supply and a data acquisition (DAQ) system.

The gear pump selected provided a constant pulsation free flow which could be set at a desired flow rate. The pump had interchangeable magnetic connected pump heads with a specific flow rate range. Analogue input and output (0 to 10 volts) protocols were used to control the pump speed and monitor the flow. The pump was interfaced with the DAQ system and therefore all communications were done via a computer. The gear pump specifications are as follows:

- Make and model: Isemaic[®] BVP-Z with a Z-183 pump head
- Flow rate range: 5 – 504 ml/min
- Maximum differential pressure: 280 kPa

A Coriolis mass flow meter was used to measure the flow rate. The flow meter had an output display screen, but the flow rate was logged via the DAQ system. The flow meter specifications are as follows:

- Make and model: Micro Motion[®], Elite Coriolis Flow and Density Meters CMFS010
- Measurement range: 15 – 1300 ml/min
- Measurement accuracy: 0.25% of flow rate (based on minimum specified flow rate)

A differential pressure transducer was used to measure the pressure drop over the test section. The measuring accuracy was defined based on the maximum rated pressure. The pressure transducer specifications are as follows:

- Make and model: Omega[®] PX409 Series, PX409-015DWUV
- Measurement range: 0 – 100 kPa
- Measurement accuracy: 0.08% of maximum rated pressure

Sixteen T-type, copper-constantan, thermocouples were utilised to measure the fluid inlet and outlet temperatures as well as the temperatures on the two sides and top outer walls of the microchannel test section. The thermocouples were made up from fine duplex insulated wire and the junction was fused using a spot welding technique. The calibration of the thermocouples is discussed in the next section. The thermocouple specifications are as follows:

- Make and model: Omega[®] fine wire duplex insulated thermocouple wire
- Type: Copper-constantan T-type
- Gauge: AWG number, #30
- Insulation: Neoflon PFA
- Un-calibrated uncertainty: 0.25 °C

The heater element was fabricated from Neoflon insulated constantan wire and was re-used for all test section. The resistance of constantan remains fairly constant over a large temperature range, therefore making it ideal for a heater element. The required wire gauge was experimentally determined by increasing the voltage through a test heater, of a certain gauge wire, until the wire deteriorated. The maximum power input was calculated from the voltage and current measurements and the wire gauge which provided an acceptable margin of safety was used. The heater parameters are as follows:

- Wire type: Constantan
- Wire gauge: #40
- Heater resistance: 25 Ω
- Heater wire length: 400 mm

The power supply selected was specified to be used on other test setups, as well, and therefore the maximum power specification was not a driving factor for the low power microchannel research conducted. The power supply has built-in voltage and current measuring capabilities which were interfaced to the DAQ system via a 0 – 10 volt protocol. The power supply specifications are as follows:

- Make and type: Kikusui[®] PWR800 DC power supply
- Maximum voltage and current: 320 V and 12.5 A
- Noise specification: 140 mV (peak to peak)
- Voltage measuring accuracy: 0.05 % of measured value + 3 mV
- Current measuring accuracy: 0.1 % of measured value + 10 mA

A National Instrument Compact DAQ[®] system was used to control the test setup and measure the required parameters. The DAQ was controlled using customised code written in Labview[®] version 9.0. The DAQ consisted of two 16 channel thermocouple cards; one eight channel 0-10 V input card; and one eight channel 4 – 20 mA input card, which were used to measure the required mass flow rate; differential pressure; voltage and current; and the temperatures. The test setup was controlled via one eight channel 0 – 10 V output card and one eight channel 4 – 20 mA output card which controlled the pump speed and power supply.

The microchannel test facility was designed and built specifically to obtain accurate and precise measurements for the specific microchannel research performed. The test facility consisted of a closed loop water system, a cooling water loop and a DAQ system. The design, building and commissioning of the test facility played a major role in ensuring the outcomes of this study.

3.8. INSTRUMENTATION CALIBRATION

Calibration of the instrumentation creates a relation between the actual measured parameter and the communication output protocol from the unit. Most instruments use a 0 – 10 V or a 4 – 20 mA output protocol. Measuring instrumentation, except the thermocouples, were calibrated by the supplier and a calibration certificate was supplied. Thermocouples were calibrated in-house to reduce the uncertainty provided by the suppliers' data sheet. The uncertainty of the instrumentation is discussed in detail in Appendix H, but a summary of the uncertainty of the measured parameters is shown in Table 3.4. The calibration of the thermocouples is briefly discussed below.

Table 3.4 Measured parameter uncertainty summary

Measured Parameter	Uncertainty
Temperature	0.113 °C
Dimensions	0.01 mm
Pressure	0.08 kPa
Flow rate	0.042 – 0.013 ml / min
Voltage	0.01 V
Current	0.01 A

3.8.1. CALIBRATION OF THE THERMOCOUPLES

The thermocouples were calibrated to improve on the standard measuring uncertainty of 0.25 °C. The thermocouple junction was made and connected to the thermocouple cards which is a module of the DAQ system. The thermal couples were submersed into a thermal bath along with a calibrated PT100 probe, with an uncertainty of 0.04 °C. The water of the thermal bath was set at a fixed temperatures ranging from 20 °C to 60 °C in 5 °C intervals. For each temperature interval the thermal bath temperature was allowed to reach steady state and the temperature measurements of the thermal couples and

the PT100 were obtained. Thermocouple readings were calibrated using a linear regression according to the PT100.

The linear regression coefficients were obtained from a post processing procedure where a best fit was obtained. The linear calibration used:

$$T_{pt100} = T_{cal,therm} = m \cdot T_{DAQ} + C \quad \left| \text{Equation 3.1} \right.$$

Where T_{pt100} is the temperature as measure by the PT100 probe, $T_{cal,therm}$ is the calibrated thermocouple reading after calibration, m is the gradient coefficient, T_{DAQ} is the uncalibrated value measured by the DAQ system and C is the offset constant.

After the calibration coefficients were obtained the maximum deviation from the PT100 probe was determined, which was combined with the uncertainty of the probe as suggested by Moffat (1988). The thermocouple card measuring uncertainty was 0.02 °C after the cold junction compensation. The labelling/naming convention of the temperature measurements is shown in Figure 3.26. Calibration coefficients and the total uncertainty after calibration is presented in Table 3.5. A maximum uncertainty 0.117 °C was calculated and will be used accordingly in the uncertainty analysis.

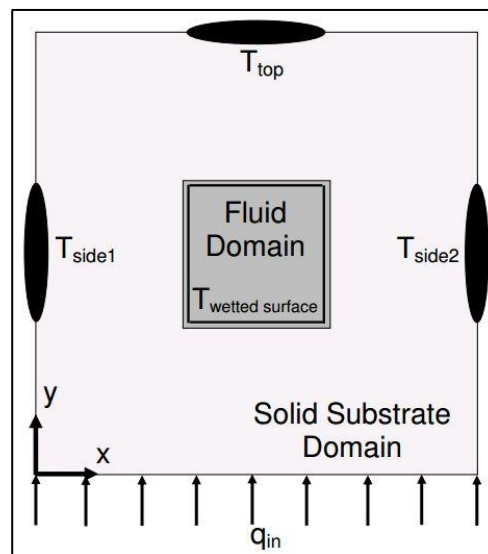


Figure 3.26 Labelling/naming convention of the temperature measurements

Table 3.5 Calibration coefficient and uncertainty for each thermocouple after calibration

Thermocouple	No.	Calibration coefficients		Uncertainty [°C]
		<i>m</i>	<i>C</i>	
Inlet manifold	1	0.0789	0.996	0.113
	2	0.0744	0.996	0.112
Outlet manifold	1	0.155	0.996	0.107
	2	0.158	0.995	0.106
T _{side1}	1	0.136	0.999	0.112
	2	0.183	0.999	0.107
	3	0.216	0.999	0.106
	4	0.363	0.999	0.104
T _{side2}	1	0.278	0.998	0.103
	2	0.314	0.999	0.103
	3	0.339	0.998	0.103
	4	0.367	0.999	0.102
T _{top}	1	0.383	0.994	0.101
	2	0.551	0.998	0.102
	3	0.465	0.995	0.102
	4	0.841	0.996	0.102
			Maximum	0.113

3.9. SUMMARY OF THE TEST SECTION AND TEST FACILITY DESIGN

The design and fabrication of the microchannel test sections and the design and assembly of the testing facility were discussed in this chapter. The microchannel test section was designed and fabricated. Cross-sectional areas of the different fabricated test sections were measured and compared to the ideal case. A maximum deviation from the ideal test section was 14.4 %. The layout of the microchannel within the solid substrate was offset horizontally by 0.12 mm for Test Section 1, 0.26 mm for Test Section 2 and 0.06 mm for Test Section 3. The length of the microchannel test section was exact to within the measuring tolerance.

The test facility was built from the ground up to accommodate the microchannel test parameters. The calibration of the thermocouples and the uncertainty of the instrumentation was determined. The design of the test sections and test facility was vital to the outcomes of the research conducted.

CHAPTER 4

TEST PROCEDURE AND MEASURED RESULTS

4.1. INTRODUCTION

In this chapter the experimental procedure and only the measured wall temperatures, inlet and outlet fluid temperatures and the pressure drop over the test section will be presented, Chapter 5 and Chapter 6 hereafter will discuss the data reduction subsequent results. The measured surface wall temperatures, inlet and outlet fluid temperatures and the differential pressure drop measurements are plotted on graphs and discussed in detail.

4.2. EXPERIMENTAL PROCEDURE

The experimental procedure was carefully defined to ensure an effective method was followed in obtaining as accurate as possible results. The procedure ensured that the test results were captured at steady state; that a full range of test measurements were recorded; and that the tests were performed in a safe manner.

The test rig was switched on and the Labview[®] based control and logging program was run. The flow of the water was started and slowly increased to a high rate, thereafter the pressure transducer pipes were bled of any air entrapped and the system was left to run with no heat input for 10 minutes. This process ensured that all the air within the tubing and test section was removed. Water within the storage tank was circulated and the tests only commenced once the bulk fluid temperature reached a steady state, which ensured that the inlet fluid temperature to the test section was constant throughout the test. The constant inlet fluid temperature was dependant on the temperature of the water in the large sump, the temperature of the sump remained relatively constant from day to day but did vary over months and as the seasons changed, hence as the ambient temperature changed.

The microchannel dimensions were used in calculating the Reynolds number based on the measured mass flow rate and average fluid temperature between the inlet and outlet. The flow rate was adjusted so that the Reynolds number was approximately 2500, which is 200 higher than the conventional transition Reynolds number of 2300, and the system was left for the flow to stabilise.

The adiabatic tests were performed from a high to a low Reynolds number as it was found that the system stabilised faster than from a low to high Reynolds number. The

flow rate was adjusted for a Reynolds number range of approximately 2500 to 250 with a change in Reynolds number of about 200 per test increment. The flow rate, differential pressure and test section temperatures were monitored and measurements were taken once the system reached steady state.

The diabatic tests were also performed from a high ($Re = 2500$) to a low ($Re = 200$) flow rate with a step increment of approximately 200 in the Reynolds number. A constant power (≈ 7.5 W) was supplied to the test section throughout the test. All measurements were only recorded once the test section reached steady state. The system took approximately 50 minutes to reach steady state per increment.

The input energy, via the heater, and the retracted energy, via the water flowing through the test section, was compared using Equation 4.1. The percentage energy balance was observed during the test to determine how much energy was lost to the environment. Energy balance results will be discussed in more detail in Chapter 6.

$$\% \text{ Energy Balance} = \frac{Q_{in} - Q_{out}}{Q_{out}} / 100 \quad \left| \text{Equation 4.1} \right.$$

Where Q_{in} is the input energy and Q_{out} is the energy removed by the water.

The energy balance; flow rate; pressure drop over the test section; and the test section temperatures were monitored and steady state was assumed when the change for each measured parameter was below 2 % over a period of three minutes. Once steady state was reached data was recorded at 20 kHz for a duration of 10 seconds for each flow rate increment. All tests were performed twice to ensure repeatability. The prescribed testing procedure was performed for all three test sections and the measured data was stored in a text based file for each test.

4.3. EXPERIMENTAL RESULTS

The measured experimental results are discussed in this sub section. The side, top and average wall temperatures, difference between the outlet and inlet temperatures and the pressure drop over the test section are presented using graphs and conclusions based on the observations are made.

A direct comparison of the measured wall temperatures, between the different test sections, cannot be made due to a difference in geometry and location of the thermocouples relative to the heating block. From the numerical analysis, as performed in Section 3.3, it is seen that the temperature gradients are significantly different for the three different test sections at the side and top measuring positions. Therefore, a direct comparison based on the side and top wall measurements could be misleading. A comparison of the heat transfer coefficient will be made in Chapter 6.

4.3.1. MEASURED SIDE WALL TEMPERATURES

Figure 4.1 and Figure 4.2 shows the left and right side wall temperatures for Test Section 1, Figure 4.3 and Figure 4.4 for Test Section 2 and Figure 4.5 and Figure 4.6 for Test Section 3, as a function of the axial position of the measurements for the different flow rates.

From Figure 4.1 and Figure 4.2, (Test Section 1), it can be seen that the wall temperatures increase along the axial direction for the first three measuring positions. However, for higher flow rates (volumetric rates approximately above 13.5 ml / min) a drop in temperature at the last axial measuring positions were observed. This is not commonly seen in similar literature. It would be expected that the wall temperatures increase along the axial direction since the bulk fluid temperature increases from the inlet to the outlet.

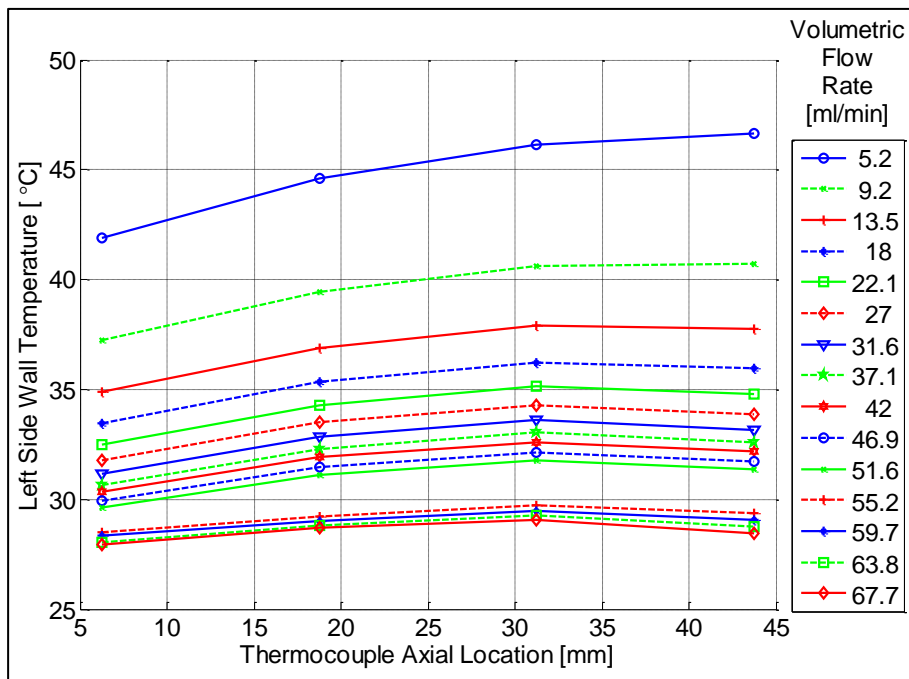


Figure 4.1 Left side wall temperatures versus the thermocouple axial location for different flow rates: Test Section 1

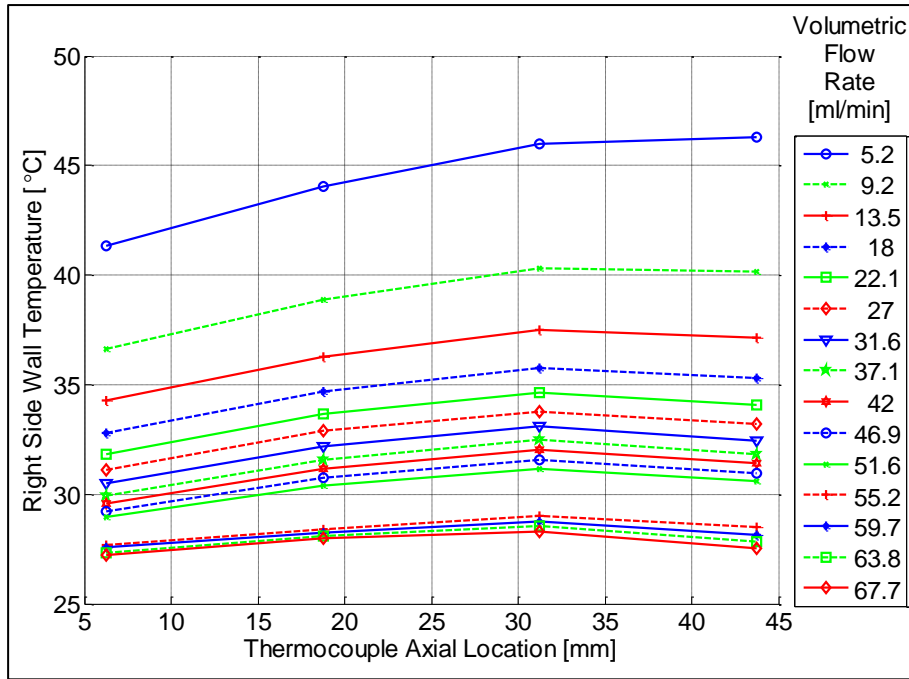


Figure 4.2 Right side wall temperatures versus the thermocouple axial location for different flow rates: Test Section 1

From Figure 4.3 and Figure 4.4, (Test Section 2), the result trend is similar to those observed for Test Section 1. The temperature increases along the axial direction and decreases as the flow rate becomes larger. Both the side wall temperatures decrease between the third and fourth measuring position when the flow rate is higher than 57.6 ml / min.

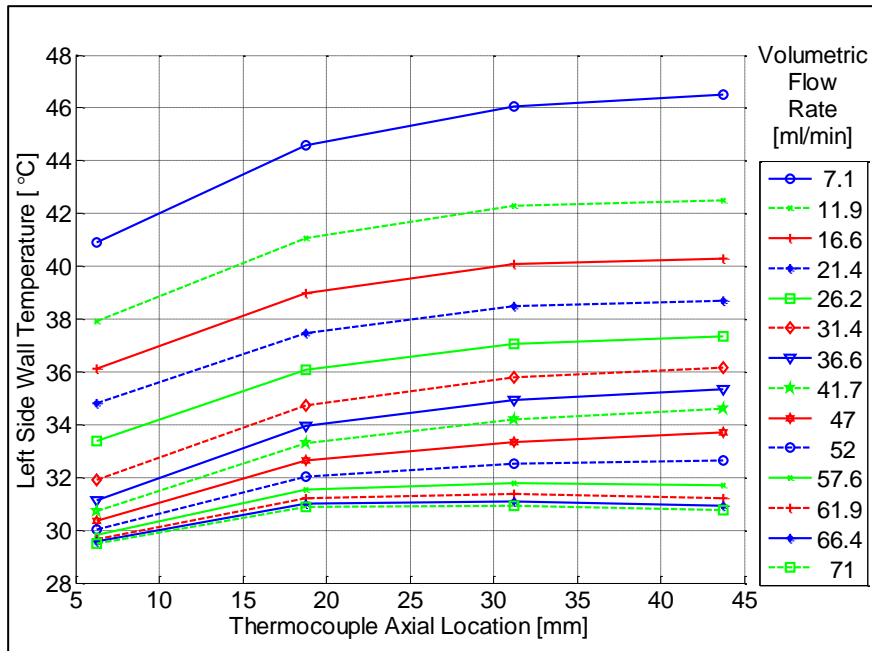


Figure 4.3 Left side wall temperatures versus the thermocouple axial location for different flow rates: Test Section 2

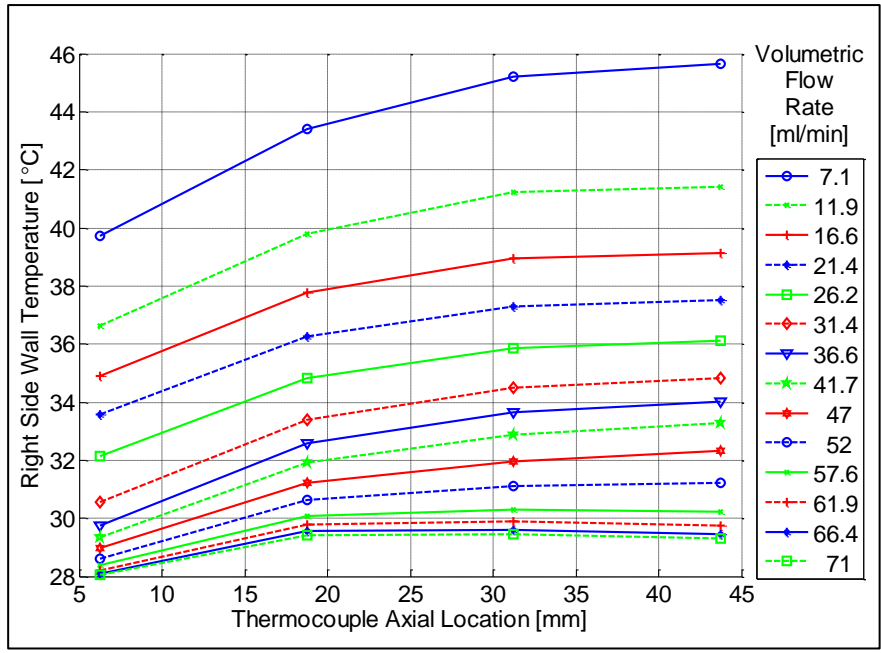


Figure 4.4 Right side wall temperatures versus the thermocouple axial location for different flow rates: Test Section 2

From Figure 4.5 and Figure 4.6, (Test Section 3), the temperature increases along the axial direction for the first three measuring positions and for the fourth measuring position the temperature decreases, as seen for the previous test section. The decrease in the temperature difference between the third and fourth measuring positions becomes larger as the flow rate increases. From the results obtained for this test section, it indicates that the phenomenon identified is flow rate dependant. The decrease in the side wall temperature at the fourth measuring location is significantly larger than for the previous two test sections.

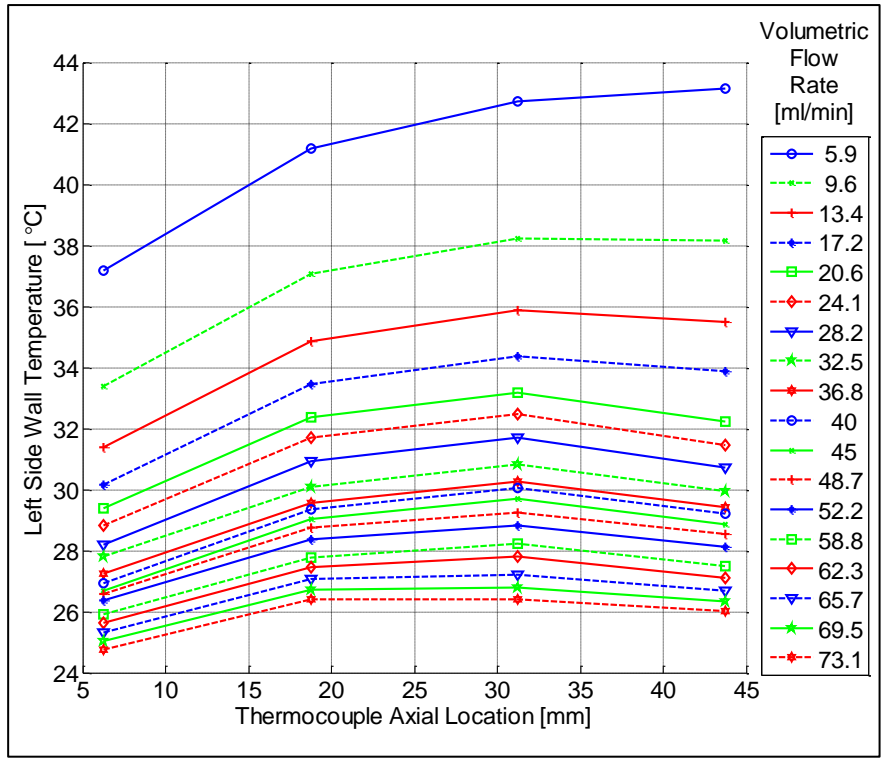


Figure 4.5 Left side wall temperatures versus the thermocouple axial location for different flow rates: Test Section 3

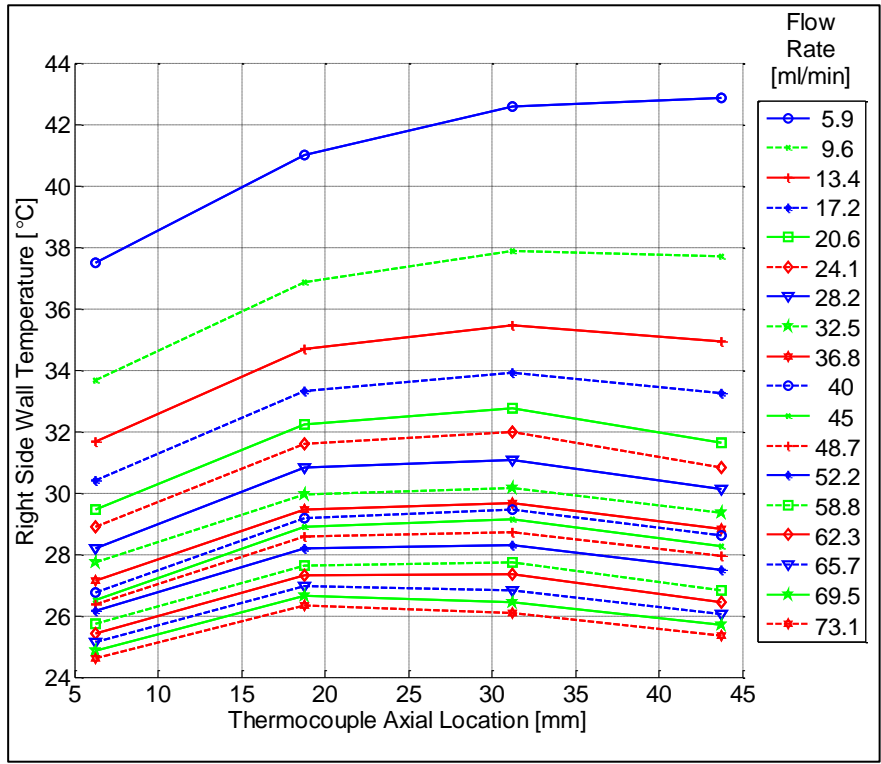


Figure 4.6 Right side wall temperatures versus the thermocouple axial location for different flow rates: Test Section 3

The following possibilities exist, which could influence the results obtained, where the side wall temperature at the last measuring position is uncharacteristic to expected

trends. The exact cause of this phenomenon is unknown and further research may be required to gain a better understanding:

- The fluid flow within the microchannel could be transiting to turbulent flow towards the end of the test section which would increase the heat transfer coefficient and hence decrease the wall temperatures.
- The sudden expansion of the test section outlet could play a role in the effect of the wall temperatures. The working fluid could be cooling the solid substrate at the end of the test section therefore decreasing the wall temperatures at the last measuring position.
- The insulation at the ends of the test section, between the microchannel and heater assembly and the inlet and outlet manifolds (refer to Section 3.5), could also influence the side wall temperatures.

The differences between the left and right side wall temperatures are plotted in Figure 4.7, Figure 4.8 and Figure 4.9 for Test Section 1, Test Section 2 and Test Section 3, respectively, as a function of the measuring position at some volumetric flow rates. The measuring uncertainty of 0.080 °C (combined uncertainty from both side wall temperatures) is also included in the plots as error bars. The axial measuring positions are shifted slightly to the right, in the graphs, for each flow rate for clarity purposes.

If the microchannels were symmetrical around the y-axis (with reference made to Figure 3.1), the thermocouples were positioned perfectly, and the thermocouples had the same thermal calibration response, the difference between the left and right side wall temperature should be zero. From Figure 4.7 to Figure 4.9 below it can be seen that a temperature difference exists. The difference in the side wall temperature becomes greater as the flow rate increases for Test Section 1 and Test Section 2, which directly relates to the magnitude of the measured temperature.

Table 3.2, the measured microchannel dimensions, indicates that the left wall is 0.12 mm thicker than the right, for Test Section 1 and from Figure 4.1, Figure 4.2 and Figure 4.7 it is seen that the left wall temperatures are higher than the right wall. For Test Section 2 the left wall is 0.26 mm thicker and for Test Section 3 is 0.06 mm. A similar observation is made where the temperature on the left wall is higher than the right wall. Therefore, the unsymmetrical layout of the microchannel in the solid substrate has an effect on the side wall temperatures.

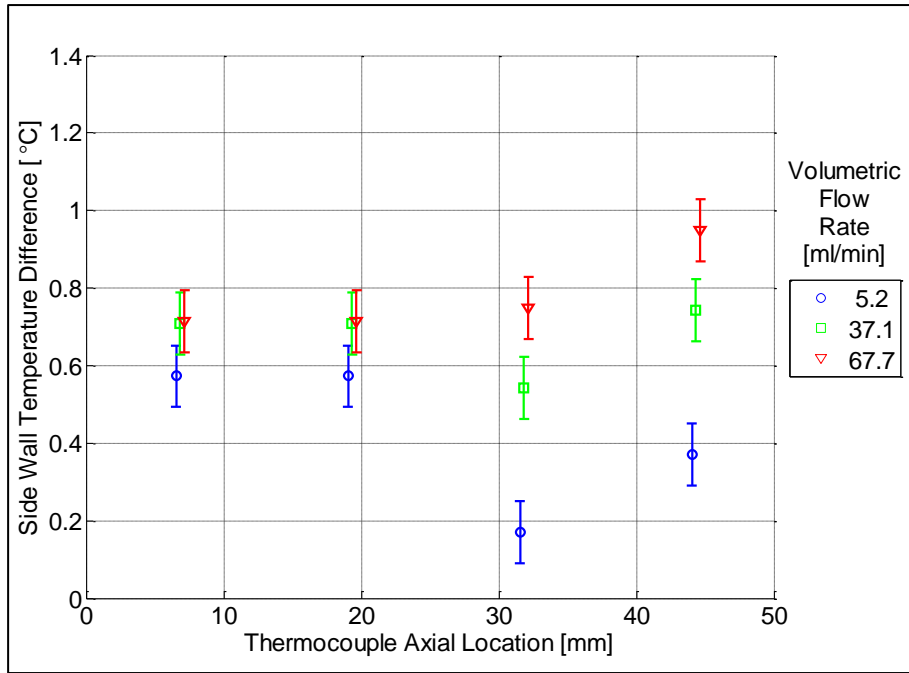


Figure 4.7 Side temperatures difference versus the thermocouple axial location for different flow rates: Test Section 1

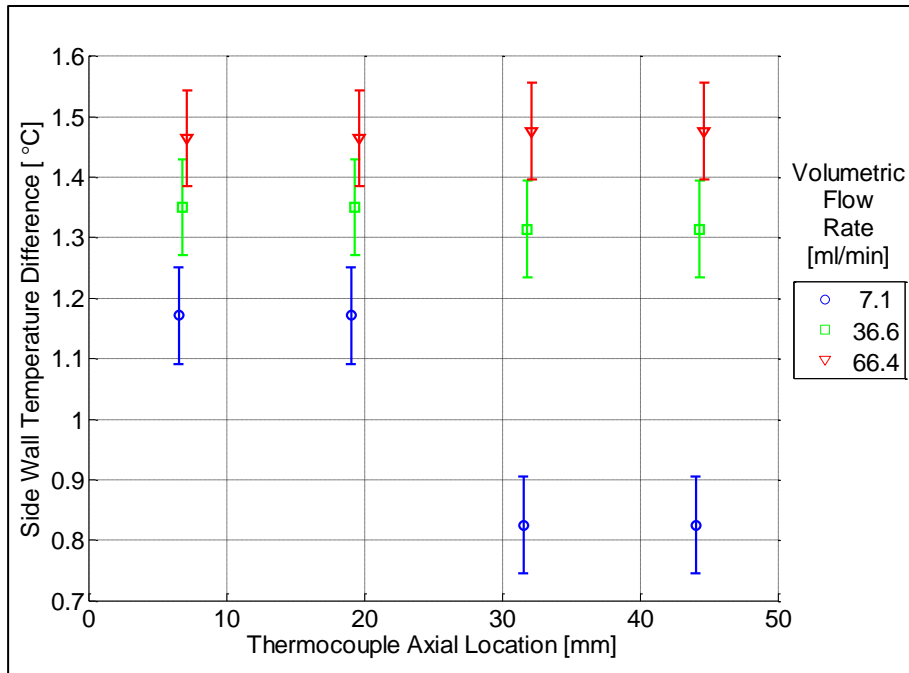


Figure 4.8 Side temperatures difference versus the thermocouple axial location for different flow rates: Test Section 2

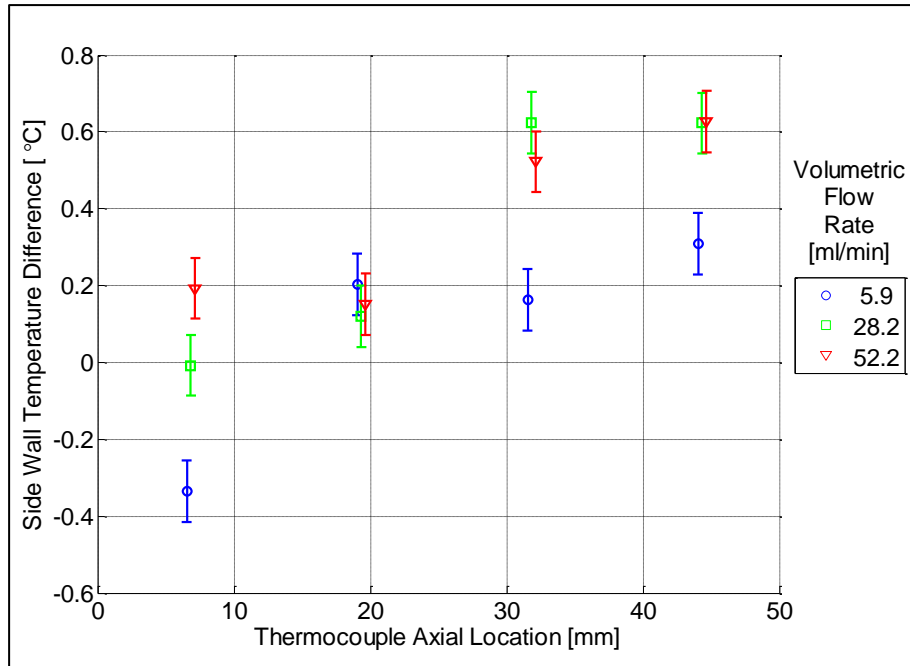


Figure 4.9 Side temperatures difference versus the thermocouple axial location for different flow rates: Test Section 3

The average difference between the left and right side wall temperatures versus the microchannel offset distance within the solid substrate is shown in Figure 4.10. The average side wall temperature difference increases as the horizontal channel offset distance increases. Therefore, as the channel offset is increased within the solid substrate a larger side wall temperature would be expected on the side wall which increases in width.

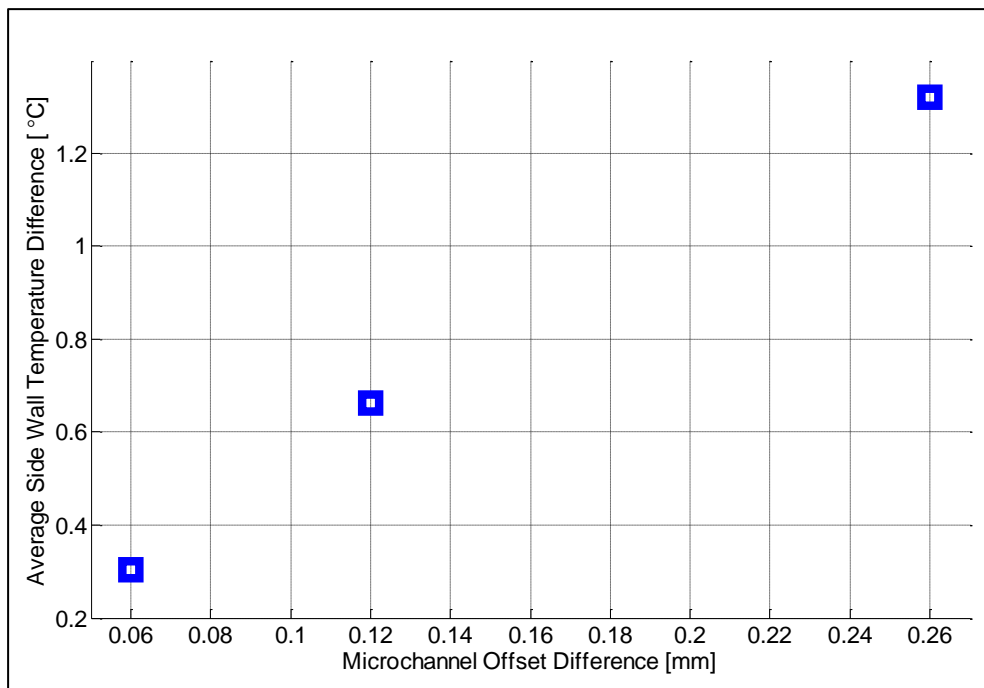


Figure 4.10 Average side wall temperature difference versus the microchannel offset distance within solid substrate

4.3.2. MEASURED TOP WALL TEMPERATURES

Figure 4.11 and Figure 4.12 shows the top wall temperatures as a function of the axial position of the measuring positions for the different flow rates for Test Section 1 and Test Section 2, respectively. The temperature increases along the axial direction and decreases as the flow rate becomes larger. Via careful comparison, it can be seen that the top wall temperatures were lower than the side-wall measurements, as expected from the numerical results used during the design phase of the test sections.

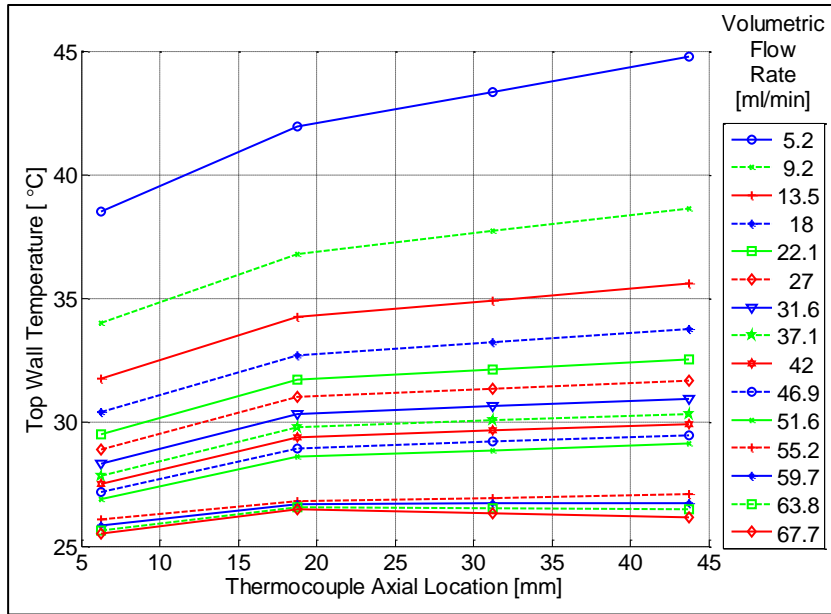


Figure 4.11 Top wall temperatures versus the thermocouple axial location for different flow rates: Test Section 1

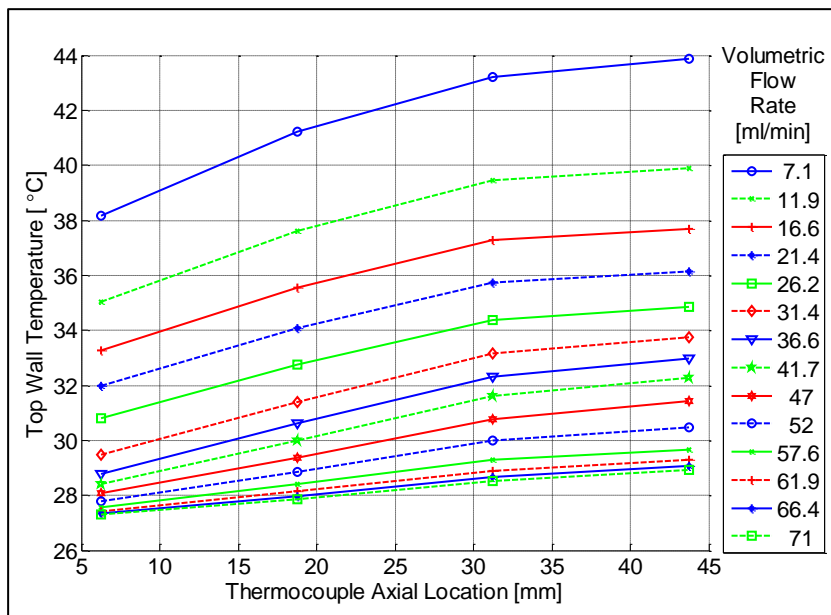


Figure 4.12 Top wall temperatures versus the thermocouple axial location for different flow rates: Test Section 2

Figure 4.13 shows the top wall temperatures as a function of the axial position of the measuring positions for the different flow rates for Test Section 3. The temperature increases along the axial direction for the first three measuring positions but for the last measuring position the temperature decreases significantly for the flow rates larger than 13.4 ml / min. Top wall temperatures obtained for Test Section 1 and Test Section 2 did not decrease between the third and fourth measuring position. The large decrease could be a result of the reasons listed in Section 4.3 but the possibility of a large measuring error at this location could also be a possibility.

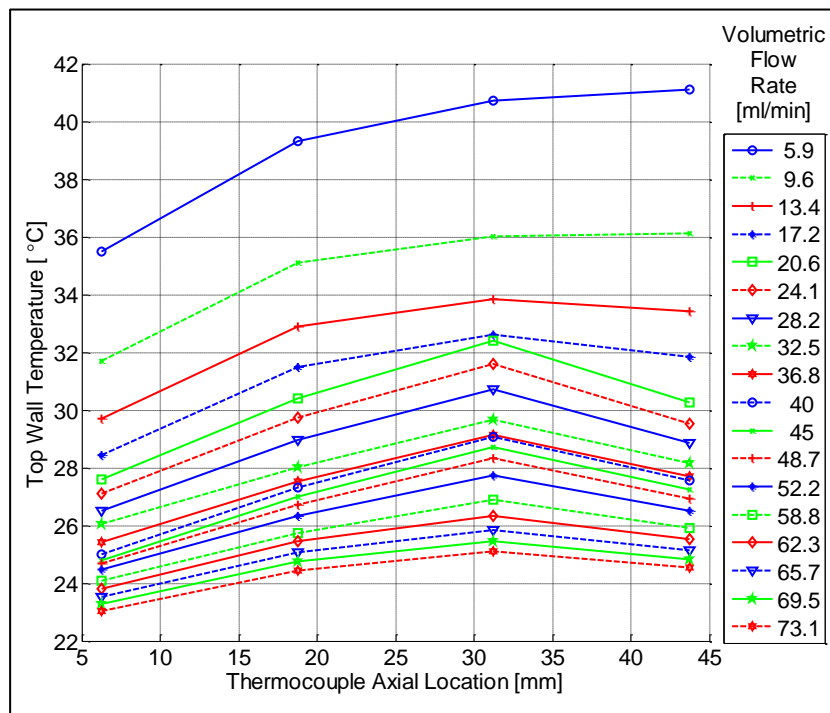


Figure 4.13 Top wall temperatures versus the thermocouple axial location for different flow rates: Test Section 3

4.3.3. MEASURED AVERAGE WALL TEMPERATURES

In Figure 4.14, Figure 4.15 and Figure 4.16 the side and top wall temperatures were averaged and plotted against the volumetric flow rate for the different measuring positions and test sections. The average wall temperature decreased as the flow rate increased for all test sections. A larger temperature change exists between the flow rate of 51.6 ml / min and 55.2 ml / min, for Test Section 1 (Figure 4.14), which indicates the onset of transition to turbulent flow. The decrease in the temperature, for Test Section 2 (Figure 4.15) and Test Section 3 (Figure 4.16), as a function of flow rate, follows a smoother curve with no sudden changes, this could indicate that the flow is only in the laminar regime. But on closer observation it can be seen for Test Section 2 there is a bulge in the average wall temperatures, which is encircled on the figure and for Test Section 3 a change in the graph trend also is visible, as encircled. This behaviour of the temperatures is uncharacteristic of expected temperature trend for flow in the laminar regime, the result of this will be discussed in detail in Chapter 6 For

Test Section 1 it is observed that the average wall temperatures decrease linearly once the flow is in the turbulent regime, for Test Section 2 the average wall temperatures decrease linearly after a flow rate of approximately 60 ml / min and for Test Section 3 approximately after a flow rate of 45 ml / min. From these observations it can be deduced that turbulent flow has been obtained for all three test sections. These findings will be confirmed when presenting the Nusselt number and friction factor results in Chapter 6.

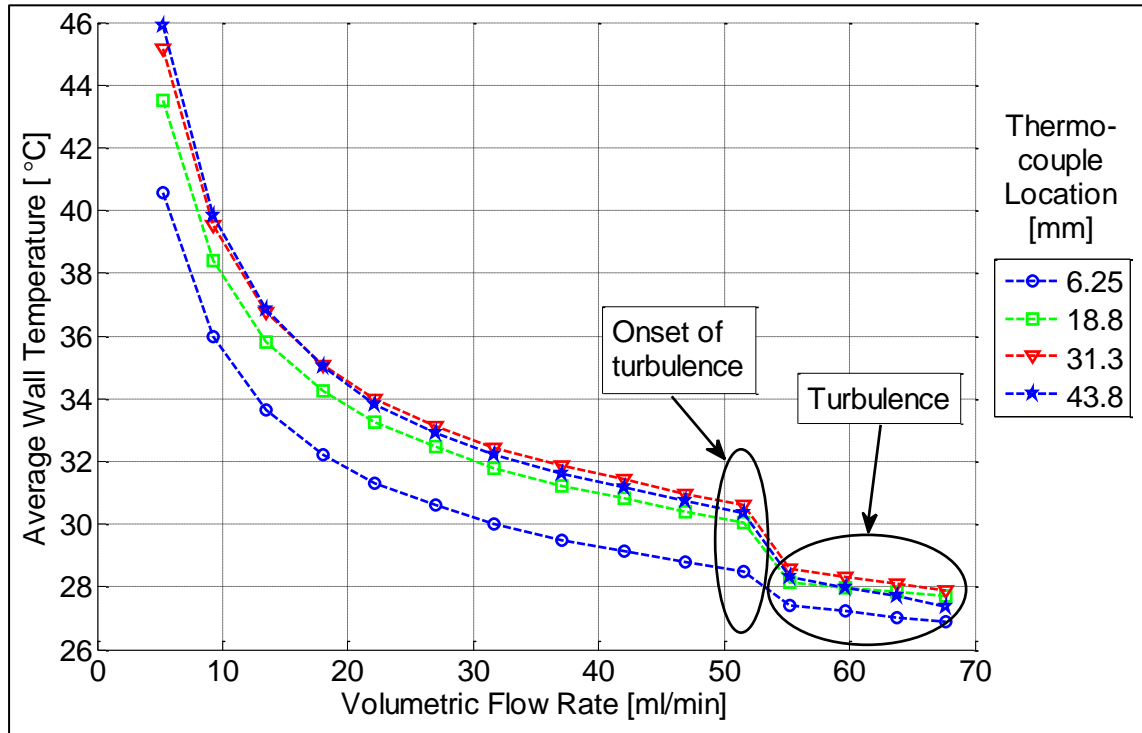


Figure 4.14 Average wall temperature versus the volumetric flow rate for the different axial measuring locations: Test Section 1

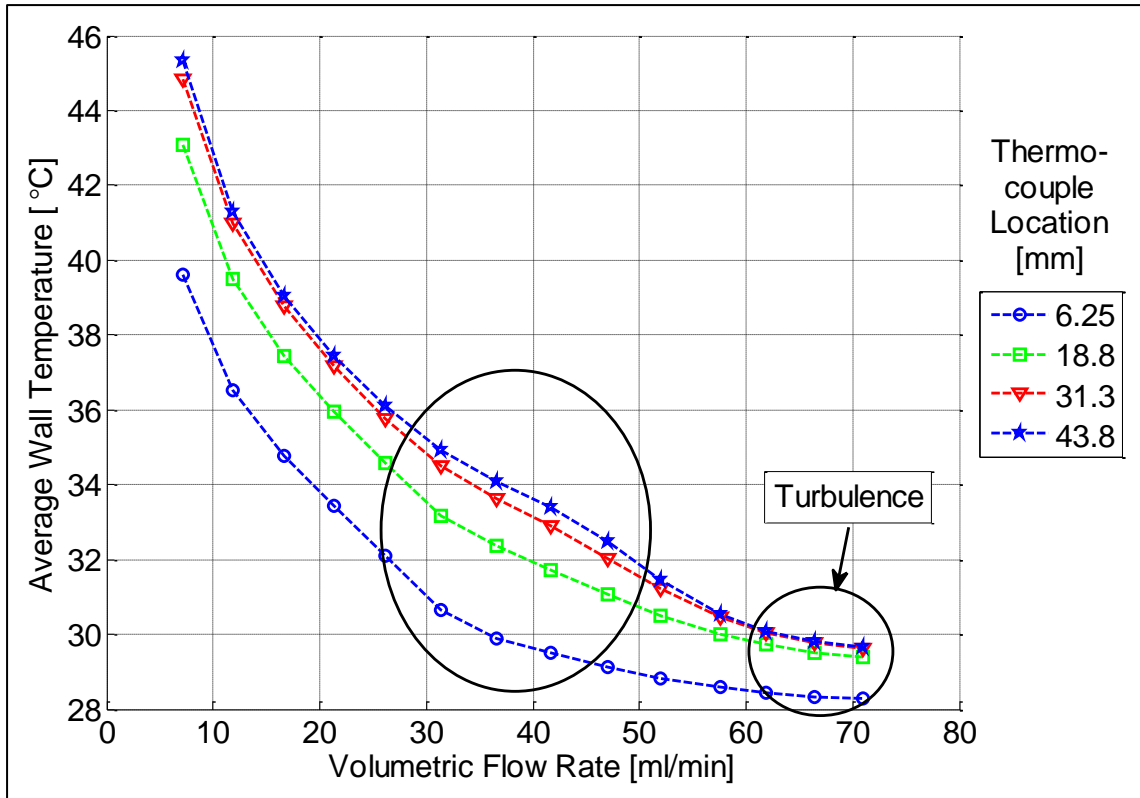


Figure 4.15 Average wall temperature versus the volumetric flow rate for the different axial measuring locations: Test Section 2

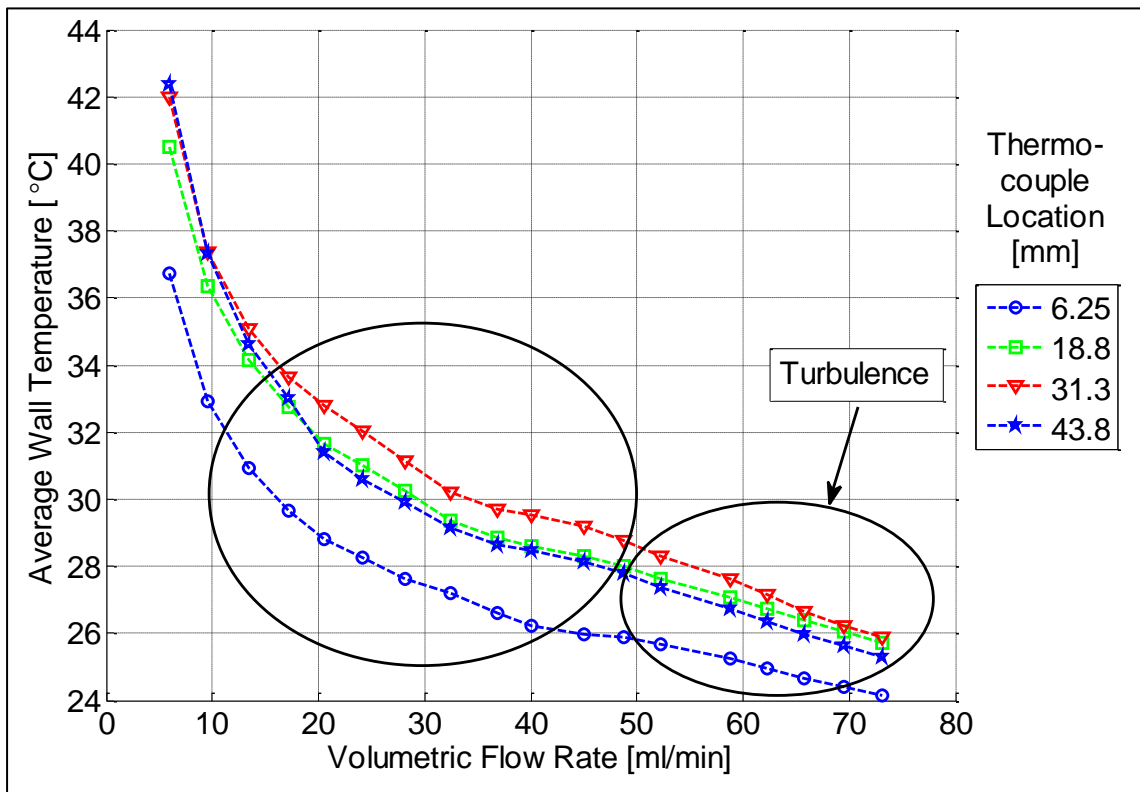


Figure 4.16 Average wall temperature versus the volumetric flow rate for the different axial measuring locations: Test Section 3

The temperature gradients between the measuring positions are plotted in Figure 4.17 for all three test sections for a low, middle and high flow rate. It can be seen that the temperature gradient decreases along the axial direction and that the temperature tends to flatten out towards the exit for the Test Section 1 and Test Section 2. The gradient tends to converge to zero towards the exit of the microchannel for the higher flow rates. It can be assumed that a thermally developed state is reached when the thermal gradient is zero. Therefore from the results it can be concluded that the test sections reach a near thermal developed state at the end of the test section for the higher flow rates. The thermal entrance length for turbulent flow is significantly shorter than for laminar flow, therefore it would be expected that the thermal gradient be nearer to zero for the higher flow rates which are in the turbulent regime. The thermally developing length is inversely proportional to the flow rate.

For Test Section 3 the temperature gradient decreases along the length of the channel but does not tend to converge to zero at the exit of the test section. The steeper gradient at the end of the microchannel test section is a result of the wall temperatures decreasing significantly between the third and fourth measuring position. As previously mentioned the possibility of a measuring error at the last measuring position could exist which will influence the gradient between the third and fourth measuring positions.

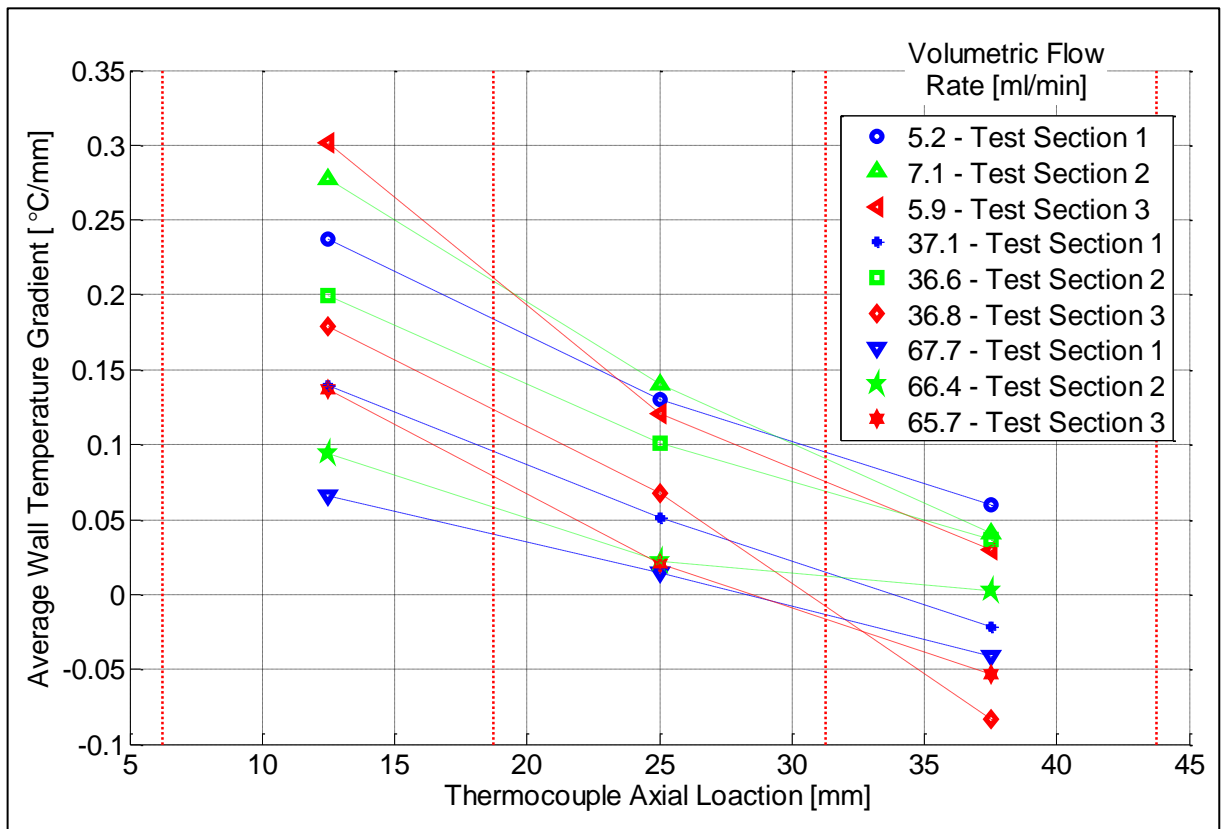


Figure 4.17 Average wall temperature gradient versus the axial measuring locations for different flow rates

4.3.4. DIFFERENCE BETWEEN THE OUTLET AND INLET FLUID TEMPERATURES

Figure 4.18 shows the fluid temperature difference between the outlet and the inlet for all three test sections. The temperature difference decreases non-linearly as the flow rate increases and the results for all three test cases are similar in magnitude for a specific volumetric flow rate. Heat input was constant for all tests, therefore the amount of energy transfer to the working fluid was similar for all three test sections.

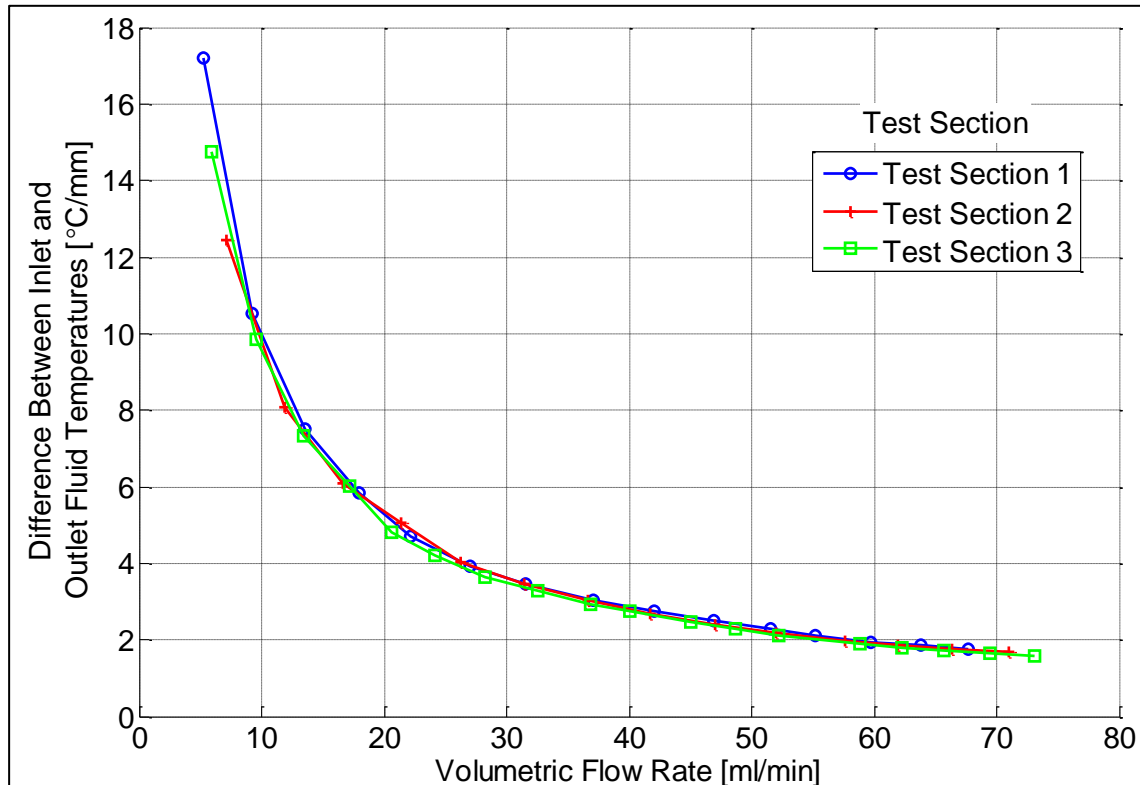


Figure 4.18 Difference between the inlet and outlet fluid temperatures versus the volumetric flow rate for the three different test sections

4.4. PRESSURE DROP MEASUREMENTS

Figure 4.19 shows both the adiabatic and diabatic pressure drops over the microchannel test section for all test sections. No correction factors were added to the results to account for the sudden contraction or frictional losses within the inlet and outlet manifolds. The pressure increases along a smooth curve for Test Section 2 and Test Section 3. For Test Section 1, at around 51.6 ml / min, the differential pressure drop increases sporadically, which indicates the onset of transitional/turbulent flow. For Test Section 2 and Test Section 3 the flow follows an exponential curve until a flow rate of approximately 60 ml / min and 45 ml / min respectively. Thereafter the pressure drop over the test sections follows a linear trend. The change in the pressure drop behaviour also indicates that the flow has transitioned into the turbulent regime. The adiabatic pressure drop is higher than the diabatic pressure drop for all test sections.

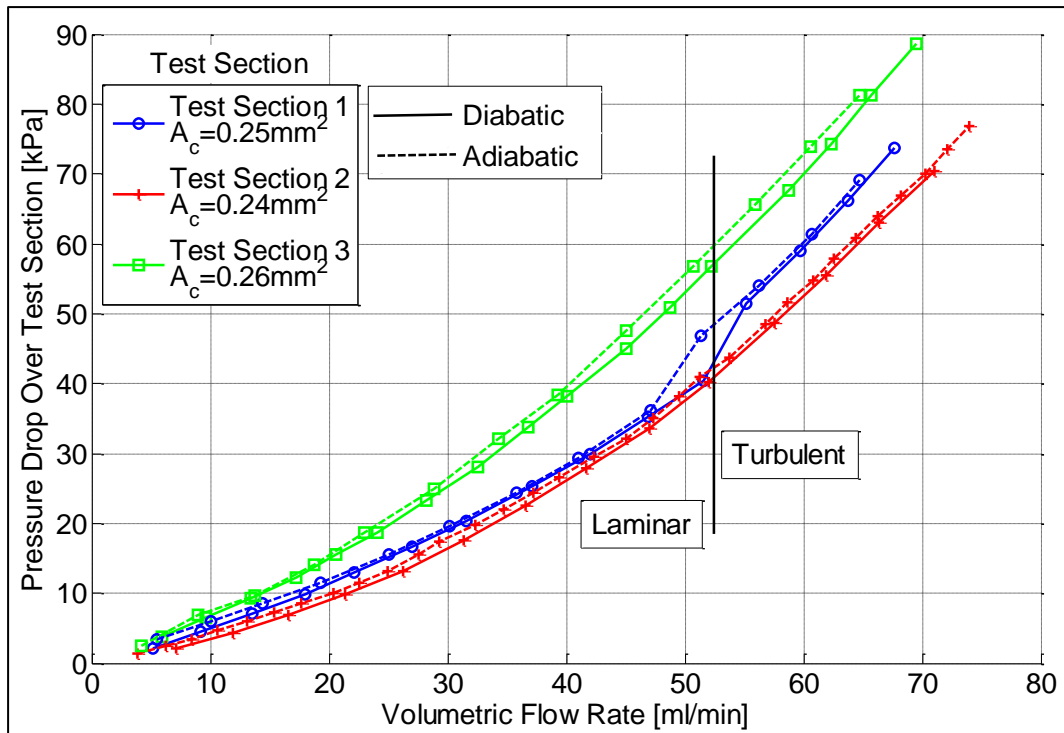


Figure 4.19 Diabatic and Adiabatic pressure drop over the test section versus the volumetric flow rate for the three different test sections: Test Section 1; Test Section 2; and Test Section 3

The cross-sectional area for each microchannel was calculated, as per the measurements in Section 3.5.3, and is labelled on Figure 4.19. The pressure drop is the highest, at a specific flow rate, for Test Section 2 which has the smallest cross-sectional area of 0.24 mm^2 . The pressure drop is the lowest for Test Section 3 which has the largest area of 2.6 mm^2 . The differential pressure drop for Test Section 1 lies between the highest and lowest and the cross-sectional area is 0.25 mm^2 . From this observation it can be concluded that the pressure drop is largely dependent on the cross-sectional area and decreases as the area becomes greater. A direct comparison of the pressure drop for the different aspect ratios cannot be made due to the differences between the cross-sectional areas of the microchannel.

4.5. SUMMARY OF THE TEST PROCEDURE AND MEASURED RESULTS

The experimental procedure and the measured data of the temperatures and differential pressure drops were presented in this chapter.

The wall temperatures, for all test sections, increased along the axial direction from the inlet to the outlet but for the higher flow rates the temperature of the last measuring position decreased. This phenomenon could be a result of the flow within the microchannel becoming turbulent; the effect of the sudden expansion at the outlet; or the effect of the insulation at the end of the test section. It was observed that the difference between the left and right side wall temperatures increased as the horizontal offset increased.

The average wall temperature decreased as the volumetric flow rate increased and an indication that turbulent flow occurred for Test Section 1 at 55 ml / min, for Test Section 2 at 60 ml / min and for Test Section 3 at 45 ml / min. The difference in the fluid temperature between the inlet and the outlet was similar for all test sections and decreased as the flow rate increased. The thermal gradient between the axial measuring positions decreased towards the end of the test section.

The differential pressure drop over the test section increased with the volumetric flow rate. Laminar to turbulent transition was also observed at similar flow rates as identified by the average wall temperatures. The differential pressure drop for the adiabatic case was higher than for the diabatic test cases. The magnitude of the pressure drop was dependent on the magnitude of the cross-sectional area, where the pressure drop increased as the cross-sectional area decreased. A direct comparison of the effect of the aspect ratio on the differential pressure drop could not be made.

CHAPTER 5

DATA REDUCTION/ANALYSIS

5.1. INTRODUCTION

In this chapter the methodology of determining the heat transfer coefficient, Reynolds number, Prandtl number, friction factor, energy balance and Colburn j-factor are discussed. Finally the uncertainty of the heat transfer and hydrodynamic parameters are determined.

5.2. HEAT TRANSFER COEFFICIENT

Because the calculation of the heat transfer coefficient requires the wetted surface wall temperature a solid conduction numerical model is required to determine the heat transfer parameters. Figure 3.26 of the labelling convention of the wall temperatures is reproduced in Figure 5.1 for clarity purposes. The purpose of the numerical model is to relate the wetted surface temperature ($T_{wetted\ sur}$) of the channel to the measured experimental temperatures on the sides (T_{side1} and T_{side2}) and top (T_{top}) walls of the solid section. A simple one-dimensional thermal resistance analysis model (commonly used to determine the heat transfer coefficient in pipes) cannot be used to determine the heat transfer coefficient due to the following reasons: The heat transfer for this study is three dimensional; the channel is not heated by an all-round uniform heat flux; and the thermal resistance of the stainless steel is low compared to material such as copper or aluminium and therefore larger thermal gradients exist within the solid substrate, which needs to be accounted for.

Obtaining temperatures at a specific position, within a solid, from temperature measurements at other locations is referred to as the inverse heat conduction problem. James et al. (1985) stated that analytical solutions, for such cases, are much more complex to solve than using a direct approach. Beck and Haji-Sheikh (1996), Shen (1999), Jin and Marin (2007) compared and derived unique numerical solutions to estimate the solutions for the inverse heat conduction case. Huang and Wang (1999) used a commercial numerical package to determine the heat flux at a specific boundary. An iterative algorithm was developed whereby adjustments were made to the boundary conditions until the solution converged. From all the literature reviewed, all the authors performed a study on the effect of the sensitivity of the models to an uncertainty of input data.

In this subsection the assumption to use a two-dimensional numerical model is verified by calculating the amount of axial conduction within the solid of the microchannel test

section. Thereafter, the numerical model that was used is discussed and the methodology/algorithm in obtaining the heat transfer coefficient is described. The sensitivity of the numerical model, to measurement uncertainties, is performed in the uncertainty analysis in Appendix H. The effect of the unsymmetrical layout of the channel within the solid substrate is investigated. Lastly, the analysis procedure used to determine the heat transfer coefficient is explained.

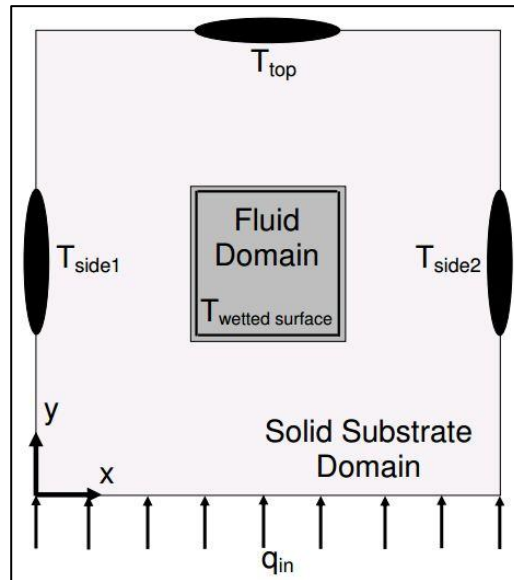


Figure 5.1 Labelling/naming convention of the temperature measurements

5.2.1. EFFECTS OF AXIAL CONDUCTION WITHIN THE MICROCHANNEL WALLS

If the axial conduction is negligible, a two-dimensional analysis is suitable to relate the measured wall temperatures to the wetted surface temperature, otherwise the only method to link them, is to perform a full three-dimensional numerical analysis. A method in determining the amount of the axial conduction within the solid walls of the microchannel was determined by Maranzana, Perry and Maillet (2004). A non-dimensional number was developed which compared the ratio of conduction heat transfer in the axial direction of the solid to the total heat transfer. Maranzana, Perry and Maillet (2004) concluded that the axial conduction can be neglected if it equates to less than 1 % of the total heat transfer.

The heat transfer in the axial direction is calculated as:

$$Q_{conduction} = \frac{k_s \cdot A_s}{L_s} \cdot \Delta T_s \quad \left| \text{Equation 5.1} \right.$$

where k_s is the thermal conductivity of stainless steel, A_s is the cross section of the solid of the microchannel, ΔT_s is the temperature difference within the stainless steel and L_s is the length of the microchannel.

The total heat transfer to the fluid is:

$$Q_{tot} = \dot{m} \cdot C_{p_f} \cdot \Delta T_f \quad \left| \text{Equation 5.2} \right.$$

where \dot{m} is the mass flow rate, C_{p_f} is the specific heat of the fluid and ΔT_f is the difference in the fluid temperature from the inlet to the outlet.

The ratio of axial heat conduction to heat input:

$$\frac{Q_{conduction}}{Q_{tot}} = \frac{k_s \cdot A_c \cdot \Delta T_s}{\dot{m} \cdot C_{p_f} \cdot L_s \cdot \Delta T_f} \quad \left| \text{Equation 5.3} \right.$$

The method as used by Maranzana, Perry and Maillet (2004) assumed that the heat conduction is one-dimensional through the same temperature difference as the fluid, therefore $\Delta T_s = \Delta T_f$

$$\frac{Q_{conduction,in}}{Q_{tot}} = \frac{k_s \cdot A_c}{\dot{m} \cdot C_{p_f} \cdot L_s} \quad \left| \text{Equation 5.4} \right.$$

Therefore the % effect of axial conduction to heat input:

$$\% \text{ axial conduction} = \left(\frac{k_s \cdot A_c}{\dot{m} \cdot C_{p_f} \cdot L_s} \right) \cdot 100 \quad \left| \text{Equation 5.5} \right.$$

The percentage of axial conduction in the microchannel solid regime is shown in Figure 5.2 and is below 0.6 % for the worst Reynolds number and test section. Therefore, the effect of the axial conduction can ignored, as it is below 1 %, and a two-dimensional model can be used.

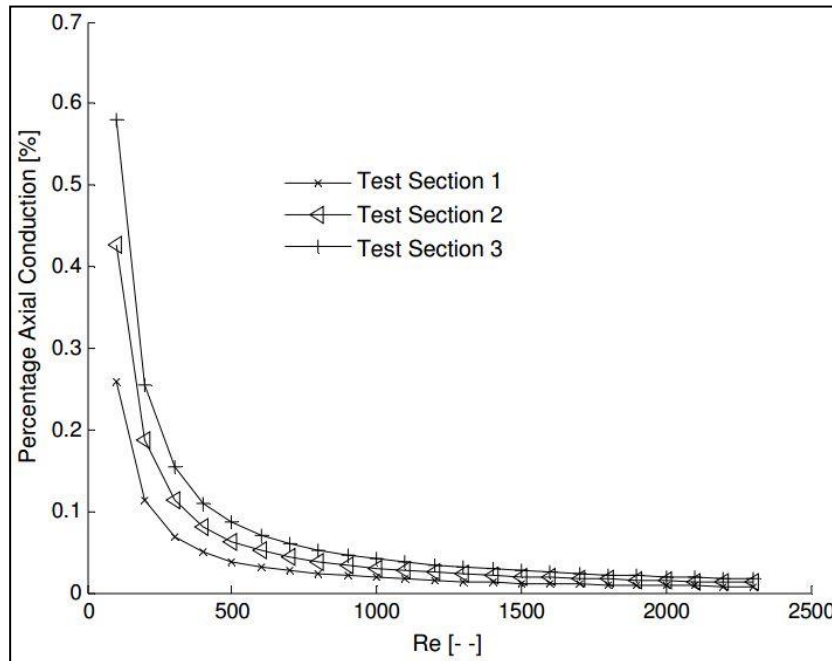


Figure 5.2 Percentage of axial conduction versus Reynolds number, based on the average fluid temperature

5.2.2. TWO-DIMENSIONAL NUMERICAL MODEL

A symmetrical two-dimensional conduction model was created which was solved using a commercial CFD package, Fluent[®]. The mesh of the numerical model is shown in Figure 5.3 which also indicates the boundary conditions and the locations where the wall temperatures were probed. By using a symmetric model it was assumed that the left (T_{side1}) and right (T_{side2}) side wall temperatures are similar as well as the actual test sections were machined perfectly symmetrical. From the results, as presented in Chapter 4, it was seen that this was not the case. A detailed investigation into the effect of the asymmetric layout is performed later in this section which validates the use of the model.

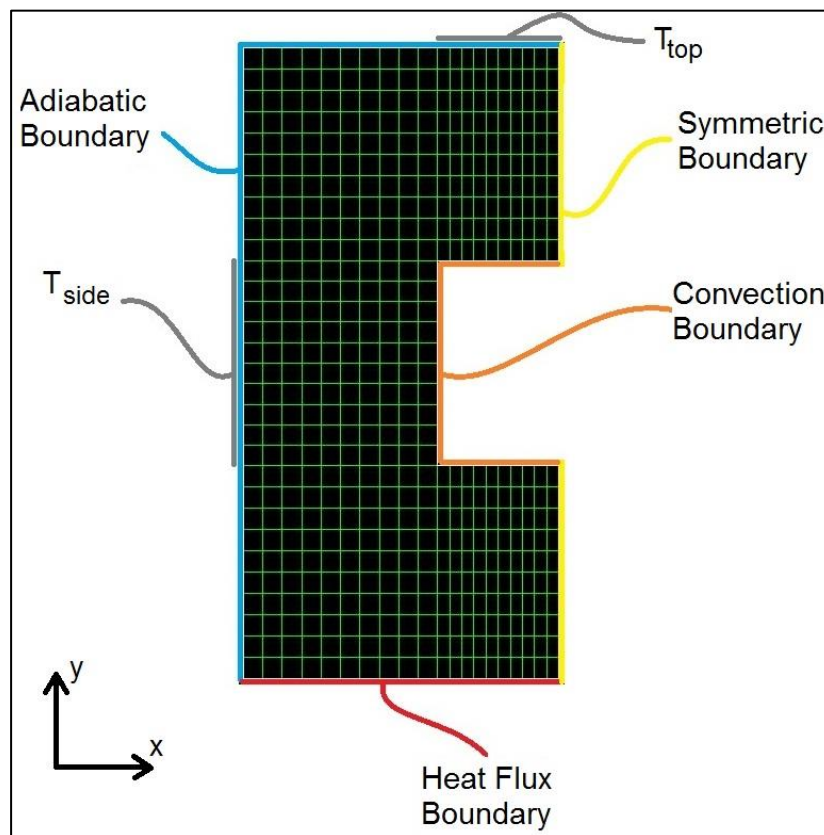


Figure 5.3 Symmetric numerical model showing the boundary conditions and the temperature measuring locations

The mesh for the three different test sections is shown in Figure 5.4. The meshes were generated based on the actual measured dimensions as presented in Figure 3.22 to Figure 3.24. Due to the asymmetrical layout of the channel within the solid substrate the average side wall thickness was used in constructing the mesh. A total of 20 first order quadrilateral elements were used across the width and 30 along the height, the fine mesh ensured that the results were independent of the mesh size and therefore could be used with confidence.

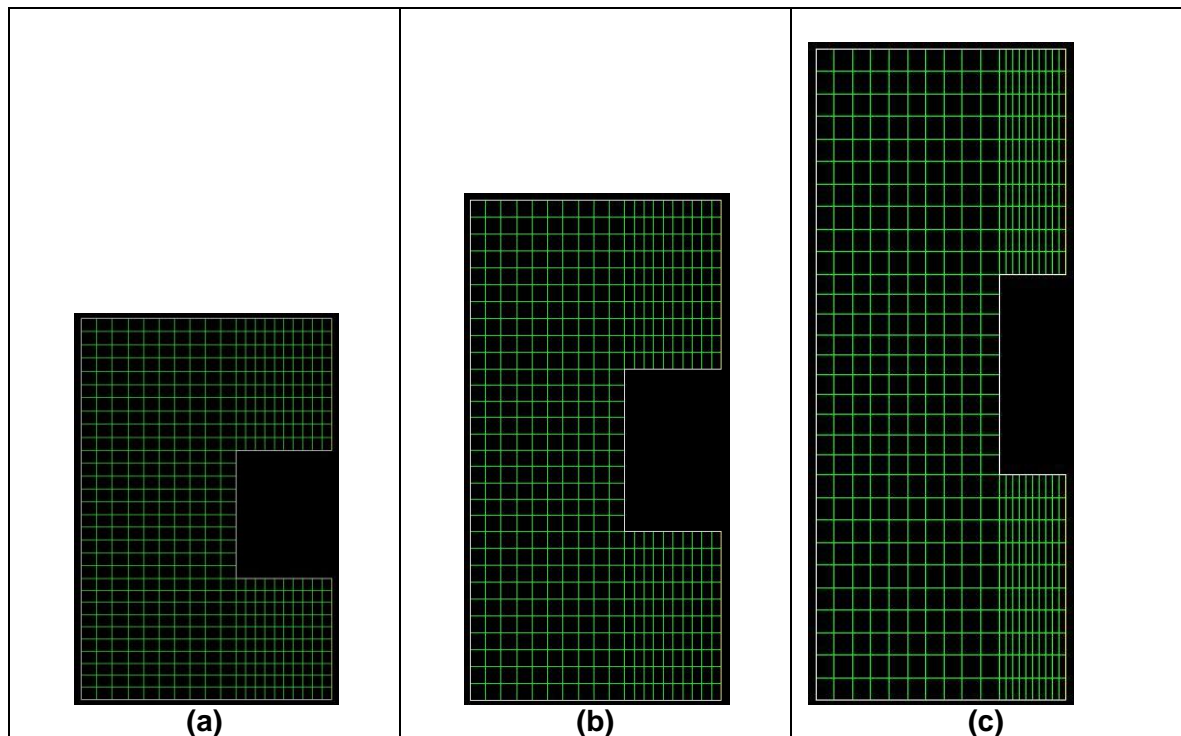


Figure 5.4 Numerical model mesh: (a) Test Section 1, (b) Test Section 2, and (c) Test Section 3

Only the solid substrate of the test section was modelled as the heat transfer coefficient of the wetted surface was required based on the measured side and top wall temperatures. The following assumptions were made for the numerical analysis:

- heat transfer was at steady state
- constant solid substrate material properties
- negligible radiation heat transfer effects
- all outer walls were perfectly adiabatic
- no heat loss was accounted for
- uniform heat flux was applied to the bottom wall
- a constant uniform distributed heat transfer coefficient on the inner walls
- a constant thermal conductivity of 15.1 W/mK for the solid substrate

Based on the above assumptions the energy equation for the solid domain is:

$$k_s \frac{\partial T}{\partial x_j} = 0 \quad \left| \text{Equation 5.6} \right.$$

The thermal boundary conditions for all outer walls of the solid substrate were adiabatic except for the bottom wall where there was a constant uniform inwards heat flux. A convection heat transfer coefficient boundary condition was applied to the wetted

channel wall. A heat transfer coefficient and a free stream temperature was required as inputs for the boundary condition. The average fluid temperature at the specific measuring position was used as the free stream temperature. A uniform convection heat transfer coefficient was assumed across all the inner walls of the microchannel.

5.2.2.1. EFFECTS OF THE ASYMMETRICAL CHANNELS WITHIN THE SOLID SUBSTRATE

The asymmetric layout of the channel within the solid substrate could result in a difference in the heat transfer characteristics of the test sections. This effect was investigated with the use of two-dimensional numerical models. A symmetric model, as described above, will not suffice in determining the effect of the offset of the microchannel and therefore the full cross section of the test section was used. The channel was offset in the horizontal direction by 0 mm, 0.0626 mm and 0.125 mm. Governing equations and boundary conditions are similar to that described in the above section, except that a symmetric boundary condition was not required as the entire cross-section was modelled.

Test Section 2 was used as the base dimension for the analysis. A constant heat flux of 10 W/cm^2 was applied to the bottom wall for all test cases. Four different simulations were analysed for each configuration where the heat transfer coefficient and the free stream temperatures were selected which covered the full range of test results. For demonstration purposes, the heat transfer coefficient, h , was selected as $25\,000 \text{ W/m}^2\text{K}$ and the free stream temperature, T_∞ , was selected to be $50 \text{ }^\circ\text{C}$. The top and side wall temperatures were monitored and recorded for each analysis.

Figure 5.5 to Figure 5.7 shows the numerical model mesh and the temperature contour plot, for the three different configurations, where $h = 25\,000 \text{ W/m}^2\text{K}$ and $T_\infty = 50 \text{ }^\circ\text{C}$. It can be seen from Figure 5.5(b) that the temperature contours are symmetrical around the vertical axis of the centre of the channel. From Figure 5.7 and Figure 5.8 it can be seen that as the microchannel is offset to the right, the temperature contour becomes asymmetrical with the temperature of the left side wall (T_{side1}) increasing. From this analysis it can be concluded that the asymmetric layout of the microchannel has an effect on the temperature contours in the solid substrate and therefore the heat transfer characteristics.

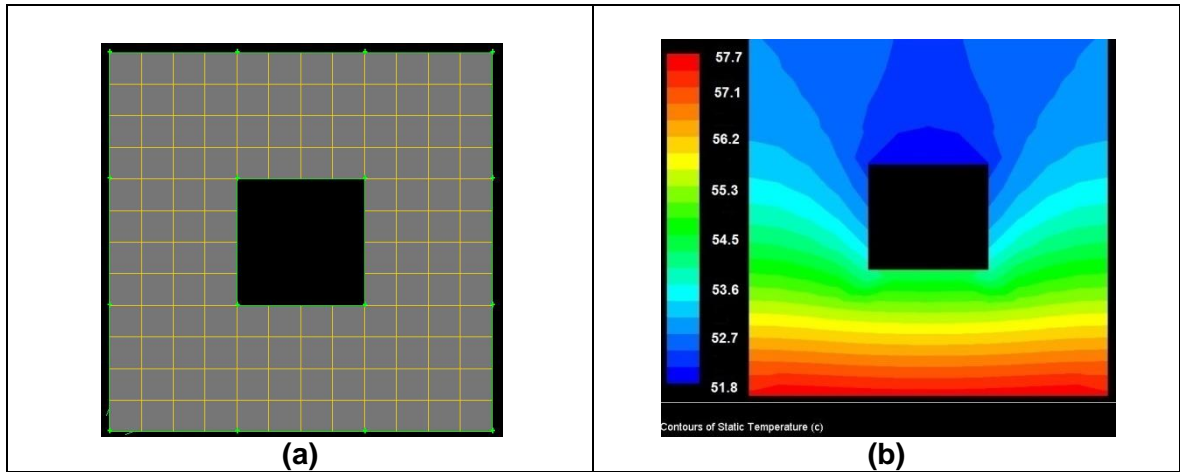


Figure 5.5 0 mm offset analysis, (a) numerical model mesh, (b) temperature contour plot where $T_{\infty} = 50\text{ }^{\circ}\text{C}$ and $h = 25\ 000\ \text{W/m}^2\text{K}$

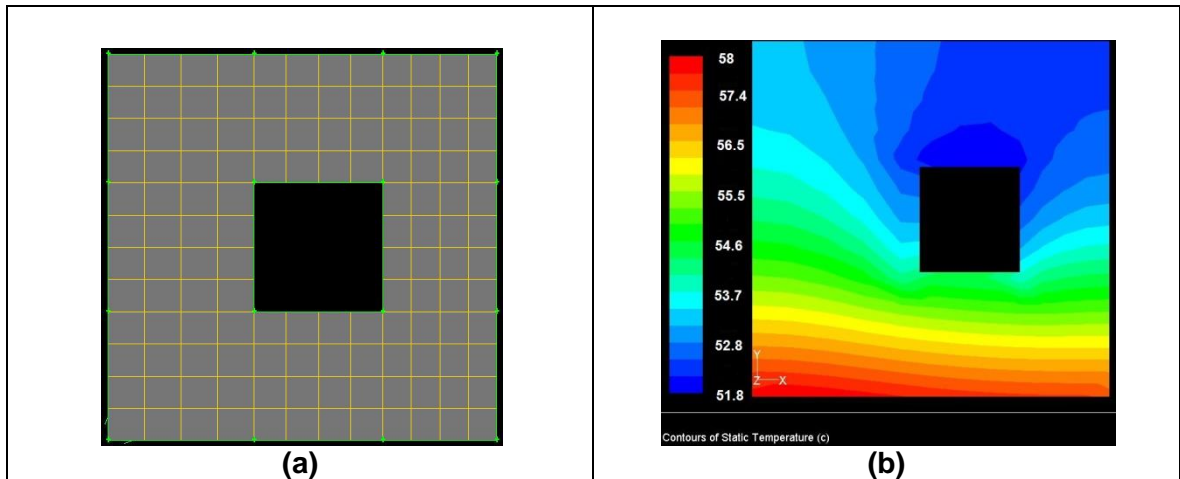


Figure 5.6 0.0625 mm offset analysis, (a) numerical model mesh, (b) temperature contour plot where $T_{\infty} = 50\text{ }^{\circ}\text{C}$ and $h = 25\ 000\ \text{W/m}^2\text{K}$

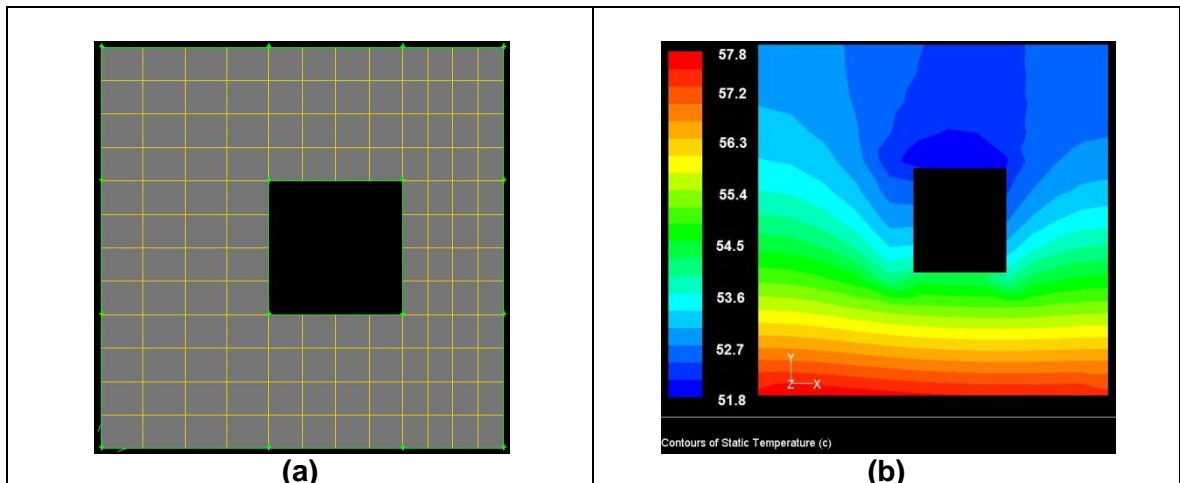


Figure 5.7 0.125 mm offset analysis, (a) numerical model mesh, (b) temperature contour plot where $T_{\infty} = 50\text{ }^{\circ}\text{C}$ and $h = 25\ 000\ \text{W/m}^2\text{K}$

The top (T_{top}) and side (T_{side1} and T_{side2}) wall temperatures are tabulated in Table 5.1 for the different simulations and configurations. The top wall temperatures remain constant as the channel is offset to the right for each simulation. The two side wall temperatures

are equal when the channel is not offset, for each simulation. As the channel is offset to the right the left wall temperature, T_{side1} , increases and the right wall temperature, T_{side2} , decreases, but when comparing the average side wall temperatures, it is relatively constant, to within 0.01 °C, of the configuration where the channel is in the centre of the solid substrate. From this it can be concluded that the same average side wall temperatures are obtained even if the channel is offset to one side.

To determine the heat transfer coefficient, h , using a symmetrical numerical model the average side wall and top wall temperature must be used. The symmetrical numerical model is shown in Figure 5.8. It can be seen, from Table 5.1, that the top and average side wall temperatures are the same for the symmetrical numerical model. The wetted surface temperature difference, due to the asymmetrical layout of the microchannel in the solid substrate, will be accounted for by using the average side wall temperatures.

Table 5.1 Numerically obtained wall temperatures for unsymmetrical channel layout and symmetric numerical model results

	$T_{\infty} = 20\text{ }^{\circ}\text{C}, h = 2\ 500\ \text{W/m}^2\text{K}$			
	Channel offset = 0 mm	Channel offset = 0.0625 mm	Channel offset = 0.125 mm	Symmetric Channel Model
$T_{top}\text{ }^{\circ}\text{C}$	49.96	48.96	48.95	49.95
$T_{side1}\text{ }^{\circ}\text{C}$	50.82	51.11	51.41	
$T_{side2}\text{ }^{\circ}\text{C}$	50.82	50.54	50.26	
$T_{side,ave}\text{ }^{\circ}\text{C}$	50.82	50.83	50.84	50.83
	$T_{\infty} = 50\text{ }^{\circ}\text{C}, h = 2\ 500\ \text{W/m}^2\text{K}$			
$T_{top}\text{ }^{\circ}\text{C}$	78.96	79.96	78.95	78.95
$T_{side1}\text{ }^{\circ}\text{C}$	80.83	81.11	81.41	
$T_{side2}\text{ }^{\circ}\text{C}$	80.83	80.54	80.26	
$T_{side,ave}\text{ }^{\circ}\text{C}$	80.83	80.83	80.84	80.83
	$T_{\infty} = 20\text{ }^{\circ}\text{C}, h = 25\ 000\ \text{W/m}^2\text{K}$			
$T_{top}\text{ }^{\circ}\text{C}$	22.42	22.41	22.42	22.41
$T_{side1}\text{ }^{\circ}\text{C}$	23.83	24.08	24.34	
$T_{side2}\text{ }^{\circ}\text{C}$	23.83	23.59	23.36	
$T_{side,ave}\text{ }^{\circ}\text{C}$	23.83	23.84	23.85	23.84
	$T_{\infty} = 50\text{ }^{\circ}\text{C}, h = 25\ 000\ \text{W/m}^2\text{K}$			
$T_{top}\text{ }^{\circ}\text{C}$	52.41	52.41	52.42	52.41
$T_{side1}\text{ }^{\circ}\text{C}$	53.84	54.08	54.34	
$T_{side2}\text{ }^{\circ}\text{C}$	53.84	53.60	53.36	
$T_{side,ave}\text{ }^{\circ}\text{C}$	53.84	53.84	53.85	53.84

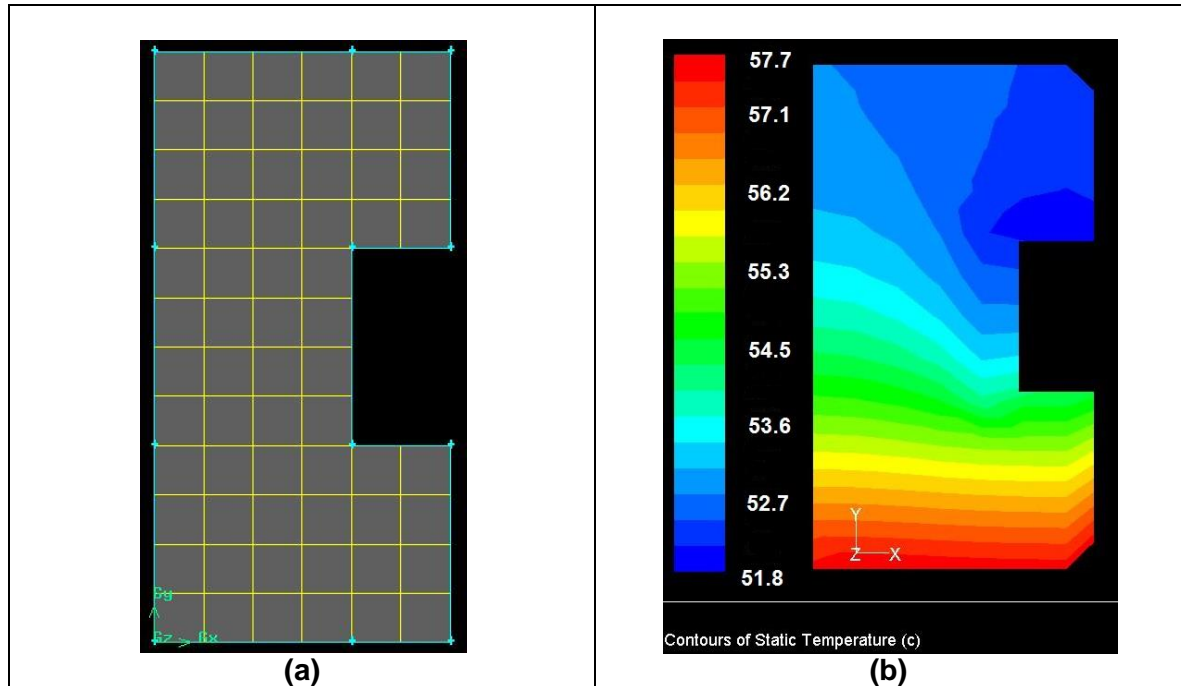


Figure 5.8 Symmetric analysis, (a) numerical model mesh, (b) temperature contour plot where $T_{\infty} = 50 \text{ }^{\circ}\text{C}$ and $h = 25\,000 \text{ W/m}^2\text{K}$

5.2.3. PROCEDURE TO DETERMINE THE EXPERIMENTAL HEAT TRANSFER COEFFICIENT

The procedure followed in obtaining the experimental heat transfer coefficient is discussed in this section. Due to the nature of the numerical analysis the magnitude of the side and top wall temperature boundaries cannot be defined, the heat transfer coefficient and the free stream temperature boundaries are defined and the side and top temperatures are calculated in the analysis. Therefore, an iterative process is required to determine the corresponding heat transfer coefficient for the equivalent side and top wall temperatures.

The average fluid temperature increases linearly from the inlet to the outlet because a uniform heat flux is applied to the test section. Therefore the average fluid temperature can be determined at each measuring position based on the axial distance from the inlet of the microchannel test section as shown in Equation 5.7. The average fluid temperature is used as the free stream temperature for the convective boundary condition.

$$T_{ave,i} = \left(\frac{T_{out} - T_{in}}{L_s} \right) L_i + T_{in} \quad \left| \text{Equation 5.7} \right.$$

where $T_{ave,i}$ is the bulk fluid temperature at the specific axial location, T_{out} is the outlet fluid temperature, T_{in} is the inlet fluid temperature, and L_i is the distance from the inlet of the test section to the axial measuring location.

A staggered three-dimensional matrix was generated which contained the heat transfer coefficient and the free stream temperature and the corresponding side and top wall temperatures. The matrix was compiled once for a specific test section, and from it, the heat transfer coefficient was obtained based on the side and top wall temperatures. The h-matrix structure is shown in Figure 5.9 with the front two-dimensional matrix containing the defined heat transfer coefficient for a specific free stream temperature, and the side and top wall temperatures obtained in the analysis. For instance, $T_{\infty,1}$ and $h_{,1}$ are selected which fully defined the convective boundary, the numerical model was solved and from the numerical analysis the corresponding side ($T_{side,1}$) and top ($T_{top,1}$) wall temperatures were obtained. The heat transfer coefficient was incrementally made larger, for instance, $h_{,2}$ and the corresponding side ($T_{side,2}$) and top ($T_{top,2}$) wall temperatures were obtained. The process was repeated accordingly and the front two-dimensional matrix was populated. The matrix was then extended into the third dimension, which structure was a duplicate of the front two-dimensional matrix but for incrementally larger free stream temperatures, which resulted in different side and top wall temperatures. The heat transfer coefficient and free stream temperature range was obtained through a trial and error method in order to cover the top and side wall temperatures which were measured for the specific test section. The magnitude of the heat transfer coefficient increment was selected in order that the change in top and side wall temperatures were within the measuring precision.

$T_{\infty,...}$	$h_{,1}$	$T_{side,1}$	$T_{top,1}$
$T_{\infty,2+i}$	$h_{,1}$	$T_{side,1}$	$T_{top,1}$
$T_{\infty,2}$	$h_{,1}$	$T_{side,1}$	$T_{top,1}$
$T_{\infty,1}$	$h_{,1}$	$T_{side,1}$	$T_{top,1}$
	$h_{,2}$	$T_{side,2}$	$T_{top,2}$
	$h_{,2+i}$	$T_{side,2+i}$	$T_{top,2+i}$
	$h_{,...}$	$T_{side,...}$	$T_{top,...}$

Figure 5.9 Structure of the three-dimensional h-matrix

Figure 5.10 shows the flow diagram of the procedure used in populating the h-matrix to further explain the method used in relating the side and top wall temperatures to the wetted surface temperature. The free stream temperature was initialised and the first outer loop (free stream temperature loop) was entered. The average heat transfer coefficient was initialised and the second inner loop (average heat transfer coefficient loop) was entered. The initialised temperatures were used to define the boundary conditions and the numerical model was solved. Side and top temperatures were obtained from the numerical model and the h-matrix was populated. The magnitude of the average heat transfer coefficient was increased by the predetermined increment and the loop was re-entered. The loop was run until the magnitude of the average heat transfer coefficient reached the pre-determined maximum. Thereafter the magnitude of the free stream temperature was increased by the pre-determined increment and the

average heat transfer coefficient loop was entered. The outer loop was run until the free stream temperature magnitude reached the pre-determined maximum. A Matlab[®] program was written which interfaced with the numerical solver, Fluent[®], via a journal file and the h-matrix was populated. The h-matrix was saved as a binary 'MAT-file' which could be loaded as required.

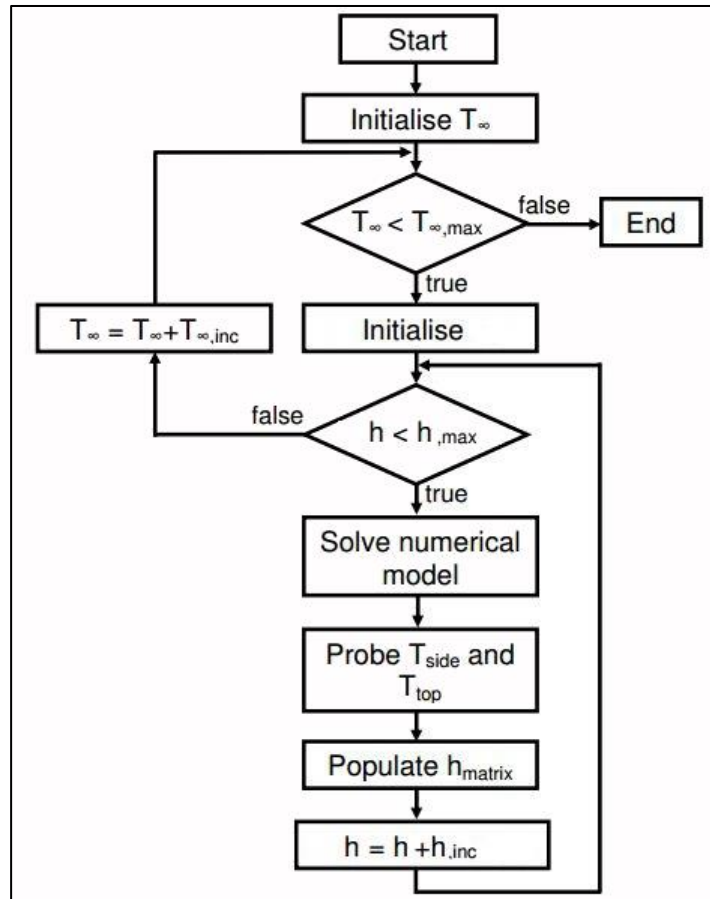


Figure 5.10 Flow diagram of the procedure to populate the h-matrix used in determining the heat transfer coefficient

After the generation of the h-matrix the average heat transfer coefficient was extracted based on the free stream, side and top wall temperatures. The first step involved obtaining the side and top wall temperatures and the average heat transfer coefficient based on the actual experimentally measured free stream temperature. This was done by interpolating the top and side wall temperatures and the average heat transfer coefficient from the h-matrix based on the actual measured free stream temperature. A two-dimensional matrix was generated with the interpolated values as shown in Figure 5.11.

$T_{\infty,1}$ <i>,inter</i>	$h_{,1}$ <i>inter</i>	$T_{side,1}$ <i>inter</i>	T_{top} <i>inter</i>
	$h_{,2}$ <i>inter</i>	$T_{side,2}$ <i>inter</i>	$T_{top,2}$ <i>inter</i>
	$h_{,2+i}$ <i>inter</i>	$T_{side,2+i}$ <i>inter</i>	$T_{top,2+i}$ <i>inter</i>
	$h_{,inter}$...	T_{side} <i>inter,...</i>	T_{top} <i>inter,...</i>

Figure 5.11 Structure of the two-dimensional h-matrix after the interpolation based on the free stream temperature

The least square of errors method, as calculated in Equation 5.8, was used to determine the average heat transfer coefficient. The position of the minimum of the least square error indicates the position of the average heat transfer coefficient, $h_{ave,i,inter}$, which best fits the measured data. The procedure was repeated for each data point and a corresponding average heat transfer coefficient was obtained.

$$\text{least square error}_i = \sqrt{(T_{top,i,interp} - T_{top,i,measured})^2 + (T_{side,i,interp} - T_{side,ave,i,measured})^2}$$

Equation 5.8

To summarise: a numerical model was used to determine the average heat transfer coefficient for each specific measuring data point and position. A three-dimensional h-matrix was generated containing the side and top wall temperatures based on the free stream temperature and the average heat transfer coefficient. From the h-matrix the least square error method was used to determine the best fit average heat transfer coefficient. For an ideal case the least square error would be zero, but due to the uncertainty and differences obtained from the experimental results the least square error would not be equal to zero. The average of the least square error across the Reynolds number range for Test Section 1 was between 0.50 °C and 0.11 °C, for Test Section 2 it was between 0.57 °C and 0.26 °C and for Test Section 3 it was between 0.38 °C and 0.18 °C. The largest errors were obtained for the first few lowest flow rates but as the flow rate increased the least square error decreased significantly. From the average heat transfer coefficient the average Nusselt number can be determined. The reduced data results are presented in Section 6.1.

5.2.4. CALCULATION OF THE NUSSELT NUMBER

The local Nusselt number was determined as follows:

$$N_{u,local}(x) = \frac{h(x) \cdot D_h}{k_f(x)} \quad \left| \text{Equation 5.9} \right.$$

Where D_h is the hydraulic diameter, k_f is the thermal conductivity of the working fluid at local temperature, and $h(x)$ is the local heat transfer coefficient. The thermal conductivity of water was determined from the equations developed by Popiel and Wojtkowiak (1998).

Where the hydraulic diameter is:

$$D_h = \frac{4 \cdot A_c}{P} = \frac{2 \cdot H_c \cdot W_c}{H_c + W_c} \quad \left| \text{Equation 5.10} \right.$$

The average heat transfer coefficient is obtained by taking the mean of the local heat transfer coefficient along the length of the microchannel. The local heat transfer coefficient is obtained, for each measuring location, from the numerical model as described in section 5.2.3. The average heat transfer heat coefficient calculated as shown in Equation 5.11.

$$h_{ave} = \frac{h(x_1) + \dots + h(x_n)}{n} \quad \left| \text{Equation 5.11} \right.$$

And the average Nusselt number is obtained as follows:

$$N_{u,ave} = \frac{h_{ave} \cdot D_h}{k_{f,ave}} \quad \left| \text{Equation 5.12} \right.$$

Where $k_{f,ave}$ is based on average bulk fluid temperature between the inlet and outlet of the test section.

5.3. REYNOLDS NUMBER AND PRANDTL NUMBER

The Reynolds numbers and Prandtl number were calculated as shown in Equation 5.13 and Equation 5.14 respectively, where the viscosity, specific heat and thermal conductivity of the fluid was based on the bulk fluid temperature. Equations developed by Popiel and Wojtkowiak (1998) were used to determine the fluid properties at specific temperatures. The Reynolds number was calculated from the measured mass flow rate.

Reynolds number:

$$Re = \frac{\dot{m}}{D_h \cdot \mu_f} \quad \left| \text{Equation 5.13} \right.$$

Prandtl number:

$$Pr = \frac{\mu_f \cdot Cp_f}{k_f} \quad \left| \text{Equation 5.14} \right.$$

where \dot{m} is the mass flow rate, μ_f is the fluid viscosity, A_c is the channel area, H_c is the channel height, W_c is the channel width, P is the perimeter of the channel and Cp_f is the specific heat of the fluid.

5.4. FRICTION FACTOR

The Darcy-Weisbach equation was used to calculate the friction factor as shown in Equation 5.15:

$$f = \frac{\Delta P \cdot D_h \cdot 2}{L_s \cdot \rho_f \cdot V^2} \quad \left| \text{Equation 5.15} \right.$$

where ΔP is the differential pressure, L_s is the length of the test section, ρ_f is the density of the fluid and V is the velocity of the fluid

The velocity of the fluid was based on the measured mass flow rate and was calculated as:

$$V = \frac{\dot{m}}{A_c \cdot \rho_f} \quad \left| \text{Equation 5.16} \right.$$

The pressure taps used to measure the pressure drop across the microchannel test section were positioned in the inlet and outlet manifold. Therefore to obtain the pressure drop across the microchannel test section, ΔP , the pressure losses between the microchannel test section and the pressure tap, ΔP_{losses} , were subtracted from the measured differential pressure, $\Delta P_{measured}$.

$$\Delta P = \Delta P_{measured} - \Delta P_{losses} \quad \left| \text{Equation 5.17} \right.$$

The sum of the pressure losses were calculated using Equation 5.18, where K is the pressure loss coefficient which is case specific.

$$\Delta P_{losses} = \sum_n K_n \cdot \frac{1}{2} \cdot \rho_f \cdot V^2 \quad \left| \text{Equation 5.18} \right.$$

The pressure loss coefficient for a sudden contraction and sudden expansion in pipes are calculated using Equation 5.19 and Equation 5.20, White (2005). A square/rectangular to round cross-sectional interface exists at the inlet and exit of the microchannel. Whereas the equations set out by White (2005) are for a round to round interface. Literature on the pressure loss coefficient for square/rectangular to round interfaces are not common and therefore Equation 5.19 and Equation 5.20 were used based on the hydraulic diameter, D_h , of the microchannel and the diameter, D , of the inlet and outlet manifold. The pressure losses were calculated based on the velocity in the smaller tube/channel and the inlet or outlet fluid temperature.

Pressure loss coefficient for a sudden contraction:

$$K_{SC} = 0.42 \cdot \left(1 - \frac{D_h^2}{D^2}\right) \quad \left| \text{Equation 5.19} \right.$$

Pressure loss coefficient for a sudden expansion:

$$K_{SE} = \left(1 - \frac{D_h^2}{D^2}\right)^2 \quad \left| \text{Equation 5.20} \right.$$

5.5. COLBURN J-FACTOR

The Colburn J-factor was calculated using Equation 5.22 which is based on the average Nusselt number.

$$j = \frac{N_{u,ave}}{Re \cdot Pr^{\frac{1}{3}}} \quad \left| \text{Equation 5.21} \right.$$

5.6. ENERGY BALANCE

The electrical energy input to the test section heater, and the heat transferred to the water was compared by means of an energy balance. The electrical energy was calculated from the product of the measured potential difference and the current of the heater and was kept constant at 7.5 W. The energy transferred to the water was calculated based on the inlet and outlet fluid temperatures, specific heat at the bulk fluid temperature and the measured mass flow rate.

Energy balance:

$$\% \text{ Energy Balance} = \frac{Q_{in} - Q_{out}}{Q_{out}} / 100 \quad \left| \text{Equation 5.22} \right.$$

where, electrical energy:

$$Q_{in} = 7.5 W$$

Equation 5.23

and, heat transferred to the water:

$$Q_{out} = \dot{m} \cdot c_{p_f} \cdot (T_{out} - T_{in})$$

Equation 5.24

5.7. UNCERTAINTY ANALYSIS

The uncertainty of the measured and analysed data was determined in a similar manner as set out by Kline and McClintock (1953), and Moffat (1988). The uncertainties were calculated within a 95 % confidence. The fluid properties and uncertainties were given by Popiel and Wojtkowiak (1998). The detailed uncertainty analysis is presented in Appendix H and only a summary of the results are presented in this sub-section.

The uncertainty of the measured parameters are shown in Table 5.2 and the uncertainty of the equations used in determining the heat transfer and dynamic parameters are shown in Table 5.3. The uncertainty of the Reynolds number is approximately 2 % and for the Prandtl number approximately 1 %. The uncertainty of the friction factor is 9.96 % on the lower range and decreases to 5.92 % for the higher range. A similar occurrence is observed for the Colburn j-factor with an uncertainty of 3.29 % at the lower range which decreases to 2.12 % for the higher range. The uncertainty increases from the lower to the higher range for the heat transfer coefficient and the Nusselt Number, with the average Nusselt number uncertainty equating to 3.62 % for the lower range and 5.03 % for the higher range.

Table 5.2 Measured parameter uncertainty summary

Measured Parameter	Uncertainty
Temperature	0.113 °C
Dimensions	0.02 mm
Pressure	0.08 kPa
Flow rate	0.042 – 0.013 ml / min
Voltage	0.01 V
Current	0.01 A

Table 5.3 Uncertainties of the equations used for a specified range

Heat transfer or hydrodynamic parameter	Range	Uncertainty
Re	200 – 2300	2.02 % - 2.00 %
Pr	~5.4	1.00 %
f	0.179 – 0.144	9.96 % - 5.92 %
j	0.011 – 0.0050	3.29 % - 2.12 %
h_{local}	2500 – 25000 W/m ² K	4.96 % - 8.51 %
Nu_{local}	2.03 – 20.33	5.62 % - 8.96 %
h_{ave}	2500 – 25000 W/m ² K	2.48 %- 4.28 %
Nu_{ave}	2.03 – 20.33	3.62 % - 5.03 %

5.8. SUMMARY OF THE DATA REDUCTION/ANALYSIS

The methodology of determining the heat transfer coefficient, friction factor, Colburn j-factor and energy balance were presented in this chapter. The effect of the axial conduction was investigated using a method suggested by Maranzana, Perry and Maillet (2004). It was found that the axial conduction was 0.6% of the total heat input to the system and therefore could be neglected. By neglecting the axial conduction within the solid substrate a two-dimensional model could be used.

A two-dimensional numerical conduction model was utilised to determine the heat transfer coefficient at the fluid to solid interface from the experimentally measured outer top and side wall temperatures. The numerical model made use of a vertical symmetry line, and so only one half of the test section was modelled. This was done to simplify the analysis. Due to manufacturing constraints, the microchannels were not machined perfectly in the middle of the solid substrate. An investigation was conducted to see the effects of the asymmetrical layout of the channel. It was found that if the average side wall thickness and the average side wall temperatures were used, the magnitude of the heat transfer coefficient was the same as if a full two-dimensional analysis was performed with the channel offset to one side. An in depth procedure was followed in determining the heat transfer coefficient and it can be found in Section 5.2.3.

CHAPTER 6

DATA REDUCTION RESULTS

6.1. INTRODUCTION

The reduced data is presented in this chapter in the form of the friction factor, local Nusselt numbers, average Nusselt number, and the Colburn j-factor for each test section. The reduced/analysed data is compared between the test sections and discussed accordingly. It is also compared to other well-known correlations commonly used in practice.

6.2. ENERGY BALANCE

The energy balance for all three test sections over the Reynolds number measuring range is shown in Figure 6.1. The energy balance for all three test sections decreases from approximately 26% at the lowest measured Reynolds number to approximately 10% at a Reynolds number larger than 600. An average of the energy balance for all three test sections was obtained and is represented on the graph as the dashed bold line. From this line it can be seen that the average energy balance decreases, with a minimum at about a Reynolds number of 1200 and then gradually increases as the Reynolds number increases.

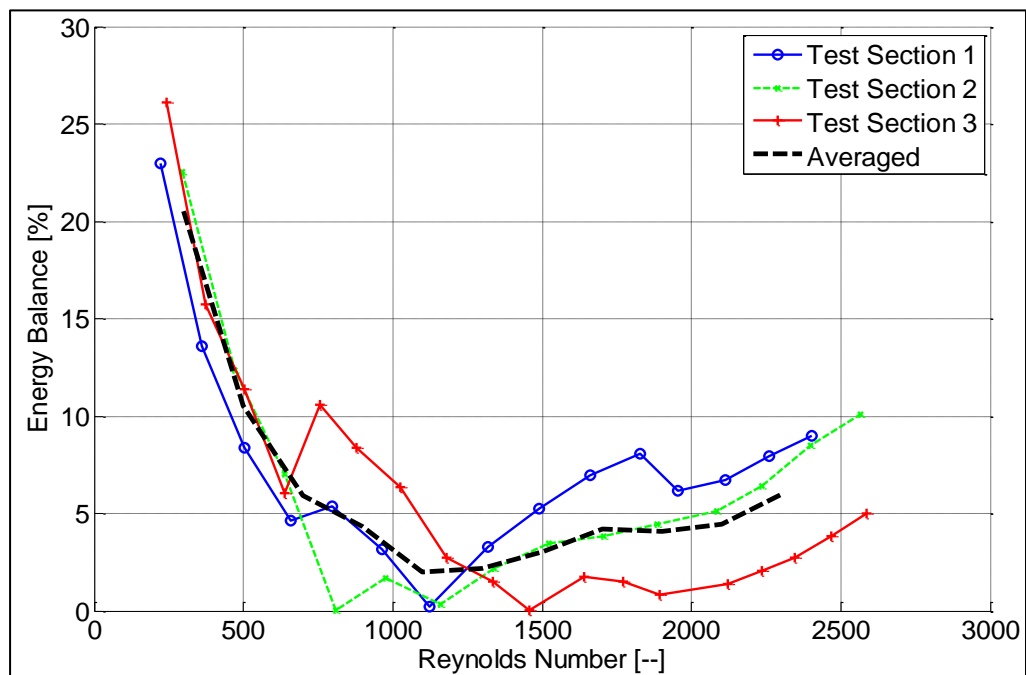


Figure 6.1 Energy balance for Test Section 1, Test Section 2 and Test Section 3 across the Reynolds number measuring range

6.3. FRICTION FACTOR

The friction factors were calculated from the measured results for all three test sections in this sub-section. The hydrodynamic developing length was calculated based on a commonly accepted correlation. The friction factors, calculated from the measured results, were compared to correlations developed by Shah and London (1978) supplemented with an apparent friction factor, using the Hagenbach's factor, to account for developing flow. Lastly the diabatic friction factors were compared to one another, highlighting the effect that the microchannels aspect ratio has on the results.

6.3.1. HYDRODYNAMIC ENTRANCE LENGTH

As the flow enters the microchannel the velocity profile begins to develop until ultimately reaching the fully developed profile. Majority of the analyses in literature assume a uniform velocity profile at the entrance of the channel, and the length of the hydrodynamic developing region is then determined by Equation 6.1 which is well-accepted in literature, Kandlikar et al. (2004). For small channels majority of the flow is in the developing regime.

$$L_h = 0.05 \cdot D_h \cdot Re \quad \left| \text{Equation 6.1} \right.$$

The hydrodynamic entrance lengths for the measured Reynolds number range is shown in Figure 6.2 for the different test sections. The hydrodynamic entrance length increases linearly as the Reynolds number increases. The length of the test section is 50 mm and therefore the Reynolds number, where the flow is only in the developing regime for Test Section 1, Test Section 2 and Test Section 3, is approximately 2000, 1900 and 2100 respectively. For all smaller Reynolds numbers the flow within the channel will be in the developing regime for a specific length and then in the fully developed regime for the rest of the length, which was taken into account in the calculations. The hydrodynamic entrance length in the turbulent flow regime is only dependant on the hydraulic diameter of the flow passage, which is generally accepted as 10 times the hydraulic diameter. All three test sections approximately have the same hydraulic diameter of 0.5 mm, thus the turbulent entrance length equates to 5 mm, which is only 10 % of the total length of the test section. Therefore the assumption is made that the flow is fully developed in the turbulent regime across the entire test section.

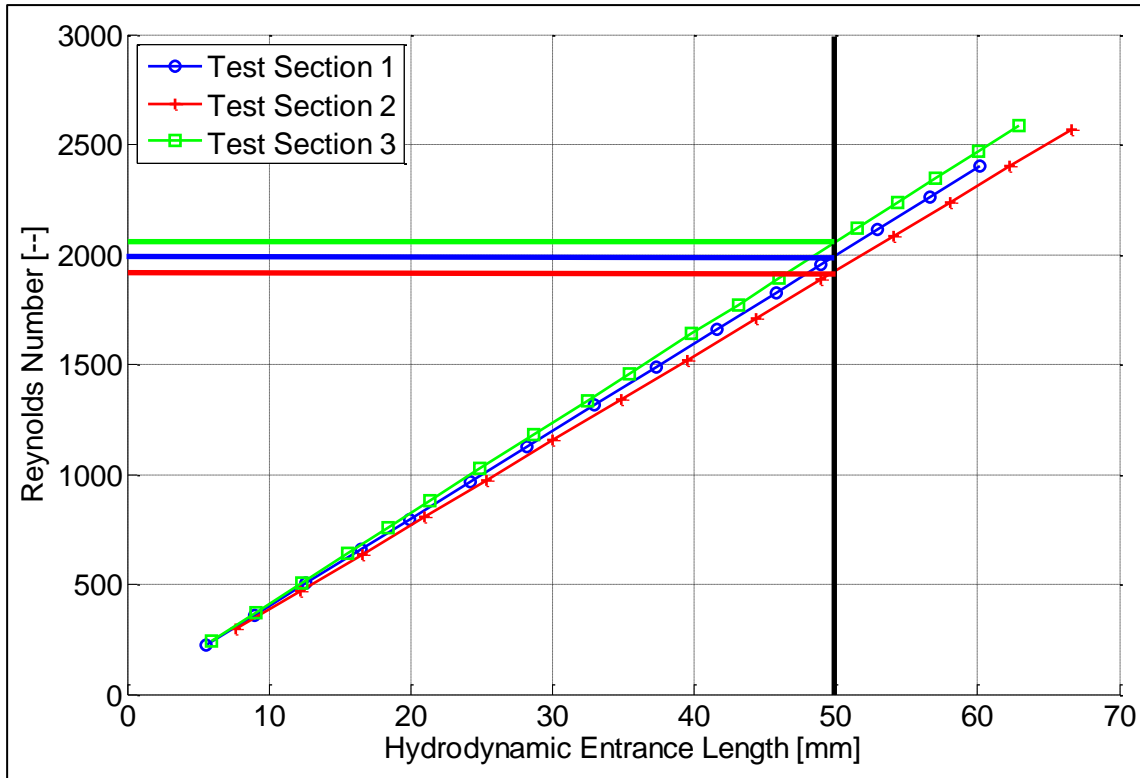


Figure 6.2 Hydrodynamic entrance length at specific Reynolds numbers for Test Section 1, Test Section 2 and Test Section 3

6.3.2. FRICTION FACTOR RESULTS

The friction factor in the laminar flow regime was determined from Equation 5.15 to Equation 5.20 for the experimental measured pressure drop for each test section. The friction factor was compared to the commonly used correlation determined by Shah and London (1978), supplemented with an apparent friction factor, using the Hagenbach's factor, to account for developing flow. Steinke and Kandlikar (2005) obtained a curve-fit equation for the Hagenbach's factor for rectangular channels. The pressure drop across the test section was obtained from the following equation:

$$\Delta P = \frac{2 \cdot f_{dev} \cdot Re \cdot \mu_f \cdot V \cdot L_h}{D_h^5} + K(\infty) \frac{\rho_f \cdot V^2}{2} \quad \left| \text{Equation 6.2} \right.$$

where f_{dev} is the friction coefficient for fully developed flow and $K(\infty)$ is the Hagenbach's factor given by, Steinke and Kandlikar (2005):

$$f \cdot Re = 24 \cdot (1 - 1.3553 \cdot \alpha_c + 1.9467 \cdot \alpha_c^2 - 1.7012 \cdot \alpha_c^3 + 0.9564 \cdot \alpha_c^4 - 0.2537 \cdot \alpha_c^5) \quad \left| \text{Equation 6.3} \right.$$

and

$$K(\infty) = 0.6796 + 1.2197 \cdot \alpha_c + 3.3089 \cdot \alpha_c^2 - 9.5921 \cdot \alpha_c^3 + 8.9089 \cdot \alpha_c^4 - 2.9959 \cdot \alpha_c^5 \quad \left| \text{Equation 6.4} \right.$$

After the pressure drop was obtained the total corresponding friction factor, which includes the effect of the developing flow, was obtained from Equation 5.15.

The friction factor for flow in the turbulent regime was determined using the well accepted Blasius equation, Cengel (2006) as shown in Equation 6.5

$$f = 0.3164 \cdot Re^{-0.25} \quad \left| \text{Equation 6.5} \right.$$

Figure 6.3 to Figure 6.6 shows the friction factors for Test Section 1, Test Section 2 and Test Section 3 for the diabatic and adiabatic experimental results and the diabatic and adiabatic correlation developed by Shah and London (1978) for laminar flow and the Blasius equation for turbulent flow. It can be seen that the experimental friction factor is smaller than the predicted theoretical values for all test sections. Experimentally measured laminar friction factor when compared to the correlation set out by Shah and London (1978) is 87 % higher for Test Section 1, 88 % higher of Test Section 2 and 56 % higher for Test Section 3.

It can also be seen, from the results of all the test sections that the diabatic friction factor is lower than the adiabatic friction factor throughout the measuring range, but the difference is larger at the lower Reynolds numbers. The average fluid temperature is larger at the lower Reynolds numbers and therefore the difference between the mean fluid temperatures between the diabatic and adiabatic tests are larger. As the temperature of the working fluid changes so does the fluid properties, such as the density and the viscosity. The friction factor is a function of these fluid properties. Thus a larger difference between the diabatic and adiabatic friction factors can be expected at the lower Reynolds number range.

The measured pressure drop over Test Section 1 (Figure 4.19) indicated that there was a sporadic increase in the pressure drop at about 51,6 ml / min could indicated the onset of transitional/turbulent flow. A similar trend was identified when observing the friction factor: there was a sporadic change in the friction factor. From the friction factor results, transition started at a Reynolds number of 1800 and the flow was fully turbulent at around a Reynolds number of 1950 for Test Section 1

No definite/sporadic transition was identified when observing the friction factor results for Test Section 2 and Test Section 3, see Figure 6.4 and Figure 6.5. But based on a change in the trend/gradient of the graphs the critical regions where transition and turbulent flow occurred was identified. For the diabatic results, of Test Section 2, transition occurred at approximately a Reynolds number of 825 and the flow was fully turbulent at a Reynolds number of 2250. For the adiabatic test case transitional flow occurred at a Reynolds number of approximately 900 and the flow was fully turbulent at 1700. For the diabatic results, for Test Section 3 the flow began to transition at a much lower Reynolds number of approximately 500 and was fully turbulent at a Reynolds

number of 1650. For the adiabatic case, transition occurred at an even earlier Reynolds number of 350 but the flow was fully turbulent at a similar Reynolds number as for the diabatic test case of 1650. Therefore for Test Section 2 and Test Section 3 the transition occurred at a much earlier Reynolds number than for Test Section 1. Commonly accepted laminar to turbulent transition is at a Reynolds Number of 2300, Cengel (2006), but the inlet and outlet conditions and surface roughness could induce the onset of early transitional flow.

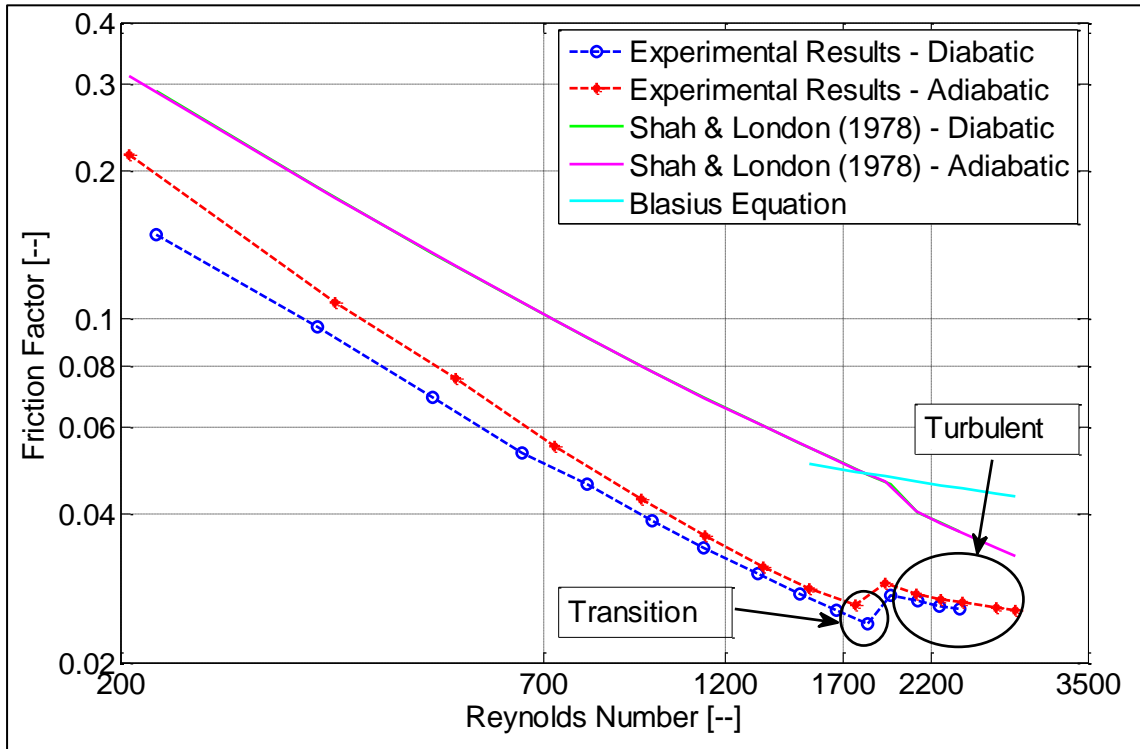


Figure 6.3 Diabatic and adiabatic friction factors versus the Reynolds number for the experimental data and Shah & London correlation, Test Section 1

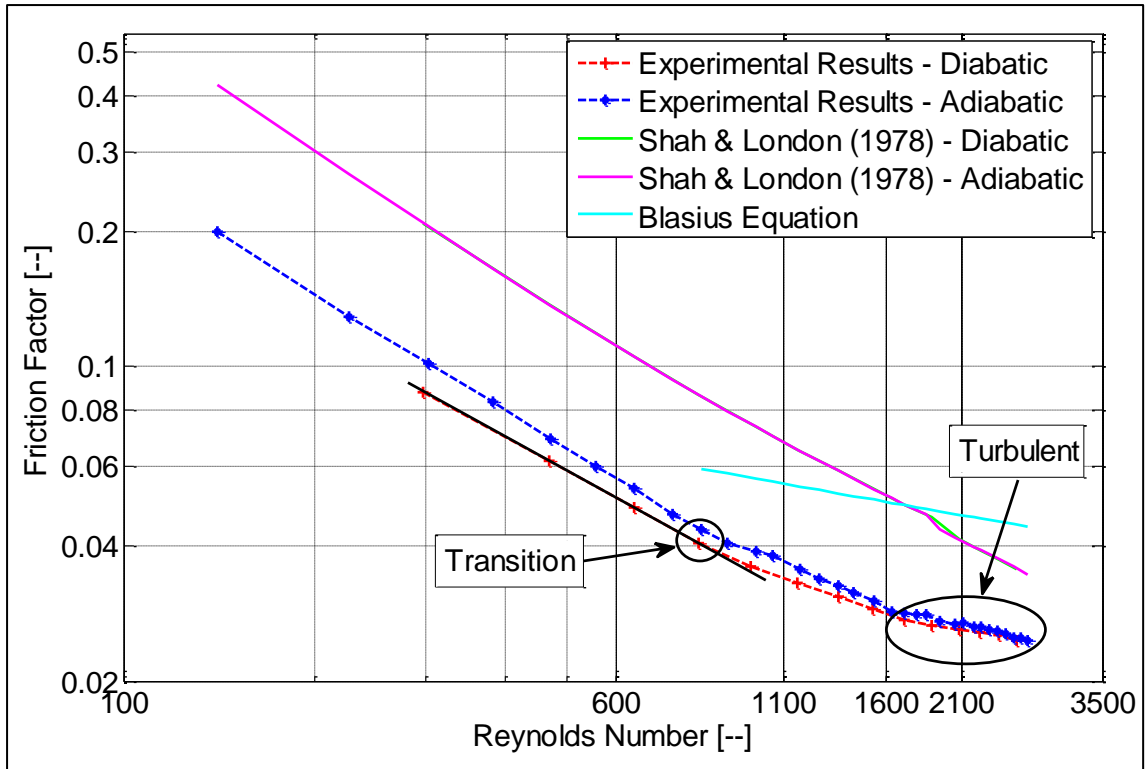


Figure 6.4 Diabatic and adiabatic friction factors versus the Reynolds number for the experimental data and Shah & London correlation, Test Section 2

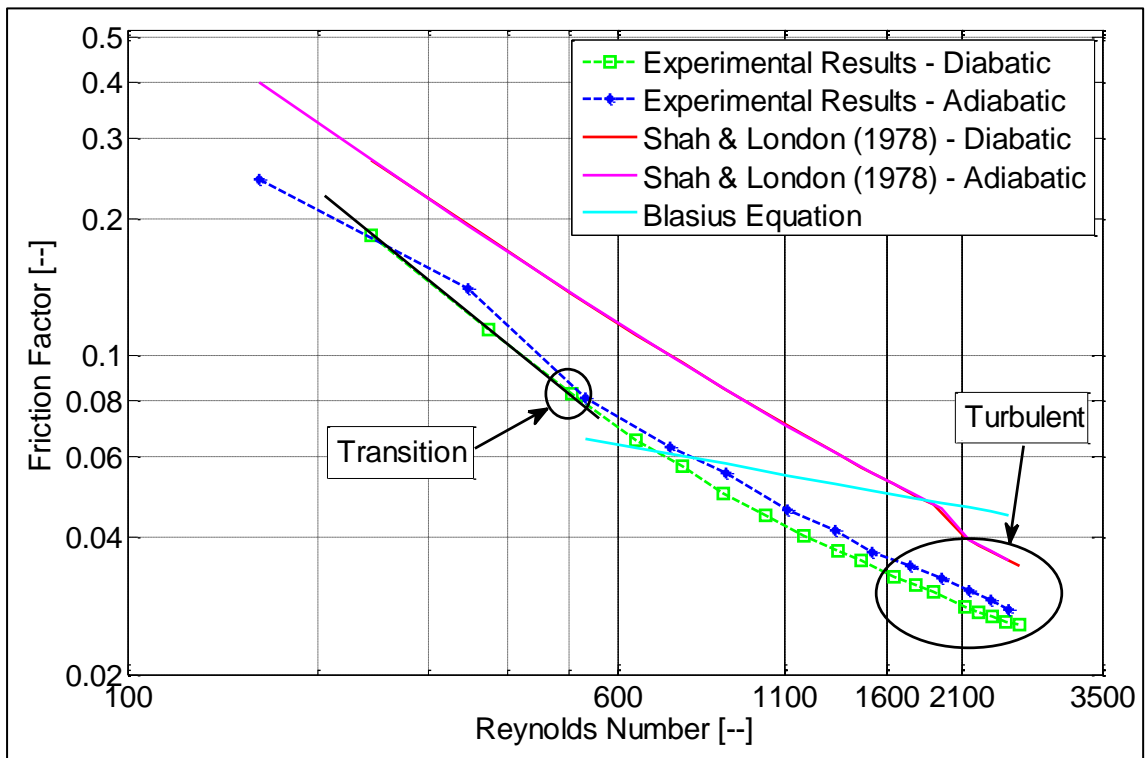


Figure 6.5 Diabatic and adiabatic friction factors versus the Reynolds number for the experimental data and Shah & London correlation, Test Section 3

The diabatic friction factors for all three test sections for the Reynolds number testing range is shown in Figure 6.6. It can be seen that the friction factor for Test Section 2 is the lowest until a Reynolds number of 1250. As the Reynolds number increases the

friction factor tends to converge to a single value for all test sections. The friction factor for Test Section 3 is the highest for the complete testing range. The aspect ratio, (calculated by using the maximum of H_c or W_c divided by the minimum of H_c or W_c) is shown in the legend. It can be observed that the friction factor is the lowest for the lowest aspect ratio (most square channel) and as the aspect ratio increases the friction factor also increases.

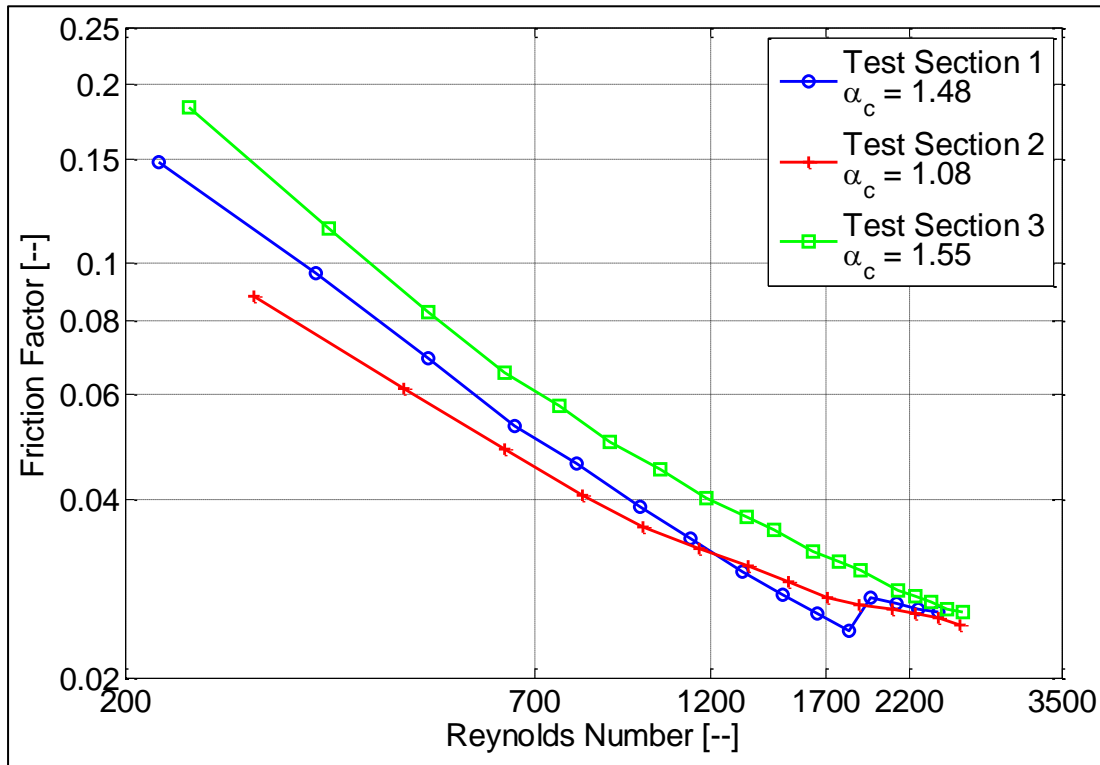


Figure 6.6 Diabatic friction factors versus the Reynolds number for the experimental data for Test Section 1, Test Section 2 and Test Section 3

6.4. HEAT TRANSFER

The Nusselt numbers were calculated from the measured results for all three test sections using the methodology as described in Section 5.2. The local Nusselt numbers were presented for the Reynolds number test range for each test section. The average Nusselt number (determined from the local heat transfer coefficient) for each test section was calculated and compared to commonly accepted correlations.

6.4.1. LOCAL NUSSULT NUMBERS

The local Nusselt number for Test Section 1 along the axial direction, of the channel, for different Reynolds numbers is shown in Figure 6.7. It can be seen that the local Nusselt number decreases from the first to the third measuring position, but increases at the last measuring position for Reynolds numbers larger than 505. This increase of the local Nusselt number near the end of the test section is not commonly seen in literature. In

Section 4.3 the average wall temperatures along the axial direction decreased at the higher Reynolds numbers between the third and fourth measuring position, which in return contributed to the un-common trend of the local Nusselt number. As mentioned previously, in Section 4.3, this phenomenon could be due to transition to turbulent flow along the length of the channel and additional cooling at the exit of the channel due to the sudden expansion and insufficient insulation. The latter two where specially checked for and such impacts where minimised as far as possible.

A large difference in the local Nusselt number magnitude for Reynolds numbers between 1827 and 1955 is seen from Figure 6.7. More heat is transferred to the working fluid in the turbulent flow regime and therefore the Nusselt number will also increase. A sporadic jump in the average wall temperatures was also observed in Section 4.3 between flow rates 51.6 ml / min ($Re = 1827$) and 55.2 ml / min ($Re = 1955$). Based on the above it could be assumed that there is a likelihood that the flow transitioned from laminar to turbulent flow at a Reynolds number between approximately 1800 and 1950.

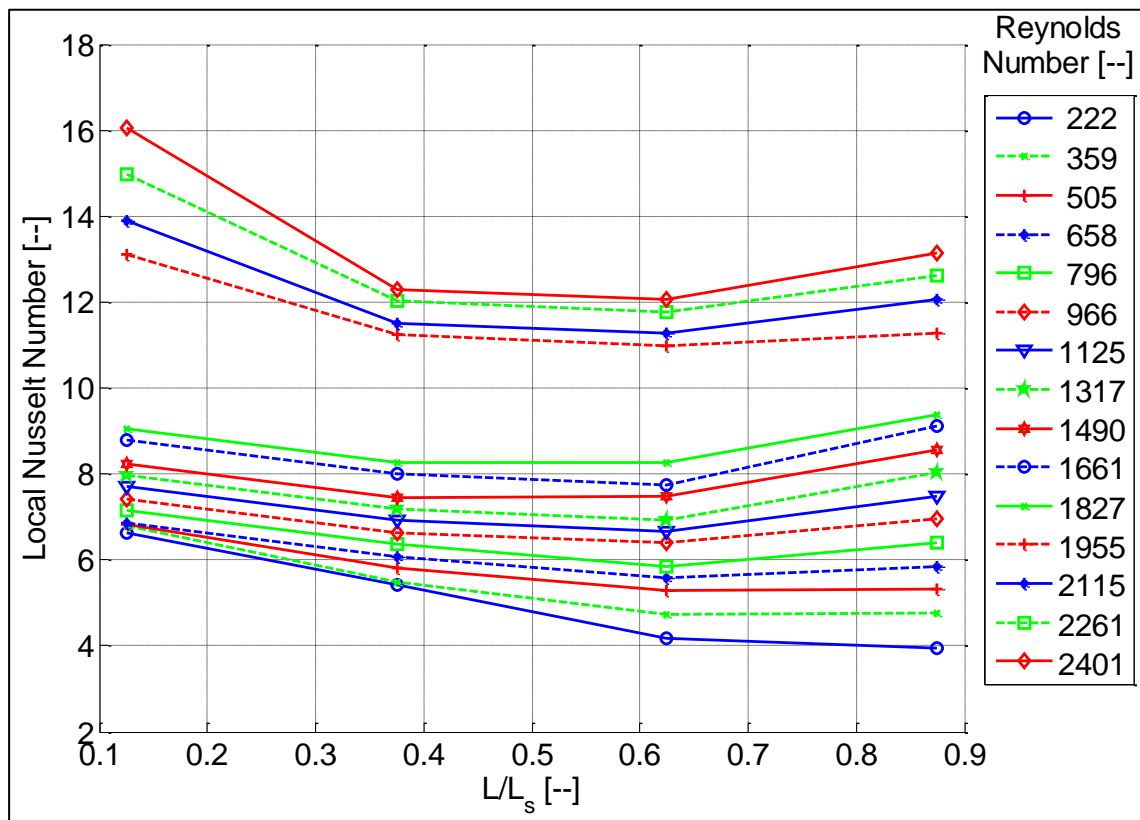


Figure 6.7 Local Nusselt numbers along the length of the microchannel test section for Reynolds number testing range – Test Section 1

The local Nusselt number for Test Section 2 along the channels axial direction is shown in Figure 6.8 for the different Reynolds numbers. A similar trend to that described for Test Section 1, where the local Nusselt number at the fourth measuring location increased rather the decreased as expected, is also observed. For Test Section 2 the Nusselt number increased at the fourth measuring position for all Reynolds numbers. At the two lowest and three highest flow rates ($Re = 296$, $Re = 470$, $Re = 2237$, $Re = 2399$, and $Re = 2566$) the local Nusselt number increased at the third measuring position,

whereas for Test Section 1 an increase was only observed at the fourth measuring position. The exact reason for this unexpected increase of the local Nusselt number could be a result of the reasons discussed for Test Section 1, but further research should be conducted to investigate this further. No evidence of transitional flow is present for Test Section 2 as the difference between the local Nusselt numbers at the different flow rates is similar.

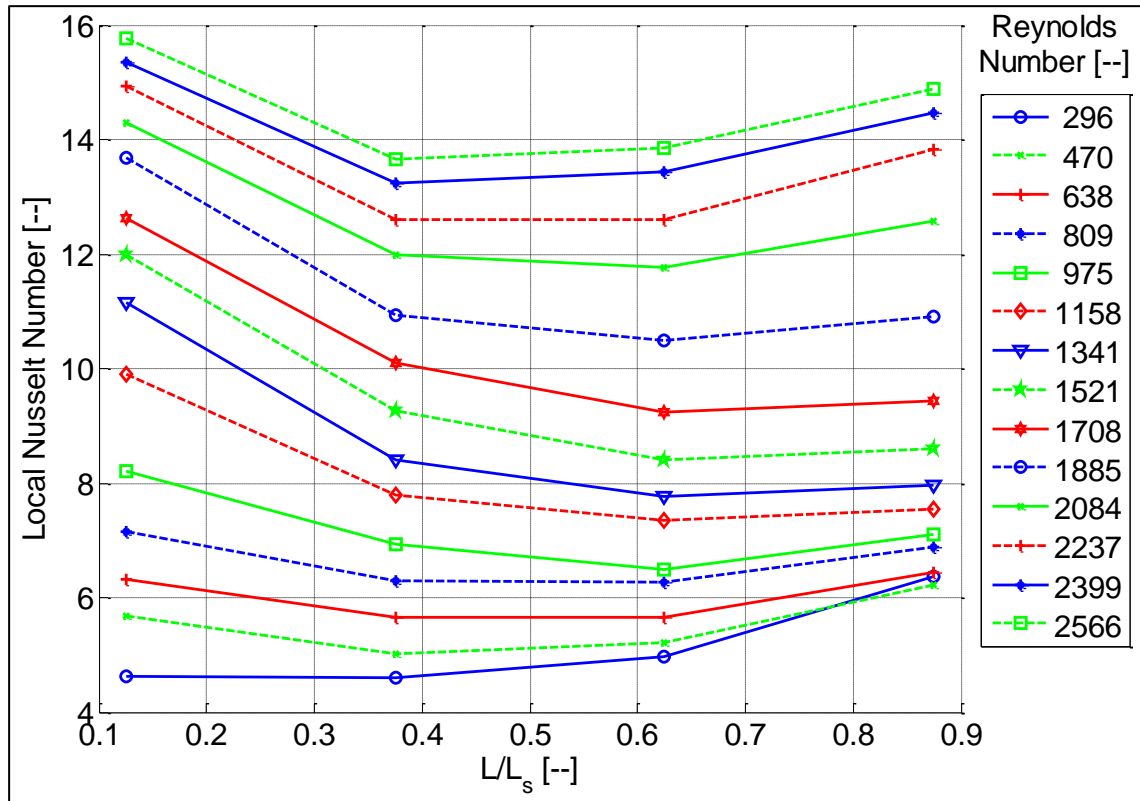


Figure 6.8 Local Nusselt numbers along the length of the microchannel test section for Reynolds number testing range – Test Section 2

The local Nusselt number for Test Section 3 along the channels axial direction is shown in Figure 6.9 for the different Reynolds numbers. A similar trend to that described for Test Section 1 and Test Section 2 is observed but, as with Test Section 2, the local Nusselt number increased at the third measuring position for the four lowest and four highest Reynolds numbers ($Re = 244$, $Re = 373$, $Re = 505$, $Re = 639$, $Re = 2235$, $Re = 2346$, $Re = 2470$, $Re = 2587$). No clear indication of transitional flow was observed as the difference between the local Nusselt numbers at the different flow rates is similar.

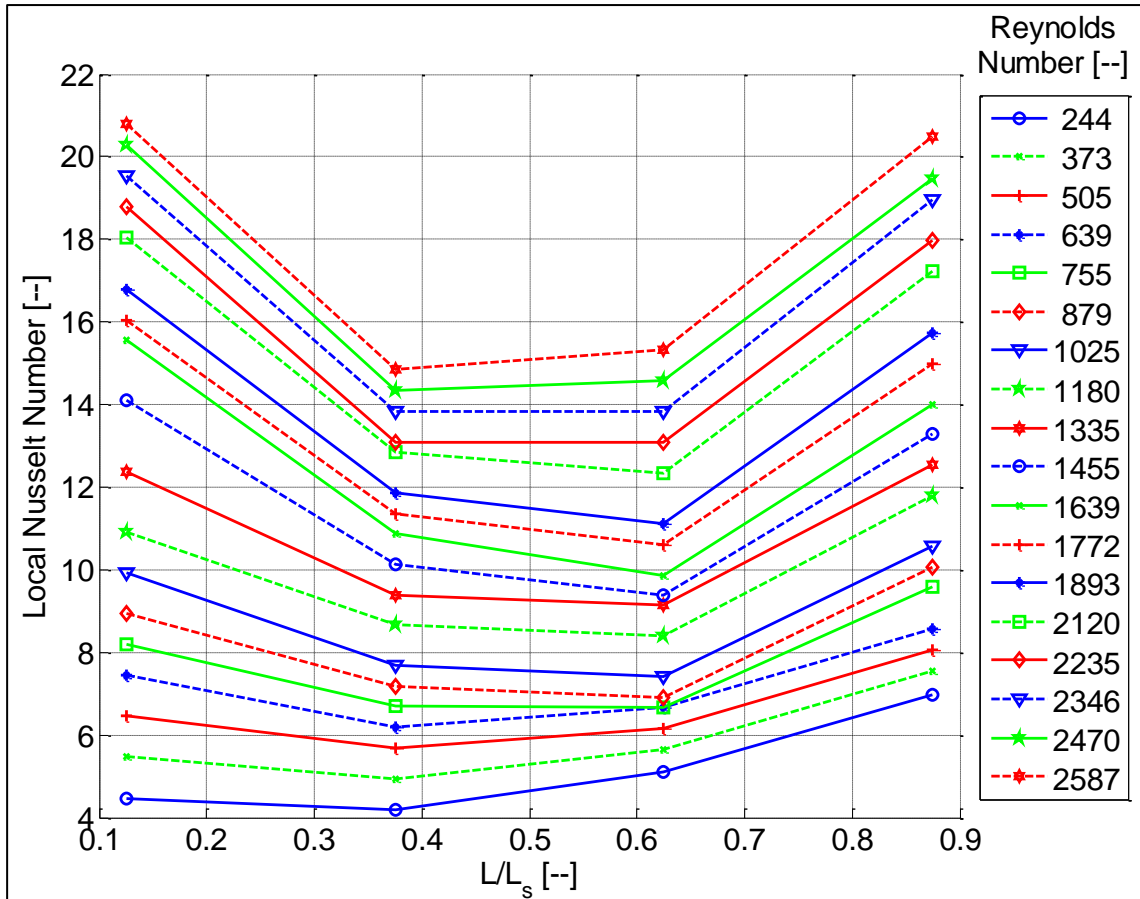


Figure 6.9 Local Nusselt numbers along the length of the microchannel test section for Reynolds number testing range – Test Section 3

Table 6.1 summarises the Reynolds number magnitudes where an increase of the local Nusselt number occurred at the third and fourth measuring positions. The aspect ratio is also tabulated for each test section. For Test Section 1 an increase was not observed at the third measuring location but an increase was observed at the last measuring position for Reynolds numbers larger than 658. For Test Section 2 and Test Section 3 an increase at the fourth measuring position was observed for all Reynolds numbers and an increase at the third location occurred at a similar Reynolds number range (approximately $640 \geq Re \geq 2235$). The increase of the local Nusselt number at the third location only occurred at aspect ratios smaller than or approximately one. Therefore from this summary it can be concluded, based on the experimental results, that the aspect ratio has a significant effect on the local Nusselt number.

Table 6.1 Summary of Reynolds numbers where the Nusselt number increased at the third and fourth measuring positions

	a_c	Nu_{local} increase at 3 rd measuring location	Nu_{local} increase at 4 th measuring location
Test Section 1	1.476	Did not occur	$Re \geq 658$
Test Section 2	1.080	$638 \geq Re \geq 2237$	$Re \geq 296$
Test Section 3	0.645	$639 \geq Re \geq 2235$	$Re \geq 244$

6.4.2. THERMAL ENTRANCE LENGTH

As the flow enters the microchannel the thermal profile begins to develop until ultimately reaching the fully developed profile. For conventional heat transfer analyses (non microchannel scale) the thermal entrance length is usually quite short with regard to the total length of the flow passage, but for microchannels the thermal developing entrance length in the laminar flow regime, is significant due to the generally shorter test sections. The laminar thermal entrance length is given by Equation 6.6, Kandlikar et al. (2004), where Phillips (1987) suggested that for rectangular channels, $c = 0.1$ whereas $c = 0.05$ for circular channels.

$$L_t = c \cdot Re \cdot Pr \cdot D_h$$

Equation 6.6

The laminar thermal entrance length was calculated for all three test sections for the Reynolds number testing range, shown in Figure 6.10, and increases linearly as the Reynolds number increases. The thermal entrance length is larger than the physical length of the test section and therefore the flow is in the thermally developing regime. The thermal entrance length of each test section varies by a small amount which is due to the small difference in the actual measured hydraulic diameter of each. All thermal calculations should take into account that the flow is in the thermal developing regime.

The thermal entrance length in the turbulent flow regime is only dependant on the hydraulic diameter of the flow passage, which is generally accepted as 10 times the hydraulic diameter. All three test sections have approximately the same hydraulic diameter of 0.5 mm, thus the turbulent entrance length equates to 5 mm, which is only 10 % of the total length of the test section. Therefore the assumption is made that the flow is fully developed in the turbulent regime across the entire test section.

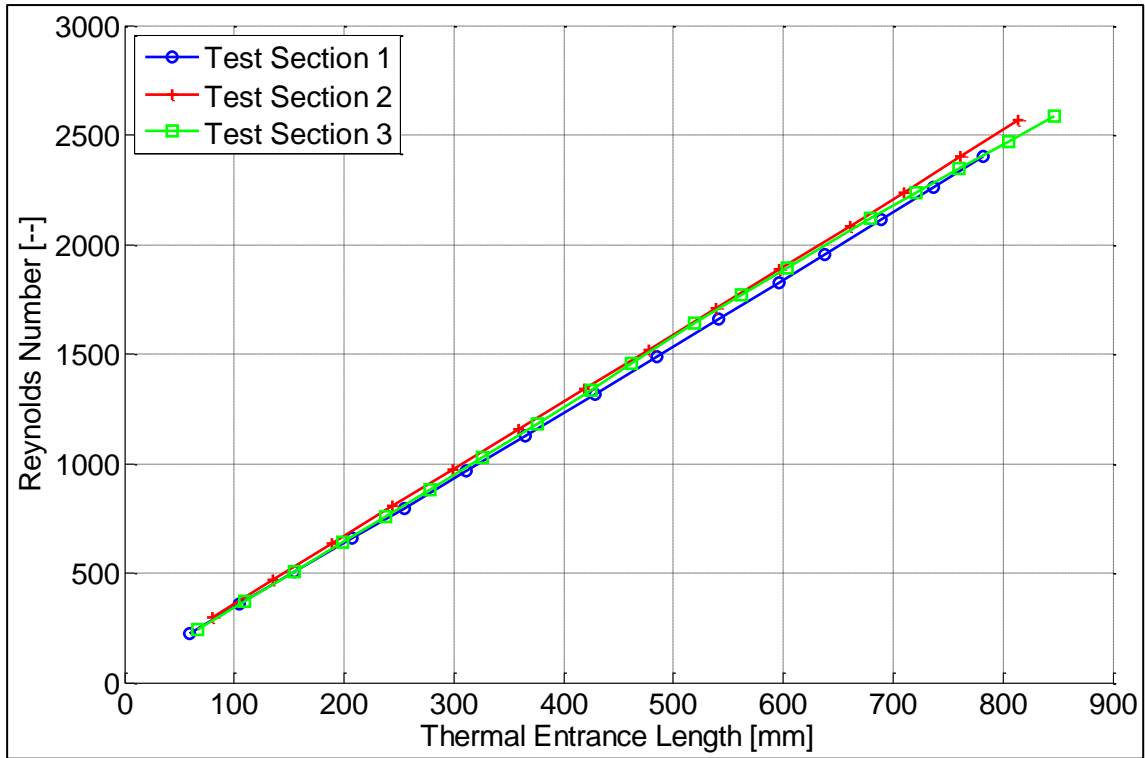


Figure 6.10 Thermal entrance length over the Reynolds number testing range for Test Section 1, Test Section 2 and Test Section 3

6.4.3. AVERAGE NUSSULT NUMBER RESULTS

A theoretical average Nusselt number can be calculated using the Hausen correlation, as was done in Section 3.4 (to obtain the approximate heat transfer parameters in the test section design phase), for laminar flow, but this correlation does not take into account the effect of the aspect ratio. Lee and Garimella (2006) developed a correlation to determine the Nusselt number in the laminar thermal developing regime for different channel aspect ratios. The authors compared the correlation obtained to conventional and available microchannel data and it was found to be in good agreement. The calculated Nusselt numbers, obtained from the experimental results, were compared to the correlation from Lee and Garimella (2006). The average Nusselt number in the turbulent flow regime was compared to the well accepted Gnielinski (1976) correlation, Cengel (2006).

The average Nusselt number in the laminar regime was calculated from the following equation, Lee and Garimella (2006):

$$Nu_{ave} = \frac{1}{C_1 \cdot (x^*)^{C_2} + C_3} + C_4 \quad \left| \text{Equation 6.7} \right.$$

where:

$$C_1 = -2.757 \times 10^{-3} \cdot \alpha_c^3 + 3.274 \times 10^{-2} \cdot \alpha_c^2 - 7.464 \times 10^{-5} \cdot \alpha_c + 4.476$$

Equation 6.8

and

$$C_2 = 6.391 \times 10^{-1}$$

Equation 6.9

and

$$C_3 = 1.604 \times 10^{-4} \cdot \alpha_c^2 - 2.622 \times 10^{-3} \cdot \alpha_c + 2.568 \times 10^{-2}$$

Equation 6.10

and

$$C_4 = 7.301 - 1.311 \times 10^1 / \alpha_c + 1.519 \times 10^1 / \alpha_c^2 - 6.094 / \alpha_c^3$$

Equation 6.11

and

$$x^* = \frac{L_s}{Re \cdot Pr \cdot D_h}$$

Equation 6.12

The average Nusselt number was calculated from the correlation as shown in Equation 6.13, Gnielinski (1976) for turbulent flow.

$$Nu_{ave} = \frac{(f/8) \cdot (Re - 1000) \cdot Pr}{1 + 12.7 \cdot (f/8)^{1/2} \cdot (Pr^{2/3} - 1)}$$

Equation 6.13

where f is calculated in accordance to Equation 5.15.

The average Nusselt numbers calculated from the experimental results and theoretical predictions are shown in Figure 6.11 for all three test sections over the Reynolds number testing range. Note that the Reynolds numbers are plotted on a log axis. If the flow was fully developed the average Nusselt number would be constant over the laminar Reynolds number range, but the flow is thermally developing and therefore it is expected that the average Nusselt number would increase with an increase in flow rate within the laminar flow regime.

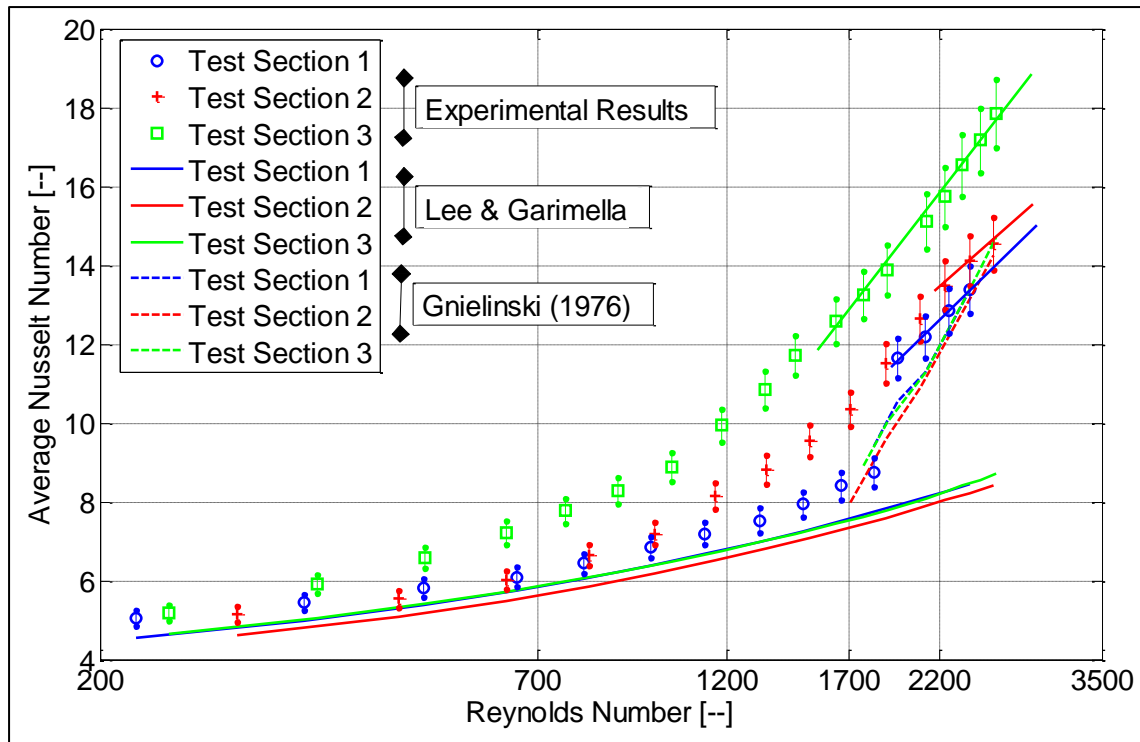


Figure 6.11 Average experimental and theoretical Nusselt numbers over the Reynolds number (logarithmic axis) testing range for Test Section 1, Test Section 2 and Test Section 3

The theoretical laminar average Nusselt numbers, for Test Section 1 and Test Section 3 are similar in magnitude and the Nusselt number for Test Section 2 is lower. In determining the average Nusselt number, according to Lee and Garimella (2006) the aspect ratio is calculated using the minimum of H_c or W_c divided by the maximum of H_c or W_c . The aspect ratio for Test Section 1 is $\alpha_c = 0.67$ and for Test Section 3 is $\alpha_c = 0.64$, which is similar, hence the magnitude of the average theoretical Nusselt number is also similar. The magnitude of the theoretical turbulent average Nusselt numbers are similar in magnitude.

A sudden jump in the average Nusselt number is observed for Test Section 1, a similar discontinuity was observed in the measured average wall temperature in Section 4.3 at the same flow rate/Reynolds number. This sporadic jump indicated a clear onset of transitional flow and hence the critical Reynolds number is approximately 1800 and the flow is fully turbulent at a Reynolds number of approximately 1950. For fully turbulent flow the Nusselt number lies on a straight line when plotted on a semi-log graph, as shown on Figure 6.11. The average Nusselt number (experimental) obtained for Test Section 1 follows a similar trend to that of the theoretical Nusselt number, when the flow is in the laminar regime, but the overall magnitude is larger. The Nusselt number of Test Section 2 is similar to the results obtained for Test Section 1 until a Reynolds number of approximately 825 and then the Nusselt number increases more rapidly. The friction factor results indicated that transitional flow also began at a Reynolds number of 825 and therefore is the cause for the deviation of the results as the heat transfer rate is larger in the transitional regime. The Nusselt number for Test Section 3 is only similar

for the first and second measuring data point and thereafter increases more rapidly than for Test Section 1 and Test Section 2. The friction factor results indicated that transitional flow began at a Reynolds number of 500, but from the average Nusselt number results it could possibly occur earlier.

The gradient of the experimental results in the turbulent regime is steeper than the theoretical prediction and the magnitude is overall larger. Test Section 1 and Test Section 2 compare more closely to the Gnielinski (1976) equation, but the results from Test Section 3 are significantly larger.

The magnitude of the experimental results differ from the theoretical predictions. The following reasons could exist:

- **Assumed Ideal Heat Flux:** The analyses used to determine the heat transfer coefficient assumed a constant heat flux in the axial direction of the test section. Due to the complexity in obtaining a constant heat flux boundary condition the possibility, in reality, could arise where a combination of constant heat flux and constant temperature boundary conditions exists. For the specific test case careful consideration was taken into account to assume a constant heat flux boundary and therefore majority of the boundary portion can be assumed at a constant heat flux and only a small portion at constant temperature. Nevertheless this non-ideal boundary condition could have an influence on the heat transfer results obtained.
- **Entrance Effects:** The entrance geometry can significantly affect the heat transfer and hydrodynamic behaviour of the test section. Koo and Kleinstreuer (2003) stated that entrance effects could be a major contributing factor to the discrepancies obtained in published results. The exact contribution that the entrance geometry has on the heat transfer results is case specific and therefore general theories are not commonly found in research. An inline sudden contraction inlet condition was used in this research and therefore even though it would, in somewhat, affect the heat transfer results it was assumed to be small as all three test section used the same inlet manifolds.
- **Surface Roughness of the Channel:** Conventionally the effect of the surface roughness of the channel walls influences the heat transfer results only in the turbulent flow regime and therefore these effects are normally ignored for laminar flow analyses. Celata (2004) suggested that the surface roughness of the channel has been the cause of deviations in published results of the heat transfer parameters both in laminar and turbulent flow.
- **Deduction of the Heat Transfer Coefficient from the Experimentally Measured Parameters:** The method used to determine the heat transfer coefficient from the measured experimental parameters could have an effect on the outcome of the results. Certain assumptions were made and were discussed in Section 5.2.
- **Measuring Errors:** Measuring errors could have also affected the heat transfer results. The uncertainties of these measurement errors were quantified in

Appendix H. Error bars are included in Figure 6.11 which indicates the range that the experimental results can lie.

From the experimental results (Figure 6.12, which is similar to Figure 6.11 except only the experimental results are shown and the channel aspect ratio and perimeter is given) it is observed that the average Nusselt number is the smallest for Test Section 1, then higher for Test Section 2 and the highest for Test Section 3 for the entire range of the tested Reynolds numbers. Therefore as the aspect ratio of the channel decreases the Nusselt number increases which is contrary to what was expected. In the design of the microchannel design section (Section 3.5) the peak temperatures were obtained from the numerical model. The peak temperature results are replicated in Figure 6.13. From the figure it can be seen that the peak temperature increases as the aspect ratio decreases, thus the deduction was made that the Nusselt numbers would decrease with a decrease in aspect ratio. But from the experimental results this was not the case, rather the complete opposite was obtained. A possible reason explaining these findings of the Nusselt number trends is discussed below.

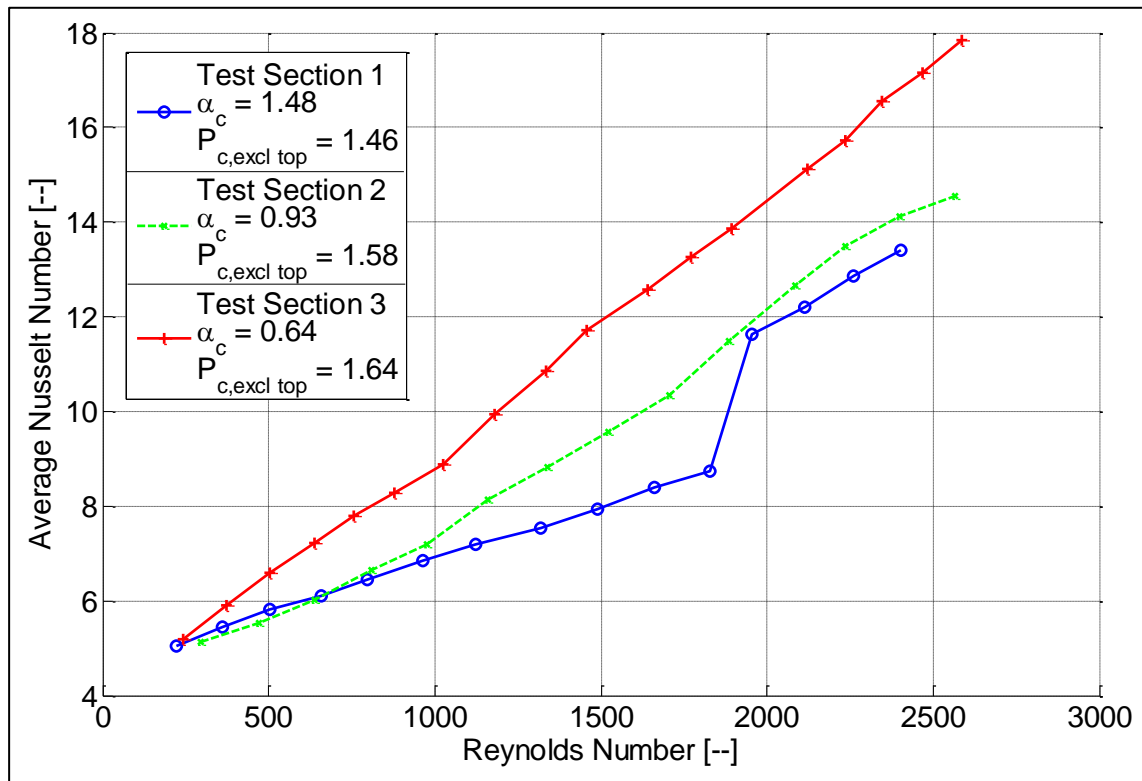


Figure 6.12 Average experimental Nusselt numbers over the Reynolds number testing range for Test Section 1, Test Section 2 and Test Section 3

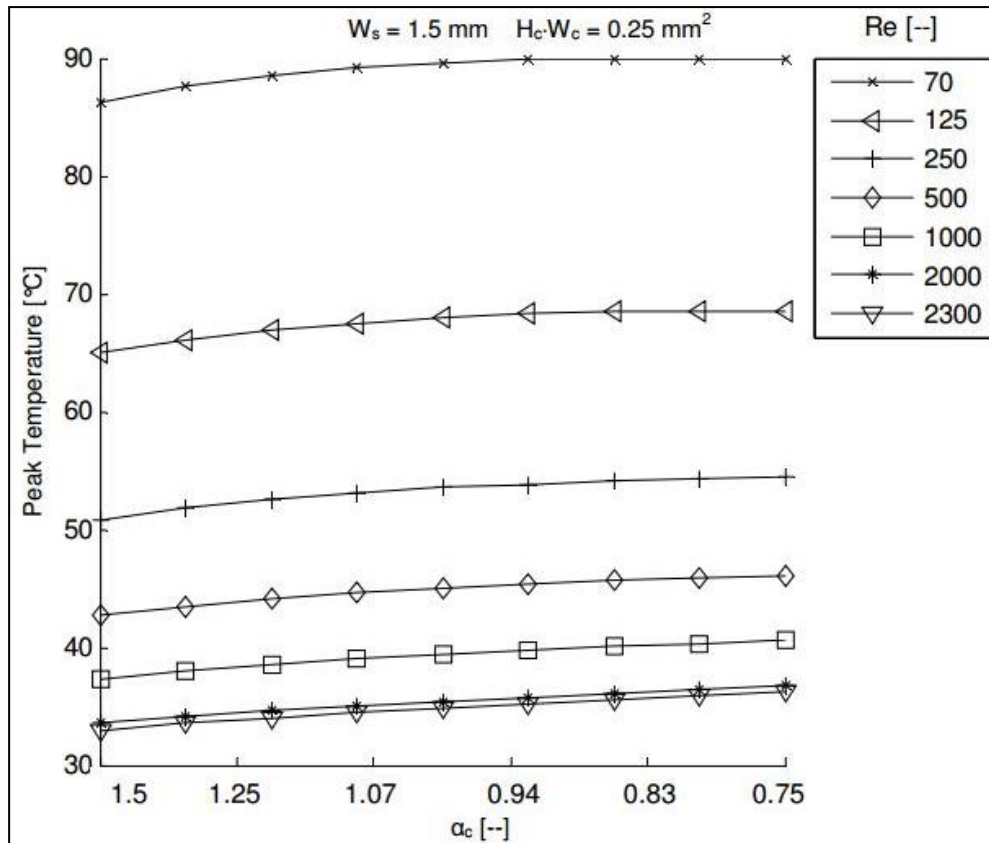


Figure 6.13 Peak temperatures for a different channel aspect ratios and Reynolds numbers, analysis as performed in Section 3.3

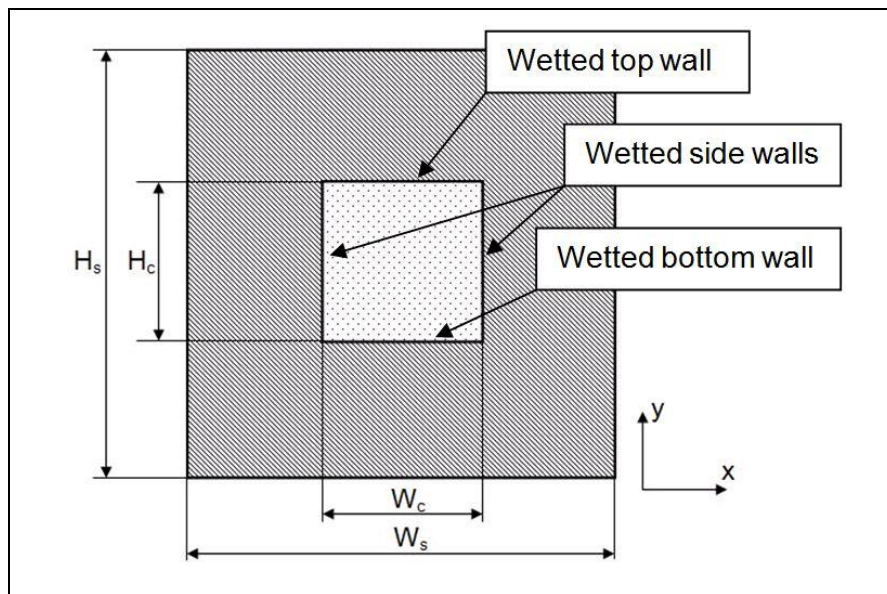
The convective heat transfer occurs at the boundary between the solid substrate and the working fluid. A conduction numerical model was used to relate the experimentally measured temperatures to the heat transfer. The model assumed a constant heat convective boundary for all four walls of the microchannel. Fedorov and Viskanta (2000) performed a conjugate numerical analysis on a single rectangular microchannel and they found that 80 % of the heat transfer was through the two wetted side walls, 11 % on the wetted bottom wall and only 9 % on the wetted top wall while being heated from the bottom outer wall. The side walls were three times larger than the top and bottom walls. From the findings of Fedorov and Viskanta (2000) it can be concluded that the heat transfer from the solid substrate to the working fluid through the top wall boundary is significantly smaller than through the other wall boundaries.

The actual dimensions and perimeter of the wetted surface are presented in Table 6.2 (replicated table from Section 3.5.3 with perimeter of channel included), it can be seen that the perimeter of the channels for all three test sections are similar. When comparing the perimeter of the channels where the wetted top wall is negated Test Section 1 has the smallest perimeter with Test Section 3 having the largest. Based on the research by Fedorov and Viskanta (2000), majority of the heat transfer occurs on the wetted side and bottom walls. The perimeter excluding the wetted top wall is included in the legend of Figure 6.11, from this it can be seen that Test Section 1 has the smallest perimeter and the lowest average Nusselt numbers, Test Section 2 has the next largest perimeter and hence the next largest average Nusselt number and

Test Section 3 has the largest perimeter and the largest average Nusselt number. Celata (2004) stated that Harms et al also found that a decrease in the channels width and increase in the channels height provided better heat transfer performance.

It can be concluded that as the aspect ratio of the channel decreases the average Nusselt number increases. During the test section design phase the numerical model used showed that the peak temperature increased as the aspect ratio decreased. From this it can be deduced that the peak temperature within the solid substrate cannot directly be related to the performance of the convective heat transfer.

Table 6.2 Test section dimensions and perimeter



	Test Section 1	Test Section 2	Test Section 3
H_c [mm]	0.42	0.54	0.62
W_c [mm]	0.66	0.50	0.40
H_s [mm]	1.14	1.64	2.98
W_s [mm]	1.52	1.50	1.50
P_c [mm]	2.08	2.08	2.04
$P_{c, \text{excl top}}$ [mm]	1.46	1.58	1.64

6.5. COLBURN J-FACTOR

The analogy of the Colburn j-factor is used to represent the heat transfer coefficient whereby the effect of the Prandtl number is negated. The Colburn j-factor was calculated using Equation 5.21 and compared to the friction factor.

The Colburn j -factor is shown in Figure 6.14 for the three test sections for the Reynolds number testing range. It is seen that the Colburn j -factor decreases as the Reynolds number increases following a smooth curve except for Test Section 1. A sporadic jump in the results for Test Section 1 at a Reynolds number of approximately 1800 indicates a clear onset of turbulent flow, as previously observed in the Nusselt number and friction factor results. From the discussion in Section 6.4.3 it was observed that the critical Reynolds number, for fully turbulent flow, for Test Section 2 and Test Section 3 was 2250 and 1650 respectively, the same is observed from the j -factor.

It is also seen that the Colburn j -factor magnitude is similar, for all three test sections, at the lowest measured Reynolds number and then tends to diverge as the Reynolds number increases. This trend was also observed for the Nusselt number results as well.

The Colburn j -factor is the smallest for Test Section 1 and increases for Test Section 2 and is the largest for Test Section 3. The Colburn j -factor is a function of the average Nusselt number and therefore the same trend was observed for both the Colburn j -factor and the average Nusselt number results.

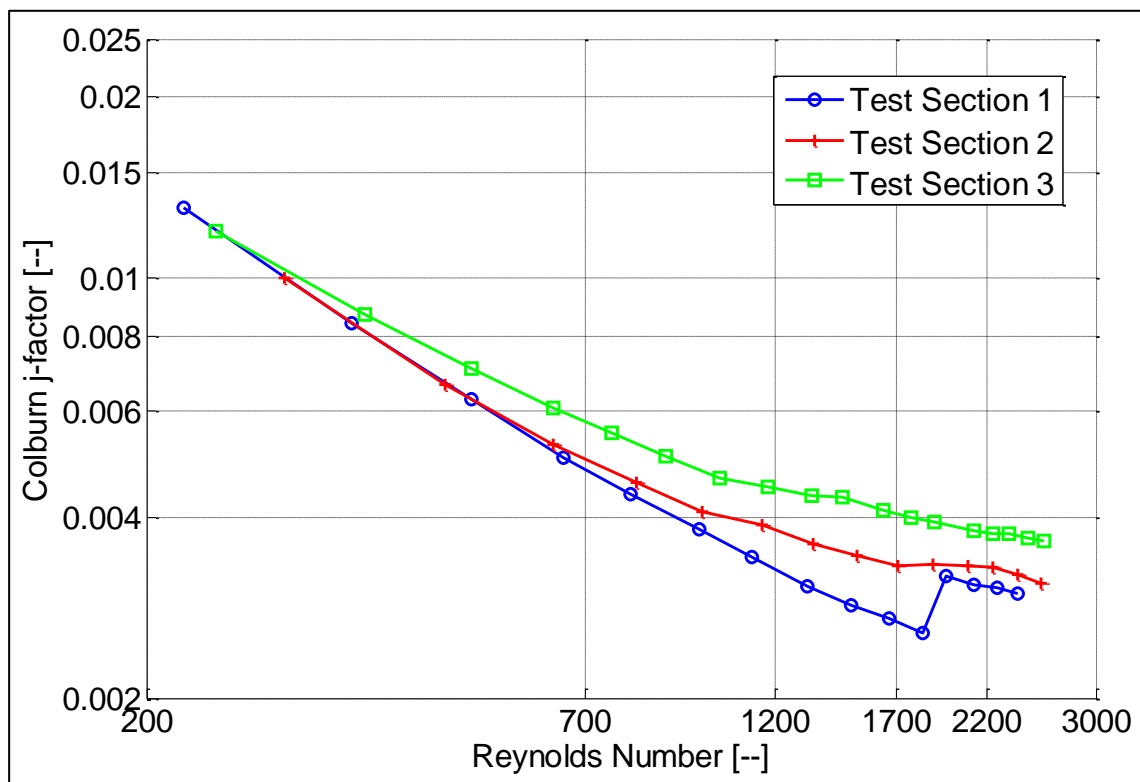


Figure 6.14 Colburn j -factor versus the Reynolds number for the experimental data for Test Section 1, Test Section 2 and Test Section 3

The Colburn j -factor and the friction factor are plotted on the same graph for the three different test sections for the Reynolds number measuring range, in Figure 6.15. It can be observed that there is, somewhat, a relation between the Colburn j -factor and the friction factor. Both decrease at similar rates at Reynolds numbers larger than approximately 500. At Reynolds number smaller than 500 the magnitude of the Colburn j -factor is similar for all three test sections whereas for the friction factor, the magnitude

is different. The sporadic jump for Test Section 1 occurs at the same Reynolds numbers for both the Colburn j-factor and the friction factor.

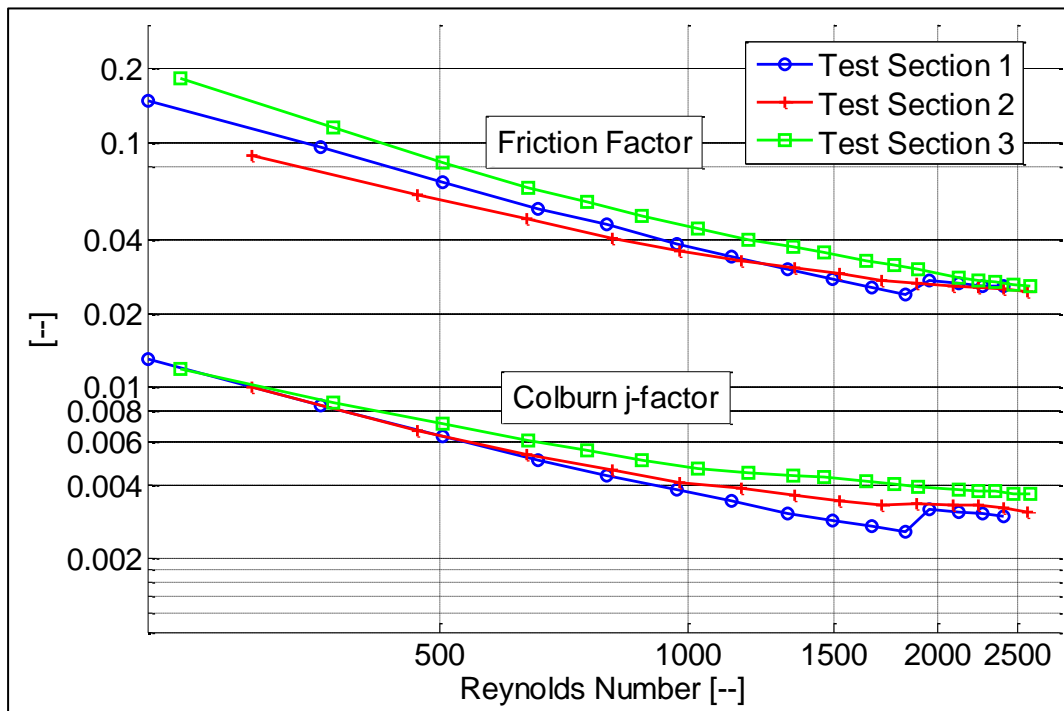


Figure 6.15 Colburn j-factor and the friction factor versus the Reynolds number for the experimental data for Test Section 1, Test Section 2 and Test Section 3

The ratio of the Colburn j-factor to the friction factor is shown in Figure 6.16. The results indicate that there is a possible relation between the two when considering Test Section 1 and Test Section 2. The results obtained for Test Section 3 are vastly different to the other two test sections. It is observed that the difference between the ratio for Test Section 1 and Test Section 2 is similar until the critical Reynolds numbers. It would be expected that the relationship would change significantly when the flow transitions to turbulence.

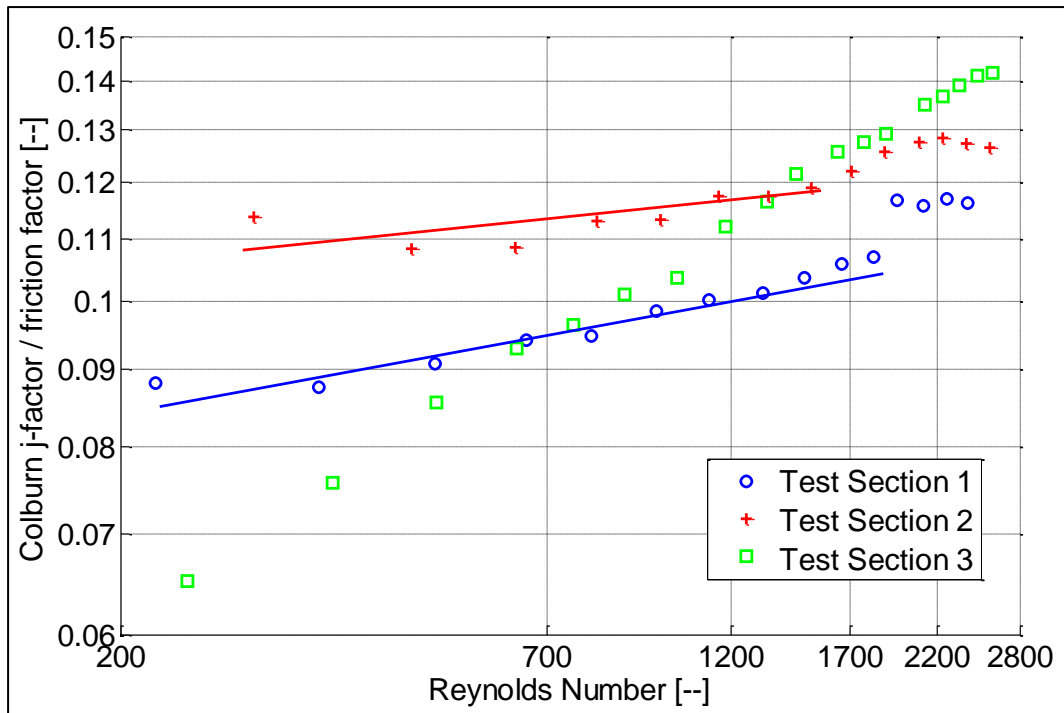


Figure 6.16 Ratio of the Colburn j-factor to the friction factor across the Reynolds number for the experimental data for Test Section 1, Test Section 2 and Test Section 3

6.6. SUMMARY OF THE DATA REDUCTION RESULTS

The friction factor for all of the test sections was lower than the theoretical predication and the diabatic friction factor was lower than the adiabatic friction factor for all test sections. The critical Reynolds number for Test Section 1 was clearly observed whereas for the other two test sections it was not the case, but regardless it did have characteristics of transitional and turbulent flow. The friction factor was the lowest for the test section with the smallest aspect ratio, where the aspect ratio was calculated taking the minimum of H_c or W_c divided by the maximum of H_c or W_c .

The local heat transfer coefficients were determined and plotted on graphs for each test section. It was found that the local Nusselt number increased, unexpectedly, towards the end on the test section for all test sections for the lower and higher Reynolds numbers.

The average Nusselt numbers for each test section were determined and compared to common correlations. It was found that the results for all the test sections compared well to the laminar theoretical prediction with the magnitude being approximately 10 % larger. Flow started to transition to turbulence at a Reynolds number of 1800 for Test Section 1 and the flow was fully turbulent at a Reynolds number of 1950. For Test Section 2 the flow started transitioning earlier at a Reynolds number of 825 and was only fully turbulent at a Reynolds number of 2250. Earlier transitional flow was identified at a Reynolds number of 500 for Test Section 3 with the flow being fully turbulent at a Reynolds number of 1650.

The average Nusselt number increased as the aspect ratio of the channel decreased. It was also observed that the peak temperature, obtained from the numerical model, (used in the design phase of the test sections) was not directly related to the thermal performance of the test sections.

The Colburn j-factor was determined and plotted on the same graph with the friction factor. The overall trend of the j-factor and the friction factor were similar. The ratio between the Colburn j-factor and the Nusselt number were also plotted and it was observed that a possible relation could exist between the j-factor and the friction factor for Test Section 1 and Test Section 2, but the results for Test Section 3 were significantly different. The laminar to transition was also observed when observing the j-factor.

The energy balance for all three test sections was obtained, ideally the energy balance should be as low as possible which would indicate that there were no energy losses. It was found that the largest percentage energy loss was for the lower and higher Reynolds numbers with the average energy balance being below 10% for Reynolds numbers larger than 600.

CHAPTER 7

CONCLUSION AND RECOMMENDATIONS

7.1. CONCLUSION

The purpose of this study was to experimentally determine the heat transfer and dynamic characteristics of a single microchannel housed in a low thermal conductive solid base material for different aspect ratios in the laminar flow regime. By using a low thermal conductive base the conjugate effects were magnified to better understand the heat transfer. The main objectives were to design and fabricate three test sections; design, construct and commission a microchannel test facility; obtain experimental results from the test sections; and analyse and discuss the results obtained.

Relevant micro and mini channel literature was reviewed and the factors that influenced the internal forced convection and conjugative heat transfer were discussed. When comparing the literature, discrepancies existed for the Nusselt number and friction factor results, authors have alluded to mechanisms for the discrepancies, but the fact of the matter is that the field of microchannel research has not yet converged to a single 'theory' or outcome.

From the reviewed literature it was found that the conduction within the solid substrate influences the overall heat transfer parameters when the solid substrates' thermal conductivity is low and when the channels hydraulic diameter is small. Surface roughness of the channel wall does in fact influence the pressure drop in laminar flow. The general trend indicated that the critical Reynolds number decreased with an increase in the surface roughness. The entrance effects also influenced the critical Reynolds number. Microchannel test sections and test facilities were reviewed which aided in the design of both for this study.

The microchannel test sections were designed and fabricated and the exact dimensions of each were measured and compared to the desired design dimensions. A maximum deviation of 14.4 % was obtained. The layout of the microchannel within the solid substrate was offset horizontally, due to fabrication limitations, by 0.12 mm for Test Section 1, 0.26 mm for Test Section 2 and 0.06 mm for Test Section 3, and due to this offset a detailed analysis was performed to determine the effects thereof.

The test facility was built from the ground up to accommodate the microchannel test parameters. Calibration of the thermocouples and the uncertainty of the instrumentation was determined and used in the uncertainty analysis.

A carefully thought-out experimental procedure was followed and the outer top and side wall temperatures at four locations, fluid inlet and outlet temperatures and differential pressure drops were measured.

From the experimental results the wall temperatures increased along the axial direction from the inlet to the outlet but for the higher flow rates the temperature at the last measuring position decreased. The reason for the unexpected increase, at the last measuring position, was not completely understood but could be a result of the flow within the microchannel becoming turbulent along the length of the channel; the effect of the sudden expansion at the outlet; or the effect of the discontinuity of the insulation at the end of the test section. Differences between the left and right side wall temperatures increased as the horizontal offset increased. The average measured wall temperature decreased as the volumetric flow rate increased and turbulent flow occurred for Test Section 1 at 55 ml / min, for Test Section 2 at 60 ml / min and for Test Section 3 at 45 ml / min respectively. The thermal gradient decreased towards the end of the microchannel which indicated that the flow became more developed along the length.

The differential pressure drop over the test section increased with the volumetric flow rate. A higher pressure drop was obtained for the test sections where the cross-sectional area was the smallest. The differential pressure drop for the adiabatic test case was higher than for the diabatic test case for all test sections. Laminar to turbulent transition was also observed, from the pressure drop, at similar flow rates as identified by the average wall temperatures.

From the temperatures and pressure drop measurements the data was reduced/analysed to determine the Nusselt number, friction factor and Colburn j-factor. The microchannel wetted surface heat transfer properties were obtained using the outer measured temperatures by reducing the data with the use of a two-dimensional numerical model. Accurate results could only be obtained if the conduction in the axial direction was negligible. The effect of the axial conduction was investigated using a method suggested by Maranzana, Perry and Maillet (2004) and it was found, for the worst case, to be only 0.6 % of the total heat input, therefore the use of a two-dimensional numerical model yielded accurate results.

The numerical model was further simplified by making use of a vertical symmetry line, therefore only one half of the test section was modelled. Due to manufacturing constraints, the microchannels were not machined perfectly in the middle of the solid substrate. An investigation was conducted to see the effects of the asymmetrical layout of the channel. It was found that if the average side wall thickness and the average side wall temperatures were used, the magnitude of the heat transfer coefficient was the same as if a full two-dimensional analysis was performed with the channel offset to one side.

The friction factor was compared to correlations developed by Shah and London (1978) supplemented with an apparent friction factor using the Hagenbach's factor to account

for developing flow in the laminar regime. The friction factor for all of the test sections was lower than the theoretical predication. The diabatic friction factor magnitude was smaller than the adiabatic friction factor for all test sections. All test sections showed signs of transitional and turbulent flow. Transitional flow occurred at Reynolds numbers 1800, 825 and 500 for Test Section 1, Test Section 2 and Test Section 3 respectively and fully turbulent flow occurred at Reynolds numbers above 1950, 2250 and 1650 for Test Section 1, Test Section 2 and Test Section 3 respectively. The friction factor was the lowest for the test section with the smallest aspect ratio, where the aspect ratio was calculated taking the minimum of H_c or W_c divided by the maximum of H_c or W_c .

The measured data was reduced/analysed using the numerical model and general heat transfer and fluid dynamic equations. Local Nusselt numbers should, conventionally, decrease along the axial direction of the channel but the results showed that there was an increase towards the end of the test section. The exact cause for this increase is not completely understood but it could be a result of the reasons as mentioned in the discussion of the measured temperature results. It is recommended that further research be conducted to better understand the identified phenomenon. Only Test Section 1 had a clear indication that the flow transitioned to the turbulent regime at approximately 1800 when considering the local Nusselt numbers.

Average Nusselt numbers for each test section were compared to a correlation developed by Lee and Garimella (2006) for laminar flow and to the Gnielinski (1976) equation for turbulent flow. The average Nusselt number for Test Section 1 compared well with the correlations with the magnitude being approximately 10 % larger. The average Nusselt number for Test Section 2 compared well until a Reynolds number of 825 and then diverged from the correlation, which was due to the flow starting to transition to turbulence. Test Section 3 only compared well until a Reynolds number of 370 and then also diverged from the correlation, the friction factor results indicated that transition occurred at a Reynolds number of 500, but the heat transfer results indicated that transition occurred earlier. The magnitude of the average Nusselt numbers were larger than the correlations, the following were suggested reasons for the findings: an ideal heat flux was assumed in the analysis which in reality could not be the case; the entrance effect could influence the results; the surface roughness could also not only affect the results in the turbulent but also in the laminar regime; in determining the constant heat transfer coefficient certain assumptions were made which could have also influenced the results; and measurement errors and uncertainties could also have affected the results. When comparing the three test sections, the average Nusselt numbers increased as the aspect ratio of the channel decreased, which was related to the perimeter (excluding the length of the microchannel top wall) of the microchannel.

The Colburn j-factors were plotted on the same graph with the friction factors, for all three test sections, which indicated that the trend between the two were similar. The ratio between the Colburn j-factor and the friction factor was plotted and a possible relationship was seen to exist, but only between Test Section 1 and Test Section 2, the results for Test Section 3 were significantly different. Therefore it is recommended that

further research be conducted to confirm this general finding. Transition from laminar to turbulent flow was also identified when observing the j-factor.

Finally, it can be concluded that the heat transfer and hydrodynamic performance for the three test sections tested were dependent on a multiple of primary parameters such as the aspect ratio, channel cross-sectional area, and channel perimeter (excluding the top wall length). Table 7.1 gives an overall summary of the results obtained, ranking the heat transfer and hydrodynamic magnitudes as: low, medium or high.

Table 7.1 Summary of all the analysed/reduced results

		Test Section 1	Test Section 2	Test Section 3
α_c - channel aspect ratio [- -]	W_c / H_c	1.476	1.080	0.645
	$\min(W_c / H_c) / \max(W_c / H_c)$	0.677	0.926	0.645
A_c - channel cross-sectional area [mm ²]		0.260	0.270	0.248
$P_{c, excl top}$ [mm]		1.46	1.58	1.64
$Re_{critical}$ Transition – Critical Reynolds number [--]		1800	825	500
$Re_{critical}$ Turbulence – Critical Reynolds number [--]		1950	2250	1650
Nu_{ave} - (Average Nusselt number) [--]		Low	Medium	High
f – Friction Factor [--]		Medium	Low	High
j – Colburn j-factor [--]		Low	Medium	High

7.2. RECOMMENDATIONS FOR FUTURE WORK

The author recommends that the following should be investigated in future studies:

- The reason for the increase in the wall temperatures and Nusselt numbers near the exit of the test section. It is suggested that different length test section be experimentally tested to determine if the phenomenon is a function of the test section length.
- The influence of the entrance effects on the friction factor and heat transfer coefficient
- Confirm and further investigate the effect of the aspect ratio on the critical Reynolds number. More test could be performed where the aspect ratio varies by a larger value. This would pronounce the effect of the aspect ratio on the heat transfer and dynamic parameters.
- If a relationship between the Colburn j-factor and the friction factor exist using various test sections with varying aspect ratios.
- The effect that the placement of the thermocouples, measuring the wall temperatures, has on the heat transfer results. A test section could be designed in such a way that high accuracy infrared thermal images could be obtained and the temperature results from conventional thermal couples could be compared.

The author recommends that the following practices be followed for further research:

- Totally independent test sections should be built and designed in such a way that they can easily be added and removed from the test bench. This will give the researcher the possibility to confirm trends identified by swapping test sections during the testing phase, and re-testing different configurations if required.
- All data reduction and comparisons should be performed before the testing phase is completed, therefore (with the independent test sections) re-testing can easily be performed to confirm the trends obtained.
- Careful consideration should be taken into account when designing the insulation for the test sections to reduce the thermal capacity, which will reduce the required time to reach steady state between testing iteration steps. The possibility of using a vacuum chamber should be considered.

REFERENCES

- BABY, B and SOBHAN, CB (2014). Numerical and experimental investigation on forced convection in meso-channels with irregular geometry of cross-section. *International Journal of Heat and Mass Transfer*, **70**, 276-288.
- BECK, JV and HAJI-SHEIKH, A (1996). Comparison of some inverse heat conduction methods using experimental data. *International Journal of Heat and Mass Transfer*, **39** (17), 3649-3657.
- BELLO-OCHEDE, T and MEYER, JP (2009). Constructual cooling channels: Application to heat transfer in microchannels heat sink. *International Journal of Emerging Multidisciplinary Fluid Sciences*, **1**, 61-83.
- CELATA, GP (2004). *Heat Transfer and Fluid Flow in Microchannels*. New York, Begell House.
- CENGAL, YA (2006). *Heat and mass transfer - A practical approach*. 2nd Edition ed., McGraw Hill.
- DIXIT, T and GHOSH, I (2015). Review of micro- and mini- channel heat sinks and heat exchangers for single phase fluids. *Renewable and Sustainable Energy Reviews*, **41**, 1291-1311.
- FEDOROV, AG and VISKANTA, R (2000). Three-dimensional conjugate heat transfer in the microchannel heat sink for electronic packaging. *International Journal of Heat and Mass Transfer*, **43**, 399-415.
- GAMRAT, G, FAVRE-MARINET, M and ASENDRYCH, D (2005). Conduction and entrance effects on laminar liquid flow and heat transfer in rectangular microchannels. *International Journal of Heat and Mass Transfer*, **48**, 2943-2954.
- GAMRAT, G, et al. (2008). An experimental study and modelling of roughness effects on laminar flow in microchannels. *Journal of Fluid Mechanics*, **594**, 399-423.
- GUERIN, LJ, et al. (1997). Simple and low cost fabrication of embedded microchannel by using a new thick-film photoplastic. In: *International Conference on Solid-State Sensors and Actuators*, USA, 16-19 June 1997. Chicago, 1419-1422.
- HAO, P, HE, F and ZHU, K (2005). Flow characteristics in a trapezoidal silicon microchannel. *Journal of Micromechanics and Microengineering*, **15**, 1362-1368.
- HERWIG, H and HAUSNER, O (2003). Critical view on "new results in micro-fluid mechanics": an example. *International Journal of Heat and Mass Flow*, **46**, 935-937.
- HETSRONI, G, et al. (2005). Heat transfer in microchannels: Comparison of experimental with theory and numerical results. *International Journal of Heat and Mass Transfer*, **48**, 5580-5601.
- HUANG, CH and WANG, SP (1999). A three-dimensional inverse heat conduction problem in estimating surface heat flux by conjugate gradient method. *International Journal of Heat and Mass Transfer*, **42** (18), 3387-3403.
- HUANG, CY, et al. (2014). The experimental investigation of axial heat conduction effect on the heat transfer analysis in microchannel flow. *International Journal of Heat and Mass Transfer*, **70**, 169-173.
- JAMES, V, et al. (1985). *Inverse Heat Conduction: Ill-Posed Problems*. vol.1. 1 ed., New York, John-Wiley and Sons.

- JIANG, J, HAO, Y and SHI, M (2008). Fluid flow and heat transfer characteristics in rectangular microchannels. *Heat Transfer - Asian Research*, **37**, 197-208.
- JIN, B and MARIN, L (2007). The method of fundamental solutions for inverse source problems associated with steady-state heat conduction. *International Journal of Numerical Methods in Engineering*, **69**, 1570-1589.
- JO, BH, et al. (2000). Three-dimensional microchannel fabrication in polydimethylsiloxane (PDMS) elastomer. *Journal of Microelectromechanical Systems*, **9** (1), 76-81.
- JUDY, J, MAYNES, D and WEBB, BW (2002). Characterization of frictional pressure drop for liquid flows through microchannels. *International Journal of Heat and Mass Transfer*, **45**, 3477-3489.
- KANDLIKAR, SG, et al. (2004). *Heat Transfer and Fluid Flow in Minichannels and Microchannels*. Elsevier.
- KANDLIKAR, A and WILLIAM, JG (2003). Evolution of microchannel flow passages - Thermohydraulic performance and fabrication technology. *Heat Transfer Engineering*, **24**, 3-17.
- KAWANO, K, et al. (1998). Microchannel heat exchanger for cooling electrical equipment. *ASME, HTD-361-3/PID-3*, 173-180.
- KLINE, SJ and MCCLINTOCK, FA (1953). Describing uncertainties in single sample experiments. *American Society of Mechanical Engineers*, **75** (1), 3-8.
- KOO, J and KLEINSTREUER, C (2003). Liquid flow in microchannels: experimental observations and computational analyses of microfluidics effects. *Journal of Micromechanics and Microengineering*, **13**, 568-579.
- KOU, H, LEE, J and CHEN, C (2008). Optimum thermal performance of microchannel heat sink by adjusting the channel width and height. *International Communications in Heat and Mass Transfer*, **35**, 577-582.
- LEE, PS and GARIMELLA, SV (2006). Thermally developing flow and heat transfer in rectangular microchannels of different aspect ratios. *International Journal of Heat and Mass Transfer*, **49**, 3060-3067.
- LEE, PS, GARIMELLA, SV and LIU, D (2005). Investigation of heat transfer in rectangular microchannels. *International Journal of Heat and Mass Transfer*, **49** (9), 1688-1704.
- LELEA, D (2007). The conjugate heat transfer of the partially heat microchannels. *Heat Mass Transfer*, **44**, 33-41.
- LI, J, PETERSON, GP and CHENG, P (2004). Three-dimensional analysis of heat transfer in a micro-heat sink with single phase flow. *International Journal of Heat and Mass Transfer*, **47**, 4215-4231.
- MALA, GM and LI, D (1999). Flow characteristics of water in microtubes. *International Journal of Heat and Mass Transfer*, **20**, 142-148.
- MARANZANA, G, PERRY, I and MAILLET, D (2004). Mini - and micro-channels: influence of axial conduction in the walls. *International Journal of Heat and Mass Transfer*, **47**, 3993-4004.
- MCCREEDY, T (2000). Fabrication techniques and materials commonly used for the production of microreactors and micro total analytical systems. *Trend in Analytical Chemistry*, **19** (6), 396-401.

- MISHAM, Y, et al. (2007). Effects of developing flow and thermal regime on momentum and heat transfer in micro-scale heat sink. *International Journal of Heat and Mass Transfer*, **50**, 3100-3114.
- MOFFAT, RJ (1988). Describing the uncertainties in Experimental Results. *Experimental Thermal and Fluid Science*, **1**, 3-17.
- MORINI, GL (2006). Scaling effects for liquid flows in microchannel. *Heat Transfer Engineering*, **27** (4), 64-73.
- MORINI, GL (2004). Single-phase convective heat transfer in microchannels: a review of experimental results. *International Journal of Thermal Sciences*, **43**, 631-651.
- NATRAJAN, VK and CHRISTENSEN, KT (2000). Non-intrusive measurements of convective heat transfer in smooth and rough wall microchannels: laminar flow. *Journal of Experimental Fluids*, **49**, 1021-1037.
- OBOT, NT (2002). Toward a better understanding of friction and heat/mass transfer in microchannels - a literature review. *Microscale Thermophysical Engineering*, **6**, 155-173.
- PAPAUTSKY, I, AMEEL, T and FRAZIER, AB (2001). A review of laminar single-phase flow in microchannels. In: *2001 ASME International Mechanical Engineering Congress and Exposition*, New York, 11-16 November 2001. New York.
- PENG, XF and PETERSON, GP (1996). Convective heat transfer and flow friction for water flow in microchannel structures. *International Journal of Heat and Mass Transfer*, **39** (12), 2599-2608.
- PENG, XF and PETERSON, GP (1995). The effects of thermofluid and geometric parameters on convection of liquids through rectangular microchannels. *International Journal of Heat and Mass Transfer*, **38** (4), 755-758.
- PHILLIPS, RJ (1987). *Forced convection, liquid cooled, microchannel heat sinks*. MS Thesis, Cambridge, Massachusetts Institute of Technology.
- PHILLIPS, RJ (1990). *Microchannel heat sinks, Advances in Thermal Modelling of Electronic Components and Systems*. New York, NY: Hemisphere Publishing Corporation.
- POPIEL, Co and WOJTKOWIAK, J (1998). Simple formulas for thermophysical properties of liquid water for heat transfer calculations (from 0degC to 150degC). *Journal of Heat Transfer*,.
- QU, W and MUDAWAR, I (2002). Analysis of three dimensional heat transfer in microchannel heat sinks. *International Journal of Heat and Mass Transfer*, **45**, 3973-3985.
- QU, W and MUDAWAR, I (2002). Experimental and numerical study of pressure drop and heat transfer in a single-phase microchannel heat sink. *International Journal of Heat and Mass Transfer*, **45**, 2549-2565.
- RAO, PN and KUNZRU, D (2007). Fabrication of microchannels on stainless steel by wet chemical etching. *Journal of Micromechanics and Microengineering*, 99-106.
- SHAH, SL (2006). Advances in Science and Technology of Compact Heat Exchangers. *Heat Transfer Engineering*, **27** (5), 3-22.
- SHAH, RK and LONDON, AL (1978). *Laminar Flow Forced Convection in Ducts, Supplement 1 to Advances in Heat Transfer*. New York, Academic Press.
- SHAH, RK and LONDON, AL (1978). *Laminar Flow Forced Convection in Ducts*. New York, Academic Press.

- SHEN, S (1999). A numerical study of inverse heat conduction problems. *Computers and Mathematics with Applications*, **38**, 173-188.
- SHEN, S, et al. (2006). Flow and heat transfer in microchannels with rough wall surface. *Energy Conversion and Management*, **47** (11-12), 1311-1325.
- SOLOVITZ, SA, STEVANVOIC, LD and BEAPRE, RA (2006). Microchannels take heatsinks to the next level. *Power Electronics Technologies*, **Nov 2006**, 14-20.
- STEINKE, ME and KANDLIKAR, SG (2005). Single-phase liquid friction factors in microchannels. In: *Second International Conference on Microchannel and Minichannels*, June 13-15. Toronto.
- TSO, CP and MAHULIKAR, SP (2000). Experimental verification of the role of the Brinkman Number in microchannels using local parameters. *International Journal of Heat and Mass Transfer*, **43**, 1837-1849.
- TUCKERMAN, DB and PEASE, RFW (1981). High-performance heat sinking for VLSI. *IEEE Devices Letters*, **EDL-2** (2), 126.
- WANG, G, HAO, J and CHENG, P (2008). An experimental and numerical study of forced convection in a microchannel with negligible axial heat conduction. *International Journal of Heat and Mass Transfer*, **38**, 1016-1020.
- WANG, BX and PENG, XF (1994). Experimental investigation on liquid forced-convection heat transfer through microchannels. *International Journal of Heat and Mass Transfer*, **37** (1), 73-82.
- WEILIN, Q, MALA, M and DONGQING, L (2000). Pressure-driven water flows in trapezoidal silicon microchannels. *International Journal of Heat and Mass Transfer*, **43**, 353-364.
- WEISBERG, A and BAU, HH (1992). Analysis of microchannel for integrated cooling. *International Journal of Heat and Mass Transfer*, **35**, 2465-2474.
- WHITE, FM (2005). *Fluid Mechanics*. Fifth Edition ed., New York, McGraw-Hill.
- ZHANG, HY, et al. (2005). Single-phase cooled microchannel heat sink for electronic packages. *Applied Thermal Engineering*, **25**, 1472-1487.

APPENDIX A

CALCULATION OF DIMENSIONAL PARAMETERS FOR THE MICROCHANNEL TEST SECTION

A1. INTRODUCTION

MatLab[®] code was written that iteratively determined the microchannel test section cross-sectional dimensions based on certain criteria/constraints, which was used during the design phase of the test sections.

A2. MATLAB[®] CODE

The MatLab[®] function below, received three inputs: H_s ; W_s ; and; $H_c \cdot W_c$. The function iterated and found an approximate solutions for H_c and W_c that satisfied α_c and α_s .

```
function [a, b] = itt(A, B, abDef)
%Initialise itteration Variables
AR = A/B;
a = 0;
b = a/AR;
ab = a*b;

%Do rough search, significance 0.1
while ab<abDef
    a = a+0.1;
    b = a/AR;
    ab = a*b;
end
%Fine itteration, significance 0.00001
while ab>abDef
    a = a-0.00001;
    b = a/AR;
    ab = a*b;
end
```

The main program calls the iteration function with a specified channel area ($H_c \cdot W_c$) and outputted the microchannel dimensions. The MatLab[®] code is shown below:

```
clc
clear all
close all
i=0;
```



```
%Constant base, ALWAYS
A = 1.5;
%This cycles constant
abDef = 0.25;

'      A      B      a      b      A_wallB_wallab
AR      ar      phi      Dh'

for B = 1:0.125:2
    i= i+1;
    data(i,1)=A;
    data(i,2)=B;
    [data(i,3), data(i,4)] =itt(A,B,abDef);
    data(i,5) = (data(i,1)-data(i,3))/2;
    data(i,6) = (data(i,2)-data(i,4))/2;
    data(i,7)= data(i,3)*data(i,4);
    data(i,8)= data(i,1)/data(i,2);
    data(i,9)= data(i,3)/data(i,4);
    data(i,10)= (data(i,3)*data(i,4))/(data(i,1)*data(i,2));
    data(i,11)= (4*data(i,3)*data(i,4))/(2*(data(i,3)+data(i,4)));

    size(i,1)= data(i,5);
    size(i,2)= data(i,3);
    size(i,3)= data(i,5);
    size(i,4)= data(i,6);
    size(i,5)= data(i,4);
    size(i,6)= data(i,6);

end

data
size
```

The output is shown in Table A1, where Φ is the volume fraction. From the results it was seen that all the wall thicknesses were above 0.2mm except for $H_c \cdot W_c = 1$ $H_s = 1$ and $H_c \cdot W_c = 1$ $H_s = 1.152$, these two dimensions were disregarded when considering the manufacturing of the microchannel test section. The channel sizes (H_c and W_c) were all above 0.4 mm therefore no constraints were required. The hydraulic diameter for all cases was below 1 mm which was required to be classified as a microchannel.

These dimensions for different dimensional parameters were used in the numerical analysis to determine which microchannel test sections should be manufactured as it is not possible to manufacture and test all the above case.

A3. CONCLUSION

MatLab[®] code was written that determined the test sections cross-section dimension based on the microchannel cross sectional area and the overall test section heights. The information obtained was used in the design phase of the test sections.



Table A1 Dimensional parameters of microchannel test section

W_s (mm)	H_s (mm)	W_c (mm)	H_c (mm)	W_s wall thickness (mm)	H_s wall thickness (mm)	A_c (mm ²)	a_s (-)	a_c (-)	Φ (-)	D_h (mm)
$A_c = 0.25$										
1.5	1	0.612	0.4082	0.4438	0.2959	0.25	1.5	1.5	0.1667	0.4899
1.5	1.125	0.577	0.433	0.4613	0.346	0.25	1.3333	1.3333	0.1481	0.4949
1.5	1.25	0.548	0.4564	0.4761	0.3968	0.25	1.2	1.2	0.1333	0.4979
1.5	1.375	0.522	0.4787	0.4889	0.4481	0.25	1.0909	1.0909	0.1212	0.4995
1.5	1.5	0.5	0.5	0.5	0.5	0.25	1	1	0.1111	0.5
1.5	1.625	0.48	0.5204	0.5098	0.5523	0.25	0.9231	0.9231	0.1026	0.4996
1.5	1.75	0.463	0.5401	0.5185	0.605	0.25	0.8571	0.8571	0.0952	0.4985
1.5	1.875	0.447	0.559	0.5264	0.658	0.25	0.8	0.8	0.0889	0.4969
1.5	2	0.43	0.577	0.534	0.711	0.25	0.75	0.75	0.0833	0.495
$A_c = 0.5$										
1.5	1	0.87	0.577	0.317	0.211	0.5	1.5	1.5	0.3333	0.693
1.5	1.125	0.82	0.612	0.342	0.256	0.5	1.333	1.333	0.2963	0.7
1.5	1.25	0.77	0.646	0.363	0.302	0.5	1.2	1.2	0.2667	0.704
1.5	1.375	0.74	0.677	0.381	0.349	0.5	1.091	1.091	0.2424	0.706
1.5	1.5	0.71	0.707	0.396	0.396	0.5	1	1	0.2222	0.707
1.5	1.625	0.68	0.736	0.41	0.445	0.5	0.923	0.923	0.2051	0.707
1.5	1.75	0.65	0.764	0.423	0.493	0.5	0.857	0.857	0.1905	0.705
1.5	1.875	0.63	0.791	0.434	0.542	0.5	0.8	0.8	0.1778	0.703
1.5	2	0.61	0.817	0.444	0.592	0.5	0.75	0.75	0.1667	0.7
$A_c = 0.75$										
1.5	1	1.06	0.707	0.22	0.146	0.75	1.5	1.5	0.5	0.849
1.5	1.125	1	0.75	0.25	0.188	0.75	1.333	1.333	0.4444	0.857
1.5	1.25	0.95	0.791	0.276	0.23	0.75	1.2	1.2	0.4	0.862
1.5	1.375	0.9	0.829	0.298	0.273	0.75	1.091	1.091	0.3636	0.865
1.5	1.5	0.87	0.866	0.317	0.317	0.75	1	1	0.3333	0.866
1.5	1.625	0.83	0.901	0.334	0.362	0.75	0.923	0.923	0.3077	0.865
1.5	1.75	0.8	0.935	0.349	0.407	0.75	0.857	0.857	0.2857	0.864
1.5	1.875	0.77	0.968	0.363	0.453	0.75	0.8	0.8	0.2667	0.861
1.5	2	0.75	1	0.375	0.5	0.75	0.75	0.75	0.25	0.857
$A_c = 1$										
1.5	1	1.22	0.817	0.138	0.092	1	1.5	1.5	0.6667	0.98
1.5	1.125	1.15	0.866	0.173	0.13	1	1.333	1.333	0.5926	0.99
1.5	1.25	1.1	0.913	0.202	0.169	1	1.2	1.2	0.5333	0.996
1.5	1.375	1.04	0.957	0.228	0.209	1	1.091	1.091	0.4848	0.999
1.5	1.5	1	1	0.25	0.25	1	1	1	0.4444	1
1.5	1.625	0.96	1.041	0.27	0.292	1	0.923	0.923	0.4102	0.999
1.5	1.75	0.93	1.08	0.287	0.335	1	0.857	0.857	0.381	0.997
1.5	1.875	0.89	1.118	0.303	0.379	1	0.8	0.8	0.3555	0.994
1.5	2	0.87	1.155	0.317	0.423	1	0.75	0.75	0.3333	0.99

APPENDIX B

NUMERICAL ANALYSIS USED TO AID THE MICROCHANNEL TEST SECTION DESIGN

B 1. INTRODUCTION

The numerical model was developed, validated and verified to ensure that the results obtained were credible and were similar to other published works. The results of all the numerical analyses were analysed to determine which three possible test sections should be fabricated and experimentally tested.

The CFD simulations were setup and performed in batches through a MatLab[®] base compiled program. The results were stored in text based files. Thereafter a post processing process was performed through MatLab[®] to obtain the results in a presentable manner.

B 2. NUMERICAL MODEL AND BOUNDARY CONDITIONS

The boundary condition for the numerical analysis, the governing equations and geometric test cases are discussed in this sub-section. The numerical models were setup and solved for each test case and the results were stored in a database which could be accessed at a later stage.

B 2.1. SIMULATION PARAMETERS

The simulation parameters for each test case are tabulated in Table B.1. The numerical model was setup based on these parameters.

Table B.1 Simulation and geometric parameter

q [W/cm ²]	10						
k_s [W/mK]	015	110	400				
Re [--]	070	125	250	500	1000	2000	2300
Test case	W_s [mm]	H_s [mm]	W_s/H_s [--]	W_c [mm]	H_c [mm]	W_c/H_c [mm]	$W_c \cdot H_c$ [mm ²]
1	1.500	1.000	1.500	0.612	0.408	1.500	0.250
2	1.500	1.125	1.333	0.577	0.433	1.333	0.250
3	1.500	1.25	1.200	0.548	0.456	1.202	0.250
4	1.500	1.375	1.091	0.522	0.479	1.090	0.250
5	1.500	1.500	1.000	0.500	0.500	1.000	0.250
6	1.500	1.625	0.923	0.48	0.52	0.923	0.250
7	1.500	1.75	0.857	0.463	0.54	0.857	0.250
8	1.500	1.875	0.800	0.447	0.559	0.800	0.250
9	1.500	2.000	0.750	0.433	0.577	0.750	0.250

B 2.2. GOVERNING EQUATIONS AND BOUNDARY CONDITIONS

The continuity, momentum and energy equations were solved using a commercial package, Fluent[®]. A convective-conduction simulation was setup with two domains, namely, the fluid and solid domain. The following assumptions were made for the numerical analysis:

- heat transfer and fluid flow was at steady state
- the flow was incompressible
- laminar flow was assumed for the entire Reynolds number range
- constant solid substrate material properties
- negligible radiation heat transfer effects
- all outer walls are perfectly adiabatic and all the energy from the solid substrate is transferred to the cooling fluid.
- smooth wall interface between the fluid and solid
- the fluid velocity was uniform at the entrance of the channel

Based on the above assumptions the continuity, momentum and energy equations for the fluid domain can be written as:

Continuity:

$$\rho_f \frac{\partial u_j}{\partial x_j} = 0$$

Equation B.1

Momentum:

$$\rho_f \frac{\partial u_j u_i}{\partial x_j} = \frac{\partial}{\partial x_j} \left(\mu_f \frac{\partial u_i}{\partial x_j} \right) + \frac{\partial}{\partial x_j} \left(\mu_f \frac{\partial u_j}{\partial x_i} \right) - \frac{2}{3} \frac{\partial}{\partial x_i} \left(\mu_f \frac{\partial u_k}{\partial x_k} \right) - \frac{\partial p_f}{\partial x_i}$$

Equation B.2

Energy:

$$\begin{aligned} \frac{\partial(\rho_f C p_f u_i T)}{\partial x_i} &= \frac{\partial}{\partial x_i} \left(k_f \frac{\partial T}{\partial x_i} \right) \\ &+ \mu_f \left(2 \left(\frac{\partial u_i}{\partial x_i} \right)^2 + \left(\frac{\partial u}{\partial y} + \frac{\partial v}{\partial x} \right)^2 \right) \\ &+ \left(\frac{\partial u}{\partial z} + \frac{\partial w}{\partial x} \right)^2 + \left(\frac{\partial v}{\partial z} + \frac{\partial w}{\partial y} \right)^2 \end{aligned}$$

Equation B.3

and for the solid domain

Momentum:

$$V_i = 0$$

Equation B.4

Energy:

$$k_f \frac{\partial T}{\partial x_j} = 0$$

Equation B.5

The interface between the solid and fluid interface was coupled by continuity in temperature and heat flux

$$q_f = q_s$$

Equation B.6

$$T_f = T_s$$

Equation B.7

where: u, v, w is the velocity, $x, y,$ is the dimensional parameter, V is the velocity, k_f is the thermal conductivity, ρ_f is the fluid density, T is the Temperature, μ_f is the viscosity, q is the heat flux, q_f is the heat flux of the fluid at the solid to fluid interface, q_s is the heat flux of the solid at the solid to fluid interface, T_f is the fluid temperature and T_s is the solid substrate temperature.

The fluid properties adopted in the numerical model were temperature dependant. The relation between the density, thermal conductivity, viscosity and specific heat to temperature were given by Popiel and Wojtkowiak (1998).

The numerical models were solved using Fluent® version 6.3.26.

All the boundary conditions for the computation domain were divided into two sections; thermal and dynamic boundary. The thermal boundary conditions for all outer walls of the solid substrate were adiabatic except for the bottom wall where there was a constant uniform inwards heat flux. The fluid inlet temperature was defined as constant uniformly distributed over the inlet region and the outlet boundary condition assumed that the fluid was fully thermally developed. This assumption does not introduce a large numerical error if the fluid is not fully thermally developed Qu and Mudawar (2002). The dynamic boundary conditions for the fluid domain assumes a no slip wall condition. The inlet velocity boundary condition was constant and uniformly distributed over the inlet area. The velocity was calculated from the Reynolds number (Re) and the inlet fluid temperature properties. The outlet boundary condition assumed that the flow was hydrodynamic fully developed.

B 3. VERIFICATION AND VALIDATION OF THE NUMERICAL MODEL

The numerical model was validated using results obtained from Qu and Mudawar (2002). The exact dimensions, materials, heat input and flow rates were used and then compared to the results obtained from the numerical model. The main difference in the modelling process was that Qu and Mudawar (2002) used constant fluid properties, whereas the fluid properties used in the numerical model were dependent on temperature. Qu and Mudawar (2002) also compared their results to experimental work done by Kawano et al. (1998). Before the comparison was performed a mesh refinement process was done to ensure mesh independence. The results of the mesh refinement are shown in Table B.2 and the mesh size was chosen as 412 500 cells since the percentage difference for the peak temperature and peak velocity was below 1%. The percentage difference was determined as shown in Equation B.8.

$$\begin{aligned} & \%difference \\ & = \left(\frac{parameter\ 1 - parameter\ 2}{\min(parameter\ 1, parameter\ 2)} \right) \cdot 100 \end{aligned} \quad \left| \begin{array}{l} \\ \\ \end{array} \right. \begin{array}{l} \\ \\ \text{Equation B.8} \end{array}$$

Where parameter 1 and parameter 2 refers to the maximum temperature in the solid substrate (T_{max}) or the maximum velocity in the fluid (V_{max}) for mesh size (i) and T_{max} or V_{max} for mesh size ($i+1$) respectively.

Table B.2 Mesh refinement results for thermal and momentum energy

Simulation Name	Mesh Size	T_{max} [°C]	% Difference (Temperature)	V_{max} [m/s]	% Difference (Momentum)
VM1520102515150	315 000	70.72		1.928	
VM2020152015100	275 000	68.89	2.656	1.897	1.634
VM2020152015150	412 500	68.9	0.015	1.892	0.264
VM2020152015200	550 000	68.73	0.247	1.885	0.371
VM2020202515150	540 000	68.96	0.335	1.892	0.371
VM2020202515200	720 000	68.84	0.174	1.885	0.371

The model was run for different Reynolds numbers and the outlet thermal resistance ($R_{t,out}$) was calculated.

$$R_{t,out} = \frac{T_{max} - T_{out}}{q} \quad \left| \text{Equation B.9} \right.$$

where T_{out} is the mean outlet fluid temperature

The results are shown in Figure B.1, it can be seen that the results do not vary by more than 10% from the result presented by Qu and Mudawar (2002). Therefore the physics of the model was validated.

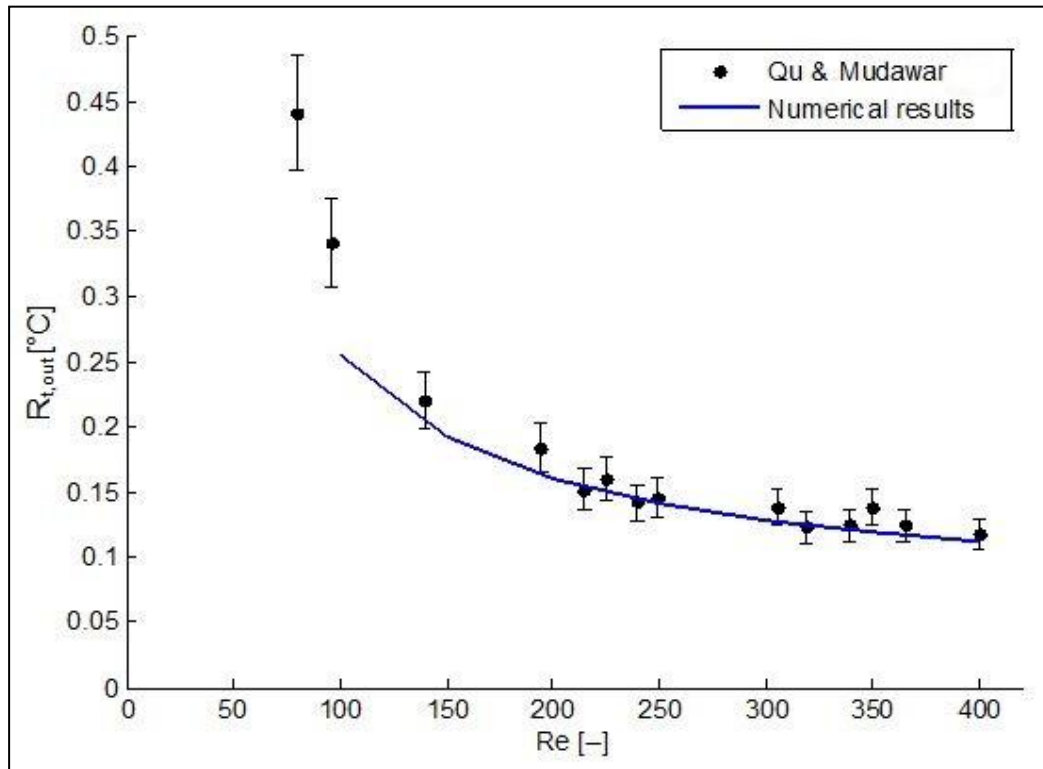


Figure B.1 Comparison between numerical predictions and experimental results (Qu and Mudawar (2002)) for the thermal resistance

A mesh independence study was performed again on the actual microchannel model. Two extreme cases with regard to the dimensional parameters and the maximum and minimum Reynolds numbers were tested. By performing the study for the extreme cases it was assumed that all the tests for the entire range were independent of the

mesh size. The peak temperature results are shown in Table B.3. The most efficient mesh size was 147 000 cells.

Table B.3 Mesh refinement results for thermal energy

File Name	Mesh Size	<i>Re</i> = 70		<i>Re</i> = 2300	
		T_{max}	% Difference	T_{max}	% Difference
Minimum Dimensional Parameter					
VM1010101010100	90000	78.79		28.70	
VM1515101010100	122500	78.96	0.046	29.23	0.177
VM1515101010120	147000	78.91	0.013	28.98	0.082
VM1515101010150	183750	78.88	0.008	28.93	0.019
VM2020151515100	250000	79.00	0.032	29.01	0.027
VM2525151515100	302500	78.98	0.004	29.35	0.114
Maximum Dimensional Parameter					
VM1010101010100	90000	78.13		28.82	
VM1515101010100	122500	78.28	0.041	29.15	0.110
VM1515101010120	147000	78.23	0.013	29.13	0.009
VM1515101010150	183750	78.22	0.005	29.07	0.019
VM2020151515100	250000	78.30	0.023	29.36	0.098

B 4. CONCLUSION

The numerical model used to aid in the design of the microchannel test section was discussed detailed in this section. The numerical model was validated against other published data and a mesh refinement procedure was followed to ensure the quality of the results obtained. The results of the numerical analysis are presented in Section 3.3.

APPENDIX C

ANALYTICAL ANALYSIS USED TO AID THE MICROCHANNEL TEST SECTION DESIGN

C 1. INTRODUCTION

An analytical study was performed on the selected microchannel geometry using conventional theory and correlations to verify the findings obtained from the numerical analysis and to determine the predicted fluid temperature difference over the test section. The Nusselt number is determined based on the Hausen correlation and the hydrodynamic pressure drop was calculated using the friction factor based on the Hagenbach's correction.

C 2. HEAT TRANSFER CALCULATIONS

An analytical calculation was performed to determine the Nusselt number and the average surface temperature of the microchannel. The calculations are presented in this section. The following assumptions are made to simplify the model:

- Steady state
- Constant heat flux along the length of the microchannel
- All four walls of the microchannel were evenly heated
- Bulk temperatures were used to determine the fluid properties
- Negligible axial conduction (this assumption will be verified in Section 5.2.1)
- One-dimensional heat convection
- The flow remains in the laminar regime

The hydraulic diameter of the channel was calculated as:

$$D_h = \frac{4 \cdot A_c}{P} = \frac{2 \cdot H_c \cdot W_c}{H_c + W_c} \quad \left| \text{Equation C.1} \right.$$

where A_c is the channel cross sectional area, P is the perimeter of the channel, H_c is the height of the channel and W_c is the width of the channel.

Cross sectional area of the channel:

$$A_c = H_c \cdot W_c \quad \left| \text{Equation C.2} \right.$$

Surface area of channel and fluid interface:

$$A_s = 2 \cdot (H_c + W_c) \cdot L_s \quad \left| \text{Equation C.3} \right.$$

where L_s is the length of the microchannel

The average temperature difference between the fluid outlet and inlet:

$$T_{dif} = T_{out} - T_{in} \quad \left| \text{Equation C.4} \right.$$

where T_{out} and T_{in} are the mean inlet and outlet fluid temperatures.

The bulk temperature of the fluid (all fluid properties will be taken at this temperature):

$$T_{bulk} = \frac{T_{out} + T_{in}}{2} \quad \left| \text{Equation C.5} \right.$$

The average outlet temperature is calculated from the first law of thermodynamics:

$$T_{out} = T_{in} + \frac{q}{\dot{m} \cdot Cp_f} \quad \left| \text{Equation C.6} \right.$$

where \dot{m} is the mass flow rate and Cp_f is the specific heat of the working fluid

The above equation requires T_{bulk} to determine Cp_f , but T_{bulk} is dependent on T_{out} , therefore an iterative process was used to determine T_{out} .

The average fluid velocity:

$$V = \frac{Re \cdot \mu_f}{\rho_f \cdot D_h} \quad \left| \text{Equation C.7} \right.$$

where μ_f is the viscosity and ρ_f is the density of the working and Re is the Reynolds number.

The mass flow rate:

$$\dot{m} = \rho_f \cdot A_c \cdot V \quad \left| \text{Equation C.8} \right.$$

The Prandtl number:

$$Pr = \frac{\mu_f \cdot Cp_f}{k_f} \quad \left| \text{Equation C.9} \right.$$

where k_f is the thermal conductivity of the fluid

The thermal developing length is:

$$L_t = 0.05 \cdot Re \cdot Pr \cdot D_h \quad \left| \text{Equation C.10} \right.$$

The Graetz number was used in calculating the mean developing Nusselt number:

$$G_z = \frac{Re \cdot Pr \cdot D_h}{L_t} \quad \left| \text{Equation C.11} \right.$$

The Hausen correlation was used to determine the mean developing Nusselt number:

$$Nu_m = Nu_\infty + K_1 \cdot \left(\frac{G_z}{1 + K_2 \cdot G_z^b} \right) \quad \left| \text{Equation C.12} \right.$$

where $K_1 = 0.14$; $K_2 = 0.05$; $b = 2/3$; $Nu_\infty = 3.9$ for $A_c = 1.5$, $Nu_\infty = 3.61$ for $A_c = 1$, $Nu_\infty = 3.7$ for $A_c = 0.75$, Kandlikar et al. (2004)

The mean convective heat transfer coefficient:

$$h_m = \frac{k_f \cdot Nu_m}{D_h} \quad \left| \text{Equation C.13} \right.$$

From this the mean surface temperature can be found by:

$$T_s = T_{bulk} + \frac{q}{h_m \cdot A_s} \quad \left| \text{Equation C.14} \right.$$

C 3. HYDRODYNAMIC CALCULATIONS

The pressure drop calculations are in two parts: firstly, when the flow is fully developed and secondly, when the flow is developing within the microchannel test section.

The Poiseuille number for fully developed flow is determined from an empirical equation suggested by (Kandlikar et al. (2004)):

$$Po = f \cdot Re = 24(1 - 1.3553 \cdot \alpha_c + 1.9467 \cdot \alpha_c^2 - 1.7013 \cdot \alpha_c^3 + 0.9564 \cdot \alpha_c^4 - 0.2537 \cdot \alpha_c^5) \quad \left| \text{Equation C.15} \right.$$

where α_c is the aspect ratio of the channel and f is the friction factor.

Therefore:

$$f = \frac{Po}{Re} \quad \left| \text{Equation C.16} \right.$$

The hydrodynamic entrance length is calculated:

$$L_h = 0.05 \cdot Re \cdot D_h$$

Equation C.17

If $L_h < L$ then the flow is fully developed at the exit of the microchannel section and a correction incremental factor is used to determine the pressure drop.

The pressure drop in the channel can be expressed as:

$$\Delta p = \frac{2 \cdot f_{app} \cdot \rho_f \cdot V^2 \cdot L_s}{D_h}$$

Equation C.18

The difference between the apparent friction factor (f_{app}) and the fully developed friction factor (f) can be expressed in terms of an incremental pressure defect:

$$K(l) = (f_{app} - f) \cdot \frac{4 \cdot L_s}{D_h}$$

Equation C.19

Therefore combining Equation C.18 and Equation C.19 the pressure drop can be expressed as:

$$\Delta P = \frac{2 \cdot (f \cdot Re) \cdot \mu_f \cdot U \cdot L_s}{D_h^2} + K(l) \frac{\rho_f \cdot V^2}{2}$$

Equation C.20

where $K(l)$ is dependant of the aspect ratio and given by (Kandlikar et al. (2004)):

$$K(l) = 0.6796 + 1.2197 \cdot \alpha_c + 3.3089 \cdot \alpha_c^2 - 9.5921 \cdot \alpha_c^3 + 8.9089 \cdot \alpha_c^4 - 2.9959 \cdot \alpha_c^5$$

Equation C.21

If $L_h > L_s$ then the flow in the channel is developing through the entire length of the channel.

Then the pressure drop over the channel is expressed as:

$$\Delta p = \frac{2 \cdot f_{app} \cdot \rho_f \cdot U^2 \cdot L_s}{D_h}$$

Equation C.22

Where f_{app} is obtained from Table C.1 where $L^+ = \frac{L(x)/D_h}{Re}$:

**Table C.1 Laminar flow friction factor in the entrance region of rectangular ducts
Kandlikar et al. (2004)**

L^+	$f_{app} Re$			
	$\alpha_c = 1$	$\alpha_c = 0.5$	$\alpha_c = 0.2$	$\alpha_c \leq 0.1$ $\alpha_c \geq 10$
0	142	142	142	287
0.001	111	111	111	112
0.003	66.0	66.0	66.1	67.5
0.005	51.8	51.8	52.2	53.0
0.007	44.6	44.6	45.3	46.2
0.009	39.9	40.0	40.6	42.1
0.01	38.0	38.2	38.9	40.4
0.015	32.1	32.5	33.3	35.6
0.02	28.6	29.1	30.2	32.4
0.03	24.6	25.3	26.7	29.7
0.04	22.4	23.2	24.9	28.2
0.05	21.0	21.8	23.7	27.4
0.06	20.0	20.8	22.9	26.8
0.07	19.3	20.1	22.4	26.4
0.08	18.7	19.6	22.0	26.1
0.09	18.2	19.1	21.7	25.8
0.1	17.8	18.8	21.4	25.6
0.2	15.8	17.0	20.1	24.7
>1.0	14.2	15.5	19.1	24.0

C 4. CONCLUSION

The analytical model used to aid in the design of the microchannel test section was discussed detailed in this section. The analytical models used the Hausen correlation to determine the Nusselt number and the Hagenbach's correlation to determine the pressure drop over the test section. The results of the analytical analysis are presented in Section 3.4.

APPENDIX D

MICROCHANNEL TEST SETUPS AND ARRANGEMENTS

D1. INTRODUCTION

An overview of microchannel test setups, arrangements and test sections found in literature are presented in this section. The literature review was performed which aided in the design of both the test facility and the test sections. Microchannel test setups have commonalities, namely: a pressure gradient must be generated over the test sections, therefore for the use of a pump, heat added to the test section, the flow rate must be determined; the pressure drops and temperatures must be measured.

D2. LITERATURE STUDY

Misham et al. (2007) designed an aluminium microchannel array test section with a polycarbonate or sapphire cover, this allowed the use of an infrared camera to monitor the temperatures as shown in Figure D.1. The channels were manufactured using a sawing process. Bulk inlet and outlet manifolds were used and the heater was manufactured from a chemical vapour deposition technique.

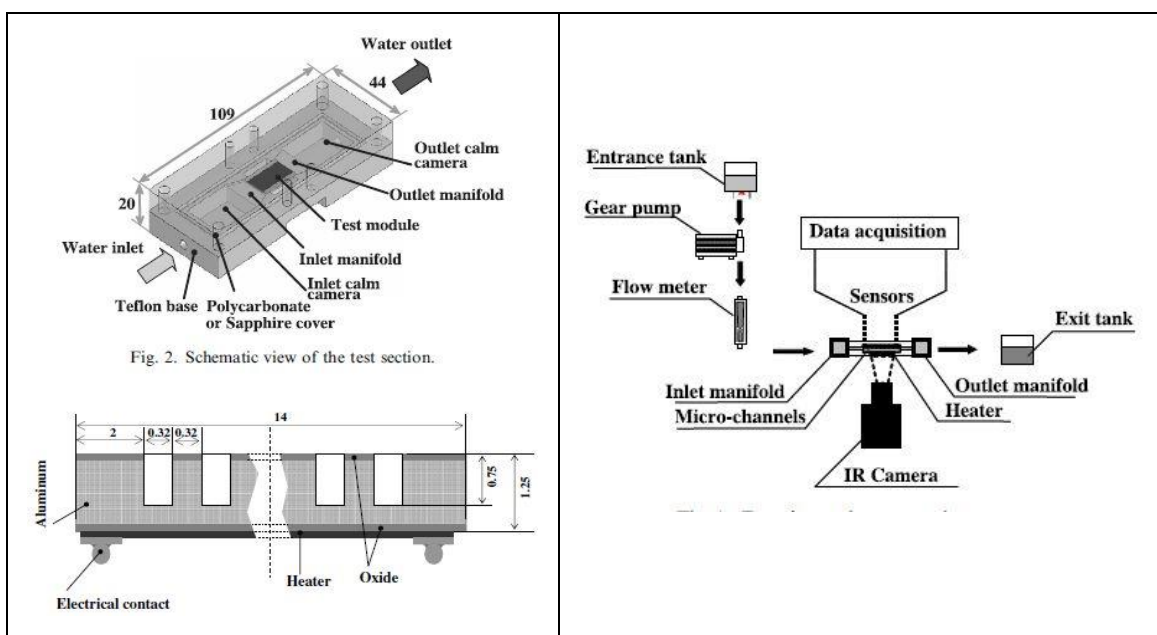


Figure D.1 Microchannel test section and test setup Misham et al. (2007)

Wang, Hao and Cheng (2008) tested a silicon trapezoidal test section that was heated by 15 microheaters. An open loop experimental setup was used as shown in Figure D.2, water flowed through a degassing unit, constant temperature bath, needle valve and then into the test section. A Labview[®] based data acquisition system was used to log the data.

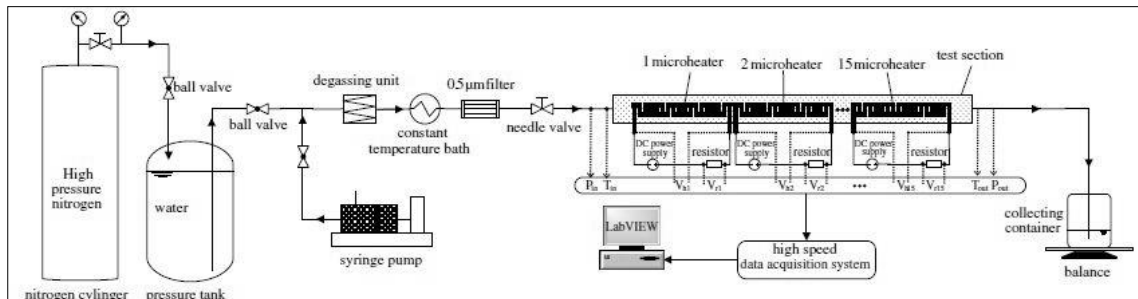


Figure D.2 Experimental test loop Wang, Hao and Cheng (2008)

Tso and Mahulikar (2000) used a simple experimental setup to perform tests to determine the effects of the Brinkman number. The test setup used an elevated tank that was kept at a constant level and a valve below the tank was adjusted to obtain the desired flow rates. The flow rates were measured using a glass beaker and a stop watch. A variable transformer supplied power to the test section heater. A strip heater was strapped to the aluminium test section supplying a constant heat flux.

Zhang et al. (2005) performed test on an aluminium array microchannel test section as shown in Figure D.3. A gear pump was used to pump the fluid and two variable area flow meters were used to measure the flow rate. The pressure drop over the array of microchannels was measured between the inlet and outlet plenum. The thermal test chip, that generated the heat, consisted of four equal resistive films with a diode sensor to measure the heaters temperature.

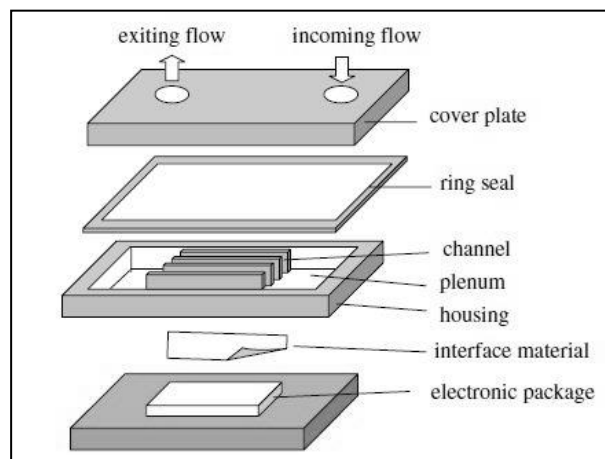


Figure D.3 Schematic diagram of a liquid cooling concept Zhang et al. (2005)

Jiang, Hao and Shi (2008) tested a rectangular copper microchannel. The test setup is shown in Figure D.4. Fluid was pumped through a control valve, flow meter and then into the test section. The water temperature in the liquid reservoir was kept constant using a thermal bath. The test section, as shown in Figure D.5, consisted of a copper

block heating base that housed 24 cartridge heaters, a thermal conductor, which measured the heat flux, and the microchannel test section. The entire test section was cast into Epotherm[®] to insulate and seal the microchannel.

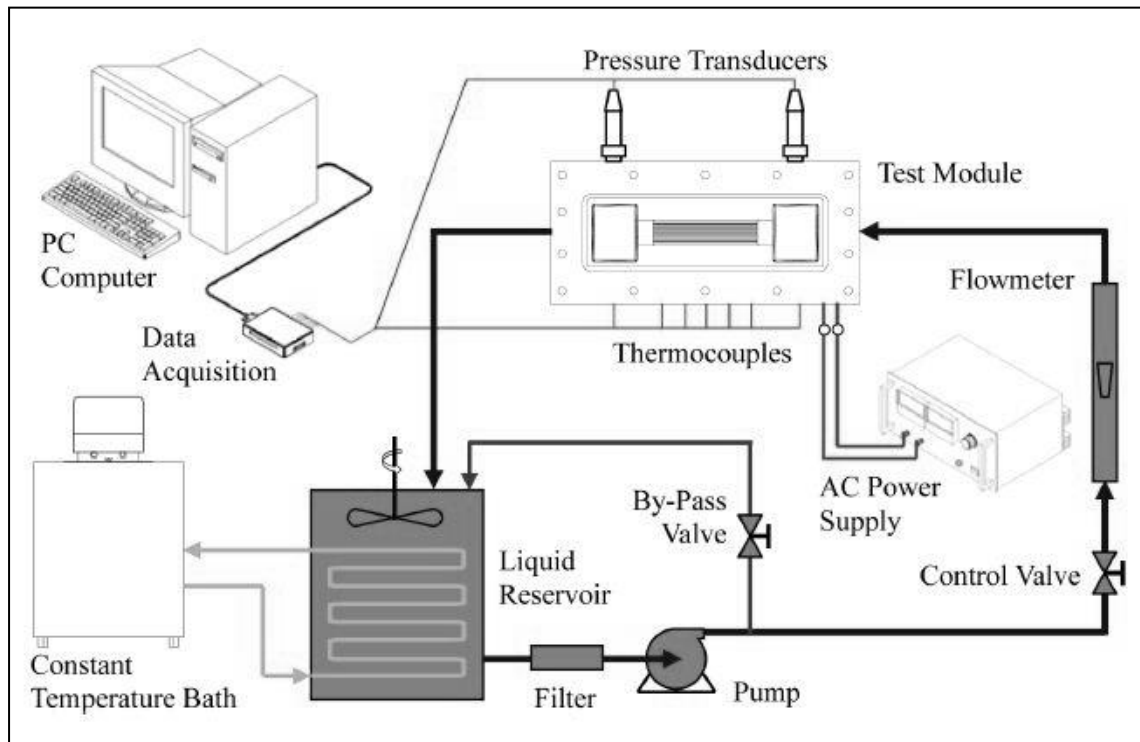


Figure D.4 Test setup Jiang, Hao and Shi (2008)

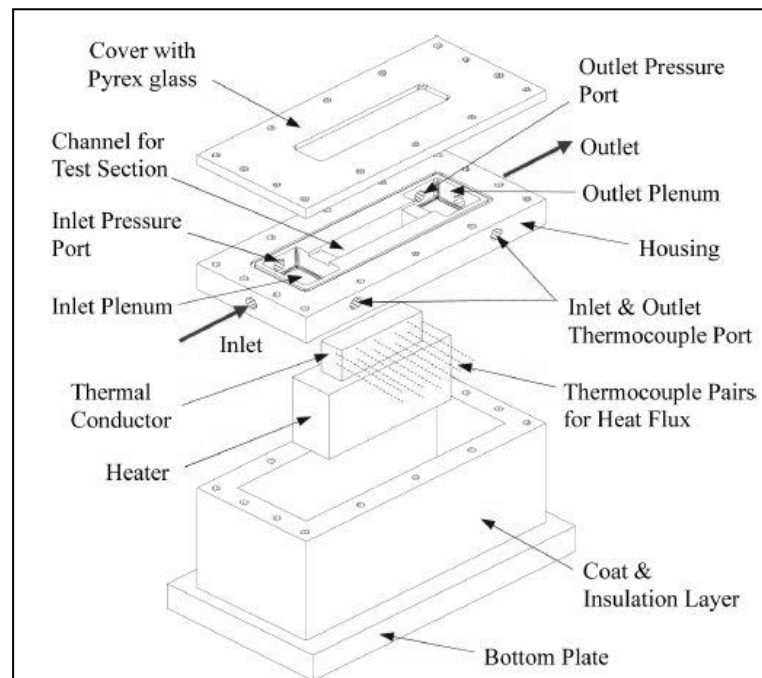


Figure D.5 Test section Jiang, Hao and Shi (2008)

Qu and Mudawar (2002) tested an array of microchannels fabricated from copper and covered with a polycarbonate lid. The test setup and test section is shown in Figure D.6 and Figure D.7. The test section was heated in a unique manner by using a copper

section with separated fins, this was done to ensure that a constant heat flux was obtained.

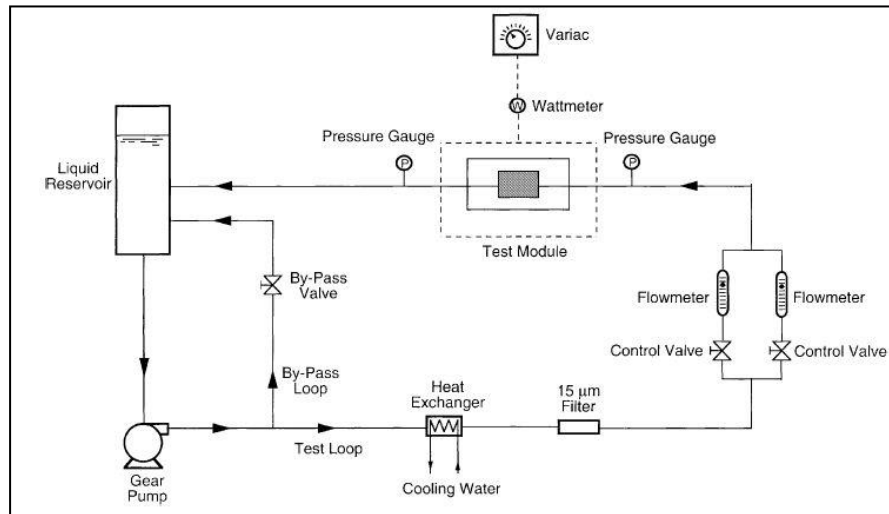


Figure D.6 Set up Qu and Mudawar (2002)

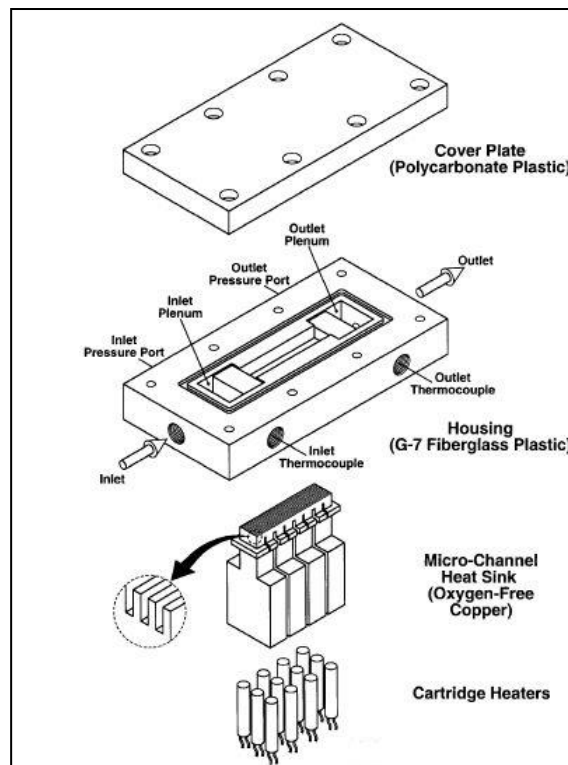


Figure D.7 Test section Qu and Mudawar (2002)

Huang et al. (2014) tested a microchannel array at Reynolds numbers ranging from 15 to 90. The test section consisted of a heater, copper plate and a microchannel array fabricated from PDMS as shown in Figure D.8. Molecule-based temperature sensors, Rhodamine B/DI water and Ru(bpy)/dope, were applied to the water and the microchannels walls were painted with a temperature sensitive paint. The working fluid and the walls of the microchannel changed colour depending on the temperature, which

was then recorded via a camera. The fluid was pumped through the test section using a syringe pump.

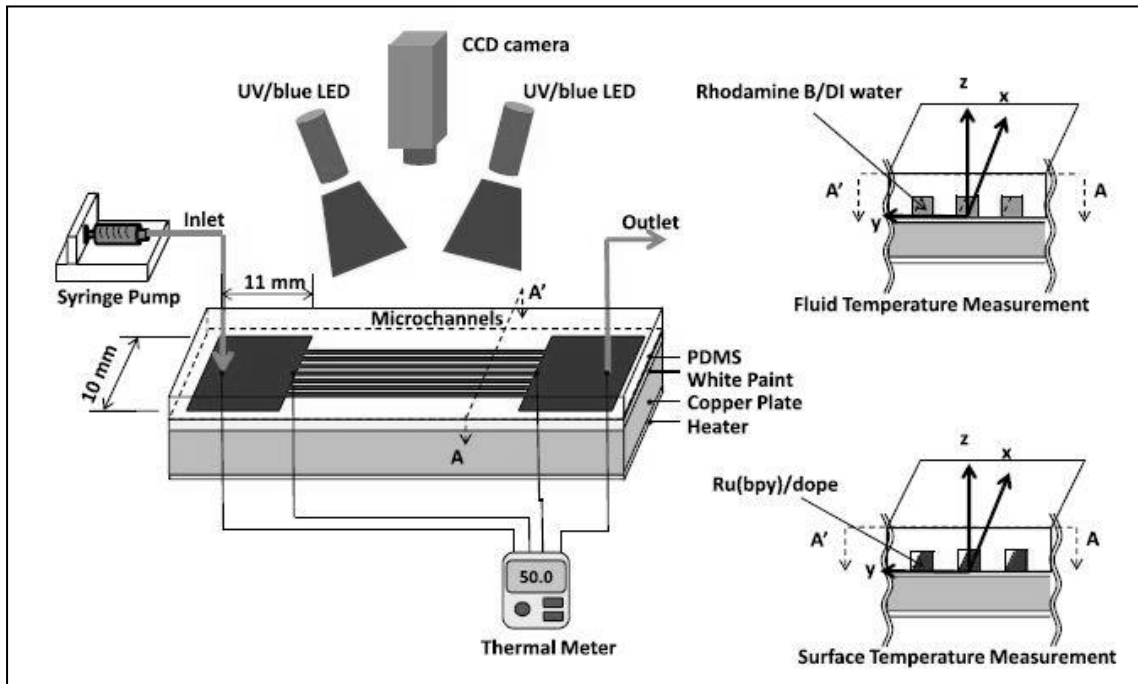


Figure D.8 Test section and test setup Huang et al. (2014)

D3. CONCLUSION

An overview of microchannel test setups, arrangements and test sections found in literature was presented. Commonalities exist between test setup and test sections and the literature overview aided in the design of both the test facility and the test sections.

APPENDIX E

OVERVIEW OF PRIOR TEST SECTION DESIGNS CONSIDERED IN THIS INVESTIGATION

E1. INTRODUCTION

Three different revisions of the test section assembly designs were built and tested. A general overview of revision one and two are presented in this section. The problems experienced with these test section assemblies were as follows: inability to position the thermocouples accurately; water leaks and; uneven heat flux distribution. Modifications were made to each revised test section to improve on the design.

E 2. TEST SECTION DESIGN REVISION 1

Test section design revision 1 assembly is shown in Figure E.1. The assembly process involved setting all the components: the microchannel; the microchannel lid; the heater; the heater base; the inlet and outlet pipes, into a complex custom designed clamping jig. Wax cores were used to keep the water flow passages open and the entire assembly was cast into resin. Once the resin had cured the jig was removed and the wax was removed by heating the test section assembly. Holes were drilled through the resin so that thermocouples could be place on the top and two side walls.

The following problems arose during the assembly and testing: the holes drilled for the thermocouple wires did not align exactly with the channel; water leaked between the microchannel and the lid; it was difficult and cumbersome to remove all the wax and it left an oily layer on the wall surfaces. The main disadvantage with this test section assembly layout was that it could not be disassembled and re-assembled due to the permanent curing of the resin.

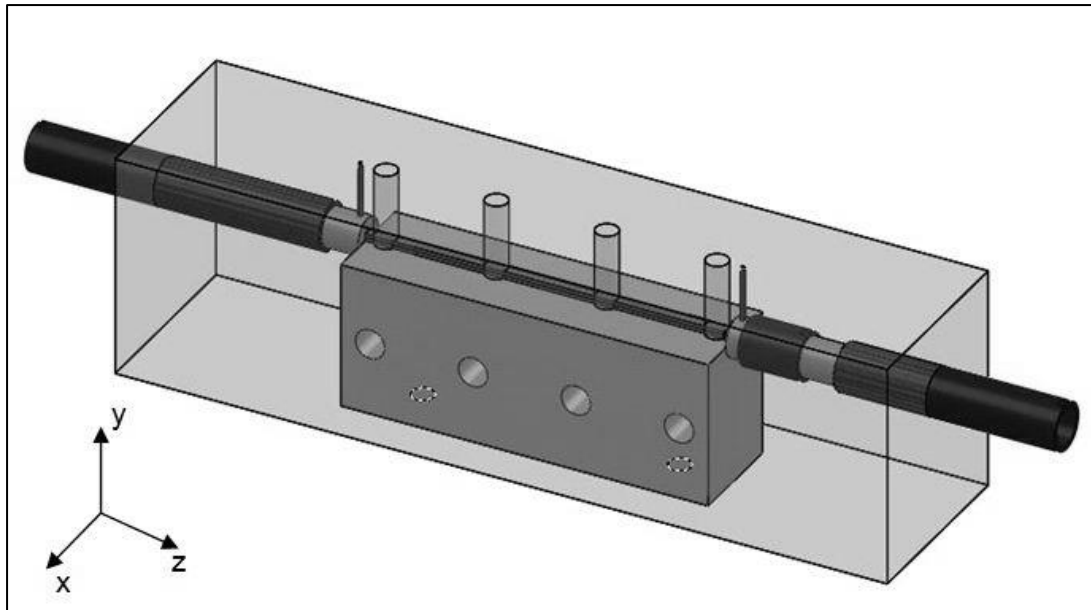


Figure E.1 Complete test section – Revision 1

A new revised test section assembly concept was required which allowed easy disassembly and re-assembly which negated the use of a casting resin. The positioning of the thermocouples had to be re-envisioned and the leaking between the microchannel and the lid had to be addressed.

E 3. TEST SECTION DESIGN REVISION 2

Test section design revision 2 is shown in Figure E.2 which is more similar to the final design apart from the heating element. The heater element used was fabricated from four lengths of #40 gauge constantan wire which was soldered together at each end. The stainless steel lid of the micro channel was glued to the top half while the microchannel was glued to the bottom half using thermal conductive glue. The inlet and outlet manifolds were similar as described in the final test section design apart from small dimensional changes.

The short falls of this test section were: the heater element did not provide a constant evenly distributed heat flux; and the electrical current flowing through the heating element was too large which caused heater burnout after about 20 hours of testing. Therefore the main problems with the test section was heater related, therefore a third revision test section was design and fabricated.

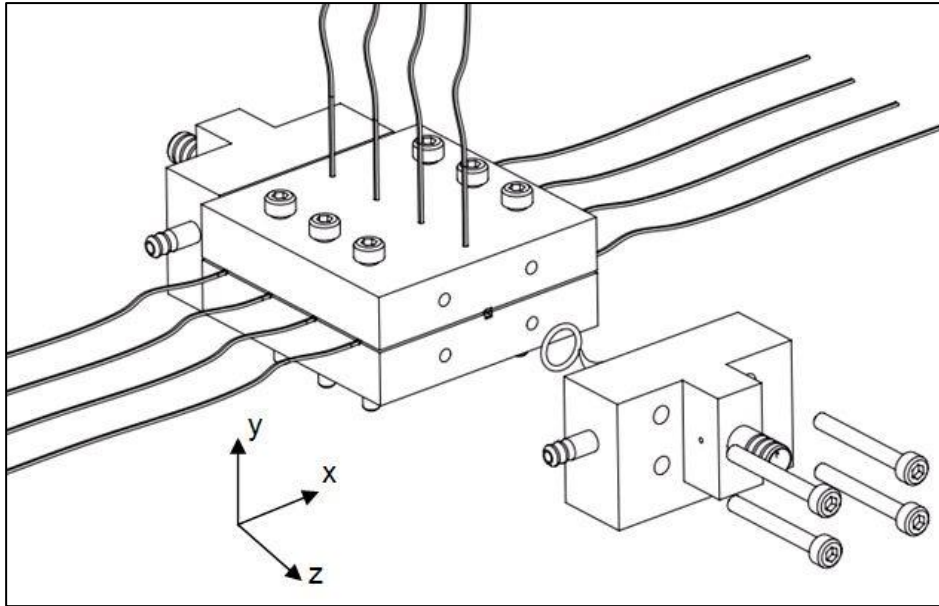


Figure E.2 Complete test section – Revision 2

E4. CONCLUSION

A general overview of revision one and two of the test sections were presented in this section. Problems were experienced with revision one and two test section assemblies and were as follows: inability to position the thermocouples accurately; water leaks and; uneven heat flux distribution. Modifications were made to each revised test section to improve on the design with revision 3 being the final.

APPENDIX F

MICROCHANNEL FABRICATION TECHNIQUES

F1. INTRODUCTION

The use of mini or micro channels in the commercial industry, has been limited due to high fabrication costs and is mainly found only in high-end products. The conventional method of fabrication does not suffice for small microchannels and therefore alternative methods have been developed Dixit and Ghosh (2015). A brief literature study on different micro fabrication techniques are discussed in this section.

F2. LITERATURE STUDY

Micro fabrication techniques have evolved over the last decade Kandlikar and William (2003). A summary of the micro fabrication techniques are shown in Figure F.1. The batch technologies are generally used in the mass production of micro and mini channels whereas the shop techniques are mainly used for one-off fabrication, such as for research test sections.

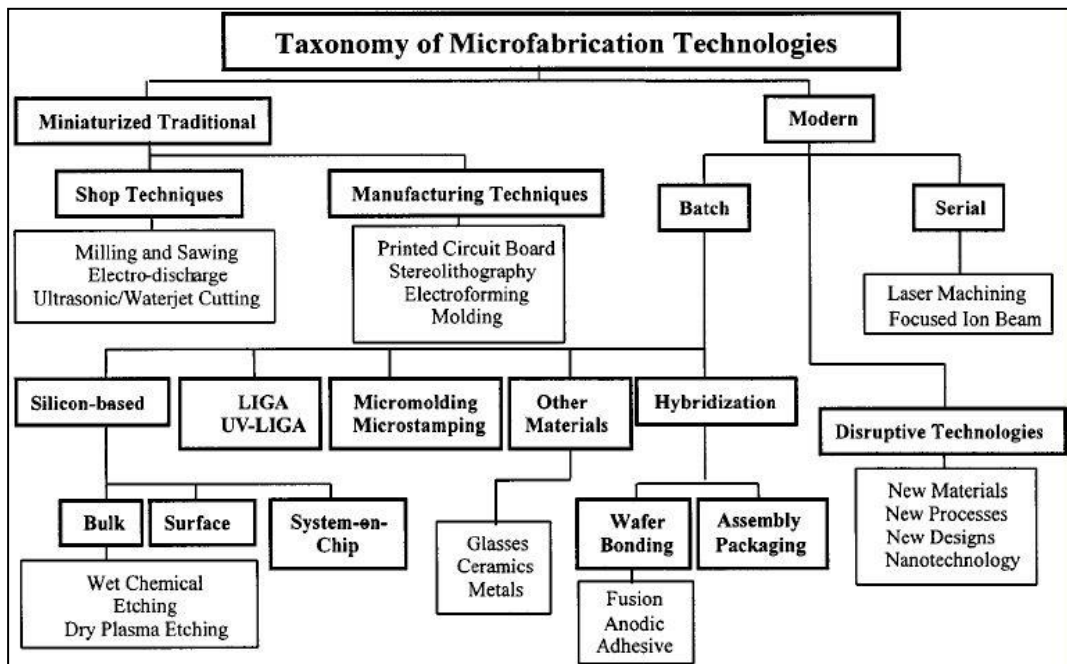


Figure F.1 Taxonomy of micro fabrication techniques Kandlikar and William (2003)

McCreedy (2000) reviewed common techniques used to fabricate microreactor and micro total analytical systems. Etching processes are most common with small differences existing between the techniques. Photolithography, wet etching and radiation-induced etching are the most common. These fabrication techniques are most commonly used for glass and silicon substrate materials. Fabrication by moulding has become more common where a negative is made and then the channel is over moulded. All the above techniques require an additional top lid to close the channel. When a gluing process is used great care must be taken as the glue can enter the channel and block it.

Rao and Kunzru (2007) used a wet chemical etching process to fabricate microchannels with a width ranging from 0.14 mm to 0.24 mm and depth of 0.055 mm to 0.16 mm. The channel side walls were sloped and the bottom corners had large radii. A resist stencil was placed on top of the stainless steel and the material was placed in etching solution, the etching time ranged from 90 minutes to 200 minutes.

Zhang et al. (2005) fabricated two microchannel heat sinks with a foot print of 10 x 10 mm² and 12 x 12 mm² with channel widths of 0.2 mm and heights of 2 mm. The channels were manufactured into aluminium using micro-end-milling.

A low cost technique was suggested by Guerin et al. (1997) where the channels were fabricated using a photo plastic material (SU-8). The process allowed for micro structures of 100 µm – 200 µm and channel aspect ratios of 20. The process involved the fabrication of microchannel paths, which were layered on a base structure, i.e. silicone, gold, aluminium or stainless steel. Jo et al. (2000) fabricated channels using a similar technique but by using a polydimethylsiloxane elastomer. Unfortunately, the material of the microchannel is limited and therefore limiting the commercial application of the technique for heat transfer applications.

F3. CONCLUSION

Different micro fabrication techniques exist which have evolved over the last decade. Conventional machining on a micro scale and wet etching are the most commonly used methods for test section design for research purposes.

APPENDIX G

TEST SECTION INSULATION CALCULATIONS

G1. INTRODUCTION

The test sections must be insulated to limit the amount of heat that gets transferred to the environment. Therefore a suitable insulation material is selected and size of insulation is determined in this section. Ideally the amount of heat loss to the environment must be kept to a minimum but it was decided that a 1 % loss would suffice.

G2. INSULATION MATERIAL SELECTION AND CALCULATIONS

Isoboard[®] was used as the external insulation, as it has a low thermal conductivity ($k_{ins} = 0.03 \text{ W / mK}$) and it is readily available from a local supplier.

The following assumptions were made in calculating the required thickness of the insulation:

- A cylindrical geometry was used for the: microchannel test section; the test section housing; and the insulation material instead of the square geometry. This assumption simplified the calculations, but the selection of the radii for the different components were conservative therefore the actual insulation would be better than calculated.
- A surface temperature was assumed to be the average between the minimum and maximum temperatures in the microchannel test section (obtained from the CFD results)
- The test section was at steady state.

The insulation layers are shown in Figure G.1 and the assumed equivalent radii for each layer, with r_1 as the test section radius, r_2 as the test section housing radius and r_3 as the insulation radius.

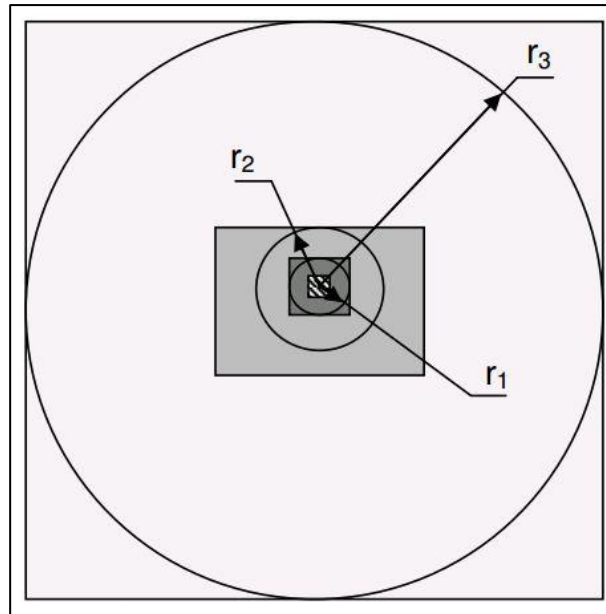


Figure G.1 Layers of insulation around the test section, r_1 = microchannel radius, r_2 = test section housing radius and r_3 = insulation radius

The constants used in the calculations are shown in Table G.1. A sample calculation is shown below:

Area (A_{ins}) of the outer insulation:

$$A_{ins} = 2 \cdot \pi \cdot r_3 \cdot L_s \quad \left| \text{Equation G1} \right.$$

where r_3 is the outer radius of the insulation, L_s is the length of the test section

Thermal resistance (R_{cond1}) of the plastic layer:

$$R_{cond1} = \frac{\ln\left(\frac{r_2}{r_1}\right)}{2 \cdot \pi \cdot k_{plast} \cdot L_s} \quad \left| \text{Equation G2} \right.$$

where r_2 is the outer radius of the test section housing, r_1 is the outer radius of the test section, k_{plast} is the thermal conductivity of the plastic used

Thermal resistance (R_{cond2}) of the Isoboard[®] insulation:

$$R_{cond2} = \frac{\ln\left(\frac{r_3}{r_2}\right)}{2 \cdot \pi \cdot k_{ins} \cdot L_s} \quad \left| \text{Equation G3} \right.$$

where k_{iso} is the thermal conductivity of the Isoboard[®]

Thermal resistance convection (R_{conv}) on the outer surface of the Isoboard[®] insulation:

$$R_{conv} = \frac{1}{2 \cdot \pi \cdot r_3 \cdot L_s \cdot h_{sur}} \quad \left| \text{Equation G4} \right.$$

where h_{sur} is the surrounding convective heat transfer coefficient

Total thermal resistance (R_{tot}):

$$R_{tot} = R_{cond1} + R_{cond2} + R_{conv} \quad \Bigg| \quad \text{Equation G5}$$

Therefore total heat loss through the epoxy and insulation:

$$Q_{loss} = \frac{T_s - T_{sur}}{R_{tot}} \quad \Bigg| \quad \text{Equation G6}$$

where T_s is the surface temperature of the test section and T_{sur} is the ambient temperature

Therefore percentage of heat loss through the epoxy and insulation:

$$\% \text{ loss} = \frac{Q_{in}}{Q_{loss}} \cdot 100 \quad \Bigg| \quad \text{Equation G7}$$

where \dot{q}_{input} is the heat input to the test section

From Table G.1, it can be concluded that the outer radius of the insulation must be 85mm to reduce the heat loss to approximately 1% of the total heat input.

Table G.1: Constants and calculations used to determine the required thickness of the insulation around the test section

k_{ins}	0.03	W/mK							
k_{plast}	0.2	W/mK							
h_{sur}	10	W/m ² K							
L_s	0.05	m							
r_1	1	mm							
r_2	13	mm							
T_s	52.5	°C							
T_{sur}	20	°C							
Q_{in}	7.5	W							
r_3		A_{ins}	R_{cond1}	R_{cond2}	R_{conv}	R_{tot}	Q_{loss}	% Loss	% Diff
mm	m	m ²	W/°C	W/°C	W/°C	W/°C	W	%	%
15	0.015	0.0047	40.82	287.33	21.22	349.38	0.093	1.2	
25	0.025	0.0079	40.82	341.53	12.73	395.09	0.082	1.1	13.1
35	0.035	0.0110	40.82	377.23	9.09	427.15	0.076	1.0	8.1
45	0.045	0.0141	40.82	403.90	7.07	451.80	0.072	1.0	5.8
55	0.055	0.0173	40.82	425.19	5.79	471.80	0.069	0.9	4.4
65	0.065	0.0204	40.82	442.92	4.90	488.64	0.067	0.9	3.6
75	0.075	0.0236	40.82	458.10	4.24	503.17	0.065	0.9	3.0
85	0.085	0.0267	40.82	471.38	3.74	515.95	0.063	0.8	2.5
95	0.095	0.0298	40.82	483.18	3.35	527.35	0.062	0.8	2.2
105	0.105	0.0330	40.82	493.80	3.03	537.65	0.060	0.8	2.0
115	0.115	0.0361	40.82	503.45	2.77	547.04	0.059	0.8	1.7
125	0.125	0.0393	40.82	512.30	2.55	555.67	0.058	0.8	1.6
135	0.135	0.0424	40.82	520.47	2.36	563.65	0.058	0.8	1.4
145	0.145	0.0456	40.82	528.05	2.20	571.07	0.057	0.8	1.3

G3. CONCLUSION

The insulation material and the size was determined by assuming the test section, housing and insulation as cylindrical geometries. An 85 mm thick insulation layer was required to limit the heat loss to under 1 % of the total heat input to the test sections.

APPENDIX H

UNCERTAINTY ANALYSIS

H 1. INTRODUCTION

The overall objective of this study was to obtain the common heat transfer and dynamic parameters, IE, the Nusselt number; the friction factor; the Colburn j-factor; and the Reynolds number. In order to obtain the accuracy of these parameters an uncertainty analysis is required. The errors obtained from the measurement equipment is the primary contributing factor which introduces uncertainty. The uncertainty is introduced from the following measured parameters: temperature; physical dimensions; differential pressure; flow rate; and electrical power input to the test section. The uncertainty of these parameters were quantified in Section H4. The uncertainty of the common heat transfer and dynamic parameters are determined in Section H5. An extensive analysis was performed, in Section H6, to obtain the uncertainty of the numerical model used to determine the heat transfer coefficient.

H 3. UNCERTAINTY THEORY

A method in determining the uncertainty was prescribe by Kline and McClintock (1953) whereby each variable is defined as the measured value plus an uncertainty, at specific odds. The uncertainty is not only valid for single point measurements but also multi point measurements. It is written in the mathematical form as:

$$x_i = x_i(\text{measured variable}) + \delta x_i(\text{uncertainty at 95\% confidence}) \quad \left| \text{Equation H 1} \right.$$

where x_i is the value of the measured variable, δx_i is the uncertainty of the measured variable with a 95 % of confidence.

Given that the result, R , is a function of several variables Moffat (1988) defined a general form of the equation of the results as:

$$R = \text{func}(x_1, x_2, \dots, x_n) \quad \left| \text{Equation H 2} \right.$$

The uncertainty of a single measurement on the result, R , would be:

$$\delta R = \frac{\partial R}{\partial x_i} \cdot \delta x_i$$

Equation H 3

The partial derivative of R with respect to x_i is known as the sensitivity coefficient, and is used to determine the effect that x_i has on the uncertainty. For a result, R , containing multiple independent variables the overall uncertainty can be determined using a root-sum-square method as described by Moffat (1988):

$$\delta R = \sqrt{\sum_{i=1}^n \left(\frac{\partial R}{\partial x_i} \cdot \delta x_i \right)^2}$$

Equation H 4

Equation H 4 is only valid if: each measurement is an independent variable; if measurements are repeated they show a Gaussian distribution; and the uncertainty of each measurement is expressed at the confidence level. If the δx_i is taken as the variance the Gaussian distribution is not a requirement.

If the result, R , is in the form of powers:

$$R = \text{func}(x_1^a, x_2^b, \dots, x_n^m)$$

Equation H 5

The relative uncertainty can be found as:

$$\frac{\delta R}{R} = \sqrt{\left(a \frac{\delta x_1}{x_1} \right)^2 + \left(b \frac{\delta x_2}{x_2} \right)^2 + \dots + \left(n \frac{\delta x_n}{x_n} \right)^2}$$

Equation H 6

The relative uncertainty, $\delta R/R$ is expressed as a percentage and x_i becomes the sensitivity coefficient.

H4. INSTRUMENTATION UNCERTAINTY

The uncertainty of the measured data influences the quality of the final results. In this sub section only the uncertainty of the measured data is considered, such as: the channel dimensions; the measured temperatures; the differential pressure drop; and the mass flow rate.

The uncertainty of the measured temperatures was calculated in Section 3.8.1 and a maximum of 0.113 °C was obtained over the calibrated temperature range. The maximum uncertainty was adopted for all temperature measurements as a more conservative approach. The uncertainty of the microchannel dimensions was 0.01 mm for all dimensions. The pressure transducer measuring uncertainty was 0.08% of rate pressure, which equates to an uncertainty of 0.08 kPa.

The uncertainty of the Coriolis flow meter is not constant over the measuring range. The uncertainty was provided by the flow meter supplier and is shown in Figure H.1. The

percentage of uncertainty of the measured value decreases as the flow rate increases and levels off at 0.01 % at a flow rate of 36,3 ml / min. At the minimum flow rate of 5 ml / min the uncertainty of the flow rate equates to 0.042 ml / min and at the maximum flow rate the uncertainty equates to 0.0125 ml / min.

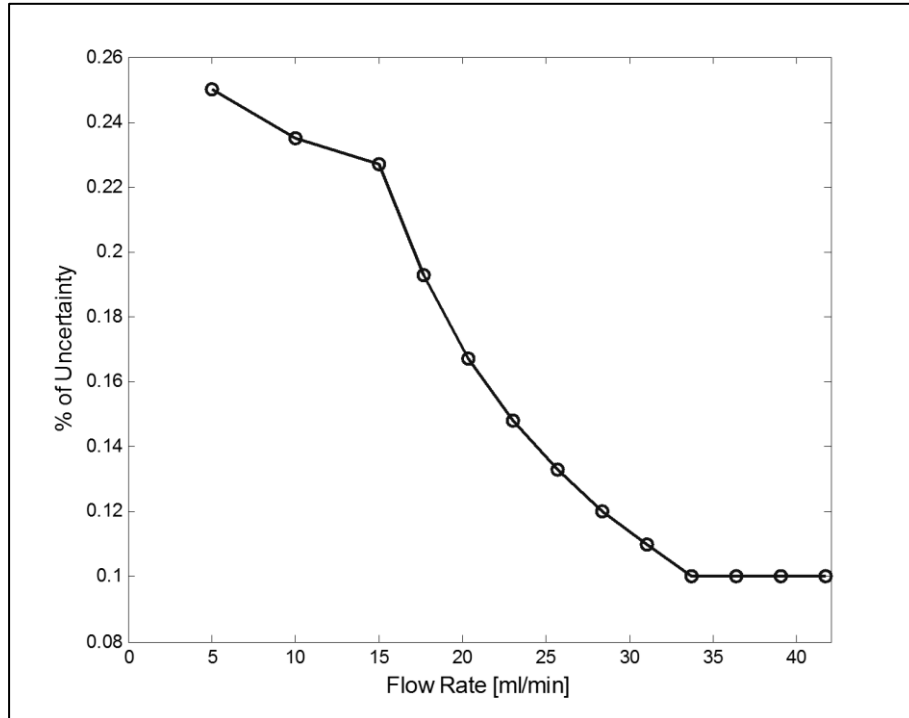


Figure H.1 Flow meter measuring uncertainty versus the measured flow rate

A constant potential difference and current was supplied to the heater of the test section. The volt meter had an accuracy of 0.05 % plus 3 mV and the amp meter had an accuracy of 0.1 % plus 10 mA, but the volt and amp meter had a display reading of 0.01 and thus was the limiting factor in determining the uncertainty. A measuring uncertainty was adopted for the potential difference and current as 0.01 V and 0.01 A respectively.

Table H.1 summarises the uncertainty of the measured parameters:

Table H.1 Measured parameter uncertainty summary

Measured Parameter	Uncertainty
Temperature	0.113 °C
Dimensions	0.01 mm
Pressure	0.08 kPa
Flow rate	0.042 – 0.013 ml / min
Voltage	0.01 V
Current	0.01 A

H5. UNCERTAINTY OF COMMON PARAMETERS

The uncertainty of the Reynolds number, Prandtl number, friction factor, Colburn j-factor, heat transfer coefficient and the Nusselt number are determined in this sub section for the lowest to the highest measuring range.

Uncertainty of Fluid Properties:

All the fluid properties and uncertainties were calculated from the equations set out by Popiel and Wojtkowiak (1998). The uncertainties are given in Table H.2

Table H.2 Uncertainty of the fluid properties

Property	Uncertainty [%]
Density	0.003
Specific heat	0.04
Thermal conductivity	2
Dynamic viscosity	1

Inlet and Outlet Fluid Temperatures:

The mean inlet or outlet fluid temperature were determined using two thermocouples at each, and was calculated accordingly:

$$T_{in} = \frac{T_{in,1} + T_{in,2}}{2} \quad \left| \text{Equation H 7} \right.$$

Each thermal couple had an uncertainty of 0.118 °C and the combined uncertainty for the inlet or the outlet mean fluid temperature was calculated according to Equation H 8. The combined uncertainty for the inlet or outlet mean fluid temperature was 0.080 °C

$$\delta T_{in} = \sqrt{\left(\frac{\delta T_{in,1}}{2}\right)^2 + \left(\frac{\delta T_{in,2}}{2}\right)^2} \quad \left| \text{Equation H 8} \right.$$

Mean Fluid Temperature at Specific measuring Locations

The mean fluid temperatures at the specific measuring positions was calculated as follows:

$$T_{ave,i} = \left(\frac{T_{out} - T_{in}}{L_s}\right)L_{,i} + T_{in} \quad \left| \text{Equation H 9} \right.$$

with its uncertainty given by:



$$\delta T_{ave,i}(x) = \sqrt{\left(\frac{\partial T_{ave,i}}{\partial T_{out}} \cdot \delta T_{out}\right)^2 + \left(\frac{\partial T_{ave,i}}{\partial T_{in}} \cdot \delta T_{in}\right)^2 + \left(\frac{\partial T_{ave,i}}{\partial L_s} \cdot \delta L_s\right)^2 + \left(\frac{\partial T_{ave,i}}{\partial L_i} \cdot \delta L_i\right)^2 + \left(\frac{\partial T_{ave,i}}{\partial T_{in}} \cdot \delta T_{in}\right)^2}$$

Equation H 10

$$\delta T_{ave,i}(x) = \sqrt{\left(\frac{L_i}{L_s} \cdot \delta T_{out}\right)^2 + \left(\frac{L_i}{L_s} \cdot \delta T_{in}\right)^2 + \left(-\frac{(T_{out} - T_{in}) \cdot L_i}{L_s^2} \cdot \delta L_s\right)^2 + \left(\frac{T_{out} - T_{in}}{L_s} \cdot \delta L_i\right)^2 + (\delta T_{in})^2}$$

Equation H 11

Hydraulic Diameter

The hydraulic diameter was calculated as follows:

$$D_h = \frac{4 \cdot A_c}{P} = \frac{2 \cdot H_c \cdot W_c}{H_c + W_c}$$

Equation H 12

with its uncertainty given by:

$$\delta D_h(x) = \sqrt{\left(\frac{\partial D_h}{\partial H_c} \cdot \delta H_c\right)^2 + \left(\frac{\partial D_h}{\partial W_c} \cdot \delta W_c\right)^2 + \left(\frac{\partial D_h}{\partial (H_c + W_c)} \cdot \delta (H_c + W_c)\right)^2}$$

Equation H 13

$$\delta D_h(x) = \sqrt{\left(\frac{W_c}{H_c + W_c} \cdot \delta H_c\right)^2 + \left(\frac{H_c}{H_c + W_c} \cdot \delta W_c\right)^2 + \left(\frac{H_c \cdot W_c}{(H_c + W_c)^2} \cdot \delta (H_c + W_c)\right)^2}$$

Equation H 14

Heat Input (Electric Heater)

The heat input energy was calculated as follows:

$$q_{in} = V \cdot I$$

Equation H 15

with the uncertainty given by:

$$\delta q = \sqrt{\left(\frac{\partial q}{\partial \Delta V} \cdot \delta \Delta V\right)^2 + \left(\frac{\partial q}{\partial I} \cdot \delta I\right)^2}$$

Equation H 16

$$\delta q = \sqrt{(I \cdot \delta \Delta V)^2 + (\Delta V \cdot \delta I)^2}$$

Equation H 17

Heater Area

The area of the heater element was calculated as follow:

$$A_{flux} = L_s \cdot W_s$$

Equation H 18

with the uncertainty given by:

$$\delta A_{flux} = \sqrt{\left(\frac{\partial A_{flux}}{\partial L_s} \delta L_s\right)^2 + \left(\frac{\partial A_{flux}}{\partial W_s} \delta W_s\right)^2}$$

Equation H 19

$$\delta A_{flux} = \sqrt{(W_s \cdot \delta L_s)^2 + (L_s \cdot \delta W_s)^2}$$

Equation H 20

Input Heat Flux

The input heat flux was calculated as follows:

$$Q_{in} = \frac{q}{A_{flux}}$$

Equation H 21

with the uncertainty given by:

$$\delta Q_{in} = \sqrt{\left(\frac{\partial Q_{in}}{\partial q} \cdot \delta q\right)^2 + \left(\frac{\partial Q_{in}}{\partial A_{flux}} \cdot \delta A_{flux}\right)^2}$$

Equation H 22

$$\delta Q_{in} = \sqrt{\left(\frac{\delta q}{A_{flux}}\right)^2 + \left(-\frac{q}{A_{flux}^2} \cdot \delta A_{flux}\right)^2}$$

Equation H 23

Reynolds Number

The Reynolds number was calculated as follows:

$$Re = \frac{\dot{m}}{D_h \cdot \mu_f}$$

Equation H 24

with the uncertainty given by:

$$\delta Re = \sqrt{\left(\frac{\partial Re}{\partial \dot{m}} \cdot \delta \dot{m}\right)^2 + \left(\frac{\partial Re}{\partial D_h} \cdot \delta D_h\right)^2 + \left(\frac{\partial Re}{\partial \mu_f} \cdot \delta \mu_f\right)^2}$$

Equation H 25

$$\begin{aligned} \delta Re &= \sqrt{\left(\frac{\delta \dot{m}}{D_h \cdot \mu_f}\right)^2 + \left(-\frac{\dot{m}}{\mu_f \cdot D_h^2} \cdot \delta D_h\right)^2 + \left(-\frac{\dot{m}}{D_h \cdot \mu_f^2} \cdot \delta \mu_f\right)^2} \end{aligned}$$

Equation H 26

Prandtl Number

The Prandtl number was calculated as follows:

$$Pr = \frac{\mu_f \cdot Cp_f}{k_f}$$

Equation H 27

with the uncertainty given by:

$$\delta Pr = \sqrt{\left(\frac{\partial Pr}{\partial \mu_f} \delta \mu_f\right)^2 + \left(\frac{\partial Pr}{\partial Cp_f} \delta Cp_f\right)^2 + \left(\frac{\partial Pr}{\partial k_f} \delta k_f\right)^2}$$

Equation H 28

$$\delta Pr = \sqrt{\left(\frac{Cp_f}{k_f} \delta \mu_f\right)^2 + \left(\frac{\mu_f}{k_f} \delta Cp_f\right)^2 + \left(\frac{\mu_f \cdot Cp_f}{k_f^2} \delta k_f\right)^2}$$

Equation H 29

Mean Fluid Velocity

The mean velocity of the fluid was calculated as follows:

$$V = \frac{\dot{m}}{A_c \cdot \rho_f}$$

Equation H 30

with the uncertainty given by:

$$\delta V = \sqrt{\left(\frac{\partial V}{\partial \dot{m}} \delta \dot{m}\right)^2 + \left(\frac{\partial V}{\partial A_c} \delta A_c\right)^2 + \left(\frac{\partial V}{\partial \rho_f} \delta \rho_f\right)^2}$$

Equation H 31

$$\delta V = \sqrt{\left(\frac{\delta \dot{m}}{A_c \cdot \rho_f}\right)^2 + \left(\frac{\dot{m}}{A_c^2 \cdot \rho_f} \delta A_c\right)^2 + \left(\frac{\dot{m}}{A_c \cdot \rho_f^2} \delta \rho_f\right)^2}$$

Equation H 32

Friction Factor

The friction factor was calculated as follows:

$$f = \frac{\Delta P \cdot D_h \cdot 2}{L_s \cdot \rho_f \cdot V^2}$$

Equation H 33

with the uncertainty given by:

$$\delta f$$

Equation H 34

$$\delta f = \sqrt{\left(\frac{D_h \cdot 2}{L_s \cdot \rho_f \cdot V^2} \delta \Delta P\right)^2 + \left(\frac{\Delta P \cdot 2}{L_s \cdot \rho_f \cdot V^2} \delta D_h\right)^2 + \left(-\frac{\Delta P \cdot D_h \cdot 2}{L_s^2 \cdot \rho_f \cdot V^2} \delta L_s\right)^2 + \left(-\frac{\Delta P \cdot D_h \cdot 2}{L_s \cdot \rho_f^2 \cdot V^2} \delta \rho_f\right)^2 + \left(-\frac{\Delta P \cdot D_h \cdot 2 \cdot 2}{L_s \cdot \rho_f \cdot V^3} \delta V\right)^2}$$

Equation H 35

Colburn J-Factor

The Colburn j-factor was calculated as follows:

$$j = \frac{Nu_{ave}}{Re \cdot Pr^{\frac{1}{3}}}$$

Equation H 36

with the uncertainty give by:

$$\delta j = \sqrt{\left(\frac{\partial j}{\partial Nu_{ave}} \delta Nu_{ave}\right)^2 + \left(\frac{\partial j}{\partial Re} \delta Re\right)^2 + \left(\frac{\partial j}{\partial Pr} \delta Pr\right)^2}$$

Equation H 37

δj

Equation H 38

Heat Out Through Fluid

The heat transfer through the fluid was calculated as follows:

$$Q_{out} = \dot{m} \cdot C_{p_f} \cdot (T_{out} - T_{in})$$

Equation H 39

with the uncertainty given by:

$$\delta Q_{out} = \sqrt{\left(\frac{\partial Q_{out}}{\partial \dot{m}} \delta \dot{m}\right)^2 + \left(\frac{\partial Q_{out}}{\partial C_{p_f}} \delta C_{p_f}\right)^2 + \left(\frac{\partial Q_{out}}{\partial (T_{out} - T_{in})} \delta (T_{out} - T_{in})\right)^2}$$

Equation H 40

$$\delta Q_{out} = \sqrt{\left(\frac{\delta \dot{m}}{C_{p_f} \cdot (T_{out} - T_{in})}\right)^2 + \left(\frac{\delta C_{p_f}}{\dot{m} \cdot (T_{out} - T_{in})}\right)^2 + \left(\frac{\delta (T_{out} - T_{in})}{C_{p_f} \cdot \dot{m}}\right)^2}$$

Equation H 41

H 5. UNCERTAINTY OF NUMERICAL MODEL – HEAT TRANSFER COEFFICIENT

The uncertainty of the heat transfer coefficient obtained from the numerical model had to be determined. The uncertainty of the heat transfer coefficient is a function of each individual uncertainty namely: the uncertainty of the dimensions of the test section cross-section; the uncertainty of the heat flux input; the uncertainty of the free stream temperature; and the uncertainty of the side and top temperatures. The effect that the uncertainty of each parameter had on the heat transfer coefficient was independently determined and thereafter it was combined using the root-sum-squared method to obtain the total uncertainty of the heat transfer coefficient. It was assumed that the uncertainty of each parameter had an independent effect on the uncertainty of the heat transfer coefficient and that the combination thereof would give the total uncertainty.

The same numerical model, as described in Section 5.2.2, was used (with the required adaptations made to determine the uncertainty effects) and hence a detailed discussion of the numerical model physics and boundary conditions is not required.

H 7.1 METHODOLOGY OF OBTAINING THE UNCERTAINTY

The uncertainty analysis was performed based for the range, and all combinations, of the heat transfer coefficient and the free stream temperature as shown in Table H.3, therefore a total of nine analyses were performed for each case. A base analysis was solved assuming all the boundary conditions were exact, this is termed the ideal case. Thereafter separate analyses were performed where each uncertainty contributing parameter adaptation was made to the ideal case. The heat transfer coefficient was iteratively changed until the side and top wall temperatures of the uncertainty case best matched that of the ideal case. The heat transfer coefficient at this point was then recorded and the uncertainty was determined from the difference based on the ideal case. The procedure was repeated for all combinations of the range as set out.

Table H.3 Parameter range used in the uncertainty analysis

Heat transfer coefficient, h, [W/m²K]	2500	13 750	25 000
Free stream temperature, T_{∞} [°C]	20	30	50

The magnitude of the uncertainty for each parameter is summarised in the Table H.4 below: The dimensional uncertainty was analysed using four cases, as shown in Figure H.2. The outer and microchannel inner walls were offset inwards and outwards by 0.005 mm each way. The uncertainty of the heat flux, free stream temperature and the side and top wall temperatures was determined based on the ideal geometry.

Table H.4 Summary of the uncertainty parameters



Parameter	Uncertainty
Dimensions	0.01 mm
Heat flux	0.121 W/cm ²
Free stream temperature	0.133 °C
Side and top wall temperatures	0.113 °C

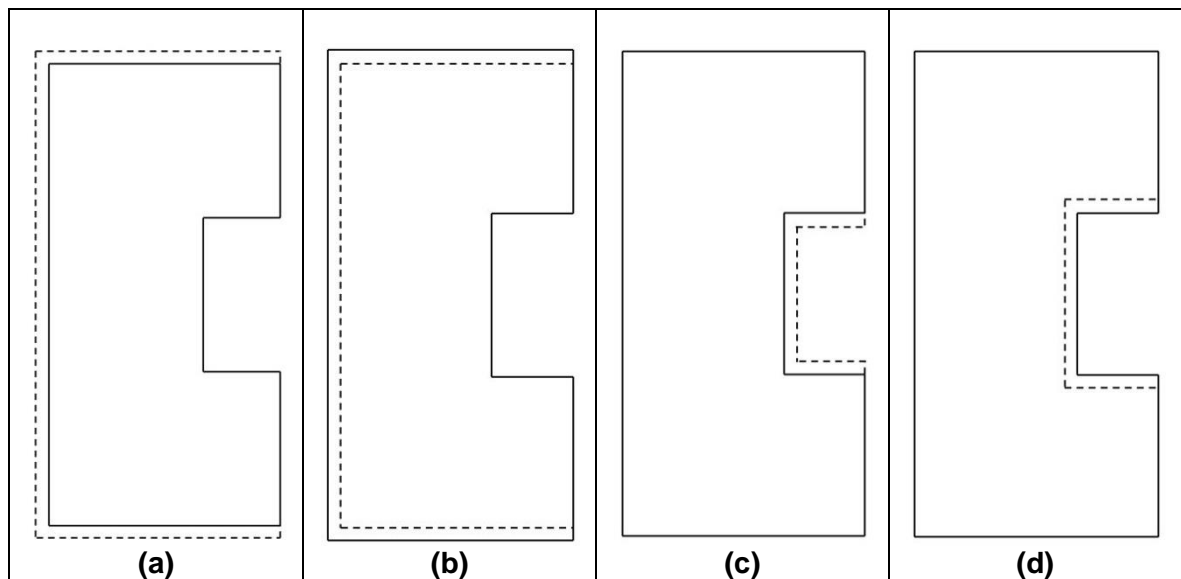


Figure H.2 Numerical model wall boundary adaption, (a) Outer walls offset 0.005 mm outwards, (b) Outer walls offset 0.005 mm inwards, (c) Microchannel inner walls offset 0.005 mm inwards, and (d) Microchannel inner walls offset 0.005 mm outwards

H 7.2 UNCERTAINTY RESULTS FOR THE HEAT TRANSFER COEFFICIENT

The combined uncertainty for the different free stream temperatures and heat transfer coefficient is presented in Figure H.3. It can be seen that the uncertainty increases as the heat transfer coefficient increases. The uncertainty at 2500 W/m²K differs the most between the different free steam temperatures, but at higher heat transfer coefficients the uncertainty is similar for the full range of free stream temperatures. The average uncertainty, over the free stream temperatures, is shown in Table H.5 and will be used further in the uncertainty calculations.

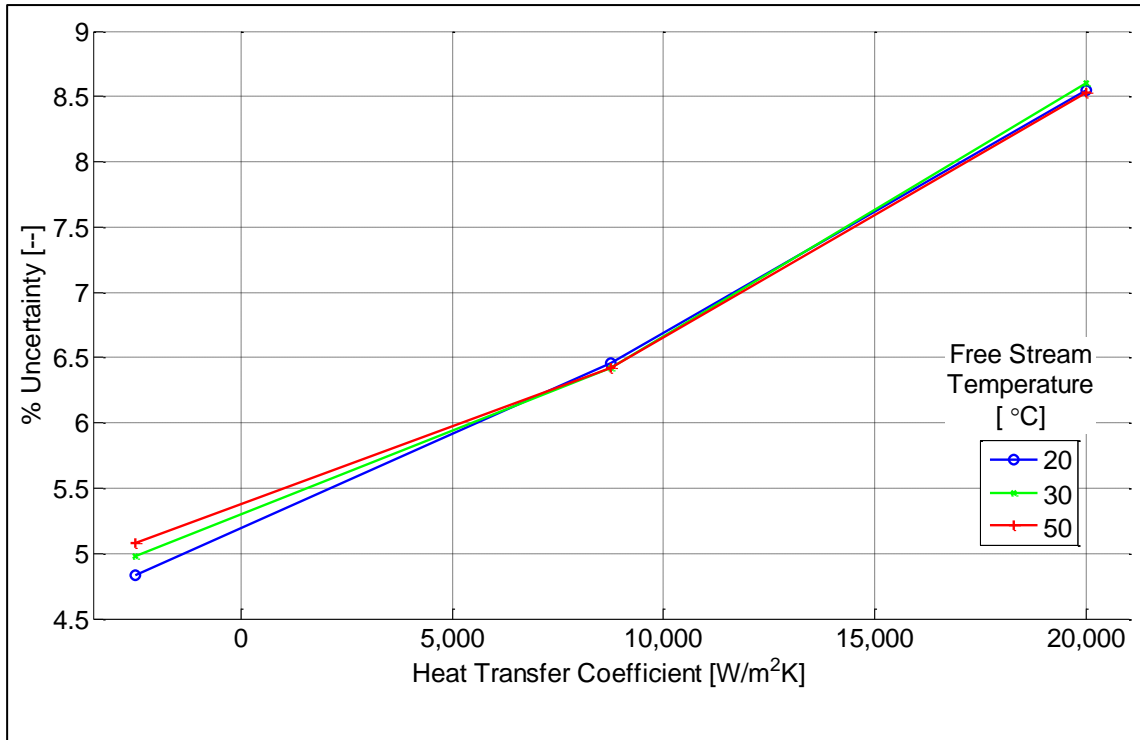


Figure H.3 Uncertainty of the heat transfer coefficient

Table H.5 Average uncertainty across the heat transfer coefficient range

Heat Transfer coefficient, h , [W/m ² K]	2 500	13 750	25 000
Uncertainty [%]	4.963	6.433	8.561

H 7.3 UNCERTAINTY OF THE NUSSLETT NUMBER

The local Nusselt number was calculated as follows:

$$N_{u,local}(x) = \frac{h(x) \cdot D_h}{k_f(x)}$$

Equation H 42

with the uncertainty given by:

$$\delta N_{u,local}(x) = \sqrt{\left(\frac{\partial N_{u,local}(x)}{\partial h(x)} \delta h\right)^2 + \left(\frac{\partial N_{u,local}(x)}{\partial D_h} \delta D_h\right)^2 + \left(\frac{\partial N_{u,local}(x)}{\partial k_f(x)} \delta k_f\right)^2}$$

Equation H 43

$$\delta N_{u,local}(x) = \sqrt{\left(\frac{D_h}{k_f(x)} \delta h\right)^2 + \left(\frac{h(x)}{k_f(x)} \delta D_h\right)^2 + \left(-\frac{h(x) \cdot D_h}{k_f(x)^2} \delta k_f\right)^2}$$

Equation H 44

The average heat transfer coefficient was calculated as follows:

$$h_{ave} = \frac{h(x_1) + \dots + h(x_n)}{n}$$

Equation H 45

with the uncertainty given by:

$$\delta h_{ave} = \sqrt{\left(\frac{\partial h_{ave}}{\partial h(x_1)} \delta h(x_1)\right)^2 + \dots + \left(\frac{\partial h_{ave}}{\partial h(x_n)} \delta h(x_n)\right)^2}$$

Equation H 46

$$\delta h_{ave} = \sqrt{\left(\frac{\delta h(x_1)}{n}\right)^2 + \dots + \left(\frac{\delta h(x_n)}{n}\right)^2}$$

Equation H 47

The average heat transfer coefficient was calculated as follows:

$$N_{u,ave} = \frac{h_{ave} \cdot D_h}{k_{f,ave}}$$

Equation H 48

with the uncertainty given by:

$$\delta N_{ave} = \sqrt{\left(\frac{\partial N_{ave}}{\partial h_{ave}} \delta h_{ave}\right)^2 + \left(\frac{\partial N_{ave}}{\partial D_h} \delta D_h\right)^2 + \left(\frac{\partial N_{ave}}{\partial k_{f,ave}} \delta k_{f,ave}\right)^2}$$

Equation H 49

$$\delta N_{ave} = \sqrt{\left(\frac{D_h}{k_{f,ave}} \delta h\right)^2 + \left(\frac{h_{ave}}{k_{f,ave}} \delta D_h\right)^2 + \left(-\frac{h_{ave} \cdot D_h}{k_{f,ave}^2} \delta k_{f,ave}\right)^2}$$

Equation H 50

H 7. CONCLUSION AND UNCERTAINTY RESULTS

The uncertainty for the heat transfer and hydrodynamic parameters was determined in this chapter. The uncertainties of the parameters discussed are presented for in Table H6 for the specific range:

Table H.6 Uncertainties of equations used for the specified range

Heat transfer or hydrodynamic parameter	Range	Uncertainty
<i>Re</i>	200 – 2300	2.02 % - 2.00 %
<i>Pr</i>	~5.4	1.00 %
<i>f</i>	0.02 – 0.15	5.29 % - 9.96 %
<i>j</i>	0.011 – 0.0050	3.29 % - 2.12 %
<i>h_{local}</i>	2500 – 25000W/m ² K	4.96 % - 8.51 %
<i>Nu_{local}</i>	2.03 – 20.33	5.62 % - 8.96 %
<i>h_{ave}</i>	2500 –	2.48 %- 4.28 %



	$25000\text{W/m}^2\text{K}$	
Nu_{ave}	2.03 – 20.33	3.62 % - 5.03 %